Development of UV-Visible Light Active Photocatalysts for Hydrogen Production from Renewable

Doctor of Philosophy

By

Imran Majeed

Inorganic/Analytical Section

Department of Chemistry

Quaid-i-Azam University, Islamabad 45320

Pakistan

2017

Development of UV-Visible Light Active Photocatalysts for Hydrogen Production from Renewable

This dissertation is submitted to the Department of Chemistry, Quaid-i-Azam University, Islamabad, in partial fulfilment of the requirements for the degree of "Doctor of Philosophy" in Inorganic Chemistry

By

Imran Majeed

Inorganic/Analytical Section

Department of Chemistry,

Quaid-i-Azam University, Islamabad 45320,

Pakistan

2017

DEDICATION

This thesis is dedicated to my parents especially my mother who has never failed to give me moral support, and all of my other family members especially Dr. Muhammad Amtiaz Nadeem for his untiring efforts to achieve this milestone and financial support.

I also dedicate this thesis to Imran Khan as a philanthropist who, so for, has been one of the greatest sources of inspiration in my life**.**

Acknowledgment

With humble and most sincere words, I am thankful to **Almighty Allah**, the Beneficent and Merciful, Who bestowed me the potential and ability to contribute a drop of material in the existing ocean of knowledge. I pay humble but great admiration to the **Holy Prophet Hazrat Muhammad** (**PBUH**) who is forever a torch of knowledge and guidance for humanity as a whole.

It is difficult to overstate my gratitude to **Dr. Muhammad Arif Nadeem.** He, with his enthusiasm, his inspiration, and his patient efforts to explain things clearly and simply, helped me to make this thesis possible. Throughout my research and thesis writing period, he provided encouragement, sound advice, good teaching, and lots of good ideas.

I feel great contentment in expressing my incredible thanks to my encouraging and inspirational co-supervisor **Dr. Muhammad Amtiaz Nadeem** (Saudi Basic Industries Corporation (SABIC), Thwal, Saudi Arabia) for introducing me to this exciting field of photocatalysis, whose exciting curiosity, worthy suggestions and discussions enabled me to complete this innovative work. It would have been much harder to accomplish this thesis without him.

I really appreciate the untiring efforts of **Dr. Amin Badshah,** Head of Analytical/Inorganic Chemistry Section, QAU, Islamabad and **Dr. Aamir Waseem** Associate Professor Chemistry Department, QAU, Islamabad during my Ph.D studies.

I am thankful to Chairman, Department of Chemistry **Dr. M Siddiq,** QAU, Islamabad, for providing necessary research facilities.

I would like to thank those people who have contributed to my understanding of science: all of my high school teachers who taught me fundamentals of science, my primary school teacher **Muhammad Yasin** who taught me to read and write when I was a kid.

I would like to express my inmost obligations to my Ph.D and M.Phil colleagues, **M. Aamir Hafeez, Mr. Ejaz Hussain, Mr. Hassan Ali, Mr. Jahanzaib Arshad, Mr. Abdul Hafeez, Syed Waqas Ali Shah, Uzma Manzoor, Shiasta Ibrahim and Umair Shamraiz,** for their moral support, fruitful suggestions and discussions and unutterable cooperation during my research work. This all is the fruit of untiring, lots of prayers, encouragement and guidance, moral and financial support of my respectable and loving parents and other family members.

Imran Majeed

Abstract

The development of the "hydrogen economy" requires new technologies for H_2 generation, of which photocatalytic water splitting by using visible light has been viewed as most promising pathway. In present study, the photocatalysts ranging from simple metal oxides and metal sulfides to more complicated systems have been studied to achieve suitable H_2 production rates from water splitting reaction The hydrogen production from water in the presence of other renewable (ethanol, glycerol, triethanolamine and ethanol water-electrolyte mixtures) were studied over three different semiconductor (TiO_2, CdS and an emerging g-C_3N_4) supports based photocatalysts. All the synthesized catalysts were characterized by various analytical techniques such as Powder X-ray Diffraction (PXRD) for determination of crystal phase composition and purity, X-ray Photoelectron Spectroscopy (XPS) for surface elemental composition, Diffused Reflectance UV-visible Spectroscopy (DRS) for optical properties, Transmission Electron Microscopy (TEM) and Scanning Electron Microscopy for particle size distribution and morphology, Photoluminescence (PL) for electron dynamics, Energy dispersive spectroscopy (EDS), Inductively Coupled Plasma Optical Emission spectroscopy (ICP-OES) and X-ray Fluorescence (XRF) for elemental composition, Brunauer Emmett Teller (BET) for surface area calculation and Thermogravimetric analysis (TGA) to study changes in physical and chemical properties of materials as a function of temperature. Hydrogen production for each photoreaction was measured by Gas Chromatograph (GC) equipped with molecular sieve capillary column and TCD detector**.** In the first section, a series of novel non-noble metal supported semiconductor photocatalysts; $Cu(OH)_2$–$Ni(OH)_2$/P25 (P25=80% anatase +20% rutile) and $Cu(OH)_2$–$Ni(OH)_2$/TNR (TNR = Titania nanorods) were prepared by co-deposition–precipitation method (total metal loading ca. 1.0 wt%) and their performance was evaluated for H_2 production. Among this series, the 0.8$Cu(OH)_2$–0.2$Ni(OH)_2$/P25 photocatalyst showed H_2 production rate of 10 and 22 mmol $h^{-1}g^{-1}$, in 20 vol% ethanol-water and 5 vol% glycerol-water mixtures, respectively. The 0.8$Cu(OH)_2$–0.2$Ni(OH)_2$/TNR photocatalyst demonstrated very high H_2 production rates of 26.6 and 35.1 mmol $h^{-1}g^{-1}$ in 20 vol% ethanol-water and 5 vol% glycerol-water mixtures, respectively. The mechanism for high hydrogen production rate over bimetallic hydroxide supported TiO_2 is investigated and established with various experimental evidences. Followed by this, a new strategy was developed to produce highly dispersed Cu and Cu_2O nanoparticles over TiO_2 by using MOF-199 $[Cu_3(BTC)_2(H_2O)_3]_n$ as a source of copper nanoparticles. The photocatalyst 1 wt% Cu/TiO_2-400 showed a hydrogen production rate

some 2.5 times higher than that of CuO deposited over TiO_2 by conventional precipitation methods. In the second section, highly crystalline and photocatalytically active hexagonal CdS nano-support was synthesized by sol-gel method and subsequently calcination in an inert atmosphere of nitrogen. Au nanoparticles were deposited over this hexagonal CdS by a novel reductive deposition KI method involving reduction of Au^{3+} ions with iodide ions and used as a model to test the effect of metal particle size as well as the reaction medium on hydrogen production activity. The photocatalyst 3 wt.% Au/CdS showed the highest performance (ca. 1 molecule of $H_2/Au_{atom}S^{-1}$) under visible light irradiation from water electrolyte medium (0.1M Na_2S–0.02 Na_2SO_3; pH 13) (92%)—ethanol (8%). The validity of this new Au loading method was established by comparing it with three other conventional methods including; deposition precipitation (DP), incipient wet impregnation (WI) and photo-deposition (PD). TEM studies of fresh and used catalysts showed that Au particle size increases (almost 5 fold) with increasing photo-irradiation time due to photo-agglomeration effect and yet no sign of deactivation was observed. A mechanism for hydrogen production from ethanol water-electrolyte mixture is presented and discussed by evaluating some intermediate formed. It is found that Au/CdS photocatalyst showing higher plasmonic effect did not necessarily produced more hydrogen in visible light range. This work also supports the electron transfer mechanism from semiconductor to metal which may further be facilitated by metal to semiconductor energy transfer mechanism due to Au surface plasmon resonance. Finally, in third section, g-C_3N_4 was synthesized by thermal condensation of melamine at various temperatures to get close packing and strong interlayers binding of *g*-C_3N_4. Pd and Ag bimetallic as well as monometallic nanoparticles were deposited to cope with two inherent drawbacks of g-C_3N_4; low visible light absorption and high recombination rate of photogenerated charge carriers. High activity of Pd-Ag/*g*-C_3N_4 photocatalyst was attributed to inherent property of palladium metal to quench photogenerated electrons by schottky barrier formation mechanism and strong silver absorption in visible range by surface plasmon resonance mechanism (SPR).

List of Publications

This thesis is based on following publications;

1- **I. Majeed,** M. Amtiaz Nadeem, M. Al-Oufi, M. Arif Nadeem, G.I.N. Waterhouse, A. Badshah, J.B. Metson, Hicham Idriss, "On the role of metal particle size and surface coverage for photo-catalytic hydrogen production: A case study of the Au/CdS system" J. Appl. Catal. B: Environ. 182 (2016) 266-276.

2- **I. Majeed**, M. Amtiaz Nadeem, E. Hussain, M. Arif Nadeem, A. Badshah, A. Iqbal, H. Idriss, Geoffrey IN Waterhouse, MA Nadeem "On the Synergism between Cu and Ni for Photocatalytic Hydrogen Production and their Potential as Substitutes of Noble Metals' ChemCatChem 8(2016)3146-3155.

3- **I. Majeed**, M. Amtiaz Nadeem, A. Badshah, Fehmida K. Kanodarwala, Hassan Ali, M. Abdullah Khan, John Arron Stride and M. Arif Nadeem, "Titania supported MOF-199 derived Cu–Cu_2O nanoparticles: highly efficient non-noble metal photocatalysts for hydrogen production from alcohol–water mixtures" Catal., Sci. Technol. 7(2017)677-686.

4- **I. Majeed,** M. Amtiaz Nadeem, E. Hussain, A. Badshah, R. Gilani, M. Arif Nadeem, "Effect of deposition method on metal loading and photocatalytic activity of Au/CdS for hydrogen production in water electrolyte mixture" Int. J. Hydrogen Energy 5(2017)3006-3018.

5- **I. Majeed,** Fehmida K. Kanodarwala, M. Amtiaz Nadeem, E. Hussain, A. Badshah, I. Hussain, J. Arron Stride, and M. Arif Nadeem, "Controlled synthesis of titania nanostructures: Exceptional hydrogen production in alcohol-water mixtures over $Cu(OH)_2$–$Ni(OH)_2$/Titania nanorods photocatalysts" Chem. Select 2(2017) 7497-7507

6- M. A. Nadeem1, **I. Majeed,** G. I. N. Waterhouse and H. Idriss, "Study of ethanol reactions on H_2 reduced Au/TiO_2 anatase and rutile: effect of metal loading on reaction selectivity" Catal." Struct. React. 1(2015) 61-70.

7- E Hussain, **I Majeed**, M Amtiaz Nadeem, A Badshah, Yuxiang Chen, M Arif Nadeem, Rongchao Jin, "Titania-Supported Palladium/Strontium Nanoparticles (Pd/Sr-NPs@ P25) for Photocatalytic H_2 Production from Water Splitting" J. Phys. Chem. C 120(2016), 17205-17213.

8- **I. Majeed**, U. Manzoor, M. Amtiaz Nadeem, E. Hussain, H. Ali, F.K. Kanodarwala, J. Arron Stride and M. Arif Nadeem, "Pd–Ag bimetallic nanoparticles decorated *g*-C_3N_4 for highly efficient H_2 production from water under visible light irradiation" Catalysis Science and Technology (2017) in press

9- **I. Majeed,** M. Amtiaz Nadeem, H. Idriss, M. Arif Nadeem, A. Badshah, "Principles, mechanisms and latest trends in water splitting on TiO_2 based catalysts" (a review). Ready for submission

Related publications during PhD studies;

1- A Ajmal, **I Majeed**, RN Malik, M Iqbal, M Arif Nadeem, I Hussain, S Yousaf, G Mustafa, MI Zafar, M Amtiaz Nadeem, "Photocatalytic degradation of textile dyes on Cu_2O-CuO/TiO_2 anatase powders" J. Environ. Chem. Eng. 4 (2016), 2138-2146.

2- A. Ajmal, **I. Majeed,** R. Naseem Malik, H. Idriss, M. Amtiaz Nadeem,"Principles and mechanisms of photocatalytic dye degradation on TiO_2 based photocatalysts: A comparative overview" RSC Advances 4(2014)37003-37026.

3- H. Ali, Fehmida K Kanodarwala, **I. Majeed**, J. Arron Stride, M. Arif Nadeem, "La_2O_3 Promoted Pd/rGO Electro-catalysts for Formic Acid Oxidation" ACS Appl. Mater. Interf. 8 (2016), 32581-32590.

4- Hassan Ali, Shahid Zaman, **Imran Majeed**, Fehmida K Kanodarwala, Muhammad Amtiaz Nadeem, John Arron Stride, Muhammad Arif Nadeem, "Porous Carbon/rGO Composite: An Ideal Support Material of Highly Efficient Palladium Electrocatalysts for the Formic Acid Oxidation Reaction" ChemElectroChem DOI: 10.1002/celc.201700879

Table of Contents

List of Figures

List of Tables

List of Schemes

List of Abbreviations

Arbitrary Unit	AU
Band Gap	E_g
Semiconductor	SC
Watt	W
Joule	J
Brunauer - Emmett – Teller	BET
Full Width at Half Maximum	FWHM
High Resolution Transmission Electron Microscopy	HRTEM
Internal Diameter	ID
Localized Surface Plasmon	LSP
Localized Surface Plasmon Resonance	LSPR
Normal Hydrogen Electrode	NHE
Scanning Electron Microscopy	SEM
Surface Plasmon	SP
Surface Plasmon Resonance	SPR
Time of Flight	TOF
Transmission Electron Spectroscopy	TEM
Ultra-violet	UV
Ultra-violet Visible	UV-Vis
Valence Band	VB
Conduction Band	CB
X-ray Photoelectron Spectroscopy	XPS
Diffused Reflectance Spectroscopy	DRS
Standard Hydrogen Electrode	SHE

Quantum Efficiency	QE
Benzene-1,3,5-Tricarboxylic Acid	BTC
Dimethylformamide	DMF
Energy Dispersive X-Ray	EDX
Inductively Coupled Plasma Optical Emission Spectroscopy	ICP-OES
Local Magnetic Moment	LMM
Metal-Organic Frameworks	MOFs
Potency of Hydrogen	pH
Powder X-Ray Diffraction	PXRD
Triethylamine	TEA
Point of Zero Charge	PZC
Electron Donors	EDs
Electron Paramagnetic Resonance	EPR
Photoluminescence	PL
Face-centred cubic	FCC
Conduction Band Minimum	CBM
Valence Band Maximum	VBM
Carbon Nanotubes	CNTs
Titania Nanorods	TNR
Titania Nanoleaves	TNL
Gas Chromatograph	GC
Thermal Conductivity Detector	TCD
Interfacial Charge Transfer	IFCT
Fast Fourier Transforms	FFT
Photodeposition	PD
Wet Impregnation	WI

Deposition Precipitation	DP
Mega Joule	MJ
Binding Energy	E_b
Hexagonal Cadmium Sulfide	h-CdS
Cubic Cadmium Sulfide	c-CdS
Graphitic Carbon Nitride	g-C_3N_4
Barrett-Joyner-Halenda	BJH

Chapter # 1

Introduction

Chapter-1 Introduction

It has been envisaged from last fifty years that a hydrogen economy will achieve a pinnacle at which hydrogen will finally replace the fossil fuels as a major energy carrier. A hydrogen era when fossil fuels used for electricity generation, transportation and chemical synthesis will be replaced by hydrogen is a long viewed dream whose fulfillment demands more technological advancements in H_2 generation, distribution and storage [1-3]. Scale up hydrogen production required to meet the current and future demands is a sizeable goal for ever growing human population predicted to increase up to 9 billion by 2048. Hydrogen is an attractive, sustainable and clean energy carrier with water is the only combustion product, provided it is generated from water splitting or other renewable resources using direct sunlight, because of the energy crisis caused by the depletion of fossil fuel reserves. Almost 85 percent of total world's energy is coming from fossil fuels. In spite of colossus research undertaken over the last three decades, the hydrogen production activity of photocatalysts reported to date from water splitting is too low to justify industrial applications. There are consistent fruitful advancements have been undertaken in photocatalysts, though more work is required to meet the targeted H_2 production rates of 120-130 mmol $h^{-1}g^{-1}$ at minimum sacrificial reagents concentrations that are needed to attract industrial interest [4]. Currently steam reforming of hydrocarbons is the largest and most economical way to yield H_2 [5] but this process generates a large amounts of carbon dioxide that is a cause of serious global warming [6]. However, exploitation and utilization of fossil fuels over a period of about 150 years, generates the combustion products that are causing serious global problems such as, greenhouse effect [7], ozone layer depletion, acid rains and pollution etc. [8]. Hydrogen, with large specific energy density, produces heat (122 MJ/Kg) more than gasoline 44 (MJ/Kg) and can also be used in fuel cells for electricity production [9, 10]. It is rapidly emerging as a sustainable and the cleanest energy source for the transportation and industrial utilities [11]. On industrial use, currently, hydrogen is non-renewable which is obtained from fossil fuels [12-18], but could in principle be generated from renewable resources such as biomass [19, 20] and water [21-26].

Fabrication of UV-visible light active photocatalysts to generate hydrogen by water splitting under solar irradiation is an attractive and environmental friendly method, which offers a way for capturing available solar energy and converting it into hydrogen [27-32]. At a power level of 1000 W/m^2, the solar energy reaches on the earth's surface by far exceeds all human energy needs [2]. The amount of energy striking the Earth from sunlight in one hour

(4.3×10^{20} J) is more than the total energy consumed on this planet in one year (4.1×10^{20} J) [33]. Since the first report on photocatalytic water splitting on TiO_2 electrodes photocatalysis have been demonstrating wide range potential applications in areas such as solar energy conversion, recycling polluted water or air, and so on [34-36]. A wide range of semiconductor photocatalysts have been evaluated in relation to H_2 production via water splitting in the presence of sacrificial agents, including oxides, oxynitrides, oxysulfides, nitrides, sulphides and others [37-42]. However, very little number of materials fulfills the basic requirements for sustainable hydrogen production from water splitting. Until now, over 130 inorganic materials and their derivatives have been applied to generate hydrogen gas through water splitting [25]. So far, no material capable of catalyzing water splitting reaction with a QE larger than 10% in visible light has been found [43, 44]. Theoretically, the lowest limit of energy required to split water is 1.23 eV but, due to energy losses, energies higher than ~2.0 eV are most common for efficient water splitting [45].

However, semiconductors with the band gap of 2.0-2.5 eV are either chemically or photochemically unstable in aqueous media. Some semiconductors have other serious drawbacks such as large overpotential for H_2 and O_2 evolution from water, too rapid recombination rate of photoinduced electron (e^-) and hole (h^+), fast thermal back reaction of H_2 and O_2 to produce H_2O and their ability to make use of available sunlight. Most of the semiconductors materials can only absorb in UV range less than 400 nm [46, 47]. Sunlight consists of 4% ultraviolet (UV) light (300-400 nm), 43% visible light (400-700 nm) and 52% infrared light (700–2500 nm) [48, 49]. In order to overcome these problem, many methods have been proposed to enhance the photocatalytic activity, including the doping of metals [50-53] and non-metal ions, deposition of noble metals, surface sensitization with dyes, addition of a holes scavenger or sacrificial electron donor and the preparation of composite semiconductors [54-58]. Major focus of research on semiconductor photocatalysts is towards three objectives; (i) to achieve tailored photoactivity and selectivity, (ii) to improve the photoefficiency, and (iii) to extend the photoresponse towards visible light region [59-61]. Presently approximately half of the total amount of hydrogen produced in the world (about 30 million metric tons/year) is utilized in ammonia synthesis. If hydrogen could be made from water, then ammonia and fertilizers could be made from totally renewable sources (nitrogen and water). Jules Verne's prediction in "The Mysterious Island" that water would be the fuel of the future could be realised [62].

1.1 Basic requirements for water splitting

1.1.1 Thermodynamic considerations

In order to achieve thermodynamically non-spontaneous, stoichiometric water splitting, band gap of photocatalyst should be wide enough (>1.23 eV) with appropriate band position to overcome energy barrier to drive H_2O reduction and oxidation and as narrow as possible to absorb wider wavelength range of readily available sunlight. Overall water splitting reactions occurring on the semiconductor surface can be described as under;

$$SC \xrightarrow{h\nu \geq E_{bg}} e^- + h^+ \quad (1)$$

$$\boldsymbol{2H_2O + 2e^-_{CB} \rightarrow H_2 + 2OH^-} \quad E^o = 0.0\ V \quad (2)$$

$$\boldsymbol{2OH^- + 2h^+_{VB} \rightarrow {}^1\!/_2\, O_2 + H_2O} \quad E^o = 1.23\ V \quad (3)$$

$$H_2O \xrightarrow{h\nu \geq E_{bg}} H_2 + {}^1\!/_2 O_2 \quad \Delta G = +\ 237\ kJ\ mol^{-1} \quad (4)$$

$$e^- + h^+ \rightarrow heat \quad (5)$$

In theory, water splitting will occur if the conduction band potential is more negative than reduction potential of proton E^o (H^+/H_2) (0.0 V versus NHE) and valence band potential is more positive than the oxidation potential of water E^o (O_2/H_2O) (1.23 V versus NHE). Band edge position can theoretically be determined using following equations at the point of zero charge (pH_{zpc}) [63, 64].

$$E_{CB} = \chi - E^e - {}^1\!/_2 E_g \quad (6)$$

$$E_{VB} = E_{CB} + E_g \quad (7)$$

Where E_{CB} and E_{VB} are the conduction band and valence band edge potential respectively, χ is the electronegativity of the semiconductor, expressed as the geometric mean of the absolute electronegativity of the constituent atoms, which is defined as the arithmetic mean of the atomic electron affinity and the first ionization energy. E^e is the energy of free electrons on the hydrogen scale ca. 4.5 eV. E_g is the band gap of the semiconductor [65]. A schematic diagram of this process is shown in (fig.1.1). Band positions of some famous semiconductors are shown in (fig. 1.2).

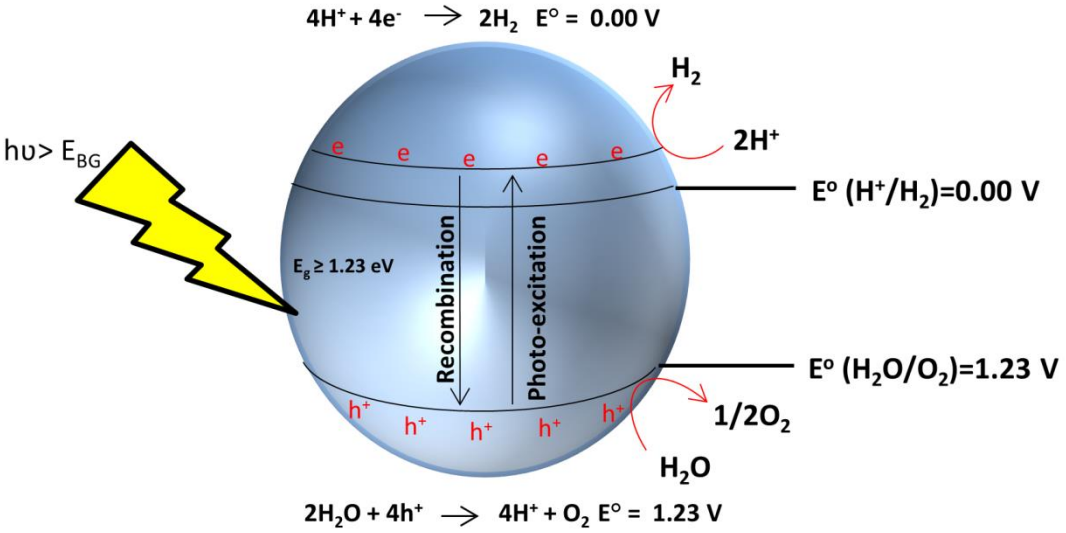

Figure 1.1: Schematic representation of hydrogen production mechanism from water splitting over semiconductor surface.

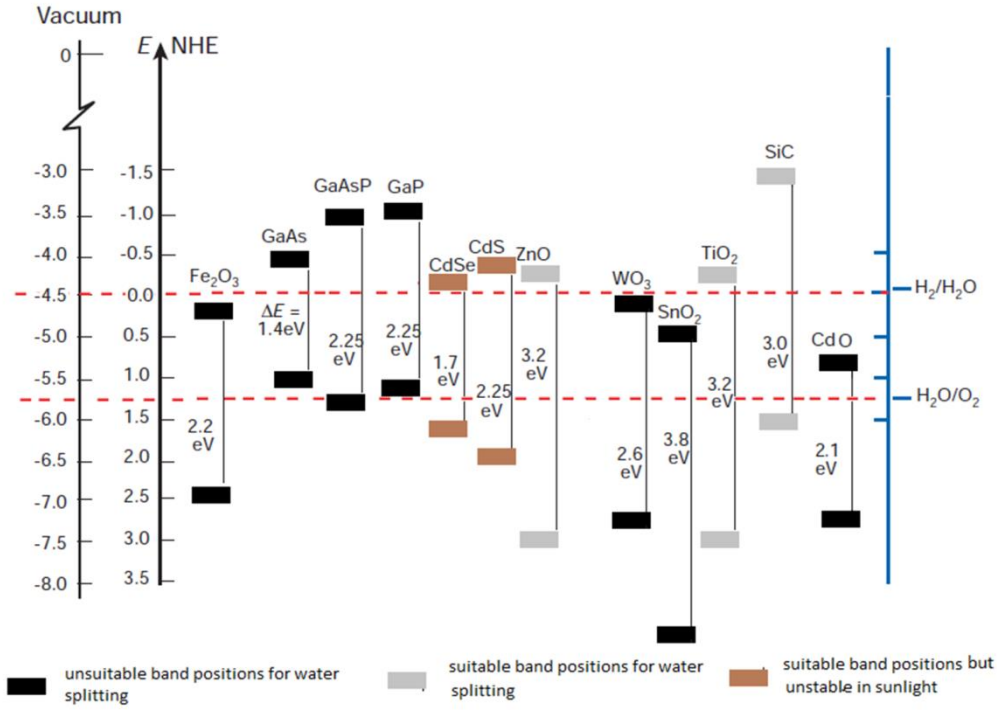

Figure 1.2: Calculated energy positions of conduction band edges and valence band edges at pH=0 for some selected semiconductors, modified from the references [66, 67].

1.1.2 Realistic considerations

From a thermodynamic point of view, any semiconductor that satisfies the above-mentioned requirements can be used for water splitting. However, under realistic conditions other

considerations including surface area, absorption coefficient, chemical stability, photo-corrosion, overpotential, electron-hole pair recombination rate and their mobility also become important [68]. The reaction rate depends on how efficiently electrons and holes move to the surface of the catalyst and are subsequently transferred to the reactants at the surface before they recombine [45, 69, 70]. Thus, suitable surface and bulk properties are required for effective photocatalysis [71].

1.2 Drawbacks of semiconductor photocatalysts for hydrogen production

Albeit the photocatalytic activity of various semiconductors can be increased by optimizing the crystal structure and chemical and physical properties, but semiconductor photocatalysts still have some serious drawbacks for photocatalytic hydrogen production from water splitting. These can be (i) a large overpotential for H_2 evolution over semiconductor surface alone [72] (ii) very high recombination rate of photogenerated charge carriers before migrating to the surface to take part in photoreactions. Time-resolved spectroscopy results have revealed that ~ 90% of photogenerated charge carriers recombine after excitation in TiO_2 [73] (iii) the rapid thermal back recombination reaction of H_2 and O_2 to produce H_2O [74]. The splitting of water into H_2 and O_2 is an uphill energy demanding process, so the backward reaction is highly favourable (iv) the inability to make use of visible light by many wide band gap semiconductors. The band gap of most studied semiconductor TiO_2 is about 3.2 eV which makes it to excite in UV light only and sunlight comprises only ca. 4–5% of UV light.

1.3 Strategies to overcome the drawbacks of semiconductor photocatalyts for hydrogen production

Many efforts have been devoted to enhance photocatalytic activity of semiconductor photocatalysts for water splitting. Surface modifications (loading) seem preferable to bulk modifications (doping), since the doping may act as recombination centers in the crystalline structure, which results a decrease in photocatalytic activity. Most effective strategies include; noble metal loading, addition of sacrificial reagents as electron donor and heterogeneous coupling of semiconductors with suitable band positions to reduce e^-/h^+ recombination. Dye sensitization and cation/anion doping are also among the widely studied approaches in wide band gap semiconductors to extend their photoresponse in visible light, as for TiO_2 but their effectiveness is limited due to photo-leaching of the dye or much reduced

electron hole separation in the presence of doped species. Loading of stable transition metals on semiconductor materials and addition of sacrificial electron donors are two most widely used strategy to overcome charge carriers recombination.

1.3.1 Metal loading

The surface deposited metal islands reduce the e^-/h^+ recombination process by quenching the electrons from the semiconductor conduction band [75] and are usually very stable even under photoirradiation in an aerated atmosphere [76-82]. It has been proposed that there is an optimum loading concentration (less than 4 wt. %), above which the observed photocatalytic activity decreases [83]. Larger amount of metal leads to a drastic decrease on the photocatalytic activity which may have a contribution from metal shadowing effects to reduce the light absorption by the semiconductor and possibility that metal loading above the optimum value may cause the metal deposits to behave as recombination sites due to an excessive negative charge accumulation, which can attract positive holes [84, 85]. There are two basic mechanisms by which metals increase the photocatalytic activity of semiconductor photocatalysts.

1.3.1.1 Schottky barrier formation mechanism

The semiconductor-metal system represents a good example illustrating space charge layers, band bending, and the formation of a Schottky barrier as shown in fig. 1.3. The highly improved separation of photogenerated charge carriers is achieved in metal-semiconductor composites by the formation of rectifying Schottky barrier at the interface due to energy difference between the conduction band of semiconductor and work function of the metal [86-90].

$$H = W_M - (W_{SC} + E_F - E_{CB}) \quad (8)$$

$$W_{sc} + E_F - E_{CB} = q_\chi \quad (9)$$

$$H = W_M - q_\chi [91] \quad (10)$$

Where H, W_M, W_{SC}, E_{CB}, E_F, and q_χ represent the barrier height, metal work function, semiconductor work function, fermi level energy, conduction band energy and electron affinity. Deposition of Ni, Cu, Ag, Pd, Pt or Au on semiconductor creates rectifying Schottky junctions, the formation of which is highly beneficial for hydrogen evolution as the fermi level (E_F) for each metal lies between the bottom of the TiO_2, CdS and g-C_3N_4 conduction band and the H_2O/H_2 redox couple (for 5 nm Au nanoparticles on TiO_2, E_F = -0.27 V) [38]. The schottky barriers with different heights are formed depending on the nature of metal

loading [70, 92-97]. This barrier only allows the one way traffic of electrons from bulk of semiconductor to metal until their Fermi levels (E_{Fs}) are aligned, a thermodynamic equilibrium is reached. When the photocatalyst is further exposed to light source, the photogenerated electrons can cause a shift of the E_F of semiconductor to form a new quasi-fermi level (E_F*) [98]. At the same time, the previously formed thermodynamic equilibrium state is destroyed and consequently the electrons continuously migrate from the semiconductor to metal. By transfer of electron from semiconductor to metal the fermi level of metal semiconductor composites shifts to more negative potential depending on the size and nature of the nanoparticles [99-101]. Small size metal particles are more effective in upward shifting of fermi level [102]. Subramanian and co-workers observed a 60 mV shift in flat band potential in 3 nm diameter gold particles as compared to 20 mV shift in 8 nm Au nanoparticles [102]. A shift of 100 mV has been reported for 2 nm Au nanoparticles [103]. Jakob and co-workers observed a 20 mV shift in the fermi level of TiO_2 for 5 nm Au particles [104]. Since the energy levels in the smaller metal nanoparticles are discrete, a greater shift in the energy levels for accumulated electrons in metal nanoparticles is expected. Such a shift in the fermi level enhances the efficiency of interfacial electron transfer to adsorbed species on the catalyst surface and causes a large build up in the capacitance of the Helmholtz layer and the diffuse double layer. The excess electron density remains mainly on the metal islands because the Helmholtz capacitance of the metal-solution interface is much higher than the space charge capacity of the metal semiconductor nanoparticles interface, even under accumulation contact [105]. Hence, one can expect the metal fermi level to shift close to the bottom of the semiconductor conduction band [102, 104]. Thus the reduction of H^+ ions to H_2 is easier over the metal surface and more efficient than over bare semiconductor surface [99, 106, 107]. The position of the fermi level that lies between the valance and conduction bands is dependent on the electron accumulation within the semiconductor particles. The C_{60}/C_{60}^- redox couple is a convenient probe for determining the Fermi level of semiconductor particles [104]. S. Vaidyanathan and co-workers probed the C_{60}^- formation during the one electron transfer from UV-excited TiO_2 to C_{60} [108]. The work functions of the metals Pt, Pd, Au, Rh, Cu, and Ag are, 5.64, 5.12, 5.1, 4.98, 4.65, and 4.26 eV, respectively. The photocatalytic activities may be in accordance with the order of work function of metal used. It is found that Au, Pd and Pt are very active for the photocatalytic H_2 production when present over semiconductor surface which may be related to greater Schottky barrier height formed due to higher work functions [91, 109, 110]. These studies also elucidate the indirect role of metals in improving the charge separation as well as promoting the interfacial charge

transfer kinetics in semiconductor photocatalysis. The exact role of the metal is still under debate. Very recently, Joo and co-workers presented an alternative role of metal as atomic hydrogen recombination site rather than as an electron transfer site to proton from the semiconductor conduction band [111]. They presented a new model where the reduction of protons takes place by the transfer of excited electrons directly from the conduction band of the semiconductor and atomic hydrogen then moves to the metal and recombines to produce molecular hydrogen.

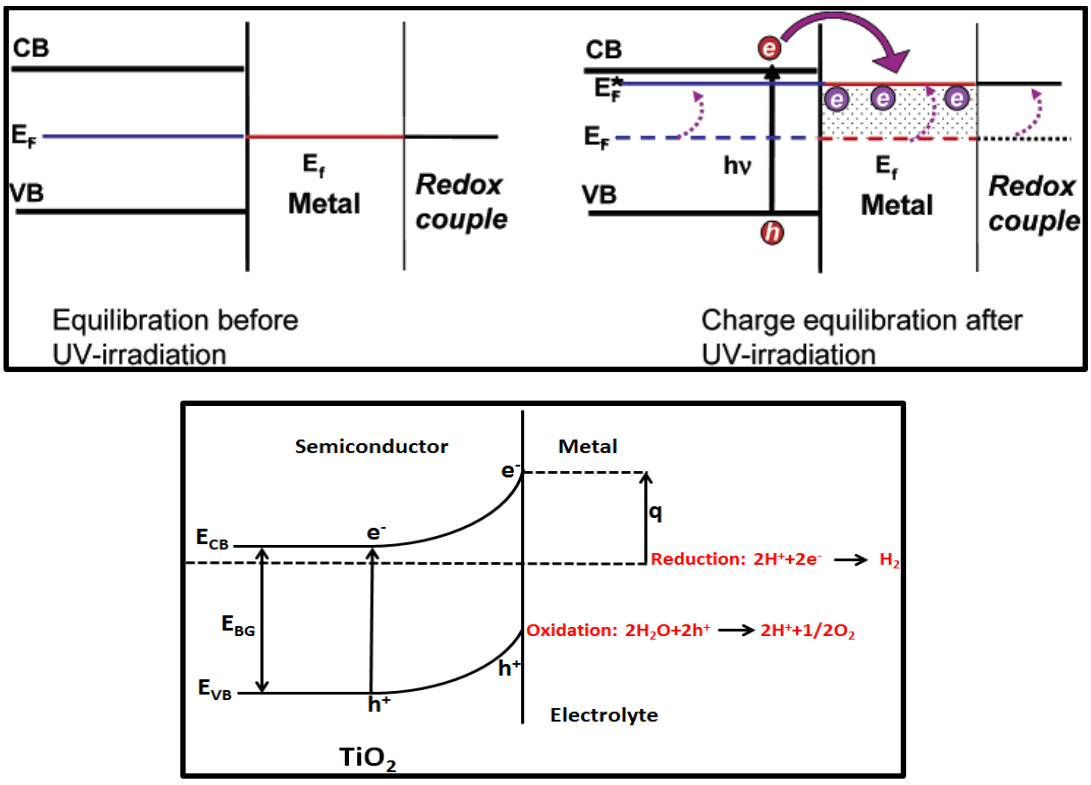

Figure 1.3: (Top) Charge distribution between TiO_2-metal nanoparticles leading to equilibration with the C_{60}/C_{60}^- redox couple, before and after UV irradiation, reproduced from ref. [102]. (Bottom) Mechanism of photocatalytic hydrogen generation over M/SC photocatalysts as a consequence of photogenerated e^-/h^+ pair and efficient charge separation induced by the Schottky barrier formation at the interface between metal nanoparticles with large work function and *n*-type semiconductors, modified from ref. [112, 113]

1.3.1.2 Surface plasmon mechanism

Surface plasmon resonance (SPR) can be described as the collective excitation of valence electrons of metals oscillating against the restoring force of positive nuclei when the frequency of impinging photons matches the natural frequency of these electrons. The resonant photon wavelength is different for different metals [114, 115]. These are few metals

which show resonance in the visible region; Au, Pd, Cu, Pt, and Ag. Among these Au and Ag are mostly studied as strong plasmonic metals in this regard [116, 117] while Pd and Pt show very weak surface plasmon effects. Cu is also a good SPR metal but it is not stable because of the formation of surface oxides [118]. Surface plasmon effect is shown by metals only in their zero oxidation states [7, 119]. The position of SPR absorption of metal nanoparticles depends on particle size, shape and the medium surrounding them [120, 121]. It is reported that unsupported Au metal nanoparticles of particular size show a linear red shift in SPR with increasing solvent polarity [122]. The reported refractive indices for TiO_2 polymorphs anatase and rutile are 2.49 and 2.61, respectively [123]. A 40 nm higher SPR is reported in Au/rutile SPR than that of Au/anatase at the same Au nanoparticle size [124, 125]. Very recently Chin and co-workers studied that SPR maxima is affected by Au particle size, shape, bonding interaction and refractive index of the support [126]. SPR can enhance the concentration of charge carriers in the metal-semiconductor system and therefore the rates of photocatalytic reactions occurring on the surface by two mechanisms. (i) SPR-mediated electron injection mechanism also called hot electron injection mechanism from metal to semiconductor (M→SC) occurs when plasmonic metal nanoparticles and semiconductor are in direct contact with each other [76, 127-133]. This mechanism is analogous to dye sensitization. Plasmonic metals are characterized by an excellent mobility of charge carriers and have almost 105 times greater cross-sectional area than typical dye-sensitizer molecules. Furthermore, the ability to tune the resonance wavelength by changing the size or shape of metal nanoparticles allows for the possibility of exploitation of entire solar spectrum. (ii) Near field electromagnetic mechanism also called energy transfer mechanism is observed when plasmonic metal are large enough (larger than ~50 nm in diameter) in size to generate the effective local electric field [117, 134, 135]. Electric field induced by photo-excited metal plasmonic nanostructures is few orders of magnitude higher than the field of photons used to photo-excite the nanostructure. These fields are spatially non-homogenous, with the highest intensity at the surface of the nanostructure and decreasing exponentially with distance from the surface within ~20–30 nm and linearly further away. As a result of this the rate of electron–hole formation near semiconductor surface increases by a few orders of magnitude.

The hot electron injection mechanism is highly operating in the wide band gap semiconductors; for example TiO_2 (E_{bg}=3.2 eV) which are enable to make use of visible light. Whereas, the energy transfer mechanism is operating in small band gap semiconductors such as CdS (E_{bg}=2.6 eV) in which local field generated by plasmonic nanoparticles excite electrons from valence to conduction band due to small band gap energy.

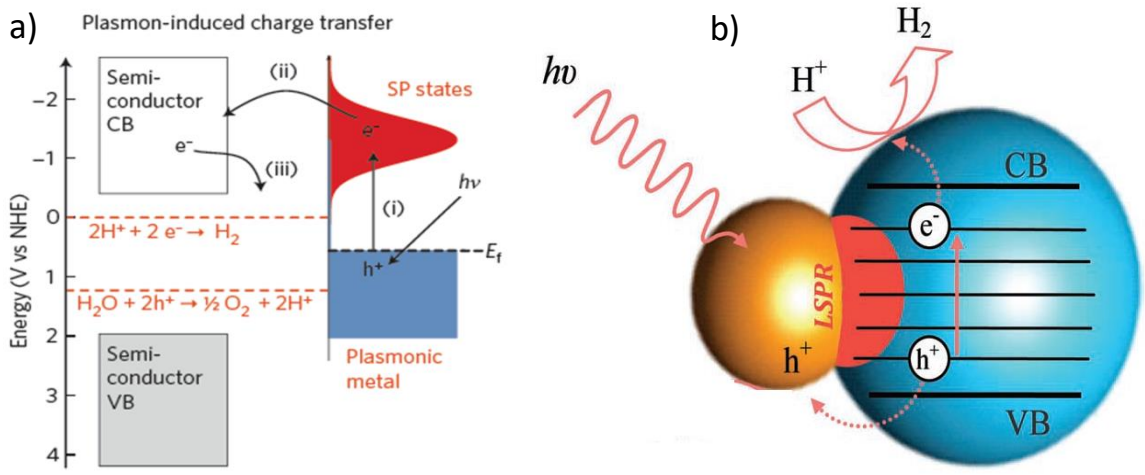

Figure 1.4: (a) Mechanism of plasmon-induced charge transfer from metal to semiconductor, I, II and III are the electronic transitions from metal to proton, reproduced from ref. [61] (b) Proposed photocatalytic process for efficient hydrogen generation based on near field LSPR under visible-light irradiation, modified from ref. [136]

1.3.2 Addition of sacrificial reagents

Many studies have concluded that the rate of hydrogen production from water is extremely slow due to a high recombination rate of photogenerated charge carriers and rapid reverse reaction. Sacrificial reagents are employed to consume one type of charge carriers at a relatively much higher rate as compared to water and leave the others to react with H_2O. Sacrificial reagents can be divided into two groups based on their electron acceptance and donation abilities. Electron acceptors consume conduction band electrons whereas electron donors consume the valence band holes of semiconductors thus increasing the lifetime of the electrons and holes available to drive water splitting reactions on the catalyst surface (fig. 1.5) [137, 138]. Electron acceptors such as Ag^+, Fe^{3+}, and Ce^{4+} are used to improve the O_2 evolution rate from the oxidation reaction of water on the catalyst surface [139]. Electron donors such as methanol, ethanol, triethanol amine, lactic acid, CN^-, EDTA, [140-144] Na_2S, Na_2SO_3, [145] S^{2-}/SO_3^{2-} [146], Ce^{4+}/Ce^{3+} [147] and IO^{-3}/I^- [148-150] and some biomass-derived carbohydrates [151, 152] are used for hydrogen production from water reduction. Ag^+ and Fe^{3+} are generally preferred as electron scavengers during water oxidation due to their suitable redox potentials. The redox potentials of these are Ag^+/Ag (0.779 V vs NHE) [153, 154] and (Fe^{3+}/Fe^{2+} 0.77 V vs NHE) [139, 155] respectively. Fe^{3+}/Fe^{2+} [156] and IO_3^-/I^- [157] are used as electron transport couples in Z-scheme for overall water splitting into

hydrogen and oxygen. Alcohols are generally preferred for water reduction reaction due to various reasons and will be discussed in detail later.

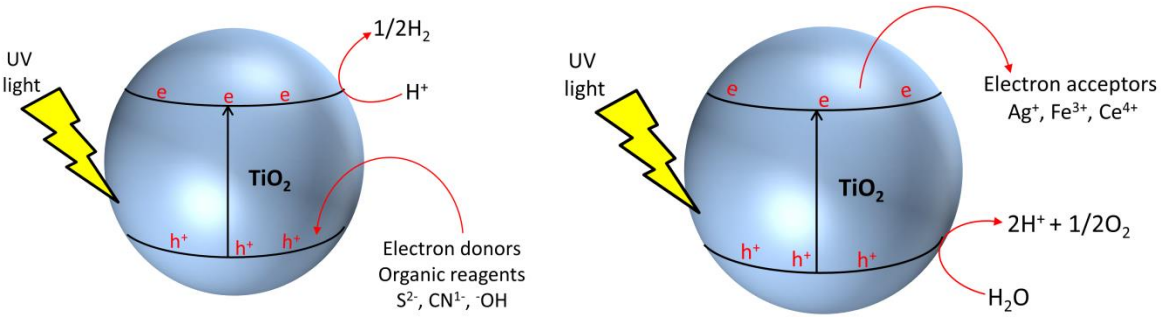

Figure 1.5: Role of electron donors and acceptors for H_2 and O_2 production over TiO_2.

It is worth to mention that some of the common sacrificial reagents have the ability to react with H_2O at wavelengths $\lambda < 300$ nm, even without the presence of photocatalysts. For example, Na_2S and Na_2SO_3 as electron donors (EDs) reduce H^+ to H_2[158, 159] and Fe^{3+} as an electron scavenger (ES) oxidizes H_2O to O_2 [160]. Liu and co-workers discovered the water reduction order with different electron donors in the absence of photocatalyst under light ($\lambda < 300$ nm) as Na_2S > Na_2SO_3 > EDTA-Na > CH_3OH > KI [161]. They also concluded that for photoreactions with and without photocatalyst, CH_3OH was good choice for water reduction and $Fe(NO_3)_3$ was the best choice for water oxidation. Sun and co-workers observed a considerable decrease in photochemical hydrogen production (634 to 23 $\mu mol\ h^{-1}$) when irradiated with light less than 300 nm wavelength from ethanol water system by decreasing the temperature of reaction mixture from 70 to 30 ^oC [162]. So, it is advisable that in order to evaluate total hydrogen production over photocatalyst under high intensity UV light, the effect of reaction temperature on photochemical hydrogen production by sacrificial reagents must be considered.

The effect of sacrificial reagent concentration on the hydrogen production rate has been widely studied. Some researchers demonstrated that the hydrogen production rate is varied as a function of sacrificial reagent concentration following a Langmuir-type isotherm resulting from active sites saturation in the presence of limited quantity of photocatalysts [55, 163-165]. Some other researchers explained that an excess methanol concentration beyond its optimum level might block the adsorption of hydronium cations at surface active sites [165]. Different sacrificial reagents have different mechanisms of hydrogen production. Some sacrificial electron donors react directly with holes while others react with different oxidizing species formed on the semiconductor surface such as $^{\cdot}OH$, H_2O_2, $^{\cdot-}O_2$ [166, 167].

1.3.2.1 Alcohols as sacrificial reagents

The addition of alcohols as sacrificial agents such as methanol, ethanol, ethylene glycol or glycerol with oxidation potentials lower than water suppresses electron hole pair recombination. Chen and coworkers studied the hydrogen production over Au/TiO_2 system using different alcohols and found the rate in decreasing order as glycerol>ethylene glycol> methanol>ethanol [126]. This rate was directly related to number of α-H atoms and OH groups. The importance of α-H adjacent to the OH groups is also previously identified as being important for achieving high rates of H_2 production in the Pd/TiO_2 system [168]. In aqueous media, the photoreaction will proceed via the formation of alpha hydroxyl radicals, which have been identified previously on TiO_2 by EPR [169, 170].

$$RCH_2–OH + h^+ (VB) \longrightarrow RCH°–OH + H^+ \quad (11)$$

$$R_2CH–OH + h^+ (VB) \longrightarrow R_2C°–OH + H^+ \quad (12)$$

From the above mechanism it is clear that why α-H is necessary to achieve high rates of hydrogen production. Considering the physical adsorption of alpha hydroxyl radicals and alcohols over the semiconductor surface, the interaction of lone pairs on OH of alcohols with unoccupied Ti 3d states is crucial. This explains the dependence of hydrogen production rates on the number of OH groups and further illustrates the probable relationship between the hydrogen production rates and alcohol polarity. The hydrogen production is also favoured on alcohols with lesser oxidation potential. The above order can also be correlated with the oxidation potentials of methanol, ethanol, ethylene glycol and glycerol 0.016, 0.084, 0.009 and 0.004 V versus NHE, respectively. The oxidation potentials of all these alcohols are significantly lower than the oxidation potential of water (1.23 V versus NHE). Hence, during photocatalysis in alcohol water systems, the alcohols will be preferentially oxidised, though water will also be oxidised through direct water splitting and alcohol photo-reforming. Greater the potential gap between valence band holes and alcohols, greater will be the hydrogen production rates. Glycerol and glycol have the lowest oxidation potential which makes them best sacrificial hole scavengers [126].

1.4 Hydrogen production over TiO_2 based photocatalysts

Transition metal oxide semiconductor nanomaterials are of great practical importance due to their stability, low cost, low toxicity, and useful photophysical properties [54, 171]. With the ability to excite electrons to the conduction band or to generate holes in the valence band, metal oxide nanomaterials can be used to perform photocatalytic reactions, such as degradation of organic pollutants [172, 173] or production of solar fuels like hydrogen [174, 175]. A wide range of semiconductor materials have been investigated in relation to solar H_2 production from water or biofuels, including oxides, sulphides, nitrides and oxynitrides [39, 176]. TiO_2 is the most promising of the entire semiconductor photocatalysts reported to date in satisfying the basic criteria for solar H_2 production. TiO_2 exists in three main polymorphic forms, all of which have electronic band gaps in the near UV region. The band gap energy of TiO_2 depends on its polymorph with the values of 3.0, 3.2 and 3.3 eV for rutile, anatase and brookite, respectively [177-179]. The conduction band edges of the three polymorphs has been a focus of recent research, with the values of -0.7, -0.5 and -0.6 eV versus NHE, respectively, being commonly reported [180, 181]. TiO_2 fulfills all the basic requirements for water splitting i.e. (i) high stability against photo-corrosion; (ii) the top of the valence band (+2.7 V vs. NHE for anatase) is more positive than the O_2/H_2O redox couple (+1.23 V vs. NHE) and the bottom of the conduction band (-0.5 V vs. NHE for anatase) is more negative than the H_2O/H_2 redox couple (0.0 V vs. NHE) [182] (iii) an appropriate electronic band gap (E_{bg}) to allow solar excitation and (iv) a sufficient photogenerated charge carriers lifetimes to allow key surface redox reactions occurring on microsecond timescales [183]. TiO_2 satisfies the above criteria for water splitting but it usually gives very low activity for hydrogen production owing to rapid recombination rates of photogenerated charge carriers and a very high overpotential for H_2 production on TiO_2 surface. These drawbacks can be overcome to some extent by adding sacrificial reagents and depositing high work function noble metals [184-188] or suitable selection of TiO_2 support morphology [189, 190]. All these factors enhance the charge separation and increase charge carriers lives in TiO_2. The valence band of TiO_2 is mainly composed of oxygen 2p orbitals hybridized with titanium 3d orbitals, while the conduction band is mainly composed of 3d orbitals of titanium as shown in (fig.1.6) [191]. When TiO_2 is irradiated with light of suitable wavelength, the valence electrons are promoted to the 3d state and because of dissimilar parity the transition probability of e^- to the valence band decreases leading to reduction in the probability of e^-/h^+ recombination [192]. This state of semiconductor is called the excited state. After excitation, the electrons and holes separate and migrate to the surface of semiconductor particle. At the surface of

semiconductor electrons reduces the proton to hydrogen and holes oxidises the water to oxygen.

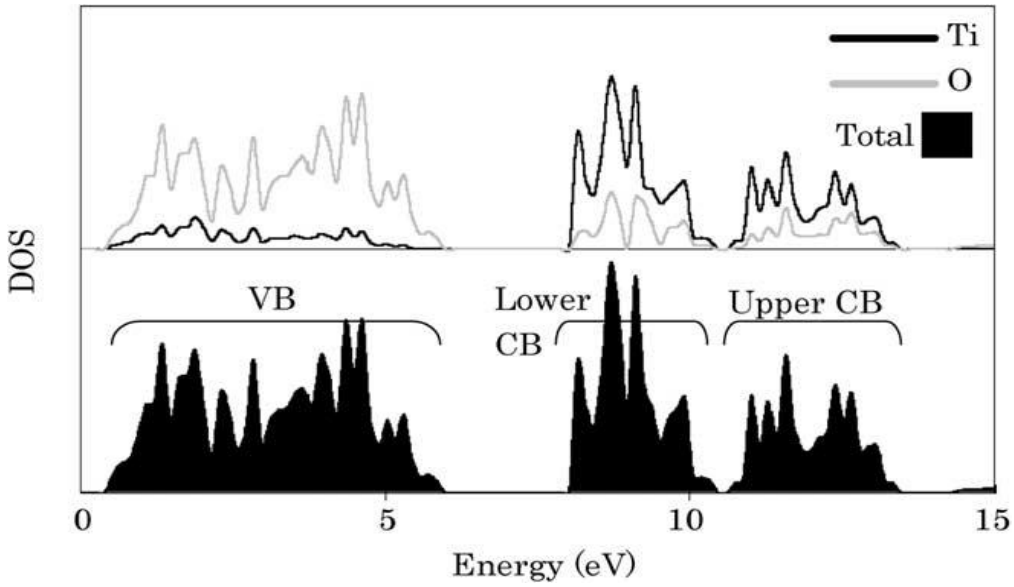

Figure 1.6: The total and projected density of states of TiO_2 (rutile) perfect crystal, reproduced from ref. [191]

1.4.1 TiO_2 Crystal Structure

TiO_2 belongs to transition metal oxide family and is typically an n-type semiconductor due to oxygen deficiencies [193]. There are three commonly known polymorphs of TiO_2 found in nature; anatase (tetragonal), brookite (orthorhombic) and rutile (tetragonal). In all three forms, titanium (Ti^{4+}) atoms are coordinated to six oxygen (O^{2-}) atoms, forming TiO_6 octahedra [194, 195]. In the anatase phase, distortion of the TiO_6 octahedron is slightly larger compared to rutile phase [72, 196], as depicted in (fig. 1.7A). In the rutile TiO_2 octahedra share edges at (001) planes to give a tetragonal structure (fig. 1.7B). This phase is stable at most temperatures and pressures up to 60 kbar. In anatase TiO_2 octahedra share corner (vertices) at (001) planes resulting in a tetragonal structure. Brookite TiO_2 belongs to the orthorhombic crystal system. Its unit cell is composed of eight formula units of TiO_2 and is formed by sharing of both edges and corners to give an orthorhombic structure (fig. 1.7C) [110, 197]. Brookite is more complicated, has a larger cell volume and is also the least dense of the three forms and is not often used for experimental investigations [198]. Cotunnite is another phase which exists under high pressure conditions and is one of the hardest materials known [199].

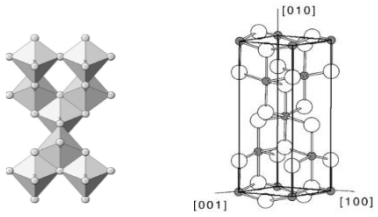

(A) TiO_2 (anatase) bulk (a) and unit cell (b)

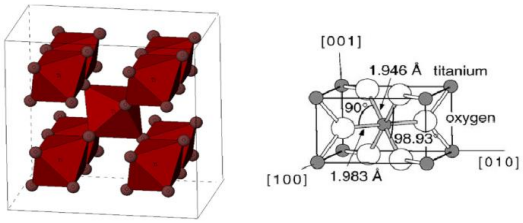

(B) TiO_2 (rutile) bulk (a) and unit cell (b)

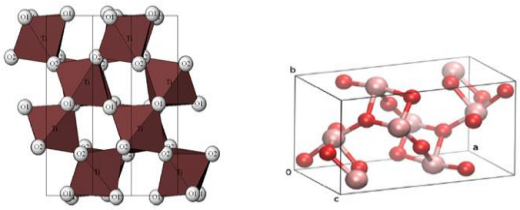

(C) TiO_2 (brookite) bulk (a) and unit cell (b)

Figure 1.7: Crystalline structures of TiO_2, reproduced from ref. [200-203]

1.4.2 Factors effecting H_2 production on TiO_2

The photocatalytic activity of pure TiO_2 depends on various parameters, which include the average nanocrystallite size, powder morphology, specific surface area, crystallinity, and phases involved [204, 205]. As a whole, the photocatalytic activity of TiO_2 for hydrogen evolution can be substantially improved by proper selection and compromise between these parameters [106].

1.4.2.1 Role of TiO_2 phase, particle size and crystallinity

The anatase and rutile phases have most often been used as photocatalysts for hydrogen production [206]. Fundamental properties like electrical, optical and thermal properties of rutile phase are well studied. In contrast, the properties of the anatase form are not well understood due to its low temperature stability. Despite of the commonly used assumption of the similarity of their electronic structures, significant differences are well documented in electrical, magnetic, and optical properties of anatase and rutile [207-213]. The activity of the rutile phase is generally very poor for most reactions [214] while anatase is generally considered as the most active [92, 215-222]. Rutile is the most stable TiO_2 polymorph, its poor photocatalytic activity is due to the fact that it is a direct band gap semiconductor which

allows fast electron-hole pair recombination following photoexcitation [223]. Anatase is an indirect band gap semiconductor, typically displaying photocatalytic hydrogen production activities 1-2 orders of magnitude higher than rutile due to longer charge carrier lifetimes and some other factors including suitable band position and band bending [224, 225]. Moreover, the photoactivity is also dependent on the kind of photocatalytic reaction on the same phase [226]. For example anatase is more active in the photocatalytic decomposition of organic compounds [227, 228] because of its higher adsorptive affinity for organic compounds than rutile [229, 230]. Rutile phase is more efficient in Ag deposition accompanied by O_2 evolution from water [231]. Some other reports also exist in the literature showing that rutile is more active in certain types of photocatalytic reactions [231, 232]. To date, very limited data is available about the photocatalytic activity of brookite, due to historical problems in synthesizing this polymorph in pure form [233]. Though it has yet to be unequivocally confirmed, brookite is considered to be an indirect band gap semiconductor, which is consistent with its photocatalytic activity being comparable to anatase in many photoreactions.

Particle size is one of the most important factors to control the phase stability of TiO_2 nanoparticles and hence their availability for photoreactions. Anatase, brookite and rutile phases are thermodynamically stable when particle size is <15 nm, 11-35 nm and > 35 nm respectively [234-240]. A number of authors have shown that the synthesis of TiO_2 consistently results in anatase nanoparticles, which transform to rutile upon reaching a particular size [239, 241, 242]. However, this size range may vary depending upon the synthesis method, calcination conditions, surface modifications and doping among others. The size range of the anatase to rutile phase transition for hydrothermal samples at 650-800 K has been predicted to be in the range of 11.4-17.6 nm. However, anatase nanocrystals are often observed over this size depending upon the temperature and surface chemistry [243-245]. Once the rutile phase is formed, it grows much faster than the anatase phase. Muscat and co-workers found that the anatase phase is more stable than the rutile at 0K [237].

The average distance between the Ti^{4+} ions in anatase is smaller compared to rutile, which makes it thermodynamically less stable. TiO_2 normally undergoes an anatase to rutile phase transformation in the range from 500–700 °C depending upon heating rate and duration [239, 241, 242, 246-248]. The anatase to rutile phase transformation most probably occurs by the formation of domains of small rutile like clusters instead of bulk rutile phase formation. It has been demonstrated that high concentration of rutile nucleation sites for the phase transformation of anatase to rutile exists at particle–particle interfaces in comparison to bulk

materials [249-252]. EPR studies have shown that intermediate tetrahedral Ti^{4+} species appear at the onset of these sites which disappears on complete transformation (fig 1.8). In photocatalytic reduction processes for example reduction of CO to CH_4 and CH_3OH such isolated tetrahedral Ti^{4+} sites are more active than octahedrally coordinated Ti^{4+} [253-258]. This enhanced activity is related to enhanced charge separation on these sites in photocatalytic reactions [259-264].

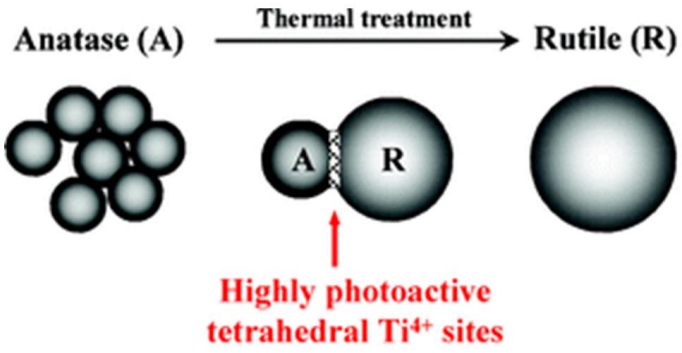

Figure 1.8: Anatase to rutile phase transformation and formation of tetrahedral Ti^{4+} sites, reproduced from ref. [265]

The formation of more active anatase phase, without formation of the rutile phase can be achieved by controlling the reaction temperature and solution pH during synthesis [266-268]. Many studies have indicated that anatase TiO_2 with a higher crystallinity and smaller particle size provides larger surface area and is favourable for hydrogen production [268-271]. High crystallinity is achieved at higher calcination temperature but the calcination process mostly leads to particle agglomeration, grain growth, anatase to rutile phase transformation, small surface area, which altogether decrease the photocatalytic activity of titania for hydrogen production [272]. Maximum photocatalytic activity per unit mass of TiO_2 bulk is generally observed at a calcination temperature of around 400 °C while maximum activity per unit surface area can be obtained at higher temperatures. Anatase to rutile phase transformation temperature can be considerably increased by adding certain complexing agents or doping with certain anions [273-276]. It has been reported that Pt in metallic form induces anatase to rutile phase transformation due to dehydroxylation effect [277]. Hung and co-workers concluded that oxidatively treated Pt/TiO_2 photocatalyst showed better tendency for hydrogen production from water due to greater percentage of anatase phase compared to reductively treated photocatalyst [278, 279]. Melián and co-workers observed a very small amount of rutile (4%) at 650 °C in samples prepared by sol gel method [280] whereas, Liu and co-

workers observed a drastic phase change from anatase to rutile at 650 ^{o}C by the presence of NiO_x nanoparticles [281]. The Lanthanide ions such as Tb, Eu and Sm have been reported not only to prohibit the phase transformation from anatase to rutile at high calcination temperature but also prevent particles from severe agglomeration [282]. Phase transformation from anatase to rutile can also be retarded by the presence of SO_4^{-2} ions [283]. It is reported that sulphate ion doping stabilizes the anatase phase by hindering the crystallite growth and maintains the morphology and porosity of the composite. Moreover, sulphate ions exist in Ti−O−S in the form of S^{6+} and easily reduce to S^{4+} by capturing photoinduced electrons [284]. These transferred electrons then facilitate the water reduction process for the formation of H_2 gas on its surface (scheme-1.1).

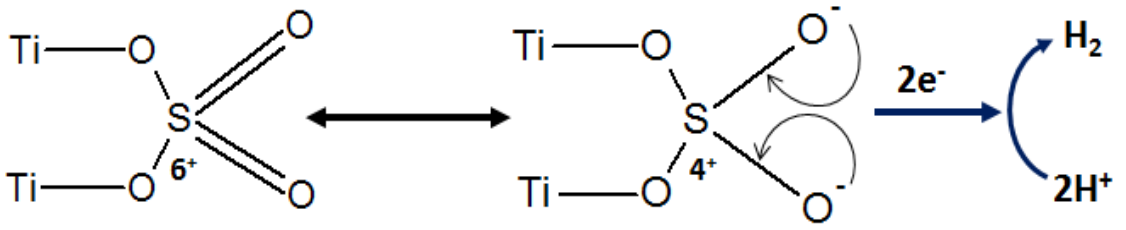

Scheme 1.1: Phase stabilization and water reduction process in sulphate ions doped anatase TiO_2

Tao and co-workers recently reported that properly doped Ni and Fe can suppress the particle growth of TiO_2 [285]. These results were in accordance with some other reports in literature [286, 287]. Luo and co-workers performed hydrogen production over chlorine and bromine doped mixed phase (30% rutile and 70% anatase) TiO_2 prepared by hydrothermal method. It was observed that by increasing the amount of HBr in synthesis solution, phase transformation occurs as pure anatase, mixed anatase/rutile, pure rutile, mixed rutile/brookite and mixed anatase/rutile/brookite. Hydrogen production was attributed to band gap narrowing and P25 like synergistic effect due to mixed anatase/rutile phase formation [288]. From the above discussion, it can be concluded that a compromise must be made between surface area and crystallinity in order to get good yield of hydrogen from water in the presence of sacrificial reagents [289].

1.4.2.2 Effect of band bending

Band bending plays an important role for the transportation of photogenerated charge carriers in photocatalysts. A contact between a semiconductor and other phases (i.e. liquid, gas, or metal) involves formation of a double layer due to redistribution of electric charges. The

transfer of the charge carriers between the semiconductor and the contact phase, or the charge carriers trapping at surface states at the interface, produces a space charge layer. The formation of space charge layers due to the mobility of charge carriers across a semiconductor/solution interface for an n-type semiconductor is explained in (fig. 1.9 top). Part (a) of fig. 1.9 top shows that semiconductor contains a uniform distribution of charges and has a flat band potential in the absence of a space charge layer. The existence of a positive charge on the interface (part b) increases the concentration of electrons near the surface within the region of the space charge layer. The space charge layer formed is called an accumulation layer. The semiconductor will show downwards band bending on going toward the surface as a result of decrease of electron potential energy due to the positively charged outer layer. When negative charges accumulate at the interface, the electron concentration is less than in the interior of the semiconductor (part c). The space charge layer formed is a depletion layer and upward band bending occurs on going toward the surface. When the depletion of the majority charge carriers extends far into the semiconductor, the fermi level can decrease below the intrinsic level, which is half way between the bottom of the conduction band and the top of the valence band. The surface region of the semiconductor appears to be p-type while the bulk still exhibits n-type behavior. This space charge layer is called an inversion layer (part d) [72].

An upward band-bending exists in TiO_2 as it is an n-type semiconductor. This results in in diffusion of photoexcited holes towards the surface, demonstrated by photo-induced transient charge separation (PITCS) measurements [290, 291]. Moreover, the surface potential barrier height (V_s) is known to be inversely proportional to the dielectric constant of the semiconductor [290, 292, 293]. The dielectric constants of single-crystal rutile and anatase are 173 and 31, respectively [293]. Due to this inherent property anatase possesses additional spontaneous surface band bending in deeper regions with a steeper potential in comparison with rutile (fig.1.9 bottom) [215, 294, 295]. As a result, many more photoexcited holes near the surface can transport quickly (1ps) toward the surface and will be trapped by surface states, resulting in higher charge separation efficiency of photon-generated carriers and hence the high photocatalytic activity [294]. It is estimated that the total number of holes transported to the surface in anatase is 16 times higher than that of rutile [216]. Total number of holes transported to the surface can be calculated analytically by procedure described in literature [296]. In rutile, however, bulk recombination of electrons and holes prevails such that only the holes very close to surface are trapped and transferred to the surface [215].

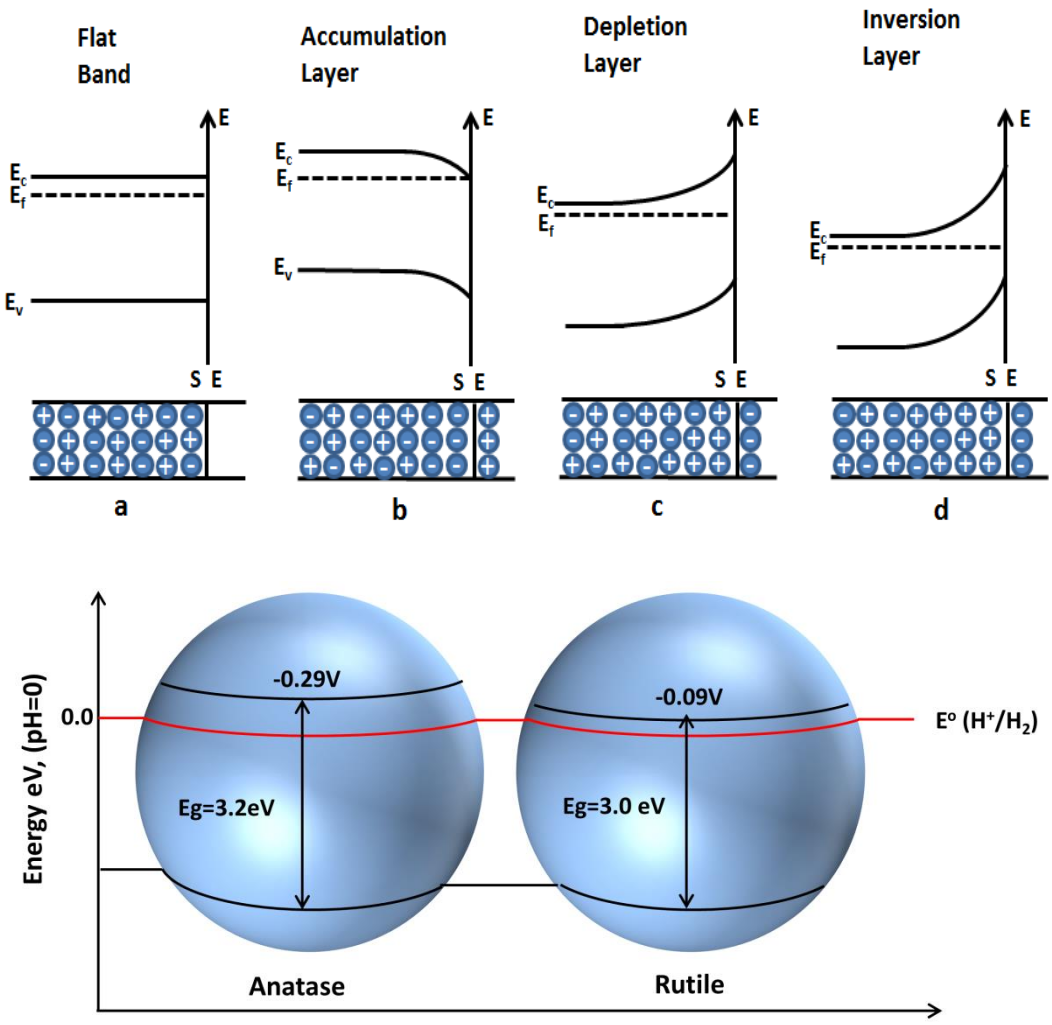

Figure 1.9: (Top) n-type semiconductor-solution interface, space charge layer formation and band bending. (Bottom) Surface band bending of (a) anatase and (b) rutile, modified from ref. [215, 294]

However, in some other studies, larger particle size rutile are reported more active than anatase particles for photooxidation of water due to necessary band bending [297] whereas anatase particles are unable to form the necessary band bending due to their smaller size [294, 298]. Apart from its size, donor density is also important to develop the band bending in a particle. For example, if the donor density is about 3 x 10^{17} cm^{-3}, a space charge layer of 100 nm is necessary to develop a potential drop of 0.3 eV. Differences in photocatalytic activities for oxidations of water indicate differences in the kinetic behavior of excess charge carriers due to different charge carrier transport properties of the respective lattices as discussed above [299]. Recently, transient photoconductance measurements have shown that the lifetime of photoexcited carriers are longer in anatase than in rutile, which may explain the

higher photocatalytic efficiency of the anatase polymorph [300]. The reason for this may be the anatase surface, which is more disordered and has larger variety of energetically non-equivalent active centers than that of rutile [301].

TiO_2 flat-band potential are reported to be at -0.16 and 0.04 V vs NHE (pH=0) for anatase and rutile TiO_2, respectively [293]. Assuming that the flat-band potential is equal to the potential of the conduction band edge E_{CB}, then the potential of the valence band edge E_{VB} is calculated to be almost constant at 3.04 V vs NHE (pH=0) for both phases. The difference in E_{CB} might account for increased photocatalytic activity of anatase phase for hydrogen production from water [216, 226]. The conduction band potential of rutile almost equates with the NHE potential, whereas anatase is shifted cathodically by about 0.3 eV where reduction may takes place relatively easily (fig. 1.9 bottom) [302]. The position of the valence band is comparable in both modifications. Therefore, the "driving force" for oxidations should be the same.

1.4.2.3 Role of e^-/h^+ recombination

Recombination is the reunion (annihilation) of photogenerated charge carriers which generally takes place by adopting three mechanisms; (i) band-to-band recombination, in which an electron from the conduction band recombines with valence band hole, (ii) trap-assisted recombination which occurs when an electron in the CB recombines indirectly with a hole in the VB at a "trap" state [303, 304] (Shockley-Read-Hall recombination SRH) and (iii) Auger recombination, which occurs when an electron-hole pair recombine in a band-to-band transition giving off energy to another electron or hole [305]. The first two mechanisms are radiative, while the third is a non-radiative recombination. When any of the above recombination occurs, the excited electron reverts to the valence band without reacting with adsorbed species [227] non-radiatively or radiatively, dissipating the energy as light or heat [26, 306].

Recombination may occur either on the surface or in the bulk. The bulk recombination can be minimized either by increasing the crystallinity or by making very small size semiconductor nanoparticles [307, 308]. In case of the nanosized crystals, the ratio of time required by the charge carriers to reach the surface and their recombination time can be increased [73, 309, 310]. The surface recombination of charge carriers can be decreased by an increase of their survival time on the surface [311-315]. The charge carriers survival time on the surface can be prolonged by many methods such as noble metal loading [50, 316-318], heterojunction coupling [319-321], metal ion doping [83], carbon and non-metal doping [322], dye

sensitization [323], and also addition of sacrificial reagents [324, 325]. The principal methods of inhibiting the CB electron and VB hole recombination are deemed to be through the loading of metal co-catalysts onto the surface of the TiO_2 and the addition of sacrificial reagents to the reaction system respectively [326]. Water splitting ability of TiO_2 remains limited due to very small fraction and survival time of photogenerated charge carriers on the surface as a result of high recombination rate [327, 328]. Anatase exhibits higher photocatalytic activity in comparison to rutile due to its 10-fold greater rate of hole trapping [225] and its smaller size as compared to thermodynamically stable rutile phase [236, 329]. It is also reported that recombination is slower in indirect band gap semiconductor (anatase) than direct band gap semiconductor (rutile) [330]. Recombination of photogenerated charge carriers also strongly depends upon the intensity of excitation radiations. At low excitation energy (electronic excitations), a small population of photogenerated charge carriers is produced near the surface which follow the first order recombination of electron hole pair. In the near surface region of the TiO_2 crystal the photogenerated charge carriers are quickly captured by the SRH mechanism due to the existence of a large number of surface defects, such as step edges, oxygen vacancies, line defects, impurities, and Ti interstitials. In addition, the surface Ti and O atoms may also be carrier traps due to the unsaturated coordination caused by the broken symmetry in the surface. On the other hand, at high charge carrier concentration followed by high intensity incident radiations (UV photon excitations), electron and holes follow a second-order band to band recombination kinetics in the bulk due to the presence of fewer defects [183].

The photoluminescence (PL) emission spectra of excited photocatalysts have been widely used to understand the lifetime of photogenerated electrons and holes since the PL emission results from the recombination of free carriers [331]. Recombination of photogenerated charge carriers is the major limitation in semiconductor photocatalysis as it reduces the overall quantum efficiency [83, 332]. Recombination and trapping of charge carriers accompanied by the competition with interfacial charge transfer determine the overall quantum efficiency especially for systems where interfacial charge transfer is rate limiting step [54, 72, 333-335].

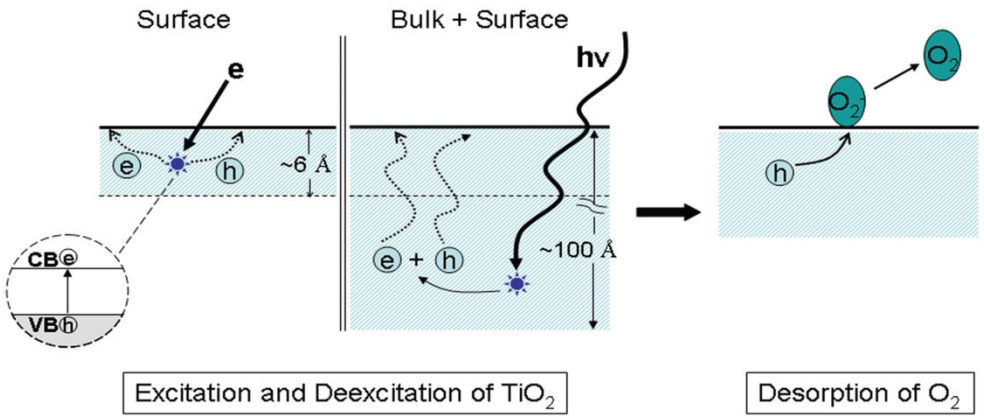

Figure 1.10: Schematic electron and photon excitation processes in TiO_2 followed by de-excitation events. In the electron-excitation, the near-surface electrons and holes quickly diffuse to the surface traps and recombine there by first-order kinetics. In the photon-excitation, the bulk electrons and holes will recombine directly in the bulk by second-order kinetics. Some of the holes are captured by O_2^- causing O_2 desorption for both electron and photon excitation, reproduced from ref. [336]

1.4.2.4 Effect of pH

The effect of solution pH on photocatalytic hydrogen production process on TiO_2 is quite complicated. The simplest way to explain is to relate it to the ionization state of the photocatalyst surface according to the following reactions [337-339];

$$\text{At pH} < \text{pH}_{zpc} \qquad Ti-OH + H^+ \rightarrow Ti-OH_2^+ \qquad (13)$$

$$\text{At pH} > \text{pH}_{zpc} \qquad Ti-OH + {}^-OH \rightarrow Ti-O^- + H_2O \qquad (14)$$

Where pH_{zpc} (point of zero charge) is the pH at which the net surface charge on semiconductor surface is zero. The point of zero charge of the TiO_2 is approximately equal to a pH from 5.8 to 6.0 [340, 341]. Therefore, at a pH < pH_{zpc}, the TiO_2 surface is positively charged and an electrostatic repulsion between the positively charged surface of the TiO_2 and the H^+ present in the solution retards the adsorption of the hydrogen cations on TiO_2 surface. Whereas at a pH > pH_{zpc}, the TiO_2 surface is negatively charged and electrostatic repulsion between the negatively charged surface of the photocatalyst and sacrificial electron donors prevents their adsorption on the surface of TiO_2 as to scavenge the holes. Thus for favourable hydrogen production activity on a semiconductor optimum initial solution pH must be close to its point of zero charge [165]. Fujita and co-workers recently proposed that at pH value of 6.6 the surface of NiO/TiO_2 was covered with maximum hydroxyl groups which promote the

adsorption of alcohols sacrificial reagents on catalyst surface through hydrogen bonding [342]. In case of metal loaded TiO_2, the oxidation state of metal can also be affected by the system pH which ultimately effects the hydrogen production. Wu and co-workers observed detrimental effect of acidic pH for hydrogen production over Cu^{1+} loaded TiO_2 where Cu^{1+} species was found unstable in acidic medium and vice versa [343].

1.4.3 H_2 production on mixed phase TiO_2

Photocatalysts having both anatase and rutile phases show relatively high hydrogen production activity due to synergistic effects between large proportion of anatase phase and low proportion of rutile phase [289]. This combination has been proposed to take advantage of the suitable band positions of both phases by decreasing the recombination rate of photogenerated charge carriers by carrier transfer from one phase to the other [344-348]. However, the mechanism has never been clarified [349]. The most widely used form of TiO_2 (P25) consists of a mixed phase of anatase and rutile in ca. 4:1 ratio. It has a surface area of ca. 50 ±15 m^2 g^{-1} [350] and is one of the best photocatalysts for water splitting among currently available commercial TiO_2 photocatalysts. Only a small number of routine lab-synthesized TiO_2 catalysts show per unit surface area activity higher than that of Degussa P25 [189, 351, 352]. There have been various attempts to explain the increased activity of P25. These include increased electron-hole separation due the transfer of electrons from anatase to a low energy rutile conduction band or electron trapping sites (fig. 1.11a) [261, 353-362]. However data supporting these models was inadequate and the phenomenon was not fully illustrated. Hurum and co-workers presented a thermodynamically allowed model by electron paramagnetic resonance (EPR) studies in which photogenerated electrons actually migrate from rutile to lower energy anatase trapping sites which are 0.8 eV lower than anatase conduction bands (fig. 1.11b) [261, 264, 363, 364]. Hurum further attributed this high activity to a synergistic effect in which the rutile phase extends the photoresponse into the visible light and proton reduction is taking place at anatase due to suitable conduction band potential [261]. It is necessary to note that this effect does not necessarily involve either sensitization or energy transfer (antenna effect) [261] as electron-hole pairs are produced in both phases. This mechanism has been supported by many other authors [365, 366]. It must be noted that intimate contact between anatase and rutile crystals is crucial for interparticle charge transfer where the synergistic effect is not observed in physically mixed phases [261, 351, 353, 366]. It has recently been shown that the creation of a surface-phase junction between anatase and rutile could improve the intrinsic photocatalytic H_2 evolution over TiO_2 [367].

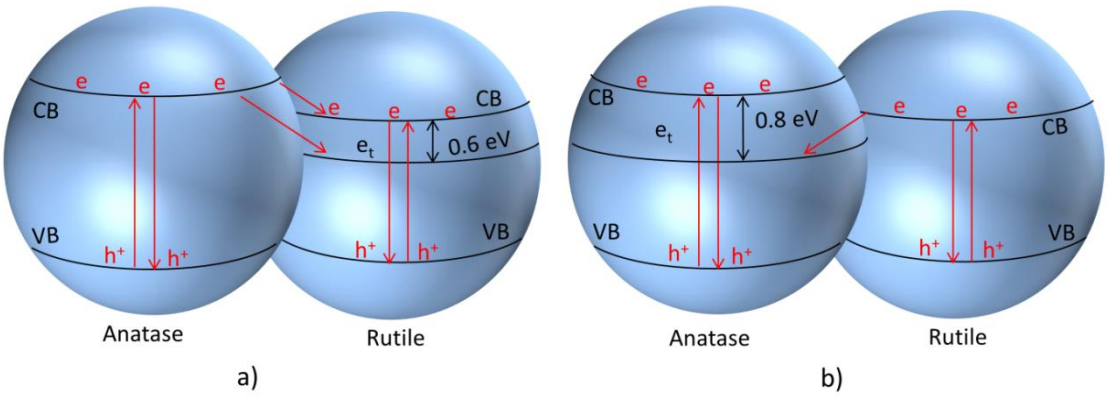

Figure 1.11: (a) Electron transfer from anatase to low energy rutile trapping sites and (b) electron transfer from rutile to low energy anatase trapping sites, modified from ref. [261]

1.4.4 Strategies to overcome drawbacks for hydrogen production over TiO_2

TiO_2 satisfies most of the criteria for water splitting but it usually gives very low activity for hydrogen production owing to rapid recombination rates of photogenerated charge carriers and a very high overpotential for H_2 production on the TiO_2 surface. These drawbacks can be overcome to some extent by adding sacrificial reagents and depositing high work function metal cocatalysts. The work functions of the noble metals Pt, Pd, Au, Rh, Cu, and Ag are, 5.64, 5.12, 5.1, 4.98, 4.65, and 4.26 eV, respectively, and are larger than that of TiO_2 (4.2 eV) [91, 109, 110]. Deposition of noble metals Pd, Pt, Au or Ag on TiO_2 creates rectifying Schottky barriers [186, 368, 369], the formation of which is highly beneficial for hydrogen evolution as the fermi level (E_F) for each metal sits between the bottom of the TiO_2 conduction band and the H_2O/H_2 redox couple (for 5 nm Au nanoparticles on TiO_2, E_F = -0.27 V) [38]. The photo-excited electrons in the conduction band of TiO_2 thus migrate to the supported metal nanoparticles, thereby suppressing electron hole pair recombination, whilst the metal nanoparticles themselves function as cathodic sites for H_2 evolution [370]. Recent studies of noble metal deposited TiO_2 have reported H_2 production rates as high as 30–40 mmol g^{-1} h^{-1} in alcohol water systems under realistic solar UV fluxes [188, 371], highlighting the potential of TiO_2-based photocatalysts for future H_2 production. However, noble metals are expensive with low natural abundance; hence they are not especially practical for the design and development of industrial photocatalysts for hydrogen production. The identification of alternative low cost co-catalysts that enhance the photocatalytic activity of TiO_2 for hydrogen production is a priority. Cu/TiO_2 and Ni/TiO_2 systems are particularly promising in this regard and represent cost-effective and efficient photocatalysts systems for solar hydrogen production [50, 372-375]. A lot of research reports exist in literature which

describe hydrogen production over Cu and Ni nanoparticles loaded TiO_2 photocatalysts [50, 373, 375-377].

1.4.5 $Cu/Cu_xO/TiO_2$: A Step towards non-noble metal approach

Recently $Cu/Cu_xO/TiO_2$ nano-composites have attracted much attention in photocatalysis. Cubic Cu_2O (E_{bg}=2.1 eV) and the monoclinic CuO (E_{bg}=1.2 eV) for bulk CuO have broad perspectives for attractive utilization as active components in photocatalysts. The CuO nanoparticles appear to develop preferentially on the TiO_2 anatase particles [378]. It is proposed that Cu^{2+} occupies octahedral sites in anatase (001) planes up to a dispersion capacity of 6.98 nm^{-2}, with oxygen ions sitting on top of Cu^{2+} cations for charge compensation [379]. Cu_2O is one of the few p-type direct band gap semiconductors which are inexpensive, nontoxic and readily available [85, 184, 380-385]. The coupling of Cu_2O with TiO_2 not only enhances the photocatalytic activity of TiO_2 but also extends the optical response from the UV to the visible range [386-388]. It is reported that Cu_2O is highly unstable and readily oxidized to metallic Cu under illumination during the photoreactions and an overall oxidation state oscillates between 0 and +1 for maximum hydrogen generation activity [50, 389]. The redox potential for (Cu_2O/Cu) exists within its band gap and thus Cu_2O is easily reduced to Cu by photoexcited electrons [390], while under the same conditions, the redox potential of Cu_2O/Cu is higher than CuO/Cu, inferring that electrons would preferentially attack Cu_2O than CuO. Since the conduction band of Cu_2O is more negative than the TiO_2 conduction band, in Cu_2O/TiO_2 systems the transfer of excited electrons from the conduction band of Cu_2O to TiO_2 is thermodynamically favorable under visible light illumination. Different Cu species Cu, Cu_2O and CuO show distinct absorption bands in the visible range between 400-800 nm in addition to the strong absorption band of TiO_2 in the UV range. These visible light absorption bands can be assigned to metallic Cu absorption (225-590 nm) [391], electronic transitions in CuO from valance to conduction band <730 nm, 3d Cu^{1+} clusters as well as $(Cu–O–Cu)^{2+}$ clusters absorbance (400-600 nm) [392] and absorbance due to d-d transition of Cu^{2+} in crystalline and bulk CuO in octahedral symmetry (600-800 nm) [391]. Besides this absorption band, an absorption shoulder located at ca. 425 nm is also observed, which can be ascribed to the direct interfacial charge transfer (IFCT) from the conduction band (VB) of TiO_2 to Cu^{2+} [393].

It is well known that oxygen vacancies are formed by the reduction of Ti^{4+} cations to Ti^{3+} states by photogenerated electrons in conduction band of TiO_2 under UV-visible light illumination. These oxygen vacancies can easily be occupied by water molecules under

ambient conditions to produce hydroxyl groups (Fig. 1.12) [394]. When hydrated Cu^{2+} ions in ethanol solution are added, the reaction between the hydrated Cu^{2+} ions with hydroxyl radicals of TiO_2 support easily occurred as following [395].

$$-Ti-OH+Cu(NO_3)_2 \rightarrow -TiO-CuO_x+HNO_3 \qquad (15)$$

During the steps of evaporation, drying and calcination, the nanosized CuO_x species are modified as Cu^0, Cu^{1+} and Cu^{2+} on the surface of TiO_2. Lalitha and co-workers reported that Cu^{2+} and Cu^{1+} species are formed at calcination temperatures of 350 ^oC and 450 ^oC respectively on P25 TiO_2 surface [376]. Glucose solvothermal method is another method used for selective formation of Cu^{1+} without formation of Cu^{2+} species on TiO_2 surface [396]. Wu and co-workers concluded that Cu^{1+} species are more active in charge transfer and photocurrent production while the Cu^{2+} species inhibit the photocurrent generation and Cu^0 does not affect the activity at low loading concentration. Furthermore when hydrated Cu^{2+} ions in ethanol solution are added then Cu^{2+} is deposited mainly as Cu^{1+} species on the TiO_2 surface. Ethanol medium prevents the atmospheric oxygen to form dissolved oxygen which refrained the formation of Cu^{2+} species. On the other hand Bandara and co-workers reported that if the deposition of Cu^{2+} ions is carried out in water solution, formation of Cu^{2+} species are favorable [397].

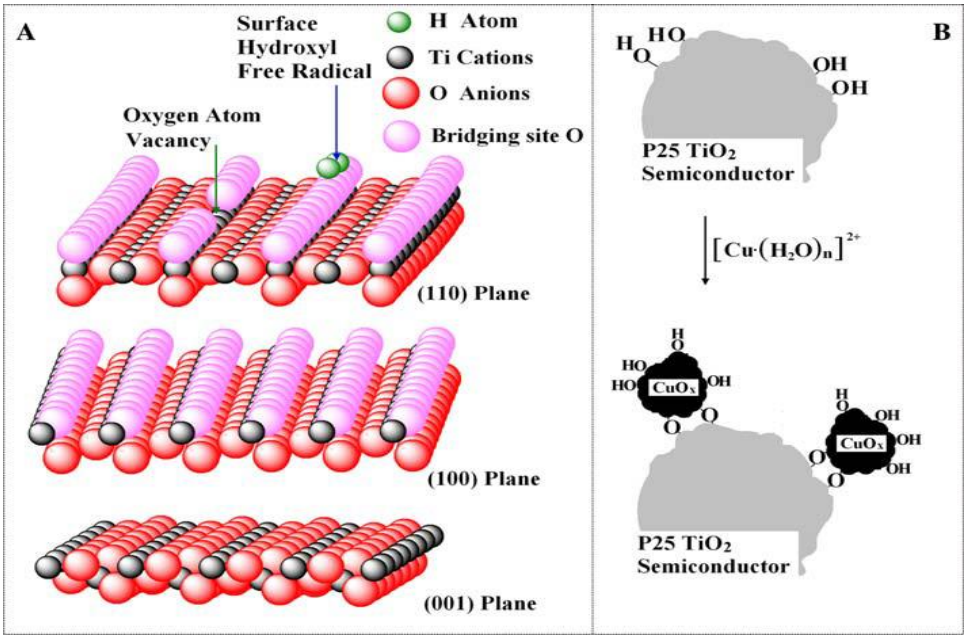

Figure 1.12: The schematic diagram of TiO_2 structure and possible formation of Cu species on TiO_2 surface, reproduced from ref. [343]

1.4.5.1 Cu_2O/TiO_2, a p-n heterojunction for hydrogen production

Cu_2O is an intrinsic p-type semiconductor with a direct band gap of 2.0–2.2 eV [390, 398]. Cu_2O/TiO_2 composites systems having appropriate energy levels with respect to both oxidation and reduction of water are reported to produce hydrogen under visible light irradiations [399-404]. Cu_2O as a p-type semiconductor when combines with a n type semiconductor (TiO_2) makes a hetero-junction of type II-staggered in Cu_2O/TiO_2 composites (Fig. 1.13) [405, 406]. According to type-II heterojunction band structure, the conduction band (CB) and valence band (VB) of coupled p-type semiconductor lie above the conduction band (CB) and valence band (VB) of TiO_2. When visible light is supplied to this nanocomposite, electrons in the conduction band of the p-type semiconductor will be thermodynamically transferred to the conduction band of the n-type semiconductor and holes remain in the valence band of the p-type semiconductor. The migration of photogenerated charge carriers can be promoted by the inner electric field established at the heterojunction interfaces also known as space charge regions [407-410]. Consequently, the recombination rates of photogenerated charge carriers will be greatly suppressed, resulting into high photocatalytic activity [405, 411]. Sinatra and co-workers observed 10 times greater rate of hydrogen production over 2% Au-Cu_2O/TiO_2 than 2% Au-TiO_2 from glycerol water mixtures due to the synergetic effect of the Cu_2O/TiO_2 p-n junction and noble metal nanoparticles [412]. Cu_2O/CdS nanostructures were also reported to have superior photocatalytic hydrogen production from water splitting due to type II hetero-junction formed at the Cu_2O/CdS interfaces [413].

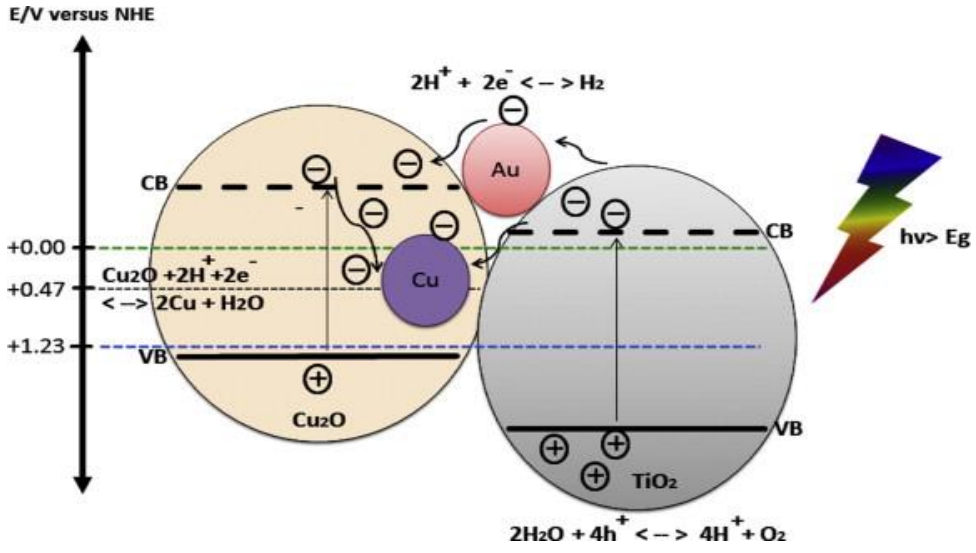

Figure 1.13: Energy band position of Cu_2O and TiO_2 aligned with redox potential of water, reproduced from ref. [414]

Zhang and co-workers studied that the deposition potential during electrodeposition of Cu_2O on TiO_2 nanotubes array (TNA) has direct effect on the morphology and visible light hydrogen production activity of as prepared Cu_2O/TiO_2 nanotubes array photocatalysts [415]. Cu_2O electrodeposited at -0.8 V had maximum exposed 111 facets and was found to have better photocatalytic activity (42 times) for hydrogen production from water-glycerol mixture. Among (110), (111), (200) and (220) planes of cubic Cu_2O, 111 face is more effective for water splitting due to higher stability. Although there is no clear explanation for the stability of Cu_2O (111) oriented materials. It has been proposed that oxidation of Cu^{1+} to Cu^{2+} is hindered on the (111) surface when compared to the other low-index surfaces. Xi and co-workers demonstrated that Cu_2O/TiO_2 photocatalyst prepared by glucose solvothermal method generated 16 times greater hydrogen form ethanol-water mixture than P25 under visible light due to the reduction of a part of Cu_2O to Cu^0 and the synergistic effect of Cu_2O and Cu (fig. 1.14). The photogenerated electrons first transferred to Cu and then to the conduction band of TiO_2, which enhanced the lifetime of photogenerated charge carriers. As a result of this synergistic effect hydrogen evolution rate on $Cu_2O/Cu/TiO_2$ was twice as on Cu_2O/TiO_2 [396]. At the same time, the reason why Cu_2O has not completely converted to Cu was explained as following:

$$Cu_2O \xrightarrow{h\nu} Cu_2O + h^+ + e^- \quad (16)$$

$$Cu_2O + H_2O + 2e^- \rightarrow 2Cu + 2OH^- \quad (17)$$

$$TiO_2 \xrightarrow{h\nu} TiO_2 + h^+ + e^- \quad (18)$$

$$2H^+ + 2e^- \rightarrow H_2 \quad (19)$$

$$Cu + h^+ \leftrightarrow Cu^{1+} + e^- \quad (20)$$

$$OH^- + h^+ \rightarrow {}^oOH \quad (21)$$

$${}^oOH + C_2H_5OH \rightarrow \text{Oxidation products} \quad (22)$$

In another recent work reduction of Cu^{1+} to Cu^0 was observed in Au/Cu_2O-TiO_2 systems due to redox potentials of Cu^{1+} within the band gap of TiO_2 [416]. Lalitha and co-workers reported the highest rate of hydrogen production to date from 5% glycerol water system under solar light irradiation over Cu_2O/P25 photocatalyst. However, the mechanism of charge dynamics was not clear in their study [376].

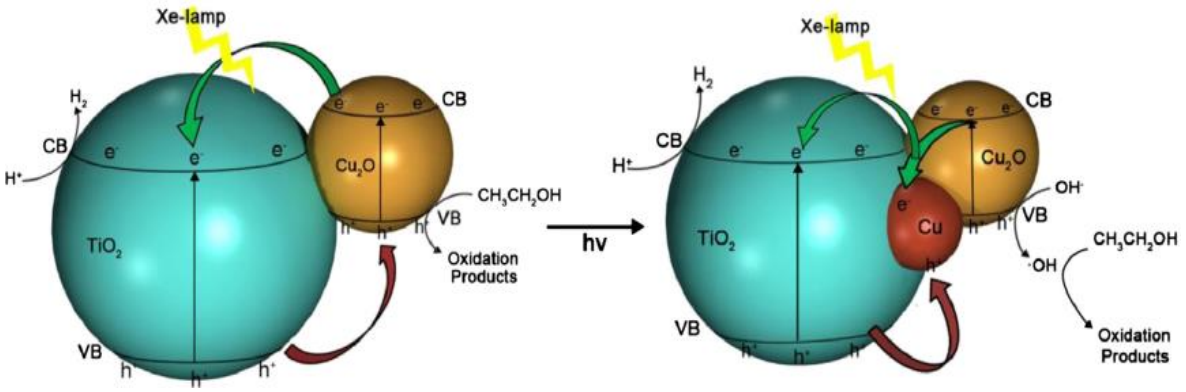

Figure 1.14: The H_2-production mechanism of $Cu_2O/Cu/TiO_2$ under Xe-lamp irradiation, reproduced from ref. [396]

1.4.5.2 Hydrogen production over CuO/TiO$_2$

CuO deposited over TiO_2 has been found to markedly enhance hydrogen production activity as compared to pure TiO_2 [53, 328, 397, 402], even sometimes more than noble metal based photocatalysts [372]. A considerable negative shift in the fermi level of the CuO by the transfer of electrons from TiO_2 is responsible to gain the necessary potential for hydrogen production on CuO. The conventional impregnation method is frequently used for the synthesis of Cu containing TiO_2 photocatalyst. It can not only ensure high dispersion of CuO on TiO_2 support, but also maintain the individual characteristics of CuO and TiO_2 without lattice trespass. The active sites for the hydrogen production are located at the periphery of Cu located over TiO_2 [372, 417]. Decrease in hydrogen production rates over Cu/TiO_2 photocatalyst with time is attributed to the adsorption of sacrificial reagents oxidation products over photocatalyst active surface and also due to decrease of Cu contents due to drop of pH by the formation of CO_2. A decrease in Cu content from 9.1 to 8.1 mol% has been observed due to Cu leaching at 5.6-4.6 drop in pH. However, catalyst preparation by sol-gel method as compared to other methods has been found to decrease deactivation rate due to not only distribution of the Cu on the surface but also in the bulk of the sample at molecular level [381]. Gombac and co-workers prepared unique design of catalyst by covering the CuO_x with porous TiO_2 using water-in-oil microemulsion method for hydrogen production from organic species. The superior activity of this system was due to the combined effect of fine Cu/CuO_x dispersion and possibility of some Cu incorporation into the TiO_2 lattice. Stability tests under reducing conditions in the presence of a sacrificial agent indicate that copper leaching was marginal. It has been observed that bulk CuO has positive conduction band potential than H^+/H_2 redox couple. However, smaller CuO particles have different electronic band structure

and conduction band potential becomes negative compared to H^+/H_2 redox couple due to quantum confinement effect [190, 418, 419].

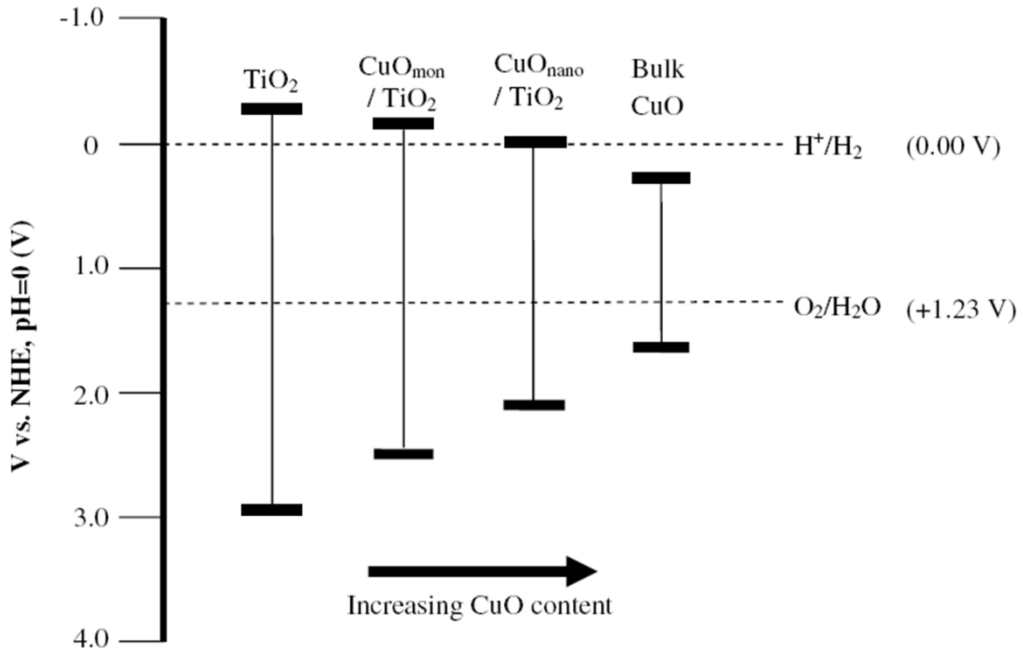

Figure 1.15: Band gap energies for TiO_2, CuO and CuO/TiO_2 photocatalysts with respect to CuO loading, reproduced from ref. [378]

We have also explored and thoroughly validated these results in the present study. The activity of CuO/TiO_2 is reported to be dependent on the nominal CuO loading, with 1.25 wt.% CuO being optimal (H_2 production rate = 20.3 mmol g^{-1} h^{-1} in 80:20 EtOH:H_2O). At this loading, a highly dispersed sub monolayer Cu(II) species on TiO_2 surfaces rather than supported CuO nanoparticles was proposed as the active site for hydrogen production. The fermi level for such adsorbed species is positive with respect to the TiO_2 conduction band, but negative with respect to the H^+/H_2 redox couple. For CuO nanoparticles of size ~3-4 nm, the band gap is around 2.3-2.6 eV as compared to bulk CuO, E_g ~1.3-1.5 eV. As the CuO nanoparticle size increases, the conduction band of CuO becomes positive with respect to H^+/H_2 redox couple, preventing direct transfer of electrons from CuO to H^+ and H_2 formation is suppressed accordingly. The inactivity of bulk CuO for H_2 production can be explained using the same rationale (fig. 1.15). These results have also been confirmed by the latest research by Jung and co-workers. At an optimum Cu loading of 0.5 wt% the CuO_x was present as relatively highly dispersed fine nanoclusters. At Cu loadings beyond 0.5 wt% a bimodal distribution of CuO_x deposits appeared with the prevalence of larger Cu deposits increasing with increasing Cu content [420].

1.4.5.3 Hydrogen production over $Cu(OH)_2/TiO_2$

The $Cu(OH)_2/TiO_2$ systems have recently shown some good results for hydrogen production. Yu and co-workers fabricated $Cu(OH)_2/TiO_2$ photocatalysts using the deposition precipitation by NaOH and reported a hydrogen production rate of 3.4 mmol h^{-1} g^{-1} in a 0.09 M ethylene glycol solution under UV irradiations. The potential of $Cu(OH)_2/Cu$, ($Cu(OH)_2 + 2e = Cu + 2^{-}OH$, E^o = -0.224 V) is slightly lower than the conduction band (-0.26 V) of anatase TiO_2 and higher than the reduction potential of H^+ ($2H^+ + 2e = H_2$, E^o= 0.000 V), which favours the electron transfer from the CB of TiO_2 to $Cu(OH)_2$ which causes the reduction of Cu^{2+} to Cu^o nanoclusters (fig. 1.16a). These Cu^o clusters promote the transfer of photo-generated electrons from the conduction band of TiO_2 to reduce H^+ [65, 331]. The possible reactions involved in this process are;

$$Cu(OH)_2 + 2e^- \rightarrow Cu + 2OH^- \quad (23)$$

$$Cu + 2e^- + 2H^+ \rightarrow Cu + H_2 \quad (24)$$

Fig. 1.16b presents the PL spectra for pure titanium nanotubes and $Cu(OH)_2$ loaded nanotubes samples which were excited at a wavelength of 260 nm. The weak PL signal intensities of $Cu(OH)_2$ loaded TiO_2 is clearly due to the quenching of electrons by Cu^{2+} in $Cu(OH)_2$. These results suggest that the Cu loaded TiO_2 is a promising future photocatalyst for water splitting and many industrial applications [421]. Although all reported hydrogen generation rates over Cu-containing TiO_2 photocatalysts are still low from an economic and practical point, however, they are strong candidates to replace highly expensive Pt and Au co-catalysts for solar H_2 production.

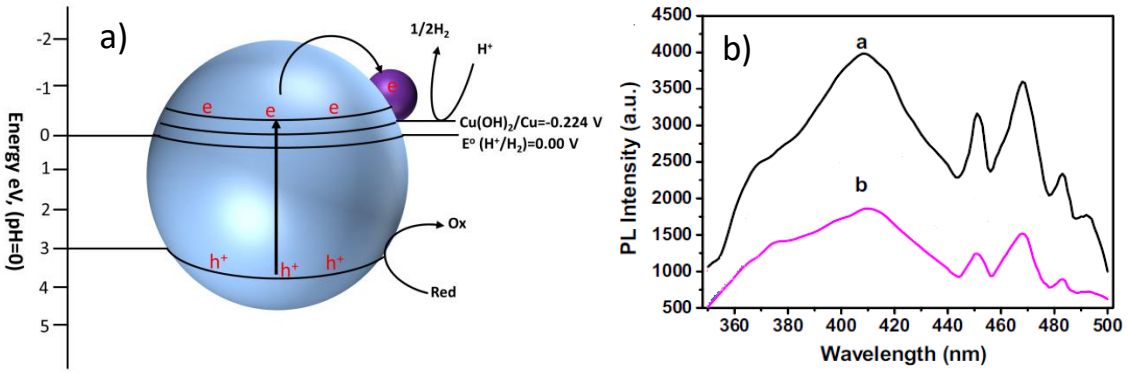

Figure 1.16: (Left) mechanism of hydrogen production over $Cu(OH)_2$ loaded TiO_2 (right) (a) Photoluminescence spectra, pure TiO_2 nanotubes and (b) Cu loaded nanotubes, reproduced from ref.[331]

1.4.6 Role of metal particles dispersion

The physical form and degree of dispersion of metal nanoparticles over base material (TiO_2) are of prime importance. A uniform dispersion of metal nanoparticles facilitates the migration of photogenerated charge carriers from semiconductor support to the metal nanoparticles and an agglomeration of the metal particles weakens the interaction of M–TiO_2 and adversely affects the photocatalytic activity [422]. A major breakthrough in depositing highly dispersed CuO nanoparticles was achieved by Yoong and co-workers [423]. They used a complex precipitation method to deposit CuO nanoparticles over TiO_2. Briefly, powder TiO_2 was dropped into solution of Cu-glycerol complex and the complex was precipitated over TiO_2 by adding NaOH (0.25 M). Highly dispersed CuO nanoparticles were deposited by heating the obtained powder at 300 ^oC in air. The metal nanoparticles particles thus obtained were evenly dispersed over TiO_2 support and did not show any localized metal deposition. Later on, Chen and co-workers used the complex precipitation method to deposit highly dispersed monolayer of CuO over (P25) TiO_2. The synthesized photocatalysts showed very challenging results for hydrogen production (20.3 mmol $h^{-1}g^{-1}$) from 80% ethanol-water mixtures. Very recently, the same group deposited NiO at (P25) TiO_2 by same method followed by reduction of NiO to Ni^o under H_2/N_2 flow (10 vol. % H_2, 100 mL min^{-1}) at 500 ^oC for 2 h. A very high rate of hydrogen production (24.3 mmol $h^{-1}g^{-1}$) from 95% ethanol-water was achieved. This was one of the highest rates of hydrogen production reported over Ni supported TiO_2 photocatalysts ever. In both these studies high rates of hydrogen production was achieved due to the fine dispersion of metal nanoparticles by the complex precipitation method. If the metal particles (Cu and Ni) are deposited over TiO_2 directly from their aqueous salts solutions then these particles tend to agglomerate in larger metal deposits.

1.4.7 TiO_2 supported MOF-199 derived highly dispersed metal nanoparticles

MOFs have been used as popular host matrix for dispersing metal and semiconductor nanoparticles [424-428]. Recently, MOFs have been used in composite photocatalysts for hydrogen production from water splitting. Lin and co-workers observed 13.8 times greater hydrogen production than CdS over a ternary composite of UiO-66/CdS/rGO from water electrolyte mixtures [429]. Wang and co-workers very recently prepared Au@CdS/MIL-101 high surface area composite for visible light hydrogen production from water electrolyte mixtures [430]. Due to high surface area, MOFs can generate well dispersed metal nanoparticles and avoid the aggregation of nanoparticles upon calcination. Recently MOF-199 was used for the synthesis of CuO nanostructures as anode materials for Li-ion batteries

[431]. Khan and co-workers synthesized Cu-CuO_x nanoparticles over porous carbon by treating the MOF-199 at 700-800 ^oC under inert atmosphere for glucose sensing applications [432]. Muller and co-workers synthesized nanosized TiO_2 by adsorption of titanium isopropoxide in nanoporous MOF-5 [433]. Lin and co-workers recently reported MOF templated highly dispersed Fe_2O_3 nanoparticles over TiO_2 for visible light hydrogen production. To date, there is no report available on the utilization of such MOF-199 to derived CuO_x nanostructures over TiO_2 for hydrogen production applications. In this study, a new, simple, inexpensive and scalable metal-organic framework (MOF-199) templated strategy for deposition of Cu-Cu_2O nanoparticles over TiO_2 is presented. Cu-containing nanoscale MOF-199 is coated with TiO_2 by solvothermal hydrolysis of TiO_2 precursor to produce MOF-199-TiO_2 composite, followed by calcination of the composite at different temperatures to produce highly dispersed Cu nanoparticles over TiO_2 for hydrogen production from water in the presence of alcohols.

1.4.8 Hydrogen production over Ni/TiO_2

It has been recently envisaged that nickel is a good choice in preparing active TiO_2 based catalysts for hydrogen production as compared with the other transition metal oxides. The enhancement in photocatalytic activity regarding Ni containing TiO_2 photocatalyst systems is, however, more complex. Different mechanisms have been suggested over nickel loaded TiO_2 depending upon the type of nickel as Ni, NiO or $Ni(OH)_2$. Yu and co-workers deposited $Ni(OH)_2$ nanoclusters on TiO_2 by a simple precipitation method and observed a hydrogen production rate of 3.0 mmol h^{-1} g^{-1} in 25 vol.% aqueous methanol under UV excitation [434]. Hydrogen evolution was attributed to the more positive redox potential of the Ni^{2+}/Ni couple compared to the conduction band of TiO_2 which served as active sites for the reduction of H^+ to H_2. It is also postulated in one study that $Ni(OH)_2$ is converted into NiO after a prolonged irradiation in the oxidizing environment provided by the reaction mixture [111]. There is some controversy in the literature about the valence and conduction band energies of NiO [435]. Values in the ranges of -0.3 to -1.0 eV are reported for the conduction band, and 2.4 to 4.3 eV for the valence band (with respect to SHE) [72]. Comparing the above values for NiO it cannot trap photogenerated electron from the conduction band of TiO_2 because the conduction band of NiO is more negative than TiO_2. However, theoretical calculations indicate that H:H recombination on NiO(100) is exothermic, with an activation barrier of only 40 kJ mol^{-1} [436]. High hydrogen production rates observed on NiO/TiO_2 containing catalysts can be rationalized in terms of the ability of NiO to act as adsorbed atomic hydrogen

recombination site after H^+ has accepted an electron directly from the conduction band of TiO_2 [111]. Very recently, Fujita and co-workers reported that the loading of NiO a p-type semiconductor over TiO_2 n-type conductor produces a p–n heterojunction which generates an internal electric field at the NiO/TiO_2 interface. This field was proposed to accelerate the electron transfer for proton reduction at NiO and thus highly suppressed the recombination of photogenerated electrons and holes. A reduction in the band gap energy (E_{bg}) was also observed by NiO loading. This band gap reduction was previously reported due to the interaction of NiO clusters with the anatase and rutile TiO_2 surfaces through Ni–O–Ti bonds and additional Ni–Ti bonds for rutile TiO_2 [281]. Such NiO/TiO_2 systems have also recently shown some very good results for hydrogen production applications [437]. Very recently hydrogen production activities of a series of Ni/TiO_2 photocatalysts in ethanol-water mixtures have been evaluated [438]. The photocatalytic activity of Ni/TiO_2 photocatalysts was found to be highly dependent on the Ni loading, with 0.5 wt. % loading being optimal affording a hydrogen production rate of 24.3 mmol $h^{-1}g^{-1}$ in 95 vol.% aqueous ethanol under UV flux equal to solar light. This high activity of the Ni/TiO_2 photocatalyst was attributed to the fermi level of Ni^o which is positive with respect to the conduction band of TiO_2, and negative with respective to the H_2O/H_2 redox couple. The high work function of nickel is also advantageous in preventing the migration of electrons backward due to excellent Schottky junction formed at this interface. In the same work 0.63 wt. % NiO/TiO_2 was tested. A long induction period observed before a constant hydrogen production rate was obtained reaching about one fourth of that Ni/TiO_2. This induction period was explained due to in-situ reduction of a fraction of NiO by hydrogen produced at the initial stage of the reaction to Ni^0. The fermi level of Ni^0 is below that of the conduction band of TiO_2 anatase.

1.4.9 Hydrogen production over bimetallic Cu-Ni/TiO_2 nanoparticles

Bimetallic heterogeneous catalysts are widely employed in many fields of catalysis, due to high performances; increased activity and selectivity to desired products, extended lifetime and high resistance to poisoning/coke and deposition/sintering arising from the cooperative interactions between the two metals. Bimetallic nanoparticles deposited on TiO_2 are expected to display altered surface morphologies, electronic and physical properties arising from physical and chemical interactions among different atoms and phases [439-444]. It is well known that the work function of a given metal decreases by alloying with other metal with a lower work function. This suggests that alloying of other metals with Pt would decrease the work function of Pt nanoparticles. Pt has the highest work function among noble metals. This

may raise the fermi level potential of the metal and promote efficient electron transfer from metal nanoparticles to proton. Bimetallic heterogeneous catalysts demonstrate excellent performance in many reactions; offer increased activity and selectivity to desired products. Bimetallic nanoparticles deposited on TiO_2 can create surface electronic states and active sites different to those realized in mono-metallic systems, due to synergistic physical and chemical interactions amongst the different atoms and phases [439-444]. For example, Pt–Cu/TiO_2 photocatalysts can selectively reduce nitrate to N_2 under UV irradiation. In contrast, nitrate is converted to ammonia or nitrite over Pt/TiO_2 or Cu/TiO_2, respectively [445]. Similarly, highly selective ammonia synthesis from nitrate can be observed over Pd–Cu/TiO_2 photocatalysts as compared to their monometallic counterparts [446]. In the present study hydrogen production over copper and nickel bimetallic hydroxide loaded TiO_2 was studied and mechanism was discussed in detail for the first time.

1.4.10 Hydrogen production over Cu-Ni supported TiO_2 nanostructures (nanotubes and nanoleaves)

Deeper understanding of the TiO_2 support (crystallite size, surface area, TiO_2 phase composition) role, may allow strategic and stepwise improvements in TiO_2 photocatalyst design and performance. The effect of the TiO_2 support on H_2 production rates in alcohol-water systems has been subject of a number of investigations [130, 180, 332, 447]. TiO_2 nanostructures such as nanorods, nanotubes, nanofibres possess attractive physical and chemical properties such as enhanced light absorption from all angles of incidence, one dimensional transfer of charge carriers to the surface, good adsorption of the reactant on the surface, prevent agglomeration in aqueous suspension, and prevention of e^-/h^+ recombination [448]. Xu and co-workers recently demonstrated that CuO supported on TiO_2 nanotubes coated with CuO by adsorption calcination method show 70% higher activity than P25 over CuO/TiO_2 catalyst for hydrogen production from water-methanol mixture. They attributed this very high activity to that 1-D tubular structure resulting into fast electron transfer due to reduced grain boundary, large surface area and high dispersion of copper component [190, 418]. Since the Hoyer discovery of hydrothermal synthesis of nanotubes [449], it has become a popular tool for tailoring TiO_2 crystallite size and crystal growth habit, whilst minimizing undesirable defects [177, 180, 450, 451]. The hydrothermal synthesis of sodium titanate ($Na_2Ti_3O_7$) nanotubes, followed by acid exchange to give hydrogen titanate ($H_2Ti_3O_7$) and finally calcination of at 400–700 ^oC, provides a promising way for fabrication of high surface area TiO_2 supports for photocatalytic hydrogen production [452]. When TiO_2 is

treated hydrothermally in highly alkaline solution, it results into the formation of nanotubes by the enhanced rupture of Ti-O-Ti bonds in the nanoparticles to form Ti-O-Na and Ti-OH lamellar sheets because of the electrostatic repulsion of the charge on sodium [453, 454]. The $Na_2Ti_3O_7$ nanosheets have negatively charged layers of edge sharing TiO_6 octahedra, with Na^+ ions occupying sites between the layers. Finally, the reaction of Ti–O–Na sheets with acid would lead to the formation of $H_2Ti_3O_7$ nanotubes by removing the electrostatic repulsion by exchange of Na^+ with H^+ at room temperature. The hydrogen titanates are thermally transformed into anatase nanorods when annealed at temperatures higher than 400 ^oC. The detailed mechanism of nanotubes formation by hydrothermal method is given elsewhere in literature [455]. This technique can also be applied to prepare a wide range of 1D TiO_2 nanostructures, such as nanotubes, nanofibres, nanowires and nano ribbons, by changing the structure or size of starting material, concentration of alkaline solution, hydrothermal reaction temperature and time [456-458].

Controlling hydrothermal reaction conditions (TiO_2/NaOH ratio, hydrothermal temperature and time, structure and size of starting materials, filling fraction of autoclave by reaction material and calcination temperature of final product) is of prime importance to get specific morphology of final product. The formation of titania nanotubes were frequently observed by hydrothermally treating TiO_2 powder in 5-10M NaOH from 110-150 ^oC for 48 hours and subsequently calcining at 400-600 ^oC [459-461], beyond 150 ^oC the formation of nanofibres is observed [462, 463]. Wu and co-workers reported the formation of rutile-anatase nanofibres by treating anatase TiO_2 at 150 ^oC in 10 M NaOH for 24 hours and calcining at 800 ^oC [464]. The same group synthesized anatase nanofibres by hydrothermal treatment of anatase TiO_2 in 10 M NaOH at 175 ^oC for 24 hours followed by calcination at 600 °C [462]. Jitputti and co-worker prepared TiO_2 nanowires by hydrothermal treatment of TiO_2 (P25) at 150 ^oC in 10 M NaOH for 72 h followed by vide range of post heat treatments [220]. D'Elia and co-workers under similar condition reported the formation of nanotubes. In these cases sizes of staring materials (TiO_2/10M NaOH) were markedly different [465]. It is also observed that nanotubes formed by hydrothermal method are converted to short nanotubes to certain calcination temperature and finally to nanofibres by further increasing the calcination temperature due to the dehydration of interlayered OH groups [4, 461]. In the present work, we systematically studied the effect of hydrothermal temperature and calcination treatments on the final morphology of TiO_2 nanostructures. Finally, hydrogen production was performed from alcohol water mixture by loading nickel and copper bimetallic hydroxides on TiO_2 nanostructures.

1.5 Hydrogen production over CdS based photocatalysts

The effective use of solar energy is important for the establishment of a sustainable economy. Apart from solar energy utilization using photovoltaic technology and direct solar heating, one approach of solar energy utilization is the use of sunlight to generate energy carriers such as hydrogen from renewable sources (water or water/bio-ethanol mixture where the latter is used in small amounts to quench e-h recombination rates) using semiconductor photo-catalysts [466, 467]. Moreover, ethanol can be synthesized from biomass, e.g., fermentation or hydrolyses of celluloses and this is not the case for other fossil fuels [313]. One of the important challenges to realize this is the development of photo-catalysts which can absorb sunlight and convert these renewables to hydrogen with efficiency that warrant scaling up of the process. A range of catalysts from simple binary metal oxides and metal sulfides to more complicated catalysts have been developed to achieve this objective [27, 39, 468]. Sulfides are attractive visible light driven photocatalysts because of their narrow band gaps with valence bands at relatively negative potentials [469-471]. For example, CdS, ZnS, $CuInS_2$-$AgInS_2$ solid solutions, etc., have shown good activity for visible light photocatalytic hydrogen production in the presence of sacrificial reagents [472-474]. TiO_2 [475-481] and CdS [482-486] attract special interest in this regard because of the relative simplicity of their chemical structure in addition to their stability.

TiO_2 is one of the most stable and active photo-catalysts known, [39, 481, 486, 487] though it suffers from the limitation of its light absorption range mostly in the UV region of solar spectrum (anatase E_g = 3.2 eV, rutile E_g = 3.0 eV). This leaves ca. 95% of incoming sunlight not utilized which limits the theoretical solar to hydrogen efficiency (STH) to around 2 % at 100% quantum efficiency (QE). On the other hand, CdS has narrower band gap (E_g = 2.4 eV) allowing for visible light absorption below 515 nm (20-25% of the solar spectrum) and a flat-band potential at -0.66 V (pH 7), which satisfy the energy requirements set by the reduction potential for H_2O with visible light [483, 484]. Moreover, the theoretical STH of CdS is around 5-6% at 100% QE. A theoretical STH in the range 5-10 % is required for industrial applications depending upon other factors including indigenous resources, sunlight intensity, daytime length, labour among others. It can be speculated that CdS has clear advantage over TiO_2 for its probability for industrial applications based on its theoretical STH.

1.5.1 CdS crystal phases

CdS has three types of crystal structures of hexagonal wurtzite, cubic zinc blende, and high-pressure rock-salt phase. Hydrogen production is only studied on cubic and hexagonal phases. It has been recognized early on, that the hexagonal structure is far more active than

the cubic one [488] despite the fact that both are direct bandgap semiconductors [489]. The hexagonal wurtzite has been intensively investigated because it is the most stable of the three phases and can be synthesized easily using various methods [490]. While the hexagonal phase has been observed in both the bulk and nanocrystalline CdS, the cubic and the rock-salt phases are observed only in nanocrystalline CdS [491]. The phase transformation between hexagonal wurtzite and cubic zinc blende involves only a simple change in symmetry, whereas the hexagonal wurtzite to high-pressure rock-salt transformation involves not only a change in symmetry (hexagonal to cubic), but also a change in the nearest-neighbor atomic coordination (from four to six). Therefore, the former phase transformation is often observed. In order to understand the structure-property relationships of wurtzite and zinc-blende CdS photocatalyst materials, it is necessary to investigate their crystallographic structure in details. The wurtzite CdS is belonging to a close-packed hexagonal wurtzite (CPH) structure. The zinc-blende CdS has a face-centered cubic (FCC) structure. These two different phases possess the same CdS_4 tetrahedron as their basic structural units. Each Cd atom is coordinated with four surrounding S atoms in a tetrahedral fashion, while four adjacent CdS_4 tetrahedron units are linked together by one S atom correspondingly [492].

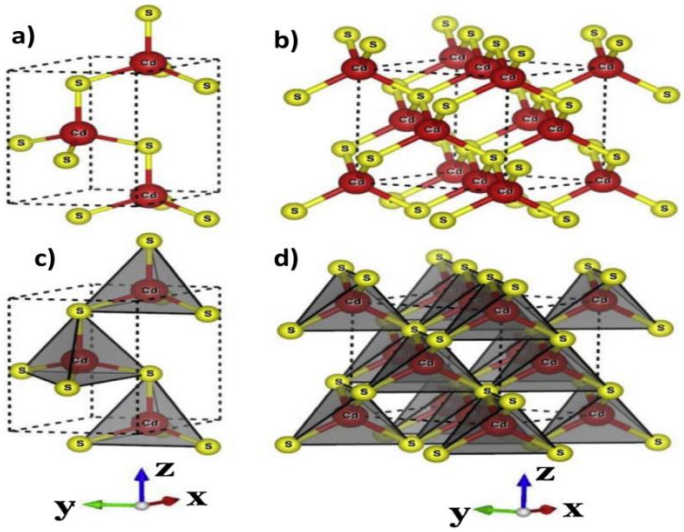

Figure 1.17: Schematic diagram of the hexagonal and cubic CdS crystal structures, a and b are the ball and stick models of hexagonal and cubic CdS, respectively; c and d are the polyhedron models of hexagonal and cubic CdS, respectively, reproduced from ref. [492]

1.5.2 Role of particles size and annealing temperature on phase transition

It is generally believed that the cubic phase is metastable and the hexagonal phase is more stable thermodynamically. The particle size is one of the important factors affecting the phase

transition from cubic zinc blende to hexagonal wurtzite. As the size of CdS nanoparticles increases, the equilibrium crystal structure tends to change from the cubic zinc blende type to the hexagonal wurtzite type. The critical size induced cubic to hexagonal transformation occurs in CdS for a size of <4 nm, indicating that the cubic zinc blende to hexagonal wurtzite transition on heating is size-driven caused by grain growth. On the other hand, the annealing temperature is also an important factor influencing the phase transition from cubic zinc blende to hexagonal wurtzite, which was found to be >300 °C. More thermodynamically stable hexagonal CdS is expected to be formed at a high annealing temperature. In previous studies, the cubic zinc blende was believed to be either (1) a nonequilibrium (metastable) phase that transforms to the stable hexagonal phase on annealing, or (2) an equilibrium phase for CdS nanoparticles. It was considered difficult to experimentally distinguish between the two models because cubic CdS can exist as stable nanocrystals; meanwhile, annealing cubic CdS nanoparticles would result both in coarsening and in thermally induced structural relaxation, finally resulting in the phase transformation to hexagonal CdS. This is the reason for unavailability of any general synthesis route for obtaining CdS with systematically controlled properties, such as particle size, phase structure, and phase composition [493-495]. Bao and co-workers introduced a novel and simple cadmium-thiourea complex thermolysis route for the formation of CdS nanocrystals with controlled dispersity, crystalline phase, composition, average grain size, and band gap [496]. Phase structure and composition of the obtained CdS nanocrystals has been optimized either by changing the ratio of thiourea to Cd or by changing the annealing temperature. With increasing thiourea/Cd molar ratio from 0.5, to 1.5, and then to 4.5, nanocrystals of cubic CdS, a mixture of cubic and hexagonal CdS, and hexagonal CdS have been obtained, respectively at wide temperature range of 150-600 °C. The phase transition from cubic to hexagonal CdS occurs at temperatures of 150-300 °C, and pure hexagonal CdS is formed at annealing temperatures higher than 600 °C. The CdS nanocrystals with the smallest crystalline domain size of about 5.8 nm are of hexagonal CdS were prepared by thermolysis of the Cd-thiourea complex with a thiourea/Cd molar ratio of 4.5 at 150 °C for one day [496].

1.5.3 Comparison of photocatalytic activities of hexagonal and cubic CdS

Although both hexagonal and cubic CdS show almost same visible light absorption capacity due to their similar band gaps (2.36 eV for hexagonal CdS and 2.32 eV for cubic CdS), the photocatalytic hydrogen generation activity of hexagonal CdS is obviously superior to that of cubic CdS [497-499]. Both hexagonal and cubic CdS belong to direct band gap

semiconductors with their conduction band minimum (CBM) and valence band maximum (VBM) are located at the same G point. It is crucial to peep into the electronic structures and estimate the charge carriers effective masses generated in photocatalysts to have a better understanding of the difference of photocatalytic activities of hexagonal and cubic CdS. To investigate the difference between the photocatalytic performances of hexagonal CdS and cubic CdS, the effects of electronic dipole moment, charge carrier effective mass and internal electric field were studied. This investigation provided new insights into the photocatalytic activity difference between hexagonal and cubic CdS photocatalysts. In the CdS_4 tetrahedron units of hexagonal CdS, the calculated Cd−S bond lengths (2.605 Å) along its [0001] direction are slightly longer than the values in other directions (2.601 Å), results into the distortion in CdS_4 tetrahedron units which causes the electric dipole moments creation along [0001] direction and calculated to be 0.04 D. However, such dipole moment is absent in cubic structure due to homogeneous Cd−S bonds (2.602 Å) in CdS_4 tetrahedron units in all directions. The higher ionic character and electronic dipole moment along [0001] direction within hexagonal CdS also result in the formation of internal electric field whereas such internal electric field does not exist in cubic CdS due to their homogenous Cd−S bond lengths [500]. It is well known that the presence of such internal electric field within crystal structures is beneficial for the efficient photogenerated charge separation and diffusion, which ultimately enhances the photocatalytic activity [501]. Therefore, the photogenerated e^-/h^+ pairs can separate more easily in hexagonal CdS. This is one of the important reasons why the hexagonal CdS usually has better photocatalytic activity than cubic CdS. Moreover, the charge carrier effective masses of hexagonal CdS are calculated to be smaller than those of cubic CdS. The smaller effective mass of photogenerated e^-/h^+ pairs can facilitate their mobility, decreases recombination rate and improve photocatalytic activity. Due to the presence of internal electric field and smaller effective mass, not surprising, hexagonal CdS generally exhibits a higher photocatalytic performances than cubic CdS [492].

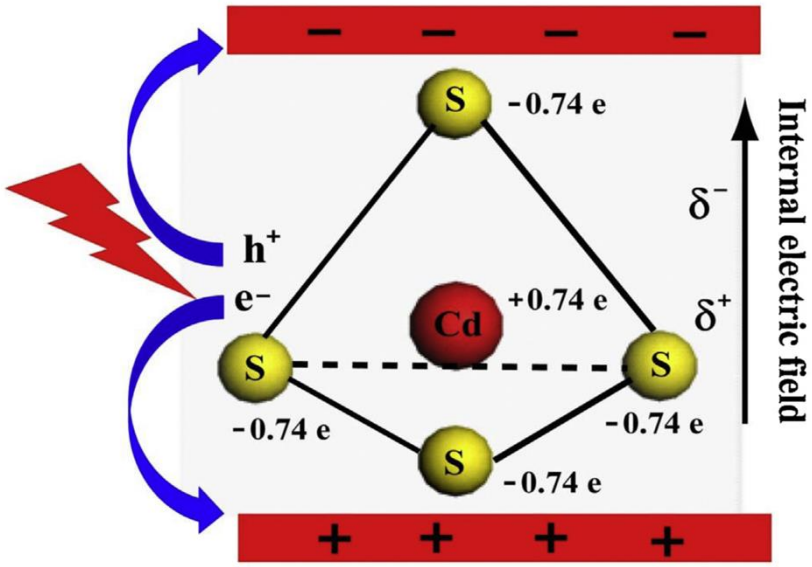

Figure 1.18: Schematic diagram of internal electric field formation along [0001] direction within hexagonal CdS, reproduced from ref. [492]

1.5.4 Cocatalysts loading

In the case of TiO_2, photogenerated electrons and holes are more stable in anatase than in rutile and thus partially explain the superior photocatalytic activity of the former [300]. There is very little data available in the case of pure CdS linking charge carrier life time to structural and photocatalytic performances. Although in some cases hexagonal CdS alone have been found to exhibit better photocatalytic activity, however in most of studies noble metals have been used as cocatalysts to increase the photocatalytic activity considerably [332]. In a photocatalytic process, noble metals particle perform a mediating role in storing and shuttling of the photogenerated electrons from the semiconductor to an electron acceptor (adsorbed H^+) [312, 502]. CdS can either be used in the presence of metals as electron accepters [503] or coupled with other suitable band gap semiconductors to prevent e^-/h^+ recombination [504, 505]. Some photocatalysts fabrication methods, especially core shell structures with other stable semiconductors to overcome the inherent photo-corrosion of CdS have shown improved CdS based photocatalysts [506]. Several researchers have conducted research on CdS modification with other metal sulfides (WS_2, MoS_2) which has shown improved photo-catalytic activities for hydrogen production compared to CdS alone [507, 508]. CdS nanoparticles are often incorporated within layered metal oxides to suppress particle growth and for development of nano-heterojunctions which quickly transfer electrons through the nanostructure while the recombination rate is effectively suppressed [469, 509-511]. CdS/TiO_2 nanotubes where the former is incorporated into the latter has been

demonstrated to show higher photocatalytic activities as compared to CdS alone [504]. CdS (core)-TiO_2 (shell) structures were also studied and has been shown to increase seven times higher photo-catalytic activity as compared to CdS alone [512-514]. Graphene considered as an ideal conductive support for nanoparticles forming hybrid structure with CdS has also been shown to enhance five times in photo-catalytic activities [515-517]. CdS has usually been coupled with noble metals such as Au, Pt, Pd, Cu, Ni, Rh, and Ru acting as co-catalyst [496, 518-520]. Metals are usually deposited on CdS particles by physical mixing with metal particles or by photo-deposition. Wang and coworkers reported an increase in hydrogen production rate by photodeposition of NiS over CdS/CNTs hybrid composite [521]. In another study Ni nanoparticles were photodeposited over CdS nanorods for hydrogen production but not all of the metal particles were deposited under prescribed reaction conditions [522]. Chen and coworkers observed that the environment of metal photodeposition (acidic, neutral or basic) plays an important role in photocatalytic hydrogen production activities [523]. It is interesting to note that the reported effects of metal deposition methods are very diverse. For example, Reber and Rusek reported that platinized CdS (Pt-CdS) obtained by the photodeposition showed an enhanced hydrogen production rate of 300 mL/h at 1.5 wt% loading of Pt [485], whereas Serpone and co-workers observed that the enhancement of hydrogen production by platinization was almost negligible [524]. Although photoplatinization is expected to make a better contact at the Pt/CdS interface than physical mixing, the former was reportedly much less effective than the latter for the photocatalytic degradation of lactic acid [525]. It has been reported that PtS is deposited on the surface of CdS under acidic environment, whereas $Pt(OH)_2$ is deposited under basic conditions [526]. These unwanted Pt species usually lower the catalytic performance, and thus subsequent heat treatment (>400 ^oC) is essentially required to convert them to metallic Pt (Pt^0) [527]. Very recently Di and co-workers observed that photodeposition of amorphous cobalt phosphate acting as water oxidation site produced very good results for hydrogen production from lactic acid water mixtures [528]. The photocatalytic activity was greatly declined by the in situ formation of $Co_3(PO_4)_2$ acting as charge recombination centre. Choice of Au in the present study was to avoid the formation of such species thus minimize as much variable as possible to have more control on experiment to draw reasonable conclusions.

1.5.5 Au/CdS photocatalytic systems

Au has recently been proved the preferred co-catalyst for hydrogen production from water splitting because it is less active for back reaction [529], have suitable work function [109]

and is highly resistant to oxidation [85]. The Au nanoparticles act as an excellent electron acceptor since Au has fermi energy level at (+0.5 V vs NHE) which is lower than the CdS conduction band energy (-1.0 V vs NHE) [530]. Moreover, under visible light irradiation, electrons can be transferred from Au particles to the conduction band of the semiconductor due to surface plasmon resonance which could be responsible for visible light photocatalytic activities [127]. Au can also enhance the activity via plasmon resonance energy transfer rather than hot electron transfer which increases the charge carriers separation in semiconductors [531]. Moreover, hydrogen production studies over Au-CdS photocatalysts are very rare [532]. Hydrogen production is mostly studied over ternary heterojunction involving Au and CdS [533-535]. Three component nano-heterojunctions (CdS-Au-TiO_2) mimicking the natural photosynthesis has also been designed and tested [156, 536]. Au(core) and CdS (shell) Au@CdS hetrostructure always provides greater stability to Au/CdS systems against self photocorrosion of CdS due to capturing of holes by Au nanoparticles by developing Au-S bonds during photoreactions [537]. Hydrogen production over Au@CdS is less as compared to Au/CdS systems because in the former case electrons are directly transferred through CdS conduction band to reduce H^+ rather than through Au nanoparticles as in latter case. In Au@CdS systems CdS becomes holes rich and therefore Au@CdS systems are more effective for holes mediated oxidation processes [530]. The Au/CdS hybrid photocatalyts exhibit greatly different electronic and optical properties than the individual components. The density functional theory (DFT) calculations predicted the orbital mixing effects between semiconductor and Au atoms, and consequent modification in the electronic properties for various applications [538]. The deposition of metal nanoparticles with controlled particle size and morphology over semiconductor photocatalysts is a big issue as there is a large lattice mismatch between the metal and semiconductor components [539]. The various parameters that are responsible for controlling the optical, electronic and optoelectronic properties of plasmonic hybrid materials are the metal particle size, shape, interparticle separation and the dielectric constant of surrounding medium. Haruta and co-workers demonstrated that gold nanoparticles in the 2 to 5 nm range show unusually high catalytic activities [529]. The metal particle size, shape and interparticle distance can be controlled by synthesis parameters. Au is mostly deposited on the semiconductor supports by the methods; photodeposition [540], deposition precipitation (DP), incipient wetness impregnation (WI) [541], spray pyrolysis [542] and adsorption of preformed Au colloids [530]. Photodeposition method is better suited for the preparation of metal particles on semiconductor surfaces, because during irradiation the metal particles form directly at places

where a reduction potential is generated. Photodeposition method for Au nanoparticles generation over semiconductors has produced some good results but it has some drawbacks. It produces large particles of size (10-30 nm) which are very large for many catalysis purposes and careful control of intensity of light is required because it has direct effect on the particle size of Au [543]. Wet impregnation method produces very small and homogeneously distributed Au particles but not all of the Au is deposited, some of the Au is lost during filtration and centrifugation processes of this method. Both deposition precipitation and wet impregnation methods produced smaller Au particles of more or less similar size (2-3 nm) with only difference in the presence of very small fraction of widely dispersed larger Au particles in the former case. One major drawback of loading preformed Au nanoparticles over semiconductor support is that an intimate contact is not developed between metal and semiconductor for the smooth flow of electrons. In the present study, Au/CdS (hexagonal phase) photocatalysts were selected as the main focus. The main objective of this work is to study the effect of Au loading and the nature of the aqueous media on the enhancement of photo-catalytic activity, effect of metal deposition methods on Au particles size and distribution for hydrogen production over Au/CdS systems in different reaction mediums. Photocatalytic hydrogen production has been studied on Au supported CdS catalysts under visible light irradiation. Au nanoparticles of size about 2–5 nm were deposited over hexagonal CdS particles using a new simple method involving reduction of Au^{3+} ions with iodide ions and finally this novel method was compared with other conventional Au loading methods.

1.5.6 H_2 production over Au-CdS systems

The conduction and valence band edges of CdS are –4.1 eV and –6.5 eV, while the fermi levels of CdS and Au are –4.3 eV and –5.1 eV, respectively [39]. When Au is deposited over CdS, a schottky barrier height of about 0.8 eV is generated at the Au/CdS interface [544]. The photo-excited electrons in the conduction band of CdS under visible light irradiation are trapped by Au particles due to the lower fermi level of Au as compared to CdS. These trapped electrons are utilized to reduce the surface H^+ to H_2 [332]. Although this view has been challenged recently where the role of Au is proposed to only help in the atomic hydrogen recombination rather than in electron trapping [111]. There has been a continuous debate about the mechanism of hydrogen production over Au/CdS systems. The two operating mechanism are often anticipated for hydrogen production over Au/CdS. The SPR-mediated electron injection mechanism also called hot electron injection mechanism from

gold to semiconductor (Au→SC) [76, 127-133] when photocatalyst is irradiated with light capable of exciting only Au SPR ≥ 520 nm and the near field electromagnetic mechanism also called energy transfer mechanism is observed when light is capable of exciting both Au and CdS nanoparticles [537]. The second mechanism involves the enhanced separation of photogenerated e^-/h^+ pairs in CdS near the interface due to the localized strong electric field from strong SPR of Au nanoparticles. It is consistently reported that very low injection yield of hot electrons generated from the plasmons in Au nanoparticles cannot significantly contribute to hydrogen production efficiency [545]. Hydrogen production efficiency is always very high due to the contribution of local electromagnetic field of Au nanoparticles for generation of electrons and holes when the light is capable of exciting both Au and CdS nanoparticles [537]. So, the role of Au might be (in addition to acting as electron sink) linked to the electric field generation upon illumination; due to its plasmonic resonance. The larger Au particles can generate greater local electric field. Wang and co-workers very recently reported a 5.3 times enhancement in local field factor $|E|^2/|E°|^2$ for Au/Fe_2O_3 system with Au particle size in the range of 13–20 nm with respect to Au particle size in 3.5–13 nm range [546]. This also indicates the absence of appreciable influence of hot electrons in the photocatalytic reaction as production of hot electrons is dominant process for smaller nanostructures [61, 547, 548]. This interpretation might be in line with energy transfer (not electron transfer) scheme recently proposed [531] and is more in line with the role of metals in photo-catalytic hydrogen production where electron transfer occurs from the conduction band to the metal and not the other way around [111].

1.5.7 Limitation of CdS for H_2 production from water-electrolyte mixtures

CdS suffers from the limitation of its own oxidation by valence band holes produced during the photoexcitation process [549, 550]. This problem is circumvented by introducing sacrificial agents with higher redox potential than the valence band of CdS to prevent it from being oxidized. The process can be represented by the equations given below.

$$(Cd^{2+}S^{2-}) + h\upsilon\ (<515\ \text{nm}) \rightarrow (Cd^{2+}S^{2-}) + e + h\ (\text{Excitation}) \quad (25)$$

$$(Cd^{2+}S^{2-}) + e + h + R \rightarrow Cd^{2+} + S^- + R^-\ (\text{Photocorrosion}) \quad (26)$$

$$(Cd^{2+}S^{2-}) + e + h + R + SA \rightarrow (Cd^{2+}S^{2-}) + R^- + SA_{ox}\ (\text{Photocatalysis}) \quad (27)$$

Where R represents an electron acceptor species and SA represents a sacrificial agent.

There are only few studies reported about Au/CdS [537, 551, 552] while other metals are used for most studies [48, 497, 552-556]. Almost all of these studies have been performed

using inorganic electrolyte (Na_2S, Na_2SO_3) as reaction medium. In the present study hydrogen production is studied from a mixture of an inorganic electrolyte (0.1M Na_2S, 0.02M Na_2SO_3; pH=13) and organic sacrificial reagent (ethanol) for the first time. The photocorrosion of CdS is decreased by the capturing of holes additionally by α-hydroxyethyl radicles produced from the reaction of ethanol and °OH radicles. The mechanism of hydrogen production from ethanol electrolyte-mixture over Au/CdS is also proposed. This study also probe into the catalyst structure after the reaction in order to probe into the restructuring of the material that has been occurred.

1.6 Hydrogen production over g-C_3N_4 based photocatalysts

Recently, carbon nitride as a metal-free photocatalyst with special electronic properties has attracted special interest for its possible applications in H_2 production, decomposition of organic pollutants and other photocatalytic applications under visible light irradiation [557, 558]. A scalable research on carbon nitride materials has been fomented since the prediction drawn by Liu and Cohen that carbon nitrides have special potential to be the ultra-hard materials [559]. Among the seven phases of carbon nitride materials, the *g*-C_3N_4 with attractive properties such as super hardness, reliable thermal and chemical endurance, wear resistance, low density, biocompatibility and water resistivity has a potential to be one of the most robust materials for various photocatalytic applications [557, 560, 561]. The *g*-C_3N_4 is very similar to graphite in structure as proven by the XRD results previously [559, 562-565]. It has been reported initially that both the triazine and tri-s-triazine units were the tectonic units in a single layer of *g*-C_3N_4. However, later on only tri-s-triazine (s-haptazine) was redefined as the only tectonic units due to its super stability. Thermal gravimetric analysis (TGA) conducted on *g*-C_3N_4 indicated that the as-prepared *g*-C_3N_4 is non-volatile and non-flammable up to 600 °C and completely decomposed on rising the temperature to 700 °C [559, 566-570]. In addition to these virtues, *g*-C_3N_4 is highly resistant to heat, strong acid and alkaline solution and is not soluble in common solvents due to the van der Waals forces between its layers stacking [571, 572]. Unlike the metal oxide photocatalysts that require expensive metal salts, g-C_3N_4 photocatalyst can be easily prepared by the thermal polymerization of cheap nitrogen containing materials such as cyanamide, dicyanamide, thiourea, melamine and urea [557, 566, 573].

Carbon nitride has emerged as an excellent material for photocatalytic hydrogen production from water under visible light absorption around 450−460 nm since the work done by Wang and co-workers [557]. The *g*-C_3N_4 is an n-type organic semiconductor with band gap of 2.7−2.8 eV. Its conduction and valence band edges are at −1.1 and 1.6 eV vs (SHE),

excellently covering both the oxidation and reduction potential of water [557]. The wave function investigations indicated that the valence and conduction band of *g*-C_3N_4 are mainly composed of nitrogen P_Z orbitals and carbon P_Z orbitals, respectively. This suggests that oxidation and reduction of water takes place independently on nitrogen and carbon atoms respectively. However, hydrogen production is limited over bare *g*-C_3N_4 due to high recombination rate of photogenerated e^-/h^+, low electrical conductivity, very low surface area usually under 10 m^2 g^{-1} and the lack of absorption above 460 nm [574, 575]. The polymeric nature of *g*-C_3N_4 allows for a wide engineering in texture, surface and electronic properties by using both organic and inorganic protocols.

Many attempts have been undertaken to overcome the drawbacks of *g*-C_3N_4 for photocatalytic performance, such as the deposition of metals Au [576], Ag [577], Pd [578], non-metal doping S [579] and semiconductor synergic effect CdS [579], $BiWO_6$ [580] and ZnO [581]. Among various strategies, the deposition of metals over *g*-C_3N_4 surface as a photoinduced electrons accepters and sacrificial reagents as holes quenchers are effectively addressing the key issue of recombination. Bu and co-workers observed enhanced photoelectric performance at Ag modified *g*-C_3N_4 due to prolonged lifetime of the photogenerated electrons and holes [582]. Chang and co-workers [578] demonstrated that Pd acts as an excellent electron quencher when present over mesoporous *g*-C_3N_4 for photodegradation of bisphenol. Additionally, the presence of sacrificial electron donors, such as triethanolamine, methanol and ethylene-diaminetetraacetic acid, is often necessary for photocatalytic H_2 production from water [575, 583].

In the present study, we attempted a fruitful effort to address two main issues of *g*-C_3N_4, i) limited visible light absorption and ii) high recombination rate of photoinduced charge carriers. In this context bimetallic Pd-Ag nanoclusters were successfully deposited over *g*-C_3N_4. A highly positive synergistic response was observed in resulting photocatalysts in which sliver present in bimetallic nanoclusters extends the visible light absorption by surface plasmon effect and Pd decreases the e^-/h^+ recombination rate by forming highly rectifying schottky barrier.

Chapter # 2

Experimental

Chapter-2 Experimental

2.1 TiO_2 based photocatalysts

2.1.1 Synthesis of $Cu(OH)_2$-$Ni(OH)_2$/P25 photocatalysts

All the reagents used were of analytical grade and used without further purification. Doubly distilled water was used in all the experiments. Commercially available Degussa P25 was obtained from Evonik Industries, Germany. In a typical synthesis, 500 mg of P25 was added to 50 mL of 0.5M NaOH and sonicated to give homogeneous slurry. The aqueous solutions of $Cu(NO_3)_2.3H_2O$ and $Ni(NO_3)_2.6H_2O$ in appropriate amounts were then added dropwise to the P25 dispersion with continuous stirring. The resulting dispersions were sonicated for 10 min and then stirred for a further 2 h. Finally, the $Cu(OH)_2$-$Ni(OH)_2$ impregnated P25 photocatalysts were collected by vacuum filtration, washed several times with water and dried in air at 80 ˚C for 24 h. the following photocatalysts were obtained via the above mentioned synthetic protocol (scheme 2.1); $1.0Cu(OH)_2$, $1.0Ni(OH)_2$, $0.5Cu(OH)_2$-$0.5Ni(OH)_2$, $0.8Cu(OH)_2$-$0.2Ni(OH)_2$ and $0.2Cu(OH)_2$-$0.8Ni(OH)_2$ with the overall 1 wt.% loading, where prefixes represent the nominal weight percentage of each metal. An optimized photocatalyst namely $0.8Cu(OH)_2$-$0.2Ni(OH)_2$/P25 was also calcined at 300 °C for 2 h to examine the effect of metal oxide formation on photocatalytic activity.

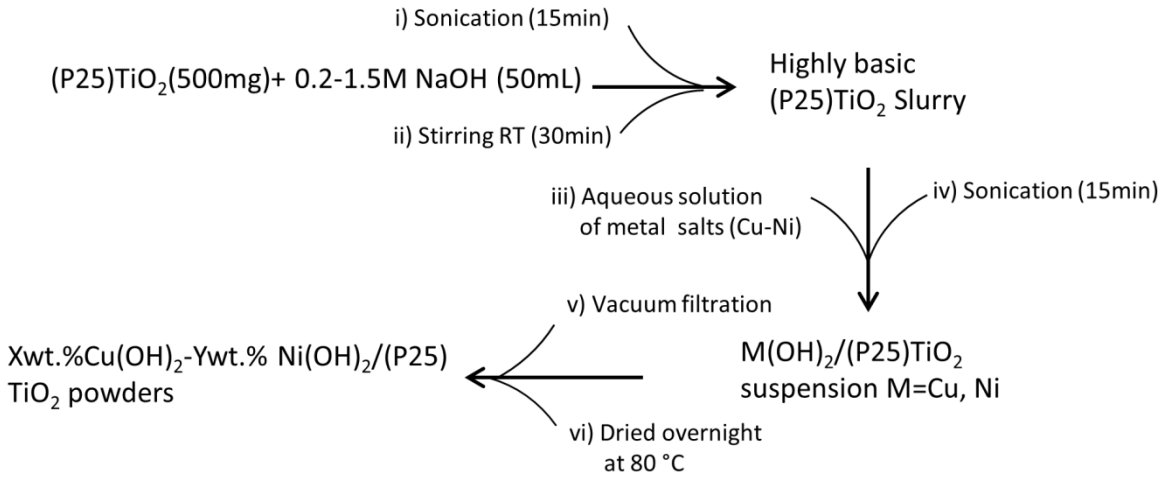

Scheme 2.1: A schematic representation of stepwise synthesis of $Cu(OH)_2$-$Ni(OH)_2$/P25 photocatalysts.

To study the effect of metal loadings on photocatalytic activity, the optimized photocatalyst $0.8Cu(OH)_2$-$0.2Ni(OH)_2$ was synthesized with the total nominal metal loadings of 0.5, 1.0, 1.5, 2.0 and 3 wt.%, respectively. The effect of NaOH concentration as precipitation solution

on metal loading was also checked by varying the concentration 0.2-1.5 M. the samples for steady-state PL and time-resolved PL spectra were prepared by dispersing the photocatalyst in absolute methanol as slurry and finally depositing the slurry as thin layer over glass slides. The observed BET surface area of TiO_2 is ca. 50 m^2/g in all catalysts.

Table 2.1: List of synthesized photocatalysts based on TiO_2 (P25) with different variables.

Sr. No.	Photocatalyst formulation	Overall metal loading wt.%	Molarity of NaOH	Calcination temp.(°C)
1	1.0$Cu(OH)_2$/P25	1	0.5	-
2	1.0$Ni(OH)_2$/P25	1	0.5	-
3	0.5$Cu(OH)_2$-0.5$Ni(OH)_2$/P25	1	0.5	-
4	0.8$Cu(OH)_2$-0.2$Ni(OH)_2$/P25	1	0.5	-
5	0.2$Cu(OH)_2$-0.8$Ni(OH)_2$/P25	1	0.5	-
6	0.8$Cu(OH)_2$-0.2$Ni(OH)_2$/P25	1	0.5	300
7	0.8$Cu(OH)_2$-0.2$Ni(OH)_2$/P25	0.5	0.5	-
8	0.8$Cu(OH)_2$-0.2$Ni(OH)_2$/P25	1.5	0.5	-
9	0.8$Cu(OH)_2$-0.2$Ni(OH)_2$/P25	2	0.5	-
10	0.8$Cu(OH)_2$-0.2$Ni(OH)_2$/P25	3	0.5	-
11	0.8$Cu(OH)_2$-0.2$Ni(OH)_2$/P25	1	0.2	-
13	0.8$Cu(OH)_2$-0.2$Ni(OH)_2$/P25	1	1	-
14	0.8$Cu(OH)_2$-0.2$Ni(OH)_2$/P25	1	1.5	-

*Hydrogen production was performed over all samples

2.1.2 Hydrothermal synthesis of Titania nanostructures (TNs)

All the reagents used were of analytical grade and used without further purification. Commercially available Degussa P25 was obtained from Evonik Industries, Germany. Doubly distilled water was used in all experiments. Sodium titanate ($Na_2Ti_3O_7$) nanostructures (nanorods and nanoleaves) were prepared by hydrothermal treatment of commercial TiO_2 (P25) powder according to the method reported elsewhere [584]. Briefly, TiO_2 (P25) powder (1 g) was dispersed in 10 M NaOH (50 mL). The white suspension obtained was sonicated for 15 min, stirred for 2 h and transferred into a 25 mL teflon-lined stainless steel autoclave. The autoclave was then placed in convection oven and heated at 110 °C, 130 °C, 150 °C and170 °C for 48 h to prepare a set of each four samples. The white precipitates of $Na_2Ti_3O_7$ thus obtained were collected by vacuum filtration, washed repeatedly with double distilled water until the pH of washing liquid was close to neutral. The

$Na_2Ti_3O_7$ nanostructures were converted to hydrogen titanate ($H_2Ti_3O_7$) nanostructures by ion exchange method. For this purpose, the sodium titanate nanostructures were suspended in 0.1 M HCl (500 mL) for 1 h. The $H_2Ti_3O_7$ nanostructures were collected by vacuum filtration, washed with double distilled water until the washing liquid was neutral to pH paper and finally dried at 80 °C for 12 h. The highly crystalline TNR_x-T photocatalyts were obtained by calcining $H_2Ti_3O_7$ nanostructures at 400 °C, 600 °C, 700 °C and 800 °C (where x and T denote the hydrothermal and calcination temperature). Depending upon experimental conditions, different morphologies of TiO_2, ranging from nanorods (TNR) to nanoleaves (TNL) were obtained.

2.1.3 Synthesis of $Cu(OH)_2$-$Ni(OH)_2$/TNs

The copper and nickel hydroxides were deposited over different TiO_2 nanostructures by deposition precipitation method. In a typical synthesis, 500 mg of TiO_2 support was suspended into 50 mL of 0.5 M NaOH and sonicated to give homogeneous slurry. However, different concentrations of NaOH were also used to study the effect of precipitation solution concentration when required. Specific volumes of aqueous solutions of $Cu(NO_3)_2.3H_2O$ and $Ni(NO_3)_2.6H_2O$ were then added dropwise to the TiO_2 dispersion with continuous stirring. The resulting dispersions were sonicated for 15 min and then stirred for further 30 min. Finally, the $Cu(OH)_2$ and $Ni(OH)_2$ impregnated TiO_2 photocatalysts were collected by vacuum filtration, washed several times with water and dried in air at 80 °C for overnight (scheme 2.2). The nominal weight percentages of Ni and Cu in the photocatalysts were 1.0$Cu(OH)_2$, 1.0$Ni(OH)_2$, 0.5$Cu(OH)_2$-0.5$Ni(OH)_2$, 0.8$Cu(OH)_2$-0.2$Ni(OH)_2$ and 0.2$Cu(OH)_2$-0.8$Ni(OH)_2$, where prefixes represent the weight percentage of each metal.

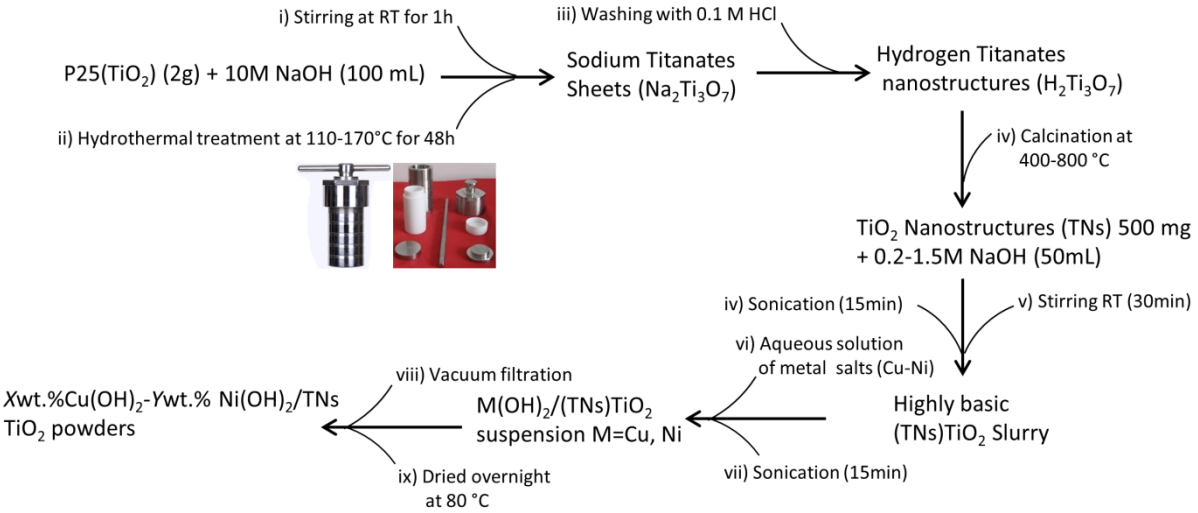

Scheme 2.2: A schematic representation of stepwise synthesis of $Cu(OH)_2$-$Ni(OH)_2$/TNs and $Cu(OH)_2$-$Ni(OH)_2$/TNL.

Table 2.2: List of synthesized photocatalysts based on TNR and TNL with different variables

Sr. No.	Photocatalyst formulation	Hydrothermal temp. (°C)	Calcination temp. (°C)	Metal loading wt.%	Molarity of NaOH
1	TNR_{110}-400-800	110	400-800	-	-
2	TNR_{130}-400-800	130	400-800	-	-
3	TNR_{150}-400-800	150	400-800	-	-
4	TNL_{170}-400-800	170	400-800	-	-
5	1.0$Ni(OH)_2$/TNR_{130}-400	130	400	1	0.5
6	1.0$Cu(OH)_2$/TNR_{130}-400	130	400	1	0.5
7	0.8$Cu(OH)_2$-0.2$Ni(OH)_2$/TNR_{130}-400	130	400	1	0.5
8	0.5$Cu(OH)_2$-0.5$Ni(OH)_2$/TNR_{130}-400	130	400	1	0.5
9	0.2$Cu(OH)_2$-0.8$Ni(OH)_2$/TNR_{130}-400	130	400	1	0.5
10	0.8$Cu(OH)_2$-0.2$Ni(OH)_2$/TNR_{130}-600	130	600	1	0.5
11	0.8$Cu(OH)_2$-0.2$Ni(OH)_2$/TNR_{130}-800	130	800	1	0.5
13	0.8$Cu(OH)_2$-0.2$Ni(OH)_2$/TNR_{110}-400	110	400	1	0.5
14	0.8$Cu(OH)_2$-0.2$Ni(OH)_2$/TNR_{150}-400	150	400	1	0.5
15	0.8$Cu(OH)_2$-0.2$Ni(OH)_2$/TNR_{170}-400	170	400	1	0.5
16	0.8$Cu(OH)_2$-0.2$Ni(OH)_2$/TNR_{130}-400	130	400	0.5	0.5
17	0.8$Cu(OH)_2$-0.2$Ni(OH)_2$/TNR_{130}-400	130	400	1.5	0.5
18	0.8$Cu(OH)_2$-0.2$Ni(OH)_2$/TNR_{130}-400	130	400	2	0.5
19	0.8$Cu(OH)_2$-0.2$Ni(OH)_2$/TNR_{130}-400	130	400	3	0.5
20	0.8$Cu(OH)_2$-0.2$Ni(OH)_2$/TNR_{130}-400	130	400	0.5	0.2
21	0.8$Cu(OH)_2$-0.2$Ni(OH)_2$/TNR_{130}-400	130	400	1.5	1
22	0.8$Cu(OH)_2$-0.2$Ni(OH)_2$/TNR_{130}-400	130	400	2	1.5

*Hydrogen production was performed over all samples

2.1.4 Synthesis of TiO_2 supported MOF-199 derived Cu-Cu_2O nanoparticles

2.1.4.1 Synthesis of MOF-199, $[Cu_3(BTC)_2(H_2O)_3]_n$

The synthesis of MOF-199 can be found elsewhere in literature [585]. Briefly, 0.72 g (3 mmol) copper nitrate trihydrate was dissolved in 20 mL of dimethylformamide (DMF). Trimesic acid (1,3,5-benzene tricarboxylic acid), 0.21g (1 mmol) was dissolved in 10 mL DMF separately in the presence of 1 mL triethylamine (Et_3N). Both these solutions were mixed together, stirred and heated to obtain blue precipitates of MOF-199. The product

obtained was filtered, washed with DMF and dried at 70 °C for 12 hours (scheme 2.3). The purity of MOF-199 was confirmed by PXRD analysis [586].

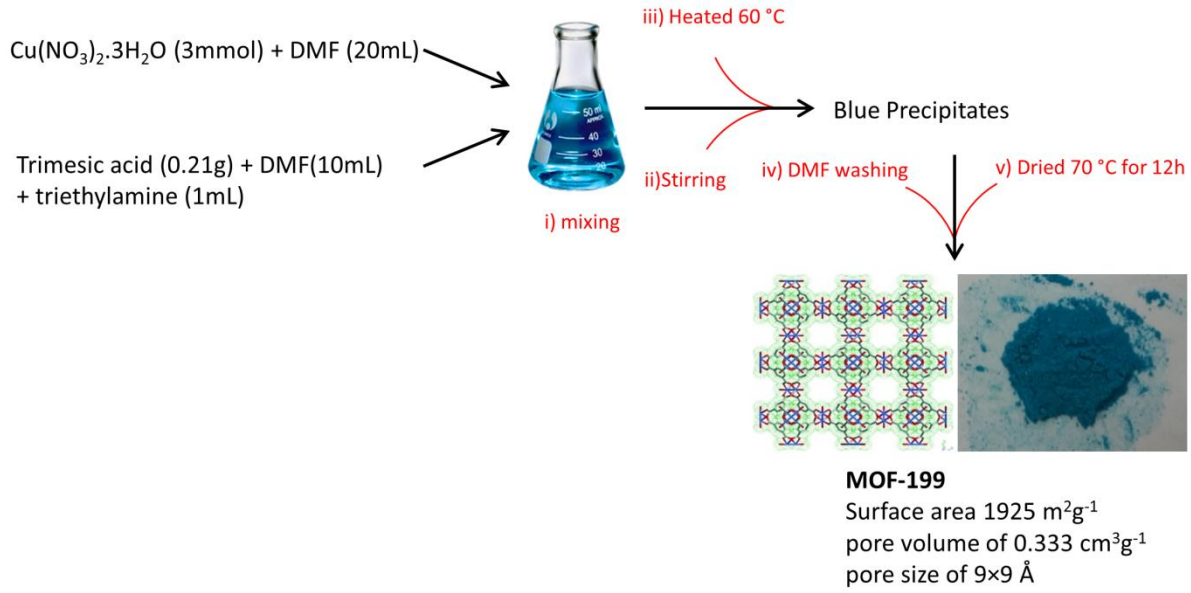

Scheme 2.3: Stepwise synthesis of MOF-199, $[Cu_3(BTC)_2(H_2O)_3]_n$ [586].

2.1.4.2 Synthesis of Cu-Cu_2O/TiO_2 (Anatase)

MOF-199 was vacuum dried at 200 °C and 250 mbar pressure (using Fistreem furnace with Vacuubrand 2008/05 vacuum pump) for 3 h to remove all the solvent molecules present in the pores. A required amount of evacuated MOF-199 was suspended in 10 mL of isopropanol by sonication for 15 min. 2 mL of titanium (IV) isopropoxide was added in above suspension and stirred for 1 h. A water-isopropanol 50:50 mixture was then added dropwise by using a burette until a greenish slurry was formed, which was left stirring for 24 h. The slurry was then transferred in a Teflon lined autoclave and heated at 80 °C for 12 h. Finally, the light green particles of TiO_2-MOF-199 composites were collected by filtration, washed with water and dried at 80 °C for 12 h. The Cu-Cu_2O nanoparticles supported on TiO_2 were obtained by calcining the TiO_2-MOF-199 composites at 350, 400, 450 and 500 °C. A colour change from light green to reddish brown indicated the conversion of MOF-199 core to Cu-Cu_2O species, which was later confirmed upon characterization. Photocatalyts with various metal wt.% loadings were also synthesized by varying the amount of MOF in TiO_2-MOF composite accordingly (scheme 2.4). TiO_2 anatase was also synthesized by the same method as above without the MOF particle incorporations.

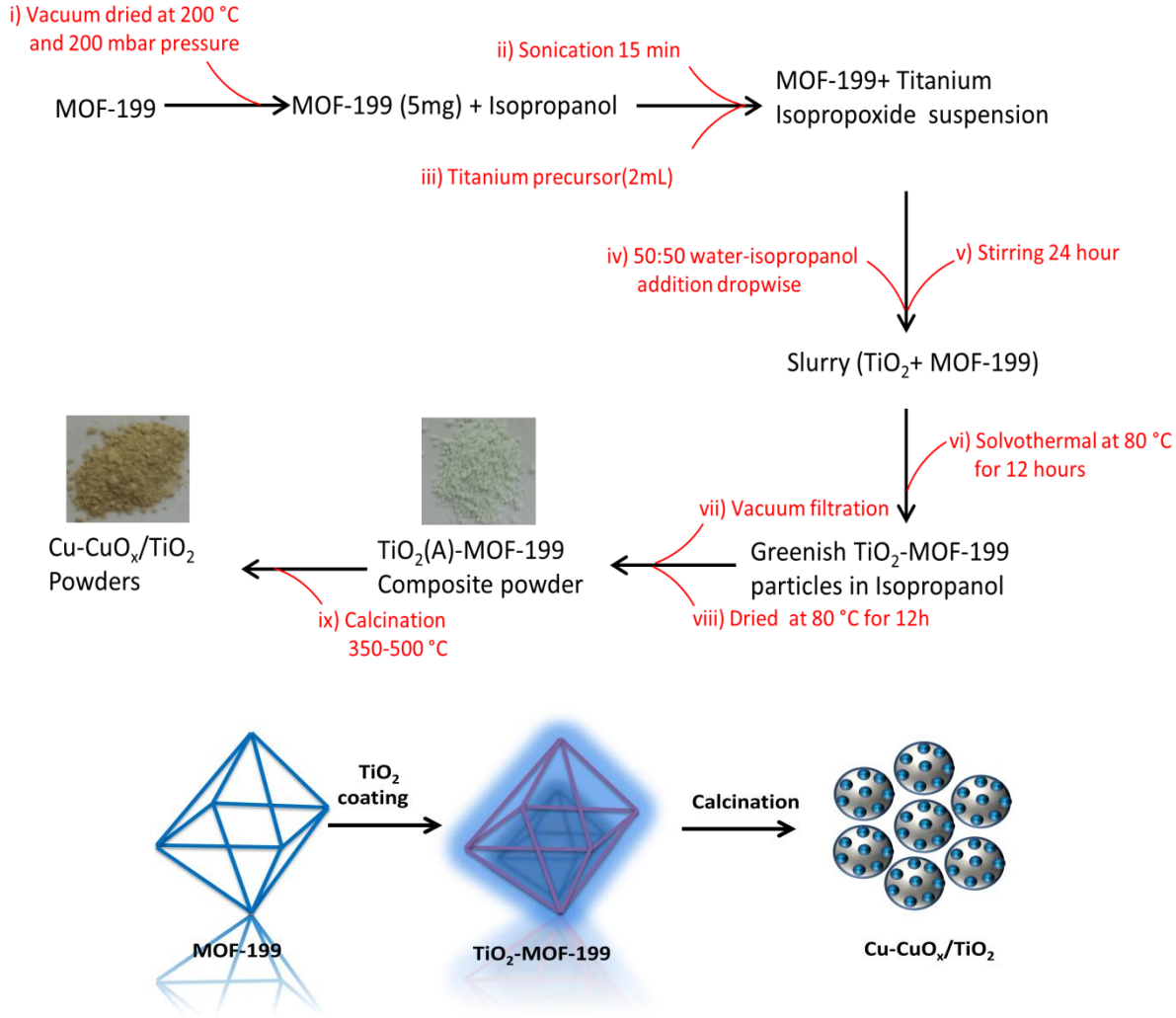

Scheme 2.4: Stepwise synthesis of MOF-199 derived Cu-CuO_x/TiO_2 photocatalysts.

Table 2.3: List of synthesized photocatalysts based on MOF-199 derived Cu-CuO_x/TiO_2 photocatalysts with different variables.

Sr. No.	Materials formulation	Metal loading wt. %	Calcination temp. (°C)	Hydrothermal Temp. (°C)
1	TiO_2 (anatase)	-	-	80
2	MOF-199		-	-
3	CuO (MOF-199)	-	400	-
4	TiO_2-MOF-199-Composite	0.5-2	-	80
5	Cu-Cu_2O/TiO_2(anatase)	1	350	80
6	Cu-Cu_2O/TiO_2(anatase)	1	400	80
7	Cu-Cu_2O/TiO_2(anatase)	0.5	400	80
8	Cu-Cu_2O/TiO_2(anatase)	1.5	400	80
9	Cu-Cu_2O/TiO_2(anatase)	2	400	80
10	CuO_x/TiO_2(anatase)	1	450	80
11	CuO_x/TiO_2(anatase)	1	500	80

*Hydrogen production was performed over all samples except sample number 2,3 and 4.

2.2 CdS based photocatalysts

2.2.1 Synthesis of CdS nanoparticles

CdS nanoparticles were synthesized by the sol-gel method using equimolar amounts of $Cd(NO_3)_2.4H_2O$ (Sigma-Aldrich, ≥ 99.0%) and $Na_2S.9H_2O$ (Kanto Chemicals, ≥ 95.5%). Briefly, 2.1 g of $Cd(NO_3)_2$ was dissolved in 50 mL of isopropanol in a beaker and stirred vigorously. After 45 minutes, 50 mL of an aqueous $Na_2S.9H_2O$ solution (0.136 M) was added drop wise over a period of one hour using a burette. The mixture was further stirred for two hours. The orange precipitates obtained were vacuum-filtered, washed five times with distilled water to remove surplus ions, and subsequently heat treated at different temperatures overnight in air or an inert atmosphere (N_2) with the aim of increasing the proportion of the more catalytically active hexagonal CdS phase (scheme 2.5).

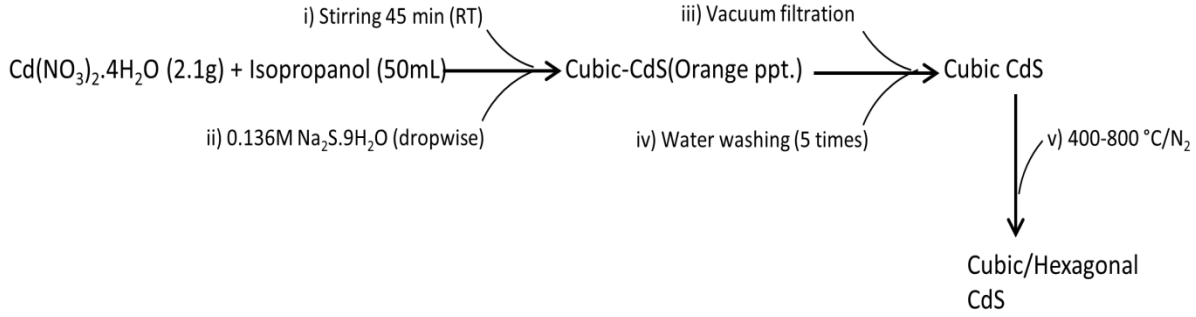

Scheme 2.5: Stepwise synthesis of cubic and hexagonal CdS

2.2.2 Loading of Au nanoparticles over h-CdS

2.2.2.1 A novel KI reduction method

Au loading was performed using a novel and facile iodide reduction method. Briefly, an aqueous solution of KI (15 mL, 5 mM, Sigma-Aldrich, ≥ 99.5%) was added to 0.1g of CdS powder. The mixture was stirred vigorously to make homogeneous slurry. Appropriate amounts of an aqueous $HAuCl_4.3H_2O$ solution (5 mM, Sigma-Aldrich, ≥ 99.999%) were added to the slurry to achieve the desired Au loading. The mixture was then sonicated for 20 min in an Elmasonic sonicator (80 watt, 50/60 Hz output frequency) until the purple color of iodine was visible. The reaction takes place as given below;

$$M^{n+} + nI^- \rightarrow M + \frac{n}{2} I_2 \qquad (28)$$

The slurry was immediately subjected to vacuum filtration and washed with excess water to remove unreacted anions and I_2. The Au/CdS powders obtained were dried at 110 °C overnight in air before characterization and photo-catalytic H_2 production tests (scheme 2.6).

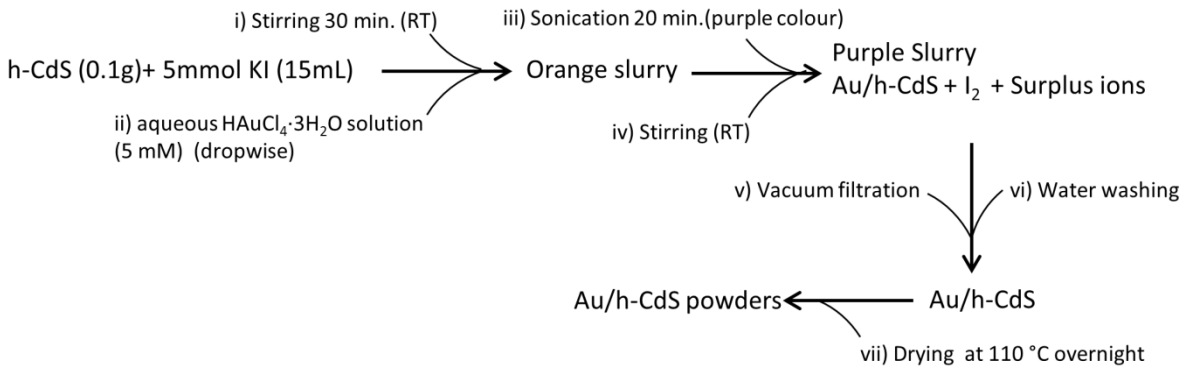

Scheme 2.6: Stepwise deposition of Au nanoparticles over h-CdS (A novel Iodide reduction method)

2.2.2.2 Deposition precipitation (DP) method

In the case of deposition precipitation (DP), 0.1g of CdS was added to 50 mL of 0.5 M NaOH and sonicated well to give a homogeneous CdS dispersion. Specific volume of aqueous solution of $HAuCl_4.3H_2O$ (0.01 M) was then added dropwise to the CdS dispersion with continuous stirring. The resulting dispersions were sonicated for 10 min and then stirred for a further 2 h. Finally, $HAuCl_4.3H_2O$ impregnated CdS photocatalyst was collected by vacuum filtration and dried at 110 °C overnight (scheme 2.7).

.

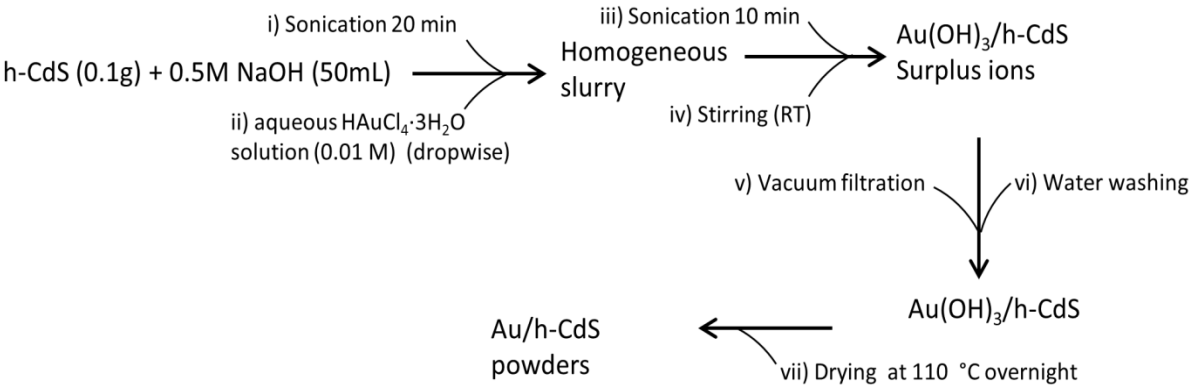

Scheme 2.7: Stepwise deposition of Au nanoparticles over hex-CdS (deposition precipitation (DP) method

2.2.2.3 Photodeposition (PD) method

In the case of photodeposition, CdS powder (0.1 g) was suspended in 50 mL of an aqueous solution of isopropanol (50 vol. %) in a 140 mL pyrex reactor. The appropriate amount of aqueous solution of $HAuCl_4.3H_2O$ (0.01 M) was injected into the reactor sealed with a rubber septum. The reactor was purged with argon (N_2) gas for 10–15 min to remove any traces of oxygen. The final solution was photo-irradiated by UV light (100 W high pressure Hg arc, 10.4 mW/cm^2) under magnetic stirring for 2 h. Thus, Au^{3+} was reduced

($Au^{3+}(HAuCl_4) \rightarrow Au°$) by photogenerated electrons of CdS and thereby deposited on its surface. After this, the solution was centrifuged, washed repeatedly with distilled water and isopropanol to remove any impurities and the powder was collected after drying (scheme 2.8) [540].

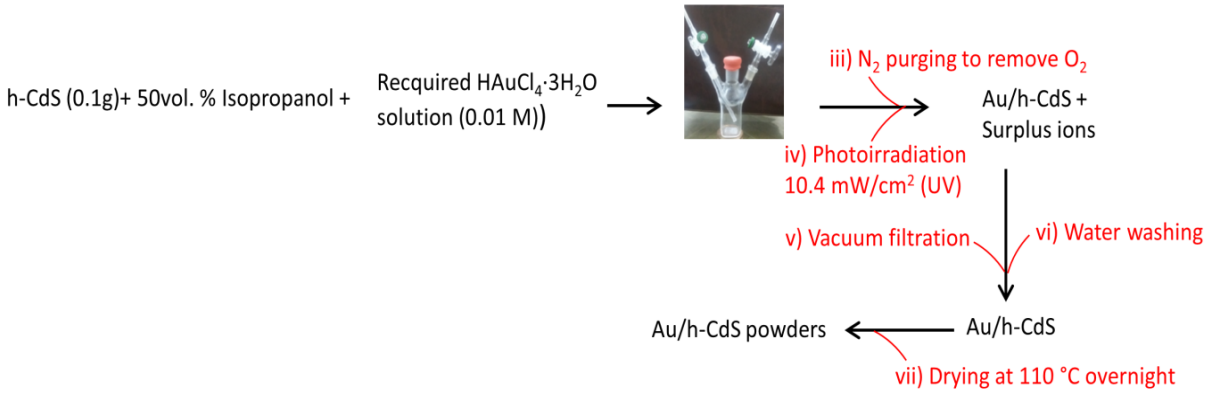

Scheme 2.8: Stepwise deposition of Au nanoparticles over hex-CdS (Incipient wetness impregnation (WI) method)

2.2.2.4 Incipient wet impregnation (WI) method

In the case of incipient wet impregnation method (WI), 0.1 g of CdS was added into appropriate amount of aqueous solution of $HAuCl_4$ (0.01 M). The solution pH was lower than 1.0. The solution was then aged at room temperature (RT) for 1 h and was washed twice with doubly distil water (50 mL). The solution was then centrifuged and the solid thus obtained was dried under vacuum at room temperature for 2h and dried at 110 ^oC to get final powder photocatalysts (scheme 2.9) [541].

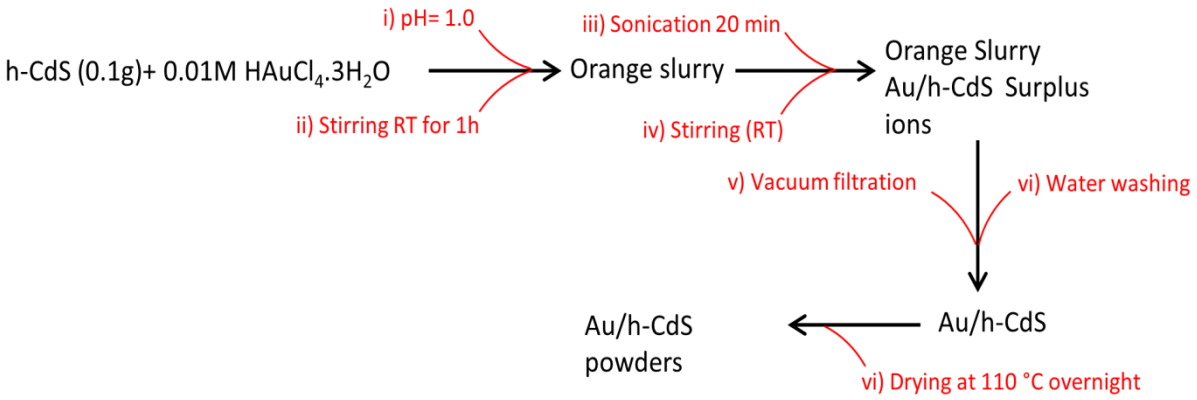

Scheme 2.9: Stepwise deposition of Au nanoparticles over hex-CdS (Incipient wetness impregnation (WI) method)

Table 2.4: List of synthesized CdS based photocatalysts with different variables.

Sr. No.	Materials formulation	Calcination temp. (°C) of CdS	Calcination atmosphere	Overall metal loading wt.%	Loading method
1	Cubic CdS	0	-	-	-
2	Cubic CdS	100-400	Air	-	-
3	$Cd(SO_4)_2$	500	Air	-	-
4	Hexagonal CdS	600	Nitrogen	-	-
5	Hexagonal CdS	800	Nitrogen	-	-
6	Au/c-CdS	400	Air	3	KI
7	Au/h-CdS	600	Nitrogen	1	KI
8	Au/h-CdS	600	Nitrogen	2	KI
9	Au/h-CdS	600	Nitrogen	3	KI
10	Au/h-CdS	600	Nitrogen	4	KI
11	Au/h-CdS	600	Nitrogen	5	KI
12	Au/h-CdS	600	Nitrogen	1	PD
13	Au/h-CdS	600	Nitrogen	2	PD
14	Au/h-CdS	600	Nitrogen	3	PD
15	Au/h-CdS	600	Nitrogen	4	PD
16	Au/h-CdS	600	Nitrogen	1	DP
17	Au/h-CdS	600	Nitrogen	2	DP
18	Au/h-CdS	600	Nitrogen	3	DP
19	Au/h-CdS	600	Nitrogen	4	DP
20	Au/h-CdS	600	Nitrogen	1	WI
21	Au/h-CdS	600	Nitrogen	2	WI
22	Au/h-CdS	600	Nitrogen	3	WI
23	Au/h-CdS	600	Nitrogen	4	WI

*Hydrogen production was performed over all samples except sample number 3

2.3 g-C_3N_4 based photocatalysts

2.3.1 Synthesis of Pd-Ag/g-C_3N_4 photocatalysts

All reagents used were of analytical grade and used without further purifications. The *g*-C_3N_4 was fabricated by directly heating the melamine in semi-closed system to retard melamine sublimation. In a typical synthesis 2g of melamine was placed in an alumina crucible covered with a lid and heated at 520-560 °C for 4 h at a heating rate of 10 °C min^{-1} in a muffle furnace. A light yellow powder of *g*-C_3N_4 was collected and ground to a fine powder (scheme 3.10). To deposit Ag and Pd nanoparticles, 0.5g of *g*-C_3N_4 powder was thoroughly dispersed in 25 mL of distilled water by sonication for 2h followed by stirring at room temperature for 30 min. an appropriate amount of $Pd(CH_3COO)_2$ and $AgNO_3$ salt solutions were added dropwise with continuous stirring. To reduce the metal nanoparticles, freshly prepared 0.1 M $NaBH_4$ ($NaBH_4$/metal, mol/mol=10) was added dropwise. The resulting slurry was left stirring for further one hour. The photocatalyst Pd-Ag/*g*-C_3N_4 was recovered by vacuum filtration, washed with water and dried at 90 °C for overnight. The as prepared powder was calcined at 350 °C for 2 hours to get final Pd_x-Ag_y/*g*-C_3N_4 photocatalysts (where

x and *y* are nominal metal loadings) (scheme 3.11). The nominal weight percentages of Pd and Ag in photocatalyts were $Ag_{1.0}$, $Pd_{1.0}$, $Pd_{0.7}$-$Ag_{0.3}$, $Pd_{0.5}$-$Pd_{0.5}$, $Pd_{0.3}$-$Ag_{0.7}$ with overall 1 wt.% loading, where subscripts represents the nominal weight percentage of each metal. Photocatalyts with various metal wt.% loadings were also synthesized by varying the amount Pd and Ag salts accordingly. The BET surface area of the as prepared *g*-C_3N_4 was ca. 8 m^2 g^{-1} in all the photocatalysts.

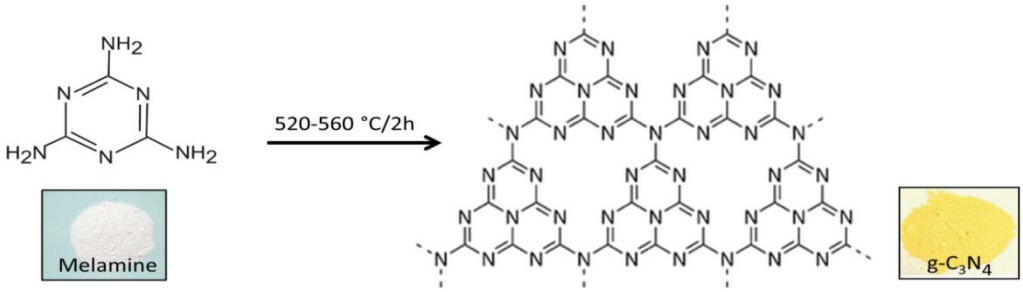

Scheme 2.10: Synthesis of g-C_3N_4 from condensation of melamine

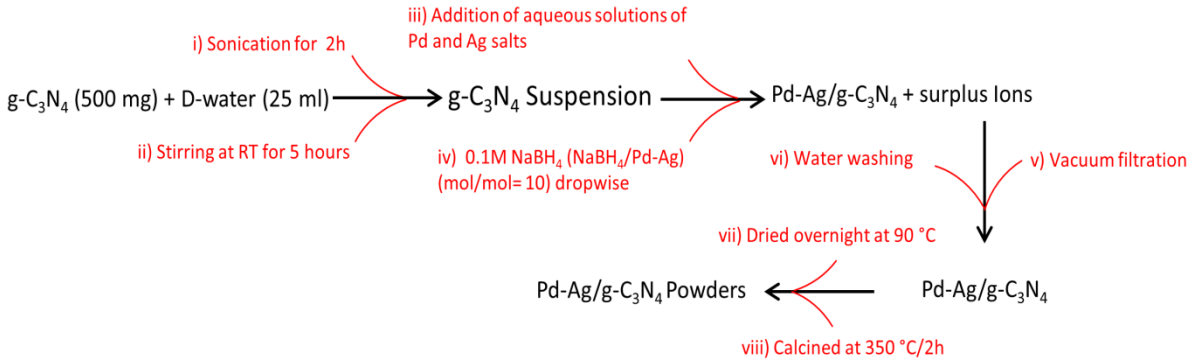

Scheme 2.11: Stepwise deposition of Pd-Ag nanoparticles over g-C_3N_4

Table 2.5: List of synthesized photocatalysts based g-C_3N_4 with different variables

Sr. No.	Materials formulation	Condensation temp. (°C)	Overall metal loading wt. %	Calcination temp. (°C)
1	g-C_3N_4(from melamine)	520-560	-	-
2	Ag_1/g-C_3N_4	-	1	350
3	Pd_1/g-C_3N_4	-	1	350
4	$Pd_{0.3}$-$Ag_{0.7}$/g-C_3N_4	-	1	350
5	$Pd_{0.5}$-$Ag_{0.5}$/g-C_3N_4	-	1	350
6	$Pd_{0.7}$-$Ag_{0.3}$/g-C_3N_4	-	1	350
7	$Pd_{0.7}$-$Ag_{0.3}$/g-C_3N_4	-	0.5	350
8	$Pd_{0.7}$-$Ag_{0.3}$/g-C_3N_4	-	1.5	350
9	$Pd_{0.7}$-$Ag_{0.3}$/g-C_3N_4	-	2	350
10	$Pd_{0.7}$-$Ag_{0.3}$/g-C_3N_4	-	3	350
11	$Pd_{0.7}$-$Ag_{0.3}$/g-C_3N_4	-	1	400
12	$Pd_{0.7}$-$Ag_{0.3}$/g-C_3N_4	-	1	450
13	$Pd_{0.7}$-$Ag_{0.3}$/g-C_3N_4	-	1	500

*Hydrogen production was performed over all samples

2.3.2 Hydrogen production experiments over TiO_2 based photocatalysts

Photocatalytic hydrogen production tests were conducted in a Pyrex reactor (140 mL). Initial tests were conducted in which catalyst amounts were changed (0.0025, 0.005, 0.01, and 0.02 g). Maximum H_2 production rate was obtained with 0.0025 g. Photocatalyst (2.5 mg, $Cu(OH)_2$-$Ni(OH)_2$/P25, $Cu(OH)_2$-$Ni(OH)_2$/TNRs or Cu-Cu_2O/TiO_2) was loaded in the reactor containing 25 mL of an aqueous alcohol-water mixture (20 vol. % ethanol or 5 vol.% glycerol). Prior to the start of each photocatalytic experiment, the reactor was continuously bubbled with nitrogen at a flow rate of 10 mL min^{-1} for 30 min to remove dissolved and headspace oxygen. Molecular oxygen can trap electrons from the TiO_2 conduction band to produce superoxide radicals which can subsequently oxidize organic sacrificial agents [587]. A Spectroline model SB-100P/F lamp (100 W, 365 nm) at a distance of 10 cm from the reactor was used for UV light excitation of the photocatalysts. The photon flux measured at the sample was ~6.5 mW cm^{-2} (comparable to UV flux in sunlight). Hydrogen generation was monitored by taking head space gas samples (0.5 mL) at regular time intervals with gas tight syringe and injecting them into the gas chromatograph (Shimadzu GC 2014) equipped with a TCD detector and molecular sieve capillary column (Length =25 mm; ID = 0.32 mm; average thickness 0.50 µm). H_2 produced through photoreaction was quantified against an internal calibration curve. The photocatalytic tests for each sample were repeated at least three times for accuracy.

Table 2.6: List of different parameters for hydrogen production experiments (TiO_2 based photocatalysts)

Sr. No.	Photocatalyst tested	Amounts tested (mg)	Optimal amount	Light source	Light intensity mW/cm^2	Sacrificial reagents
1	$Cu(OH)_2$-$Ni(OH)_2$/P25	2.5-20	2.5	SB-100P/F lamp (100 W, 365 nm)	~6.5	20% ethanol-water
2	$Cu(OH)_2$-$Ni(OH)_2$/P25	2.5-20	2.5	SB-100P/F lamp (100 W, 365 nm)	~6.5	5% glycerol-water
3	$Cu(OH)_2$-$Ni(OH)_2$/TNRs	2.5-20	2.5	SB-100P/F lamp (100 W, 365 nm)	~6.5	20% ethanol-water
4	$Cu(OH)_2$-$Ni(OH)_2$/TNRs	2.5-20	2.5	SB-100P/F lamp (100 W, 365 nm)	~6.5	5% glycerol-water
5	Cu-Cu_2O/TiO_2 (Anatase)	2.5-20	2.5	SB-100P/F lamp (100 W, 365 nm)	~6.5	5% glycerol-water
6	$Cu(OH)_2$-$Ni(OH)_2$/P25 Calcined 400 °C	2.5-20	2.5	SB-100P/F lamp (100 W, 365 nm)	~6.5	20% ethanol-water

Figure 2.1: Lab set up for photocatalytic hydrogen production measurements

2.3.2.1 Photocatalyst recyclability tests

The recyclability of 0.8Cu(OH)$_2$-0.2Ni(OH)$_2$/P25, 0.8Cu(OH)$_2$-0.2Ni(OH)$_2$/TNRs was investigated in 20 vol. % ethanol-water mixtures and for Cu-Cu$_2$O/TiO$_2$ photocatalyst in 5 vol. % glycerol-water mixtures for 16 h. Hydrogen production in each case was continuously monitored for a fixed time period of 4 h. After the completion of each run the reactor was purged with nitrogen at same flow rate to remove hydrogen produced during previous run.

2.3.3 Hydrogen production experiments over CdS based photocatalysts

Photoreactions over the Au/CdS were conducted in ethanol, water-electrolyte (0.1M Na_2S, 0.02M Na_2SO_3; pH = 13) and a mixture of both at a total volume of 25 mL in a 140 mL Pyrex reactor. Initial tests were conducted in which catalysts amounts were changed (0.005, 0.01, and 0.02 g). Maximum H_2 production rate was obtained with 0.01 g. Hydrogen production tests, therefore, carried out the tests at this catalyst concentration (0.4g/L_{Liquid}). The decrease in H_2 production rate with a further increase in catalyst amount might be related to shadowing of some of catalyst particles by other particles directly in front of the light source and is further explained in the result and discussion section. Prior to the start of each photocatalytic experiment, the reactor was continuously bubbled with nitrogen at a flow rate of 10 mL min^{-1} for 30 min to remove dissolved and headspace oxygen. A 500 W Warrior WEHL halogen bulb lamp with irradiation flux of 35 mW cm^{-2} at a distance of ca. 30 cm from the reactor was used as a light source. The mixture was continuously stirred with a magnetic stirrer and cooled with an electric fan to maintain a constant temperature of ca. 25

^{o}C. Gas samples (1 mL) were taken after appropriate intervals typically 15-30 minutes with a gas tight syringe and analyzed using a Shimadzu Gas Chromatograph Model GC 2014 equipped with a TCD detector and molecular sieve capillary column (Length = 25 m; ID = 0.32 mm; average thickness 0.50 µm). Hydrogen quantification was performed using a calibration curve. The apparent quantum yield was calculated under similar photo-catalytic reaction condition using the following equation [588].

$$\text{Apparent quantum yield} = \frac{\text{Number of } H_2 \text{ molecules produced} \times 2}{\text{Number of incident photons}} \times 100 \qquad (29)$$

The lamp produced radiation within the 350-900 nm range. However, CdS with band gap of 2.4 eV can be excited only by radiations below ca. 520 nm. The lamp power was calculated using wavelength versus intensity curve (fig. 2.20) and by comparing the area under radiation capable of excitation with the total integrated area under curve. The apparent quantum yield, based on the reactor configuration and the area of reactor exposed to light (13.93 cm^2) was found equal to 16.3%. The apparent quantum yield based on the complete radiation spectrum of the lamp was equal to ca. 4%.

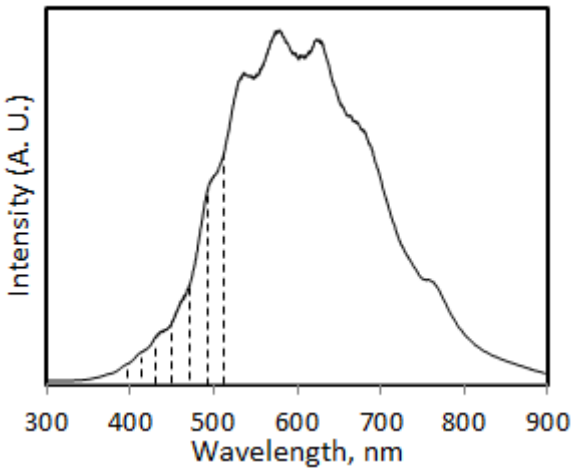

Figure 2.2: Wavelength versus intensity curve for radiation from a 500 W Warrior WEHL halogen bulb lamp with irradiation flux of 35 mW cm^{-2} at a distance of ca. 30 cm from the reactor. Shaded area represents the fraction of radiation capable of CdS excitation.

2.3.3.1 Photocatalyst recyclability tests

The recyclability of all Au/CdS photocatalyst was investigated in ethanol-water-electrolyte mixtures for 16 h. Hydrogen production in each case was continuously monitored for a fixed

time period of 4 hours. After the completion of each run the reactor was purged with nitrogen at the same flow rate to remove hydrogen produced during the previous run.

2.3.4 Hydrogen production experiments over g-C_3N_4 based photocatalysts

Photocatalytic hydrogen production tests were conducted in a Pyrex reactor (140 mL). Photocatalyst (2.5 mg) was loaded in the reactor containing 10% triethanolamine water mixtures. Prior to the start of each photocatalytic experiment, the reactor was continuously bubbled with nitrogen at a flow rate of 10 mL min^{-1} for 30 min to remove dissolved and headspace oxygen. All experiments were performed between 10.00 am to 4.00 pm in clear days of March, 2017. The reactor was placed (33º 44'50'N 73º 08'20'E, Islamabad 45320, Pakistan) under direct sunlight. The average horizontal global solar irradiation during experiments was measured using handheld pyranometer type 105HP from SolData Instruments and was found equal to 840 Wm^{-2} (300-1100 nm). Hydrogen generation was monitored by taking gas head space samples (0.5 mL) at regular time intervals and injecting them into the gas chromatograph (Shimadzu GC 2014) equipped with a TCD detector and molecular sieve capillary column (Length = 25 mm; ID = 0.32 mm; average thickness 0.50 µm). H_2 produced during photoreaction was quantified against an internal calibration curve.

Table 2.7: List of all parameters for hydrogen production experiments for CdS and g-C_3N_4 based photocatalysts.

Sr. No.	Photocatalyst tested	Amounts tested (mg)	Optimal amount	Light source	Light intensity mW/cm^2	Sacrificial reagents
1	0.5-5wt.% Au/CdS (KI method)	5-20	10	500 W Warrior WEHL halogen lamp	~35	8-92 vol.% ethanol-water electrolyte mix.
2	3wt.% Au/CdS (KI method)	5-20	10	500 W Warrior WEHL halogen lamp	~35	0.1M Na_2S, 0.02M Na_2SO_3
3	3wt.% Au/CdS (KI method)	5-20	10	500 W Warrior WEHL halogen lamp	~35	8% ethanol-water mixtures
4	0.5-5wt.% Au/CdS (WI method)	5-20	10	500 W Warrior WEHL halogen lamp	~35	8-92 vol.% ethanol-water electrolyte mix
5	0.5-5wt.% Au/CdS (PD method)	5-20	10	500 W Warrior WEHL halogen lamp	~35	8-92 vol.% ethanol-water electrolyte mix
6	0.5-5wt.% Au/CdS (DP method)	5-20	10	500 W Warrior WEHL halogen lamp	~35	8-92 vol.% ethanol-water electrolyte mix
7	Pd-Ag/g-C_3N_4	2.5-10	10	Halogen lamp	~35	10 vol.% triethanolamine water mixtures

2.3.4.1 Photocatalyst recyclability tests

The activity and stability of $Pd_{0.7}$-$Ag_{0.3}$/*g*-C_3N_4 photocatalyst was investigated in 10 vol. % triethanolamine-water mixture. Photocatalytic hydrogen production was observed over the duration of the experiments (16 h). After the completion of each run the reactor was purged with nitrogen at the same flow rate to remove hydrogen produced during the previous run.

2.3.5 Dye degradation experiments over $Cu(OH)_2$-$Ni(OH)_2$/P25 photocatalysts

Rhodamine B dye degradation experiments were performed over P25, 1.0$Ni(OH)_2$/P25, 1.0$Cu(OH)_2$/P25 and 0.8$Cu(OH)_2$-0.2$Ni(OH)_2$/P25 to study the electron transfer mechanisms (discussed later). Rhodamine B photodegradation experiments were conducted in a 140 mL pyrex reactor containing 40 mL of aqueous Rhodamine B (12 mg L^{-1}) and 10 mg of photocatalyst. Prior to starting an experiment, the reaction mixture was stirred in the dark for one hour to establish the adsorption-desorption equilibrium of the dye on the catalyst surface. The same irradiation set up was used as described in the hydrogen production experiment section. At regular intervals, a small portion of reaction mixture was collected by pipette, centrifuged to remove suspended photocatalyst particles and the absorbance (400-600nm) was measured by UV spectrophotometer (lambda 25 Perkin Elmer). For radical trap experiments, 5 mL of 50 mmol solutions of Na_2EDTA or benzoquinone were added directly in the initial reaction mixture. Negligible Rhodamine B degradation was observed under UV in the absence of a photocatalyst.

2.3.6 Photocatalysts characterization

The synthesized photocatalysts were fully characterized i.e. structurally, morphologically, optically, and to find out the surface characteristics, via using following analytical tools and specific instruments.

2.3.6.1 Powder X-ray diffraction (PXRD)

Powder XRD patterns were collected on a Siemens D5000 Diffractometer equipped with a curved graphite filter monochromator. XRD data was collected over the 2θ range 20-70^o (step size 0.05^o, scan rate 2^o min^{-1}) using Cu Kα X-rays (λ= 1.5418 Å, 40 mA, 40 kV). Anatase and rutile crystallite sizes (L) were determined using the Scherrer equation ($L = 0.9\lambda/\beta\cos\theta$) and line-widths of the anatase (101) reflection at 2θ = 25.3^o and the rutile (110) reflection at 2θ = 27.4^o, respectively. The particle size of g-C_3N_4 was calculated by taking the line width of the (002) reflection at 2θ =27.4^o interlayer stacking of aromatic systems.

PXRD Principle: It is one of the primary techniques used for the identification and characterization of materials based on their diffraction patterns to evaluate their structural phases. A powder material sample is placed in a holder, then the sample is illuminated with x-rays of a fixed wave-length and the intensity of the reflected radiation is recorded using a goniometer. This data is then analyzed for the reflection angle to calculate the inter-atomic spacing (D value in Angstrom units - 10^{-8} cm) by sing Bragg's law $n\lambda = 2d \sin \theta$.

where

λ = wavelength of the incident X-ray
d =Interplaner spacing of the crystal
θ = angle between the lattice plane and the X-rays
n = an integer

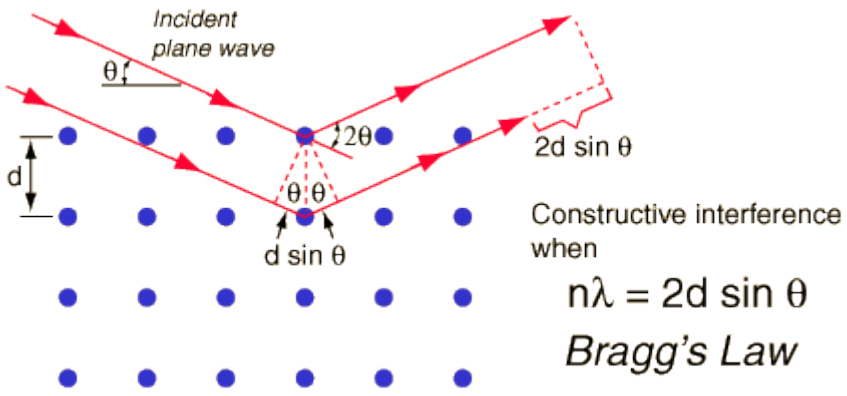

Figure 2.3: Illustration of Bragg's law

2.3.6.2 UV-visible diffused reflectance spectroscopy

UV–vis absorbance spectra of the photocatalysts were collected over the wavelength range of 200–900 nm at the slit width of 2 nm on a Thermo Fisher Scientific UV–Vis spectrophotometer equipped with praying mantis diffuse reflectance accessory and an integrating sphere, having a 60 mm internal diameter. The base-line correction was performed using $BaSO_4$ as the reference.

2.3.6.3 Transmission electron microscopy (TEM)

TEM analyses were performed by using a Philips CM 200 field emission TEM operating at an accelerating voltage of 200 kV, with a Bruker SDD (silicon drift detector) EDAX system was used for transmission electron microscopy. The microscope is also equipped with a SIS CCD camera, which enables high-resolution digital imaging. In order to analyse the sample with TEM, it is necessary to disperse the particles in a solvent. A small quantity of the solid

sample was mixed with 2 mL of toluene and sonicated for 10 - 15 mins. 1-2 drops of this dispersion were deposited onto a 200 mesh carbon grid with a Pasteur pipette. These grids were then mounted onto sample holders and inserted into the TEM, allowing the sample to be viewed and imaged (in transmission) at near-atomic scale.

2.3.6.4 X-ray photoelectron spectroscopy (XPS)

XPS data was collected using a Kratos Axis UltraDLD equipped with a hemispherical electron energy analyzer operated in the hybrid lens mode at 90^{o} take off angle with respect to the specimen surface and an analysis chamber at base pressure ~1×10^{-9} Torr. Samples were excited using monochromatic Al Kα X-rays (1486.69 eV) with X-ray source operating at 150 W. Samples were gently pressed into thin pellets of ~0.1 mm thickness for the analyses. A charge neutralization system was used to alleviate sample charge build up during analysis. Survey scans were collected at a pass energy of 80 eV over the binding energy range 1200-0 eV, while core level scans were collected with a pass energy of 20 eV. The spectra were calibrated against the C1s signal at 284.80 eV from adventitious hydrocarbons. The relative concentration of the identified elements were calculated using peak areas of Ti2p, O1s, C1s and Cu2p core level signals where the peak fitting was performed using Casa XPS Version 2.2.88 software package. Relative sensitivity factors, based on instrument modified Schofield cross-sections were used in the quantification procedure (7.81, 2.93, 1 and 25.39 for Ti2p, O 1s, C1s and Cu2p respectively). The chemical states of Ti, O, C and Cu were determined from narrow scan spectra taken at pass energy of 20 eV over the Ti2p, O1s, C1s and Cu2p regions (50 sweeps/150 ms dwell time), respectively. For Au/CdS systems the surface chemical states of the elements present were determined from narrow scan spectra taken at pass energy 20 eV over the C1s, O1s, and S2p, Au4f and Cd3d regions (30 sweeps/150 ms dwell time). The raw XPS data was deconvoluted using Casa XPS peak fitting software using a Shirley background for C1s, O1s, S2p and Au4f peaks whilst a Tougaard background was used for the Cd3d peaks as the Shirley back-ground could not be applied due to the linear background between Cd $3d_{3/2}$and Cd $3d_{5/2}$ peaks.

XPS Principle

The XPS can be used to gain information about elemental composition of the surface (top 1–10 nm usually) except hydrogen and helium with a detection limit as low as 0.3 %, chemical or electronic state of each element in the surface, elemental composition across the surface (line profiling or mapping), and as a function of ion beam etching (depth profiling). The process of acquiring XPS data starts from the preparation of the solid samples which are

then placed in a vacuum environment with a base pressure of *ca.* 10^{-8} torr. The sample surface is irradiated with X–ray photons which interact with an inner shell electron of the atom as a result of which the energy of the X–ray photon is transferred to the electron. If the electron receives enough energy it escapes the surface of the sample creating a photoelectron of a specific energy. The photoelectrons are separated and counted according to the difference in energy which is related to the atomic or molecular environment of their origin.

The energy of the incident photons can be given by the Einstein relation:

$$E = h\nu \qquad (30)$$

Where,

h = Planck's constant (6.62×10^{-34} Js)

ν = Frequency (Hz) of the radiation

The kinetic energy E_K of emitted photoelectron is measurable, so the binding energy of the electron E_B can be calculated from the Einstein equation:

$$E_B = h\nu - E_K - \varphi \qquad (31)$$

Where,

E_B = Binding energy of the electron

E_K = Kinetic energy of the emitted photoelectron

$h\nu$ = Energy of the incident X–ray beam

Φ = Work function of the solid

Binding energy is unique for each element and is used to identify the sample composition. Also the number of photoelectrons emitted has a direct relationship to the concentration of the emitting atom in the sample under study. An electron energy analyser is used to measure the kinetic energy distribution of the emitted photoelectrons to give an XPS peak.

2.3.6.5 Brunauer–Emmett–Teller (BET)

Brunauer Emmett Teller (BET) is used to measure the surface area of solid samples by physical adsorption of gas molecules on a solid surface. In this technique probing gases are utilized as adsorbate that does not react chemically with the solid material surfaces. N_2 is the most frequently used adsorbate for surface probing by BET methods. For this reason, standard BET analysis is often performed at N_2 (77 K) boiling temperature. N_2 physisorption isotherms were collected on Micromeritics Tristar 3000 at liquid N_2 temperature (−195 °C). Specific surface areas were calculated according to the Brunauer–Emmett–Teller (BET)

method [589]. Cumulative pore volumes and average pore diameters were calculated from the adsorption isotherms by the Barrett–Joyner–Halenda (BJH) method [590]. The samples were degassed at 50 °C under vacuum for 1 h prior to analysis.

2.3.6.6 Steady-state and time-resolved photoluminescence (PL)

Steady-state and time-resolved photoluminescence (PL) measurements were carried out using a Flau Time 300 (FT-300) steady state and life-time spectrometer, PicoQuant GmbH, Germany. The PL was measured following pulsed LED laser excitation source, PLS-300, centered at 305 nm with full width half maximum (FWHM) of ~ 416 ps and pulse energy 0.077 pJ. The PL curves were fitted by using Easy Tau and FluoFit software. Samples were prepared by dispersing the powder in methanol to make homogeneous slurry. The fine layer of slurry was then deposited over glass slides and dried at 60 °C for 30 min.

2.3.6.7 Thermogravimetric analysis (TGA)

Thermogravimetric analysis of MOF-199 $[Cu_3(BTC)_2(H_2O)_3]_n$ was carried out in a TGA/SDT851e (MettlerToledo-Switzerland) thermo-balance under N_2 flow with the temperature ramp of 10 °C min^{-1} from 50 - 500 °C. Weight loss versus temperature was continuously recorded during the experiment. Vacuum Fistreem furnace with Vacuubrand 2008/05 vacuum pump was used to dry samples.

2.3.6.8 Inductively coupled plasma optical emission spectroscopy

In order to monitor elemental composition of various photocatalysts, inductively coupled plasma optical emission spectroscopy (ICP-OES; Model: Optima 8300, Perkin-Elmer) measurement were carried out. The samples for the ICP-OES measurements were prepared by dissolving powder samples in HNO_3:H_2O solution.

Chapter # 3

Results, Discussion & Conclusions

Chapter-3 Results, Discussion and Conclusions

3.1 TiO_2 based photocatalysts

3.1.1 $Cu(OH)_2$-$Ni(OH)_2$/P25 and $Cu(OH)_2$-$Ni(OH)_2$/TiO_2 nanostructures (nanorods and nanoleaves) photocatalysts

In this section characterization results of bimetallic hydroxide loaded nanostructures supports and typical TiO_2 support P25 (80% anatase +20% rutile) are thoroughly discussed. A comparison is made between the hydrogen production rates with the aim to fabricate highly efficient and economical (noble metal free) photocatalysts for hydrogen production from water in the presence of other renewable (ethanol or glycerol).

3.1.1.1 Powder XRD analysis

Powder XRD patterns for all $Cu(OH)_2$-$Ni(OH)_2$/P25 photocatalysts are shown in Fig.3.1 and are dominated by peaks due to anatase and rutile. No obvious change in the anatase and rutile diffraction peak positions is seen suggesting that the metal hydroxide species are finely dispersed over the support. The low loadings would also make identification of $Ni(OH)_2$ and $Cu(OH)_2$ difficult. Anatase and rutile crystallite size determined using the Scherrer equation were 28 nm and 36 nm, respectively. Characteristic anatase and rutile peaks are labeled.

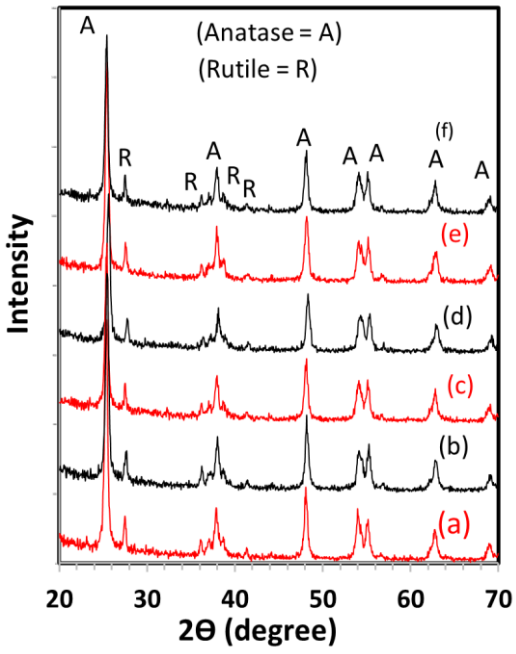

Figure 3.1: Powder XRD patterns of (a) 1.0$Cu(OH)_2$/P25 (b) 1.0$NiOH)_2$/P25 (c) 0.2$Cu(OH)_2$-0.8$Ni(OH)_2$/P25 (d) 0.5$Cu(OH)_2$-0.5$Ni(OH)_2$/P25 (e) 0.8$Cu(OH)_2$-0.2$Ni(OH)_2$ /P25 and (f) 0.8$Cu(OH)_2$-0.2$Ni(OH)_2$/P25 (calcined).

In order to prepare the highly crystalline and higher surface area TiO_2 nanorods from titanate precursors, a quick screening was carried out to find the suitable hydrothermal and post calcination temperature. The PXRD patterns (Fig. 3.2a) show that as prepared titanate nanostructures at hydrothermal temperatures ranging from 130-150 °C show good crystalline behavior. A reasonable explanation for this is that temperature lower than 130 °C lead to less cleavage of Ti–O–Ti bonds to form Ti–O–Na, which is the initial stage in synthesizing titanate nanostructures. Treatment at higher temperature than 130 °C would start to destroy the lamellar $Na_2Ti_3O_4$, an intermediate in the TiO_2 nanostructures TNRs formation process [455]. Hydrothermal treatment at temperatures higher than 150 °C almost completely destroys the lamellar layers of $Na_2Ti_3O_7$ which transform into a nanoleaves morphology (Fig. 3.6). The maximum BET surface area was found for nanotubes like structures synthesized at 110-130 °C (Table 3.1).

Table 3.1: BET surface area values of TiO_2 nanorods and leaves.

HT Treatment (°C)	BET Surface Area (m^2 g^{-1})	BET Surface Area (m^2 g^{-1}) after calcination		
		400 °C	600 °C	800 °C
110	129	79	51	18
130	148	48	38	24
150	108	35	28	21
170	15	14	14	13

Previous studies suggested that calcination of $H_2Ti_3O_7$ in air at 350 °C for few hours is sufficient for the complete transformation of $H_2Ti_3O_7 \rightarrow 3TiO_2 + H_2O$ [591]. Fig. (3.2a-b) shows the XRD patterns $H_2Ti_3O_7$ nanostructures as prepared and after calcination for 2 h at 400 °C, 600 °C and 800 °C. For the calcination temperatures between 400 °C and 600 °C, anatase was the only phase identified by XRD, with the characteristic anatase reflections that sharpen and intensify with an increase in temperature indicating better ordering of the crystal lattices. The anatase to rutile phase transition temperature is known to depend upon the method of synthesis and the initial anatase crystallite size [74–78]. Many studies have been suggested that the anatase crystallite size needs to reach 30 nm prior to the commencement of phase transition to rutile [592, 593]. The XRD data suggest that the onset temperature for anatase to rutile phase transition decreases with increasing the hydrothermal temperature. Nanostructures prepared at 170 °C exhibit anatase to rutile conversion temperature below 600 °C. The nanotube like structures prepared at 110 °C to 150 °C show higher transition temperatures due to higher thermal stability. It is also well known that with the increase of

crystallinity the surface area decreases due to an increase of crystallite sizes. Therefore, nanorods prepared at 130 hydrothermal and 400 °C calcination temperatures were selected for further investigation due to higher surface area and crystallinity.

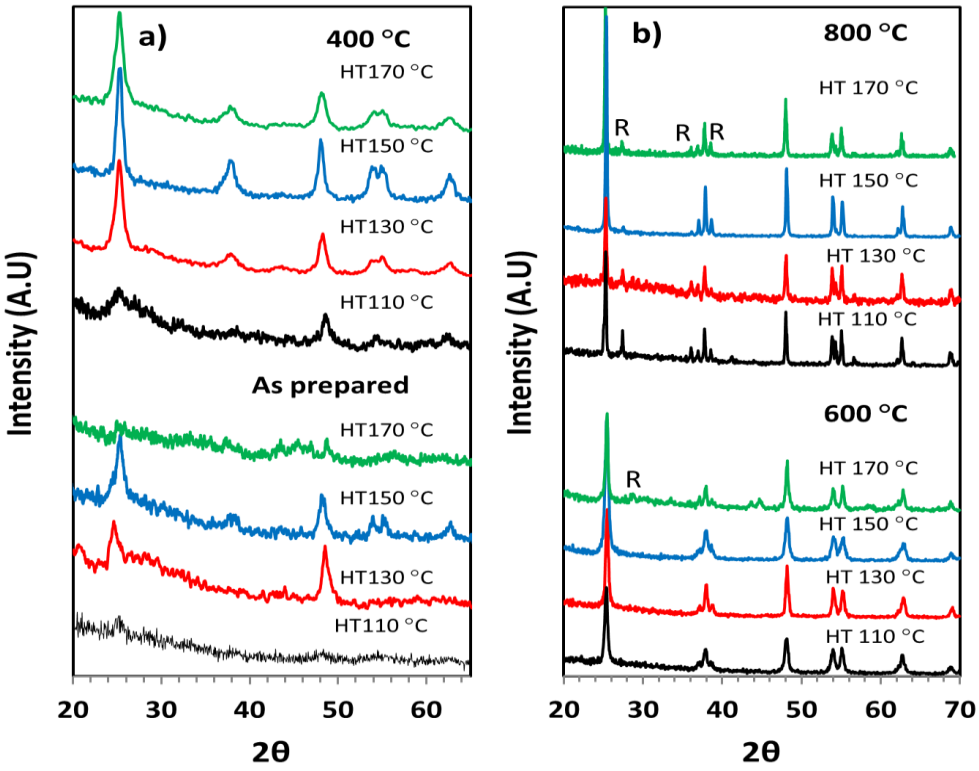

Figure 3.2: PXRD results of TiO_2 nanorods prepared at 110-170 °C hydrothermal temperature and post calcined from 400-800 °C.

3.1.1.2 UV-visible diffuse reflectance measurements

Fig. 3.3(a) shows UV-visible diffuse reflectance spectra for the different mono and bimetallic photocatalysts using P25 support, whilst Fig. 3.3b compares fresh and used $0.8Cu(OH)_2$-$0.2Ni(OH)_2$/P25. All catalysts showed intense absorption below 400 nm, due to the P25 support (E_g = 3.15 eV). The absorption edges of all metal containing photocatalysts showed absorption in the visible region due to overlap between the TiO_2 and metal hydroxide complexes absorption. It has been reported that Ni3d and Cu3d states can mix with the TiO_2 conduction band at the interface region and decrease the band gap energy between Ti3d and O2p states of TiO_2 [594]. The absorption spectra of fresh bimetallic photocatalysts show a broad band centred above 600 nm and a small absorption shoulder at 450 nm. The absorption shoulder at 450 nm is partly due to the interfacial charge transfer (IFCT) from TiO_2 conduction band to M^{2+} cations (where M = Cu and Ni) [504, 595, 596]. The enhanced absorption above 600 nm can be assigned to Ni^{2+} d-d (600-800 nm) and Cu^{2+} d-d (700-800

nm) transitions. The increased absorption around 450-600 nm for the used photocatalyst in fig.3.3b is likely due to the formation of Cu^{1+} oxide species during photoreactions [597].

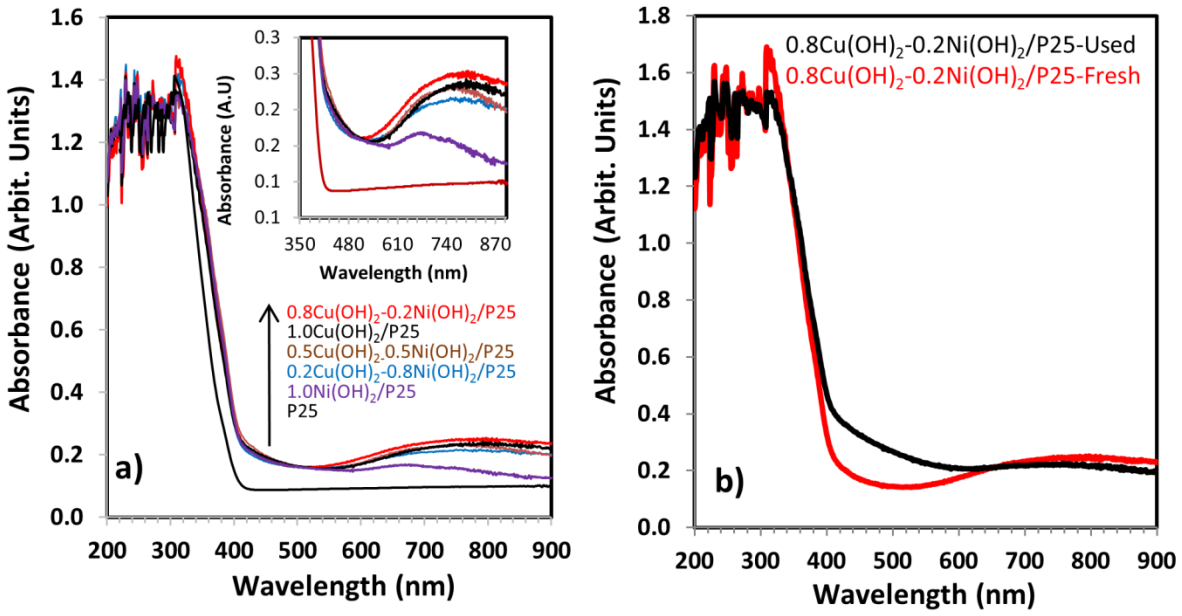

Figure 3.3: (a) UV-Vis spectra of P25, "as prepared" mono- and bimetallic photocatalysts as indicated; (b) UV-Vis of as prepared and used $0.8Cu(OH)_2$-$0.2Ni(OH)_2/TiO_2$.

Optical properties of other TiO_2 nanostructures prepared at different hydrothermal conditions and followed by calcination at various temperatures are shown in fig.3.4. The absorption edge of TiO_2 nanostructures (rods and leaves) is slightly blue shifted to 390 nm as compared to P25 due to the presence of the anatase phase. The comparison of optical absorption of nanostructures prepared at different hydrothermal treatments and calcination temperature is given in fig 3.4. Uncalcined nanotube like structures prepared at different hydrothermal temperatures show the same absorption except nanoleaves like structures prepared at 170 °C which show extended absorption in the visible range up to 550 nm (fig.3.4a). This might be due to the scattering and trapping of light in the nanoleaves morphology that disappear after calcination at 600 °C due to destruction of the nanoleaves morphology to anatase nanoparticles. All nanostructures calcined at 800 °C show a red shift in absorption and have similar optical behaviour due to the formation of a rutile phase and probably destruction of nanorods/nanoleaves morphology at high temperature (fig.3.4d). The UV-visible diffuse reflectance spectra for the different mono and bimetallic hydroxides over TNR_{130}-400, are shown in Fig. 3.4e whilst Fig. 3.4f compares the absorption of TNR_{130}, TNR_{130}-400 and fresh $0.8Cu(OH)_2$-$0.2Ni(OH)_2/TNR_{130}$-400. It is important to note that both mono and bimetallic supported titania nanorods showed more intense absorbance in the visible range as compared

to P25 nanoparticles. There are two main reasons behind this; 1) the development of more intimate contacts between hydroxides and nanorods support due to greater anatase phase as compared to P25 (discussed later). 2) Enhanced visible light trapping by the nanorods morphology.

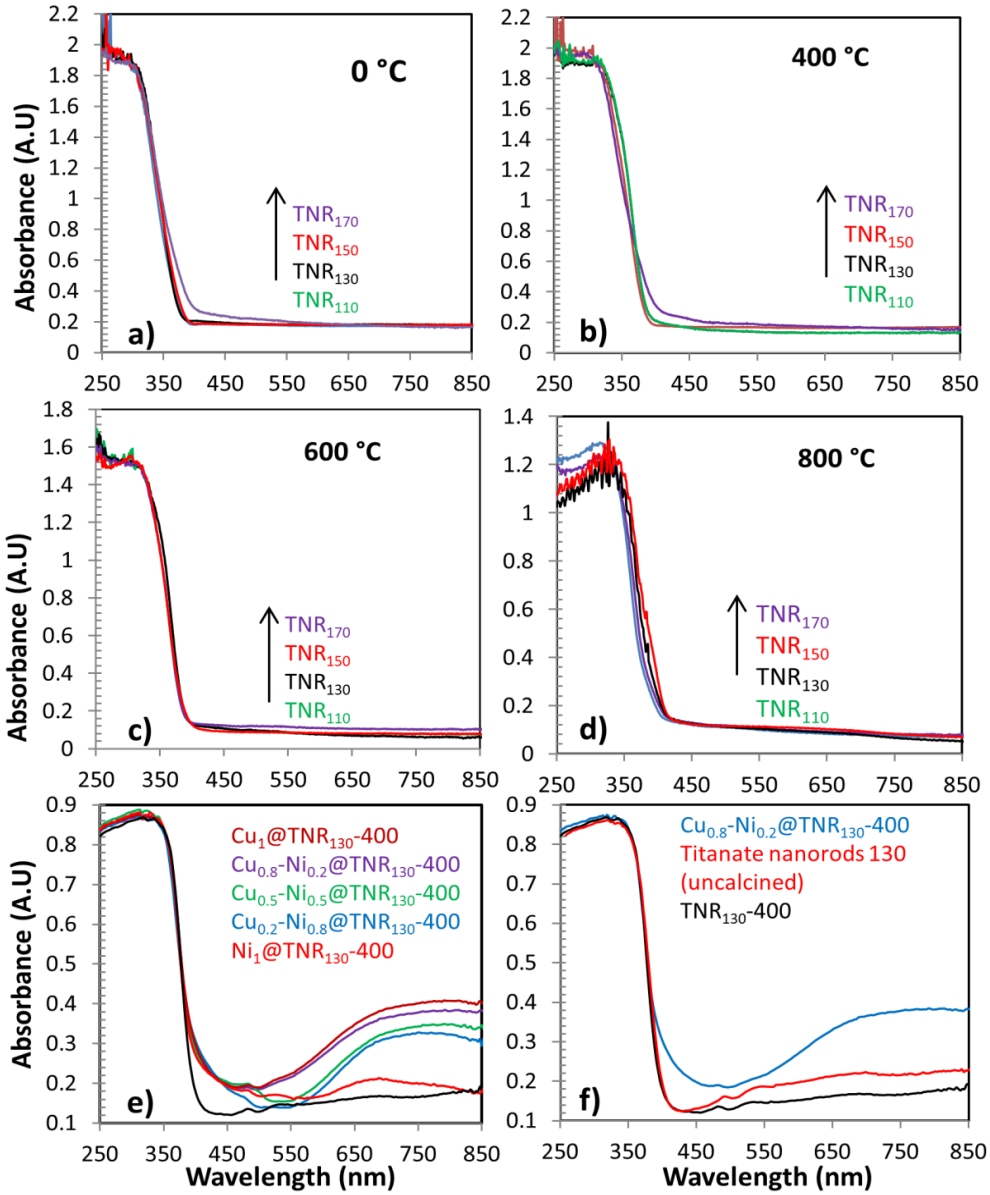

Figure 3.4: UV/Vis spectra of (a-d) TiO_2 nanostructures prepared at various hydrothermal and calcination temperatures. (e-f) TNR_{130}-400, "as prepared" mono and bimetallic photocatalysts as indicated, UV/Vis comparison of TNR_{130}, TNR_{130}-400 and 0.8$Cu(OH)_2$–0.2 $Ni(OH)_2$/ TNR_{130}-400.

3.1.1.3 TEM and SEM analysis

TEM images for 1$Cu(OH)_2$/P25 photocatalyst are shown in Fig. 3.5 at different magnifications. P25 is known to compose of small spherical anatase crystallites of average

size 20–30 nm and larger rutile crystallites with average size 40–60 nm, both of which are evident in the TEM images. It is very difficult to discern metal hydroxide nanoparticles on the surface of the TiO_2 using TEM due to the similarity in the atomic number of Ni, Cu and Ti among other factors (fig. 3.5a & b). It has been reported that hydroxide nanoparticles on TiO_2 support could only be identified with any certainty at a metal loadings of greater than 5 wt. % $M(OH)_2$ loading (M = Ni, Cu) [434, 598]. It is likely that the hydroxide nanoparticles are present in a very small size (1-3 nm) as seen in the magnified TEM image only (Fig. 3.5b). The presence of small metal hydroxide particles suggests a strong interaction with P25 support.

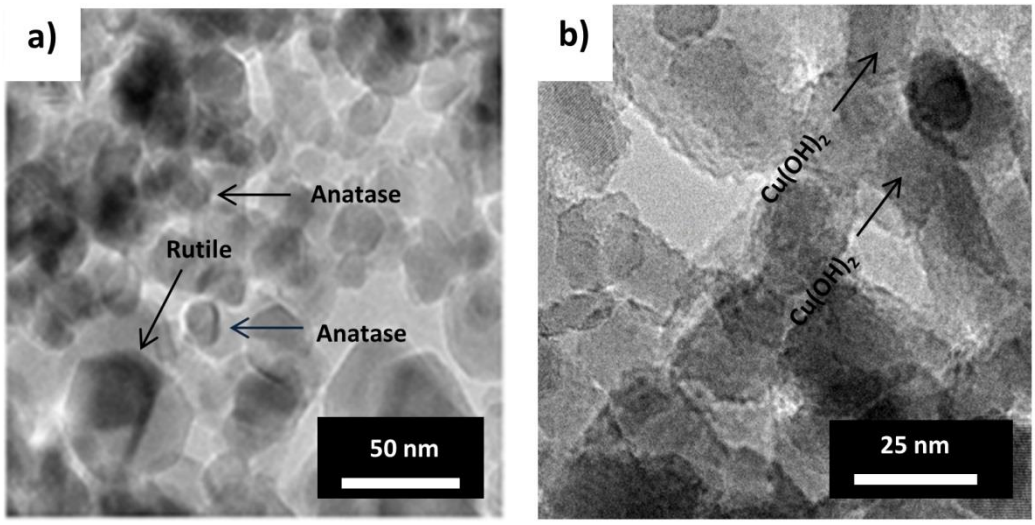

Figure 3.5: TEM images of fresh $1Cu(OH)_2$/P25 photocatalyst.

Fig. 3.6 (a-d) shows the SEM images of ($H_2Ti_3O_4$) titanate nanostructures precursors obtained at 110-170 °C. It is clear from the images that on going from 110 to 150 °C hydrothermal treatments of titanate nanotube precursors aggregates are gradually converted into loosely and randomly tangled structures. Surprisingly, when the temperature was increased beyond 150 °C, these nanotubes like structures were converted into new leaf like morphology fig. 3.6 (d). The maximum surface area ranging from 110 to 150 °C hydrothermal treatments was observed for nanostructures precursors synthesized at 130 °C. Titanate nanotubes precursor aggregates obtained at 110-150 °C hydrothermal treatment were converted into TiO_2 nanorods on calcination.

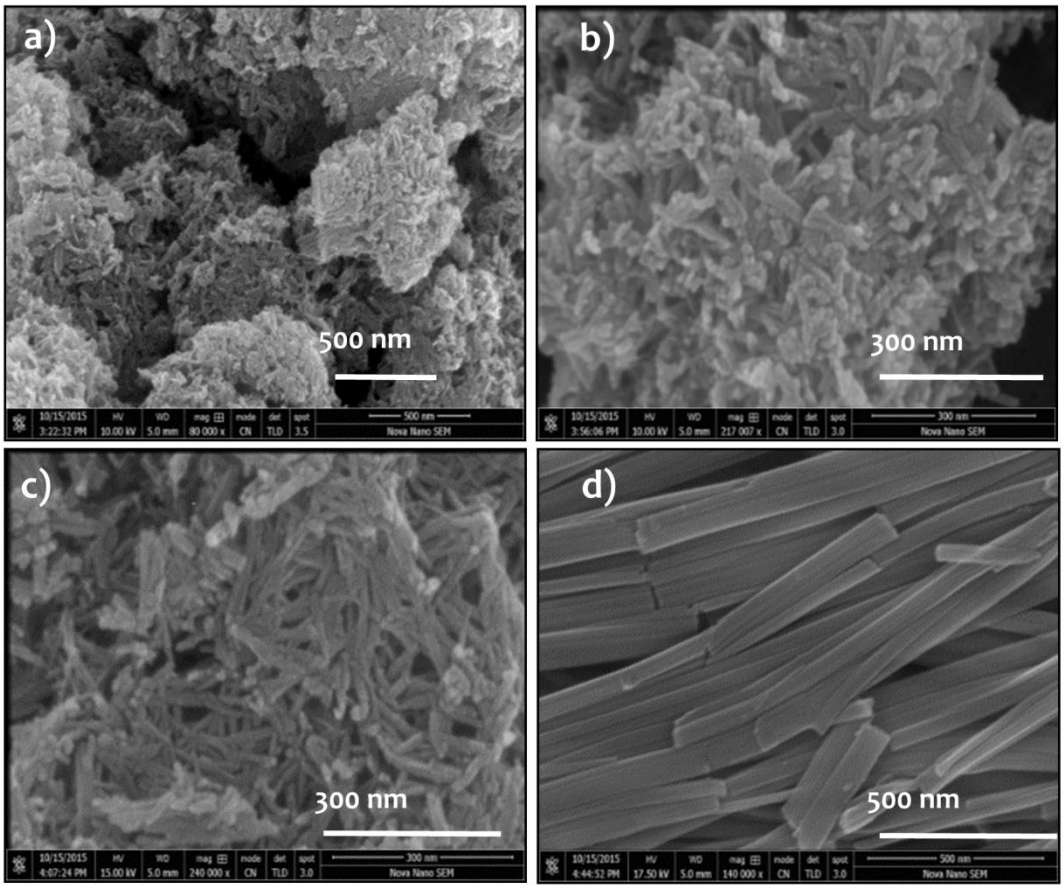

Figure 3.6: SEM images of a) $TNRs_{110}$ b) $TNRs_{130}$ c) $TNRs_{150}$ and d) $TNRs_{170}$.

Fig. 3.7 (a-c) shows the TiO_2 nanorods obtained after calcination of titanate nanostructure precursors (110-150 °C) at 400 °C. Well shaped TiO_2 nanorods are formed by calcining titanate nanotube like precursors at 400 °C formed at 130 and 150 °C hydrothermal temperature fig. 7(b-c). The fig. 3.7(d) represents a TEM image of Cu and Ni bimetallic hydroxides loaded over nanorods obtained by calcining nanotube precursors obtained at 130 °C hydrothermal and 400 °C calcination temperatures (TNR_{130}-400), which shows an average rod length of 35-40 nm and 4-6 nm diameter. Highly dispersed bimetallic hydroxide nanoparticles of 1-3 nm size can be clearly spotted over entire length of the nanorods. Very small and highly dispersed metal hydroxide nanoparticles are responsible for higher metal to support interface ratio which facilitates the greater number of charge carriers transferred to the metal cocatalysts for proton reduction. The presence of Cu and Ni is also confirmed by energy dispersive spectroscopy (EDS) (fig.3.7 bottom). Fig.3.7d inset represents a fast Fourier transform (FFT) image of TNR_{130}-400 further validating that nanorods prepared are purely comprised of anatase phase.

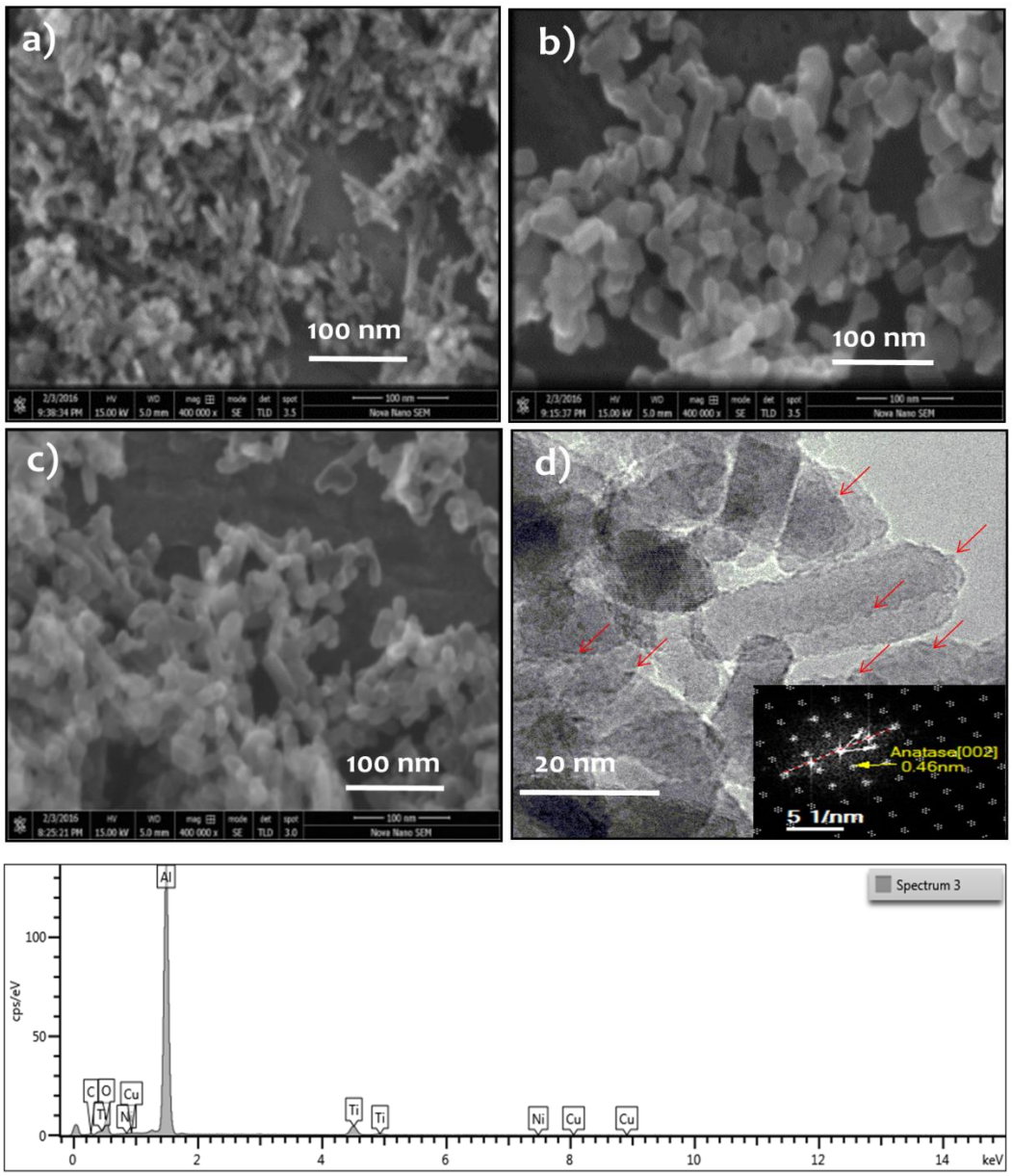

Figure 3.7: (top) SEM images of a) TNR_{110}-400 b) TNR_{130}-400 c) TNR_{150}-400 and d) TEM images of $M(OH)_2$-TNR_{130}-400 (bottom) Energy dispersive spectroscopic (EDS) analysis of $M(OH)_2$-TNR_{130}-400.

3.1.1.4 XPS studies

The XPS Cu2p region for different Cu oxidation states has been studied thoroughly and has shown in Fig. 3.8b [599-601]. Typical XPS $Cu2p_{3/2}$ values for Cu^0 and Cu^+ are observed between 932.3-932.5 eV making Cu^0 and Cu^+ difficult to distinguish while that of Cu^{2+} is 1 eV higher at about 933.6 eV. XPS Cu2p of Cu^{2+} has characteristic satellites at about 6 eV above $Cu2p_{3/2}$ peak due to the open $3d^9$ shell structure giving rise to multiple splitting [173, 602]. Fig. 3.8a shows the reference Ni2p spectra for different Ni oxidation states. The binding

energy position of Ni2p peaks at 855.6 eV and 873.2 eV and the presence of additional strong non-symmetrical features on the higher binding energy side of both Ni2p peaks indicate that Ni is present as Ni^{2+}. Ni^{2+} is a paramagnetic ion which shows additional ‘‘shake-up’’ satellite features at ~ 6 eV above the main $Ni2p_{3/2}$ peaks.

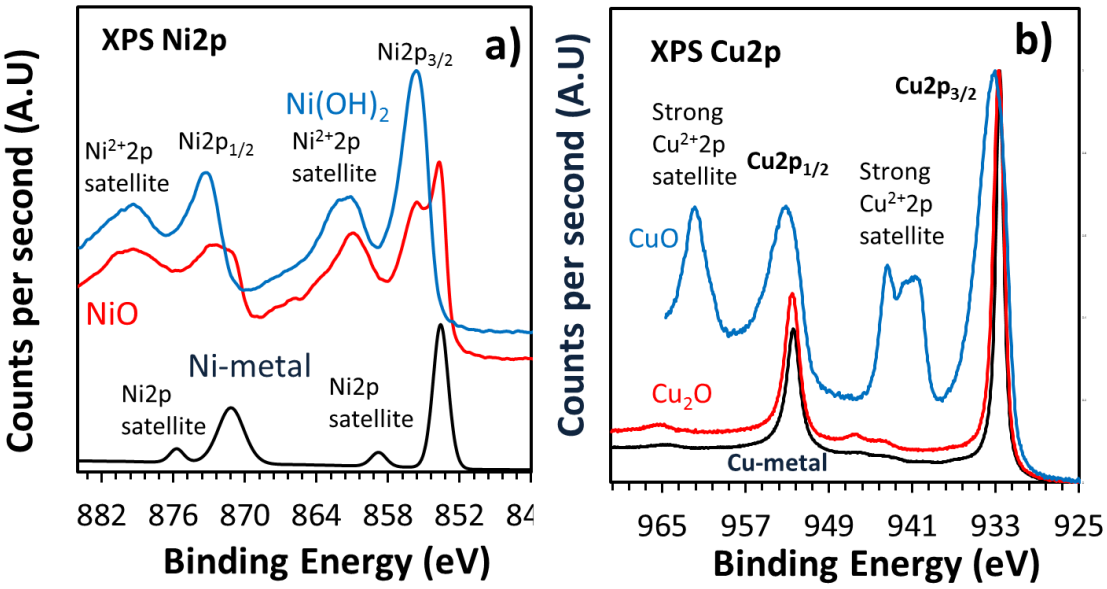

Figure 3.8: Reference Cu2p and Ni2p XPS spectra.

Fig. 3.9 presents Cu2p, Ni2p, Ti2p, C1s and O1s XPS spectra of fresh $0.8Cu(OH)_2$-$0.2Ni(OH)_2$/P25 photocatalyst and Cu2p, Ni2p spectra of all fresh photocatalysts. Nitrogen was the only other element detected with overall atomic % less than 0.5%. It can be noted that copper is detected in its reduced state (Cu^0/Cu^{1+}) while nickel is detected as $Ni(OH)_2$ in 0.98 and 0.19 at. %, respectively (Table 3.2). $Ni2p_{3/2}$ and $Ni2p_{1/2}$ peaks are observed at 855.6 eV and 873.2 eV, respectively. The binding energy position, presence of multiple splitting and additional ‘‘shake-up’’ satellite features at ~ 6 eV above the Ni2p peaks indicate that Ni is present as $Ni(OH)_2$. Fig. 3.10 presents Cu2p and Ni2p XPS spectra of $1.0Cu(OH)_2/TNR_{130}$-400 and $1.0Ni(OH)_2/TNR_{130}$-400 photocatalysts. A surprise detection of Cu in reduced state in all cases in present study is due to Cu^{2+} reduction in sub-nanometeric $Cu(OH)_2$ precipitates by the transfer of electrons from the TiO_2 conduction band under high intensity X-rays. Photocatalyst preparation conditions and strong absorption of Cu (II) d-d (700-800 nm) observed in the case of UV-VIS studies is a solid evidence of copper presence as Cu^{2+} in fresh samples [603]. The absence of multiple split of Ni2p peaks indicates that Ni^{2+} is mainly present in the form of its hydroxide. This is due to the fact that Ni^{2+} in $Ni(OH)_2$ cannot be

reduced during XPS measurements as its redox potential is more negative than the redox potential of conduction band electrons (discussed in later section in detail).

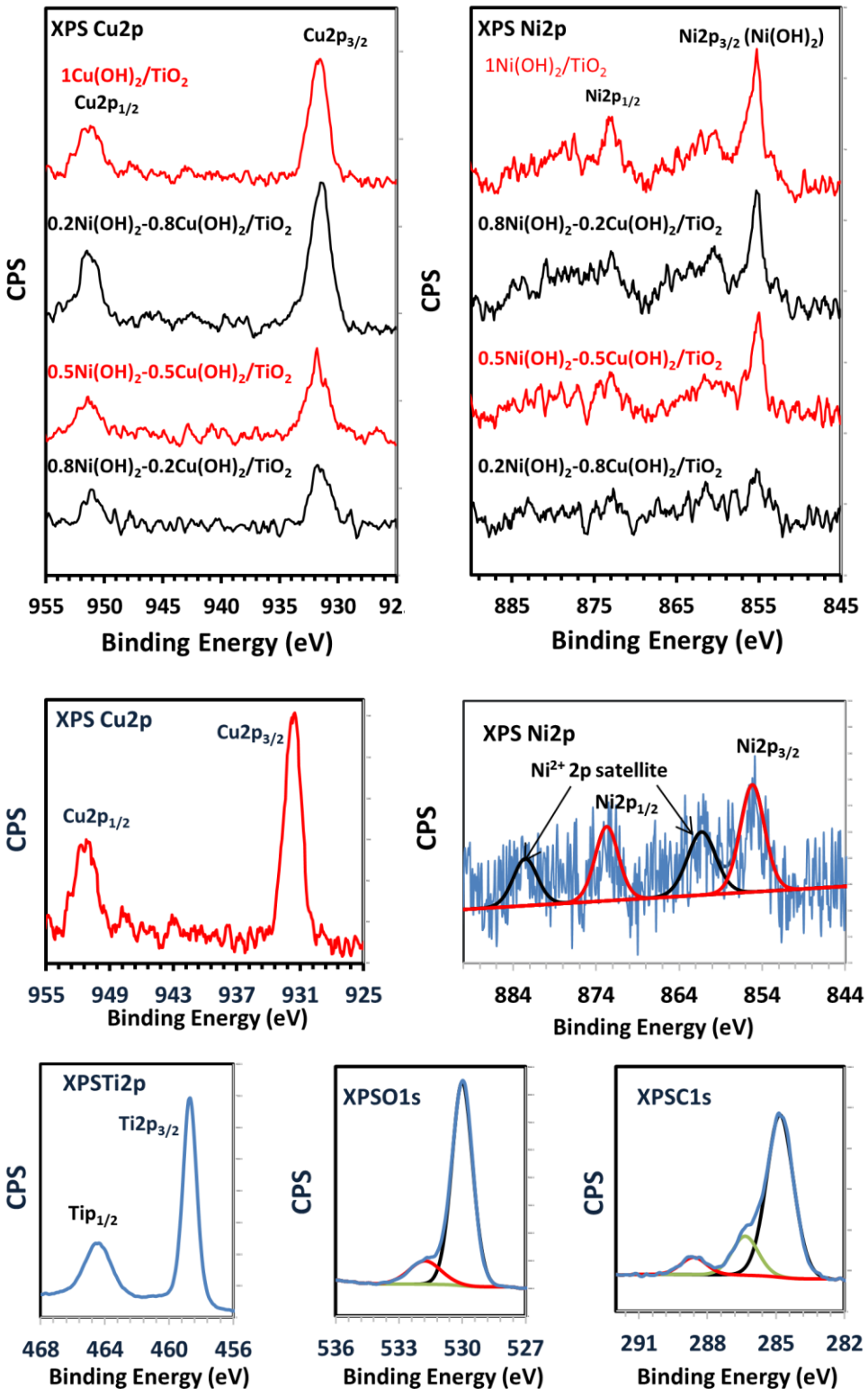

Figure 3.9: XPS results of fresh bimetallic $Cu(OH)_2$-$Ni(OH)_2$/P25 photocatalysts.

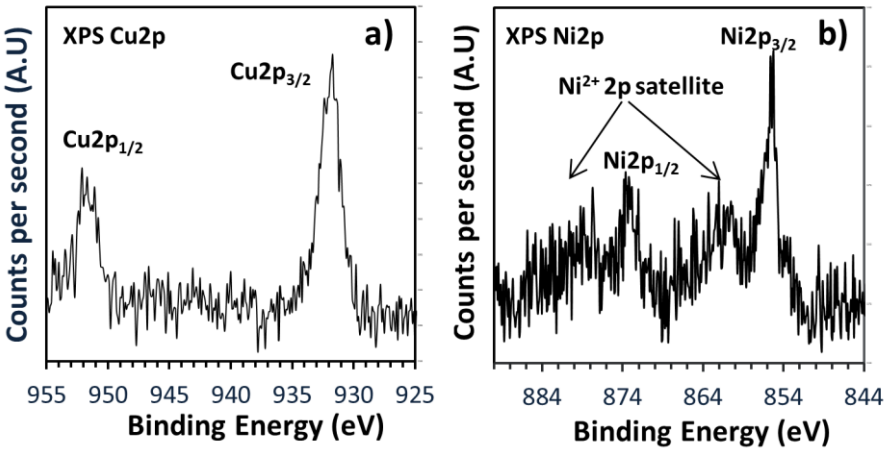

Figure 3.10: XPS analysis of 1.0Cu(OH)$_2$/TNR$_{130}$-400 and 1.0Ni(OH)$_2$/TNR$_{130}$-400.

Table 3.2: XPS analysis of fresh bimetallic 0.8Cu(OH)$_2$-0.2Ni(OH)$_2$/P25 photocatalyst.

Chemical Comp.	Core Level	Peak Position	FWHM (eV)	at.% Conc.
TiO_2	Ti2p$_{3/2}$	458.7	1.0	33.8
	Ti2p$_{1/2}$	464.4	1.9	
Metal oxide	O1s	530	1.1	46.4
Metal hydroxide		532.1	2.1	
Carbon (adv.)	C1s	284.8	1.4	19.6
C-O-C (adv.)		286.4	1.3	
C-O=C (Adv.)		288.6	1.3	
Cu/Cu_2O	Cu2p$_{3/2}$	932.4	1.7	0.39
	Cu2p$_{1/2}$	952.2	2.1	
Ni(OH)$_2$	Ni2p$_{3/2}$	855.6	2.1	0.10
	Ni2p$_{1/2}$	873.2	2.5	

3.1.2 Photoreactions

3.1.2.1 H_2 production

Photocatalytic H_2 production was evaluated using either ethanol or glycerol as sacrificial agent. Degussa P25 and TNR$_{130}$-400 showed negligible activity because of rapid conduction band electrons and valence band holes recombination rate of TiO_2 and due to the absence of atomic hydrogen recombination center for hydrogen evolution [111, 604]. Fig. 3.11a-b shows the effect of precipitation solution concentration (during catalyst preparation) on hydrogen production rate using 0.5Cu(OH)$_2$-0.5Ni(OH)$_2$/P25 and 0.8Cu(OH)$_2$-0.2Ni(OH)$_2$/TNR$_{130}$-400 photocatalysts respectively. The decrease in hydrogen production

rate with an increase or decrease in NaOH concentration around optimum is probably due to better dispersion or agglomeration of metal hydroxides particles on TiO_2 support surface, respectively. The effect of metal loading concentration was studied by increasing the overall loading amount from 0.5-3 wt. % (fig. 3.11c-d). Optimum hydrogen production rate was obtained for nominal loading amount of 1 wt. %. A slight decrease in activity at 1.5 wt. % metal loading was observed after that a sharp decrease in activity was observed from 2-3% loadings. The decrease in photocatalytic activity with increasing metal loading has been observed by many other workers for which no clear explanation is yet known [605-609]. Upon increasing of metal particle coverage, a larger fraction of the semiconductor surface may become unavailable for light adsorption. It can also result in increasing surface defects at metal-semiconductor inter-face leading to an increase in electron-hole recombination centers. For further study, the overall nominal metal loading was kept at 1 wt. % and 0.5 M NaOH solution was used as the precipitating agent.

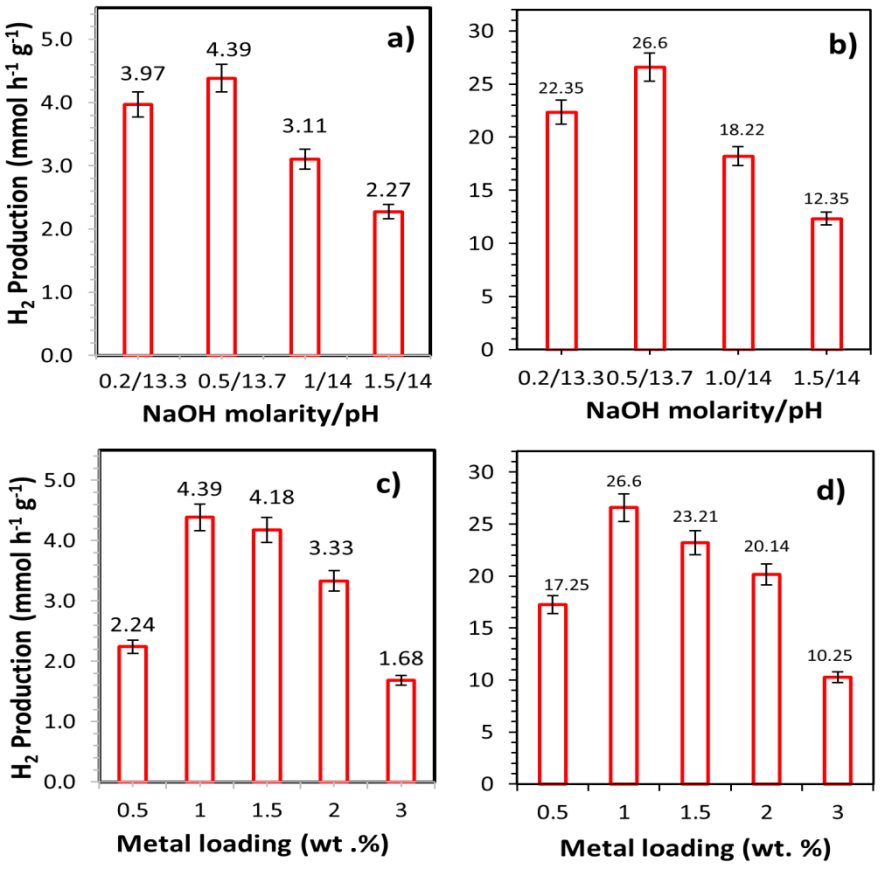

Figure 3.11: (a-b) Effect of NaOH concentration as precipitation solution for H_2 production and (b-c) Effect of metal loading amount on H_2 production in 20 vol. % ethanol-water mixtures over $0.5Cu(OH)_2$-$0.5Ni(OH)_2$/P25 and $0.8Cu(OH)_2$-$0.2Ni(OH)_2$/TNR_{130}-400 photocatalysts respectively.

Comparison of hydrogen production in 20 vol. % ethanol-water mixtures on various samples is shown in fig. 3.12 & 3.13. Hydrogen production experiments in different ethanol to water volume ratios on 0.8$Cu(OH)_2$-0.2$Ni(OH)_2$/P25 catalyst were also performed. An increase in rates with an increase in ethanol proportion as seen in fig. 3.14 was noticed. Further investigations were performed in 20 vol. % ethanol-water mixture to afford reliable measurement due to the amount of hydrogen produced with our experimental set up while keeping the ethanol concentration as minimum as possible. 1.0$Ni(OH)_2$/P25 and 1.0$Ni(OH)_2$/TNR_{130}-400 were the least active catalysts with hydrogen production rate two times less when compared to 1.0$Cu(OH)_2$/P25 and 1.0$Cu(OH)_2$/TNR_{130}-400. Hydrogen production rates increase with increase in Cu wt. % ratio in bimetallic catalysts. 0.8$Cu(OH)_2$-0.2$Ni(OH)_2$/P25 and 0.8$Cu(OH)_2$-0.2$Ni(OH)_2$/TNR_{130}-400 were found to be the most active photocatalysts. However, 0.8$Cu(OH)_2$-0.2$Ni(OH)_2$/P25 catalyst losses its activity considerably if calcined at 300 ^oC. Since the BET surface area of TiO_2 P25 did not change upon calcination at 300 ^oC, the deactivation could be linked to the formation of particles of oxides of Cu and Ni that are more difficult to reduce and therefor do not provide the needed Schottky barrier for electron transfer to occur. It was important to note that the hydrogen production rate over 0.8$Cu(OH)_2$–0.2$Ni(OH)_2$/P25 (10.25 mmol $h^{-1}g^{-1}$) was ~2.5 times less than 0.8$Cu(OH)_2$–0.2$Ni(OH)_2$/TNR_{130}-400 (26.6 mmol $h^{-1}g^{-1}$) photocatalyst from 20 vol. % ethanol-water mixtures. The enhanced activity of TNR_{130}-400 as compared to TiO_2 nanoparticles can be ascribed to their outstanding charge transport and long carrier lifetime properties due to following characteristics i) effective vectorial charge transfer due to nanorod structure ii) the charge carriers can not only easily move along the longitudinal direction of the nanostructure, they also have to cover short distance to emerge at the surface transversely iii) lower number of surface defects, thus small number of recombination centers [610].

In comparison with ethanol-water mixture, glycerol-water mixture showed higher rate of hydrogen production (fig. 3.15 & 3.16). In general, alcohols with lower oxidation potential, larger number of α-H atoms and hydroxyl groups deliver higher hydrogen production rates [611]. The oxidation potential, number of α-H atoms and hydroxyl groups are 0.004V, 5 and 3 for glycerol while it is 0.084 V, 2 and 1 for ethanol, respectively [612]. In alcohol-water mixture, the photoreaction is initiated by the reaction of an alcohol with hole in the TiO_2 valence band to form α-hydroxyl radicals. The formation of alpha hydroxyl radicals have been identified previously on TiO_2 using EPR and has been proposed by many others [170, 613-615]. Lower hydrogen production rate was observed for glycerol concentrations greater than 20 vol. % (data not shown) due to an increase in reaction mixture viscosity.

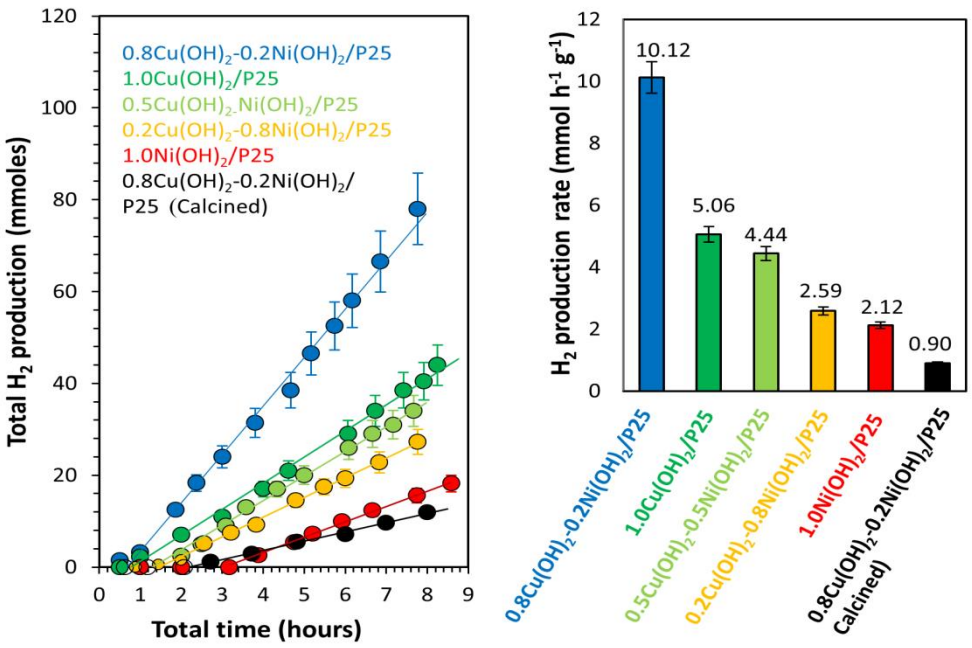

Figure 3.12: Comparison of the photocatalytic activities of $0.8Cu(OH)_2$-$0.2Ni(OH)_2$/P25, $1.0Cu(OH)_2$/P25, $0.5Cu(OH)_2$-$0.5Ni(OH)_2$/P25, $0.2Cu(OH)_2$-$0.8Ni(OH)_2$/P25, $1.0Ni(OH)_2$/P25 and $0.8Cu(OH)_2$-$0.2Ni(OH)_2$/P25 (calcined) samples for the photocatalytic H_2 production in 20 vol. % ethanol-water mixture.

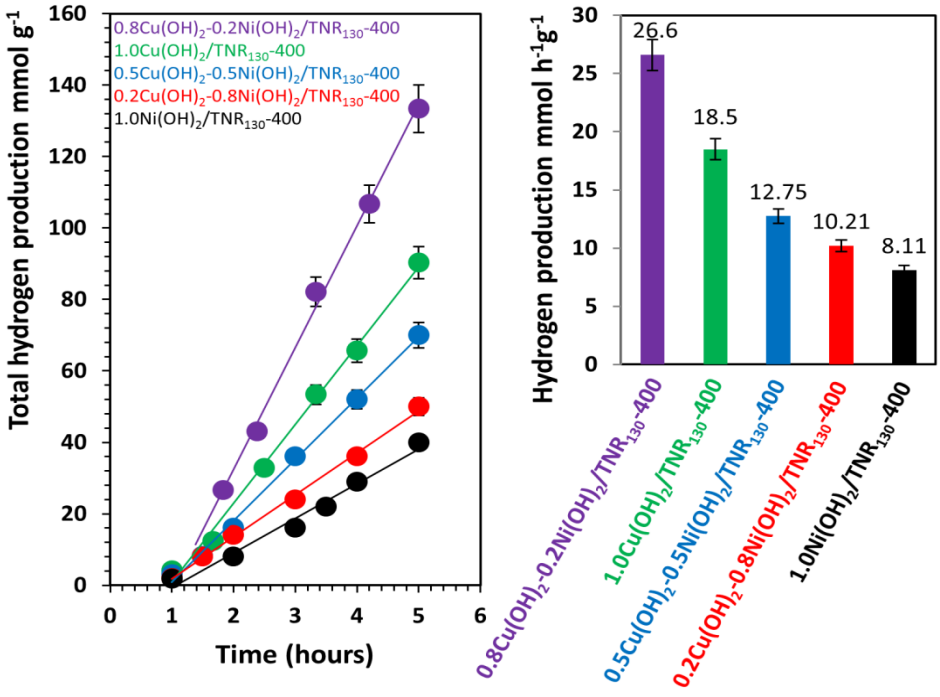

Figure 3.13: Comparison of the photocatalytic activities of $0.8Cu(OH)_2$–$0.2Ni(OH)_2$/TNR_{130}-400, $1.0Cu(OH)_2$/TNR_{130}-400, $0.5Cu(OH)_2$–$0.5Ni(OH)_2$/TNR_{130}-400, $0.2Cu(OH)_2$–$0.8Ni(OH)_2$ /TNR_{130}-400, $1.0Ni(OH)_2$/TNR_{130}-400 samples for the photocatalytic H_2 production in 20 vol.% ethanol-water mixture.

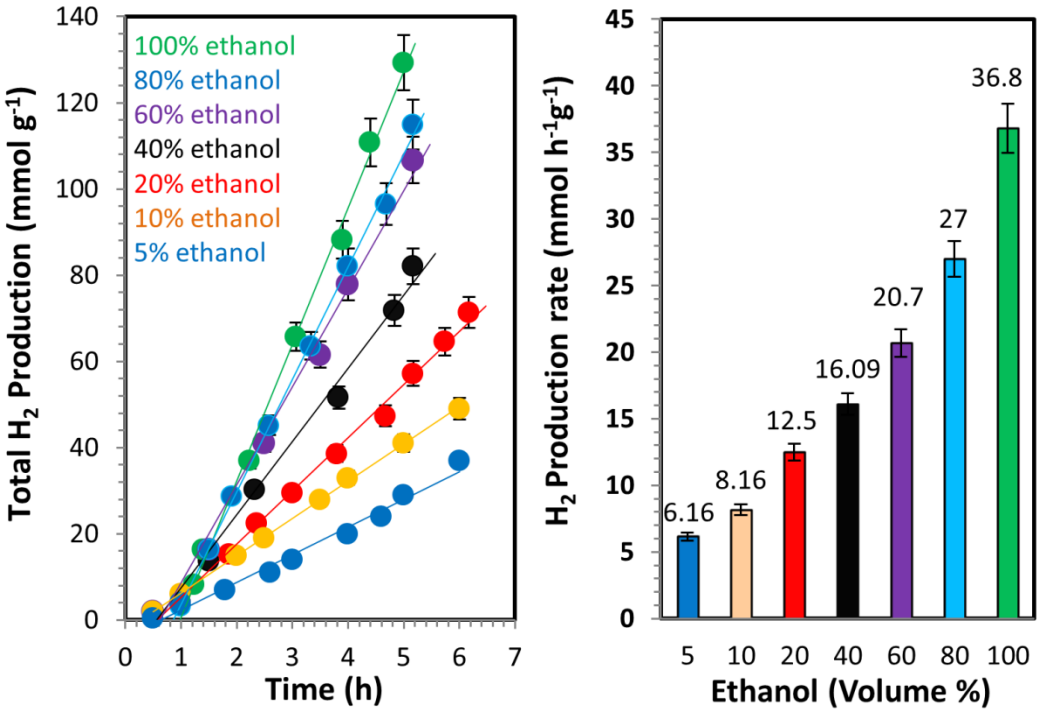

Figure 3.14: Comparison of hydrogen production on 0.8Cu(OH)$_2$-0.2Ni(OH)$_2$/P25 from aqueous solution with different ethanol volume percentages.

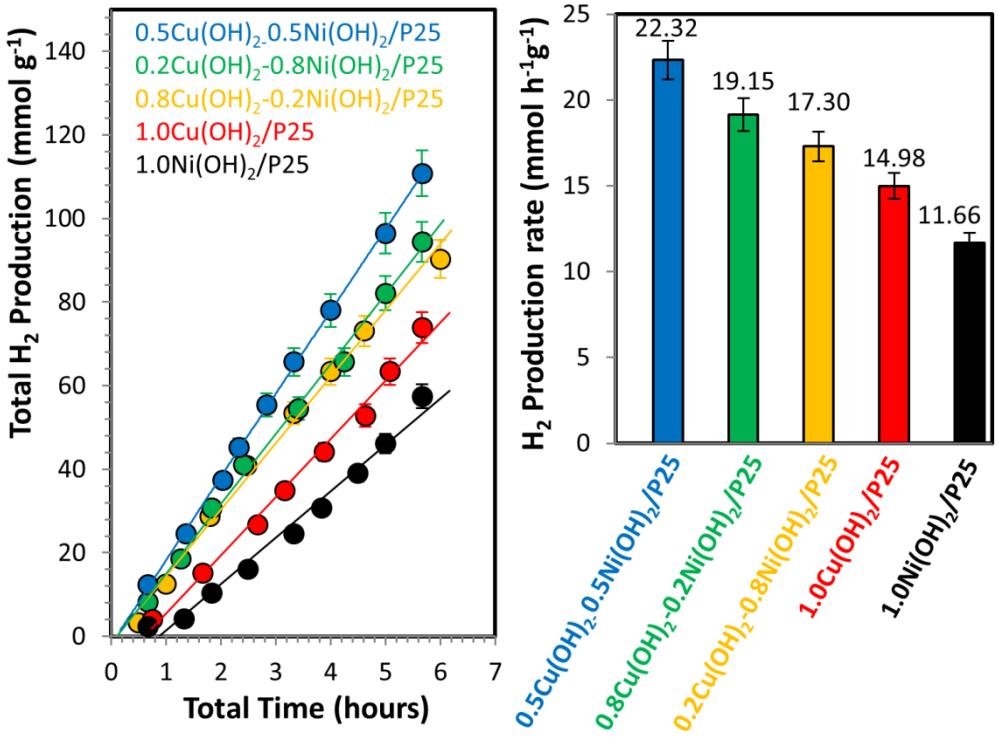

Figure 3.15: Comparison of the photocatalytic activities of 0.8Cu(OH)$_2$-0.2Ni(OH)$_2$/P25, 0.2Cu(OH)$_2$-0.8Ni(OH)$_2$/P25, 0.5Cu(OH)$_2$-0.5Ni(OH)$_2$/P25, 1.0Cu(OH)$_2$/P25 and 1.0NiOH)$_2$/ P25 samples for the photocatalytic H_2 production from 5 vol. % glycerol-water mixture.

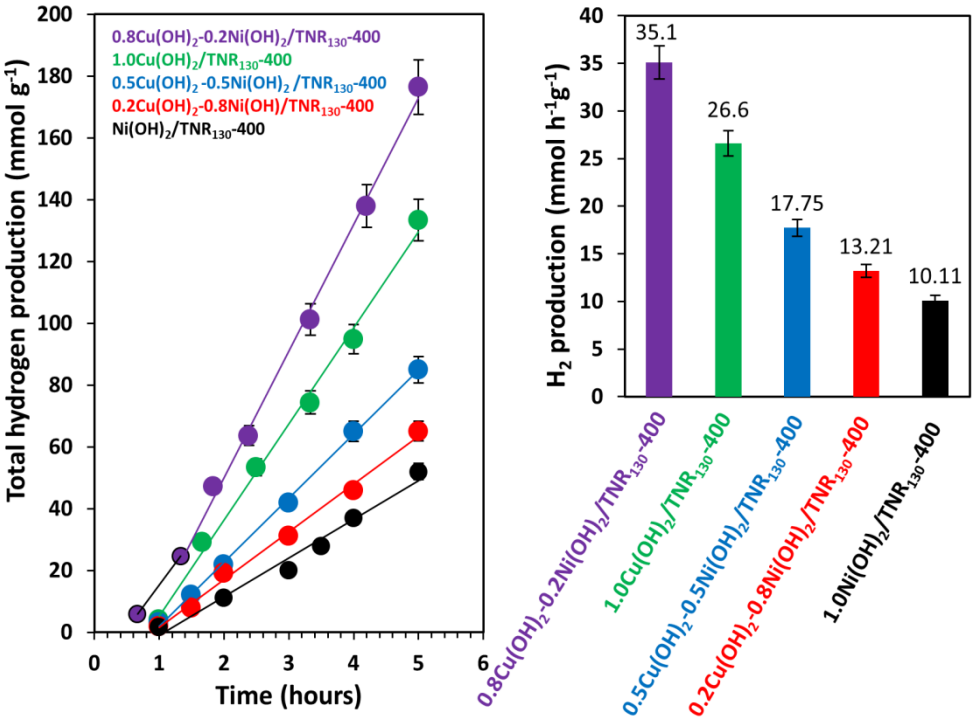

Figure 3.16: Comparison of the photocatalytic activities of $0.8Cu(OH)_2$–$0.2Ni(OH)_2$/TNR_{130}-400, $1.0Cu(OH)_2$./TNR_{130}-400, $0.5Cu(OH)_2$–$0.5Ni(OH)_2$/TNR_{130}-400, $0.2Cu(OH)_2$–$0.8Ni(OH)_2$/TNR_{130}-400, $1.0Ni(OH)_2$/TNR_{130}-400 samples for the photocatalytic H_2 production in 5 vol.% glycerol-water mixture.

Inspection of the hydrogen production with time indicates an induction period in both cases. Two particular points are however, worth mentioning. First, $Ni(OH)_2$ catalysts had the longer induction period in both cases, also others Ni containing catalysts showed longer induction periods that increased with concentration. Second, glycerol and water mixtures showed a much shorter induction period when compared to that of ethanol and water mixture. In a previous work [611] a relationship between hydrogen production rates and the exponential of redox potential has been shown, following Marcus theory [616].The rates for glycerol were about twice as fast when compared to those for ethanol reactions. The results reported in this study on Cu and Ni are thus not too different indicating that the main drive for the reaction (at least on TiO_2) is the difference of oxidation potential of the donor molecules and the valence band of the semiconductor. From Table 3.3, it can be noted that better hydrogen production rates are obtained with the bimetallic composition used in this study when compared to monometallic catalysts reported in literature.

.

Table 3.3: Comparison of hydrogen production rates over Cu and Ni containing photocatalysts reported in literature with the present study.

Metal Loading (Deposition method)	Sacrificial Reagents	Irradiation Source	H_2 (mmol $h^{-1}g^{-1}$)	Ref.
1 wt. % Cu-Ni/TNR_{130}-400 (Impregnation)	5% glycerol-water	100W (UV)	35.1	Present study
1 wt. % Cu-Ni/P25 (Impregnation)	5 % glycerol-water	100W lamp (UV)	22.32	Present study
1 wt. % Cu-Ni/P25 (Solvothermal0	37% methanol-water	300W (UV)	13.5	2015 [617]
29 mol% $Cu(OH)_2$/P25 (Precipitation)	0.09M ethylene glycol-water	3W (UV)	3.42	2011 [326]
1.25 wt.% CuO/TiO_2 (Complex precipitation)	80% ethanol-water	100W (UV)	20.3	2013 [378]
1.3 wt% CuO/P25 Impregnation	0.1M glycerol-water	3W (UV)	2.06	2011 [419]
0.5 mol% $Ni(OH)_2$/P25 (DP)	25% methanol-water	3W (UV)	3.056	2011 [618]
1 wt% Cu_2O/P25 (Impregnation)	20% ethanol-water	200W (UV)	3.48	2009 [343]
8 atom %Cu/P25 (Chemical reduction)	10% methanol – water	400W (UV)	20	2010 [381]
1.25 wt% Ni/P25, (Complex precipitation)	95% ethanol- water	100W (UV)	20.7	2015 [619]
1.2 wt% Cu/TiO_2 (anatase) (Incipient wetness)	30% methanol-water	208W (UV)	3.2	2004 [50]
1.5 wt% NiO/TiO_2 (anatase) (Single step sol gel)	10% methanol-water	300W (UV)	0.162	2005 [375]
0.5 mol% $Ni(OH)_2$/P25 (DP)	25% methanol-water	3W (UV)	3.056	2011 [618]
4wt% Au/P25, Photodeposition	5% ethanol-water	450W (UV-Vis)	6.12	2013 [543]
0.8 wt% Au/TiO_2 (anatase) (Photodeposition)	25% methanol-water	400W (UV)	1.54	2014 [620]
1 wt% Au/TiO_2(anatase) (Flam spray pyrolysis)	6% methanol-water	250W (UV-Vis)	8	2008 [92]
1 wt% Au/TiO_2 (anatase) (Photodeposition)	50% methanol-water	2.4W (UV)	8.4	2012 [621]
0.5Au-0.5Pt/TiO_2 (anatase) (Impregnation)	50% ethanol-water	125W (UV	8	2013 [622]
1 wt% Pd/TiO_2 (anatase + rutile nanofibres)	50% ethanol-water	8W UV-B	16.2	2015 [623]
1.5%Au/P25 (DP with Urea)	80% ethanol-water	100 W (UV)	32.2	2015 [584]
0.25Au-0.75Pd/P25	25% glycerol-water	100W (UV)	19.6	2014 [624]
1% Pt/P25 (DP with Urea)	10% glycerol water	200 W (UV)	27.1	2015 [625]
2% NiO/TiO_2 (anatase + rutile) (Impregnation)	16% glycerol-water	500W (UV)	1.23	2016 [342]

The activity and stability of both 0.8$Cu(OH)_2$-0.2$Ni(OH)_2$/P25 and 0.8$Cu(OH)_2$-0.2$Ni(OH)_2$/TNR_{130}-400 catalysts were investigated in 20 vol. % ethanol-water mixture. As can be seen from Fig. 3.17a, stable photocatalytic hydrogen production was observed over

$0.8Cu(OH)_2$-$0.2Ni(OH)_2$/P25 for the duration of the experiments (16 h). The slight decrease in rate with time (<15% for forth run) was due to the deposition of photocatalysts particles (clearly seen with naked eye) on reactor walls with time, thus effecting the incoming radiations. When recyclability tests were performed over $0.8Cu(OH)_2$-$0.2Ni(OH)_2$/TNR_{130}-400 with similar bimetallic loading, no decrease in hydrogen production rates was observed over same length of time due to less deposition of nanorods with reactor walls Fig. 3.17b.

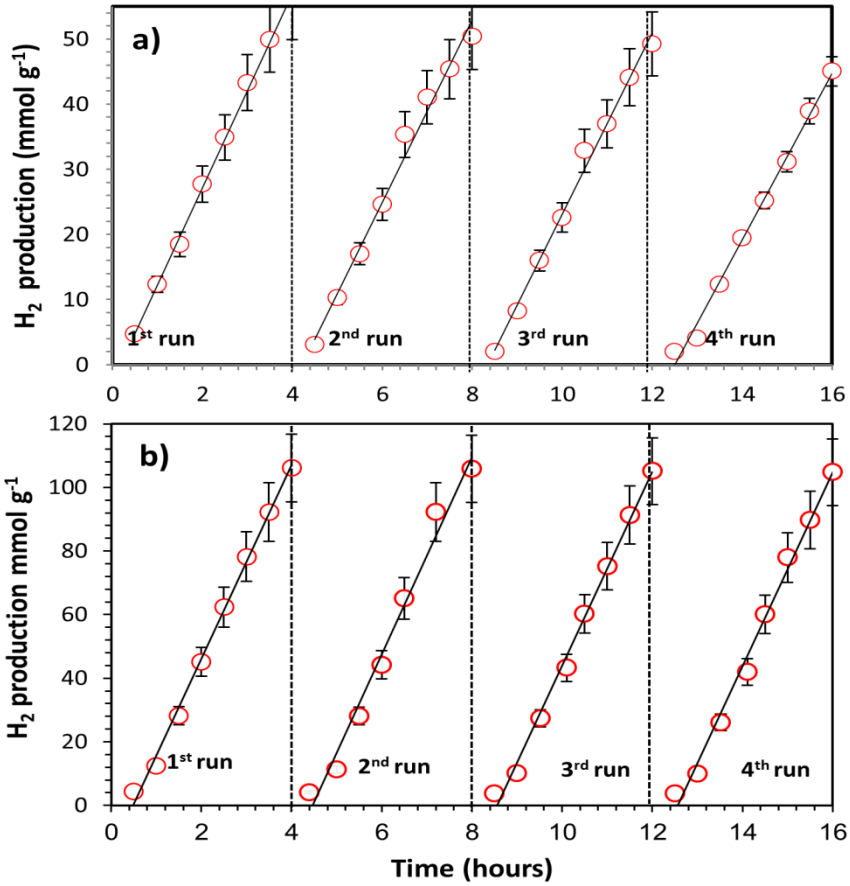

Figure 3.17: Recyclability of hydrogen production on $0.8Cu(OH)_2$-$0.2Ni(OH)_2$/P25 and $0.8Cu(OH)_2$–$0.2Ni(OH)_2$/TNR_{130}-400 catalysts using 20 vol. % ethanol-water mixture.

Photoreaction tests were performed over $0.8Cu(OH)_2$–$0.2Ni(OH)_2$/TNR_x-T to investigate the effect of hydrothermal treatment and calcination temperature (where x= 110 °C, 130 °C, 150 °C, and 170 °C and T= 400 °C, 600 °C and 800 °C). As it was shown in fig. 3.18a, the maximum hydrogen production rate is observed on $0.8Cu(OH)_2$–$0.2Ni(OH)_2$/TNR_{130}-400 due to high surface area and high crystallinity obtained under these conditions. Albeit TNRs fabricated at 110 °C have slightly lower surface area but lower hydrogen production rate was observed due to less crystallinity as well as distorted (amorphous) TNRs symmetry as observed in XRD and TEM analysis. The effect of calcination temperature over

$0.8Cu(OH)_2–0.2Ni(OH)_2/TNR_{130}$ for hydrogen production was also studied and shown in fig. 3.18b. High rate of hydrogen production achieved at 400 °C calcination temperature might be due to the optimization between crystallinity and surface area. No matter how much crystallinity is increased on increasing the calcination temperature beyond 400 °C, less amount of hydrogen production was observed due to increase of particle size which decreases the surface area.

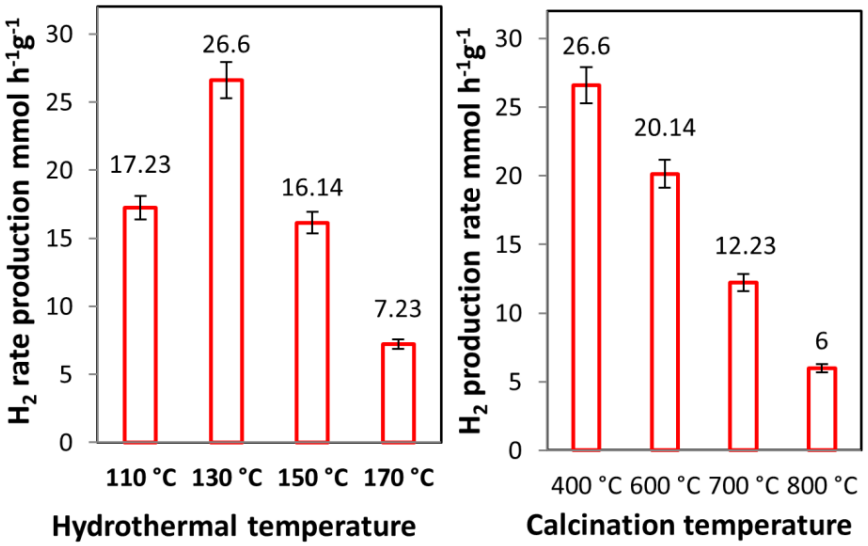

Figure 3.18: Effect of hydrothermal treatment and calcination temperature on $0.8Cu(OH)_2–0.2Ni(OH)_2/TNR$.

Fig. 3.19 shows digital photographs of the mono and bimetallic hydroxide supported over TiO_2 (P25) photocatalysts as-prepared and under UV light. In each case 20 mg of photocatalyst was suspended in 20 vol. % ethanol-water mixture with total volume of 25 ml. For the as-prepared photocatalysts, the light blue-green color increased with an increase in $Cu(OH)_2$ loading due to the presence of octahedrally coordinated Cu^{2+} ions [626]. The grey color of calcined $0.8Cu(OH)_2$-$0.2Ni(OH)_2/P25$ catalyst indicates the formation of metal oxides [606]. Under photoreaction conditions, colour change increases gradually with an increase in amount of $Cu(OH)_2$ while no change is observed in $Ni(OH)_2$ containing catalysts. The later observation might be due to the fact that Ni^{2+} in $Ni(OH)_2$ cannot be reduced under given conditions. Upon exposure to air the change in $Cu(OH)_2/P25$ colour reverted back to the original colour most likely due to re-oxidation of Cu^0.

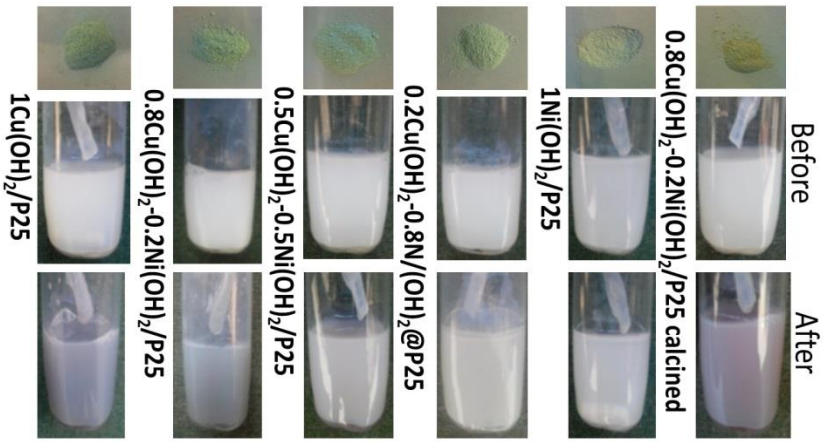

Figure 3.19: Digital photographs of as prepared and slurry phase catalysts before and during UV irradiation (3h).

3.1.3 Electron/hole transfer

3.1.3.1 Steady-state and time-resolved PL studies

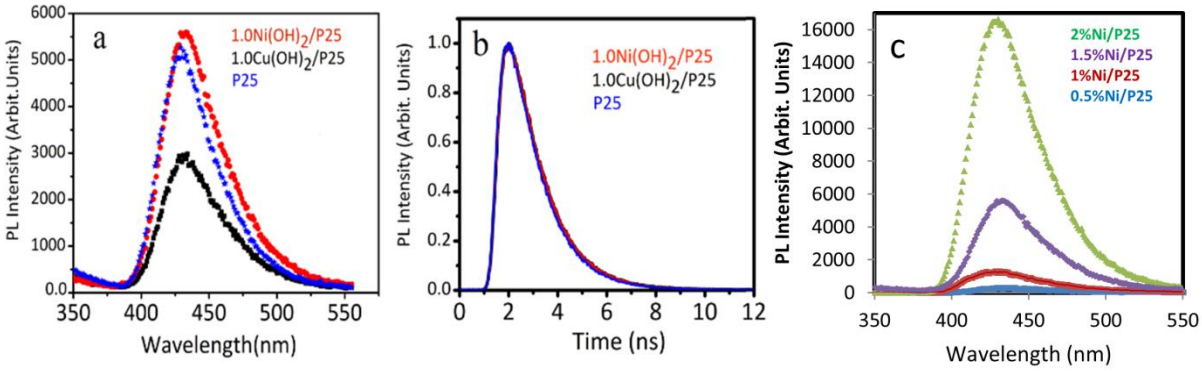

Figure 3.20: (a) Steady-state PL (b) time-resolved PL spectra following excitation at 305 nm (c) Steady-state PL as function of Ni loading in $Ni(OH)_2$/P25.

In order to get insight regarding the electron transfer dynamics, steady-state and time-resolved PL of the P25, 1.0$Cu(OH)_2$/P25 and 1.0$Ni(OH)_2$/P25 samples were conducted and results are presented in Fig. 3.20a & b. Fig. 3.20a demonstrates that 1.0$Cu(OH)_2$/P25 exhibits PL ~2 times lower in intensity as compared to P25. This is a clear indication of photo-excited electron transfer from the conduction band of the P25 to the $Cu(OH)_2$. On the contrary, P25 and 1.0NiOH)$_2$/P25 exhibit similar intensities. The presence of Ni may also passivates the surface thus resulting in slight increase in the PL intensity. To confirm this, PL measurements as function of $Ni(OH)_2$ loading were performed (fig. 3.20c). PL intensity was observed to increase with an increase in loading. In order to get understanding regarding the electron

transfer rate time-resolved PL were conducted. A decrease in PL life-times of 1.0$Cu(OH)_2$/P25 was anticipated as a result of electron transfer from the photo-excited P25 to $Cu(OH)_2$ as compared to P25. But rather the same PL kinetics behaviour was observed for all three samples. This strongly suggests that the electron transfer occurs much faster than the instruments response function ~500 ps of our time-correlated single photon set-up. The measured PL kinetics was best fitted by the built-in single exponential model ($\tau = Ae^{-kt}$, where τ, A, k and t are time constant, amplitude in counts, first order rate constant and time, respectively) suggesting a time constant of ~1.24 ns ± 0.006 ns, indicating the PL is originating through the same state for all three samples

3.1.3.2 Rhodamine B dye degradation studies

Table 3.4 presents Rhodamine B dye degradation over P25, 1.0$Ni(OH)_2$/P25, 1.0$Cu(OH)_2$/P25 and 0.8$Cu(OH)_2$-0.2$Ni(OH)_2$/P25, catalyst in the absence or presence of either a hole (Na_2EDTA) or an electron scavenger (benzoquinone) [627]. The objective here is to further probe into the electron/hole transfer process in the presence of Cu and Ni hydroxides. The absorption spectra were collected in 400-600 nm range during the monitoring process. To test the activity, a fixed time was taken for the dye degradation (the time needed to decompose 80% of the dye). It was noted that the time required to degrade the dye is longer in the case of metal loaded catalysts as compared to P25 alone in all cases. This indicates that doping TiO_2 with these elements decreases its activity, in sharp contrast with hydrogen production. More specifically, the dye degradation time is longer over all Cu supported catalysts as compared to 1.0$Ni(OH)_2$/P25 (comparable to that of TiO_2 alone). It is to be noted that this is also opposite to hydrogen production results. The reason is most likely competition of CB electrons. In other words, the suitable reduction potential of Cu in $Cu(OH)_2$/P25 as a result of which there is competition between ($Cu^{2+} + 2e^-(CB) \rightarrow Cu^0$) and ($O_2 + e^-(CB) \rightarrow O_2^{-\cdot}$) reaction. However, in the case of $Ni(OH)_2$/P25, the conduction band electrons are unable to reduce Ni in $Ni(OH)_2$ which are therefore exclusively used to form superoxide radicals that in turn oxidize the dye. To probe further into this, we have investigated the effect of hole and electron scavengers on the dye degradation time. In the presence of Na_2EDTA, a hole scavenger, the rate of dye degradation over the all catalysts was close to that obtained without any scavenger. However, the degradation was much slower in the presence of benzoquinone as a superoxide radical scavenger (Table 3.4). These results also suggest that role of ^oOH radicals or h^+ is negligible in this degradation process while electrons/superoxide radical are the main active species.

Table 3.4: Results of Rhodamine B dye degradation over different photocatalysts. Degradation is taken as that needed to decompose 80% of the dye.

Photocatalyst	Hole scavenger	Superoxide scavenger	Degradation time (minutes)
P25	-	-	32
1.0$NiOH)_2$/P25	-	-	38
1.0$NiOH)_2$/P25	Na_2EDTA		38
1.0$NiOH)_2$/P25		Benzoquinone	70
1.0$Cu(OH)_2$/P25	-	-	110
1.0$Cu(OH)_2$/P25	Na_2EDTA	-	105
1.0$Cu(OH)_2$/P25	-	Benzoquinone	170
0.8$Cu(OH)_2$-0.2$Ni(OH)_2$/P25	-	-	90
0.8$Cu(OH)_2$-0.2$Ni(OH)_2$/P25	Na_2EDTA	-	90
0.8$Cu(OH)_2$-0.2$Ni(OH)_2$/P25	-	Benzoquinone	135

3.1.4 Hydrogen production mechanism

Both P25 and TNR_{130}-400 themselves exhibit negligible hydrogen production activity (0.104 & 0.087 mmol h^{-1} g^{-1}). However, activity is remarkably improved after 1 wt. % Cu loading to (ca. 14.19 & 17.5 mmol $h^{-1}g^{-1}$) for glycerol-water mixtures, respectively. The reduction potential of $Cu(OH)_2$/Cu is slightly lower than the conduction band potential of anatase and rutile TiO_2 ($Cu(OH)_2 + 2e^- = Cu + 2OH^-$, $E^o = -0.224$ V (Fig. 3.21). Under photoreaction conditions, electrons can directly transfer from the CB of TiO_2 to $Cu(OH)_2$ nanoclusters to reduce Cu^{2+} to Cu^0 as shown in Fig. 3.22 & 3.23. This direct conversion can be supported by four observations in this study. **i).** Instant colour change on exposing the catalysts slurry to UV radiations in the presence of a sacrificial regent. This change in colour gradually decreases with a decrease in Cu content (Fig. 3.19). **ii).** The presence of Cu in its reduced state in all XPS results due to the excitation of TiO_2 electrons by X-rays and their subsequent transfer to $Cu(OH)_2$ nanoclusters. **iii).** Two times lower PL intensity in the case of 1.0$Cu(OH)_2$/P25 as compared to P25 indicating photo-excited electron transfer from the CB of the P25 to the $Cu(OH)_2$. **iv).** About three times decrease in dye degradation rate on $Cu(OH)_2$ loaded P25 as compared to P25 alone due the competition between electron transfer from conduction band of TiO_2 to $Cu(OH)_2$ and dye molecule probably via superoxide radical ($O_2^{-\cdot}$) formation. This is further supported by an increase in dye degradation time in the presence of superoxide scavenger benzoquinone while no change in dye degradation time

was observed in the presence of a hole scavenger Na_2EDTA (Table 3.4) [627]. In the metallic state Cu acts as a co-catalyst for electron transfer to proton for hydrogen production [85].

The rate of hydrogen production observed with similar loading of Ni was far less as compared to that of Cu loading (Figs. 3.15 & 3.16). The reduction potential of Ni $(OH)_2$/Ni ($Ni(OH)_2 + 2e^- = Ni + 2OH^-$ $E^o = -0.76$ V) is more negative than the conduction band potential of TiO_2 (fig. 3.21). Thus, the electron transfer from CB band of TiO_2 to $Ni(OH)_2$ is thermodynamically unfavourable. While there is clear evidence from photoluminescence experiments and dye degradation experiments that $Ni(OH)_2$ level lies above the TiO_2 CB for the photocatalysts used in this study, stable H_2 production on monometallic $Ni(OH)_2$ loaded catalysts is observed during hydrogen production experiments. Further, $0.8Cu(OH)_2$-$0.2Ni(OH)_2$/P25 exhibit higher activity as compared to both $1.0Ni(OH)_2$/P25 and $1.0Cu(OH)_2$/P25. These observations reject the possibility of $Ni(OH)_2$ to remain inactive under photoreaction conditions. Typically in a photoreaction experiment involving ethanol or glycerol as sacrificial agent, the pH of the reaction mixture drops to ca. 4 within the first hour due to their oxidation to produce CO_2. There is a possibility of $Ni(OH)_2$ dissolution in the reaction mixture as a Ni^{2+} concentration of 0.1mole L^{-1} at pH = 6 is predicted in equilibrium with $Ni(OH)_2$ [628]. To confirm this, we performed photoreactions with increased amount of 1% $Ni(OH)_2$/P25 catalyst (100 mg) to allow the Ni^{2+} detection in the reaction mixture filtrate using dimethylglyoxime (DMG) as a complexing agent. The appearance of red colour after 3h clearly indicated the dissolution of Ni^{2+} in alcohol-water mixture. Based on these observations, stable hydrogen production and the appropriate redox potential of Ni^{2+}/Ni couple (-0.23 V), it is proposed that $Ni(OH)_2$ is first dissolved into the reaction mixture and Ni^{2+}(aq) thus formed is then photo-deposited on over P25 or TNRs as shown in Fig. 3.22 & 3.23. This is also supported by the observation that relatively longer induction time is needed to observe hydrogen production in the case of Ni containing catalysts (Fig. 3.12, 3.13, 3.15 and 3.16).

Considerable hydrogen production rates in the case of $1.0Cu(OH)_2$/P25 and $1.0Cu(OH)_2/TNR_{130}$-400 was due to its appropriate work function (5.1 eV). A very high rate of hydrogen production 22.32 mmol $h^{-1}g^{-1}$ on $0.8Cu(OH)_2$-$0.2Ni(OH)_2$/P25 and 35.1 mmol $h^{-1}g^{-1}$ on $0.8Cu(OH)_2$-$0.2Ni(OH)_2/TNR_{130}$-400 in 5 vol. % glycerol-water mixture observed as compared to other catalysts with similar overall wt. % metal loading can be ascribed to synergistic effect of Cu deposited directly from $Cu(OH)_2$ precipitates and re-adsorption of Ni^0 from the Ni^{2+} cations in the solution. These Ni^{2+} ions may selectively be photo-deposited over electron rich sites on P25 or TNRs surface which are away from Cu nanoclusters or on Cu

nanoclusters themselves forming Cu/Ni alloy (Fig. 3.22 & 3.23). It is also reported that proper composition of Cu/Ni alloy has the more suitable Schottky barrier height [617]. The reducibility of Ni is enhanced in Cu/Ni alloy due to a considerably less negative ΔG^o of Cu oxide formation (-129 kJ mol^{-1}) when compared to that of Ni oxide formation (-430 kJ mol^{-1}) [629, 630], which is favourable for water reduction [617]. The decrease of hydrogen production rate from $0.5Cu(OH)_2$-$0.5Ni(OH)_2$ to $0.2Cu(OH)_2$-$0.8Ni(OH)_2$ is due to the gradual decrease of Cu amount. A very little hydrogen production rate observed on $0.8Cu(OH)_2$-$0.2Ni(OH)_2$/P25 calcined at 300 ^oC in air might be due to conversion of $Cu(OH)_2$ and $Ni(OH)_2$ to their respective oxides (CuO and NiO, respectively) and their subsequent growth to larger particle size by sintering. CuO/Cu redox potential is above that of TiO_2 conduction band such that electrons cannot be transferred from TiO_2 to CuO (Fig. 3.21). This explanation is also in line with what has been reported previously where a decrease in H_2 production rate with an increase of CuO particle size was observed [606].

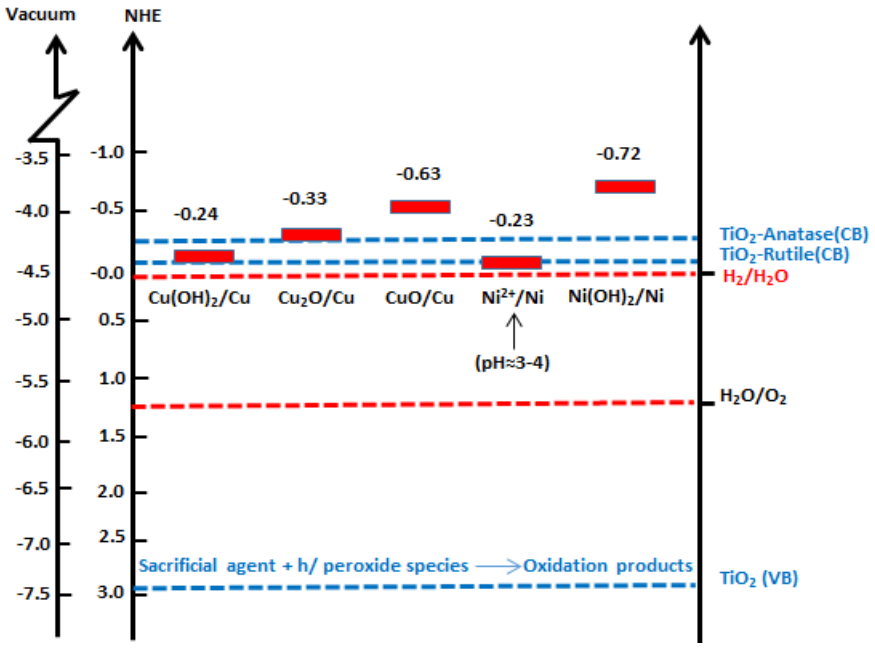

Figure 3.21: Schematic illustration for hydrogen production, charge transfer, separation and chemical conversions in $Ni(OH)_2$ and $Cu(OH)_2$ nano-clusters modified TiO_2 system [631].

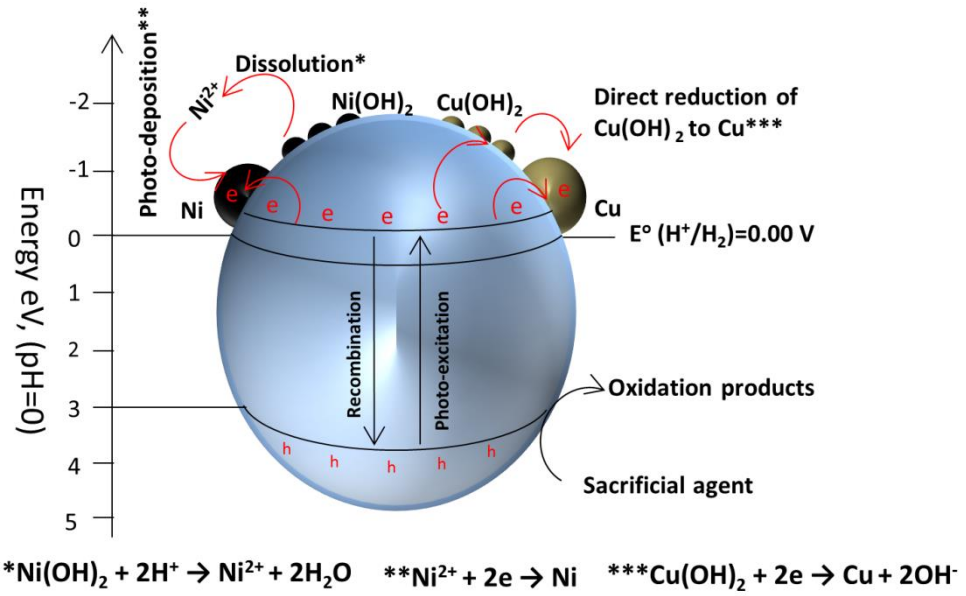

Figure 3.22: Schematic illustration for hydrogen production, charge transfer, separation and chemical conversions in $Ni(OH)_2$-$Cu(OH)_2$/P25 systems under photoreaction conditions [631].

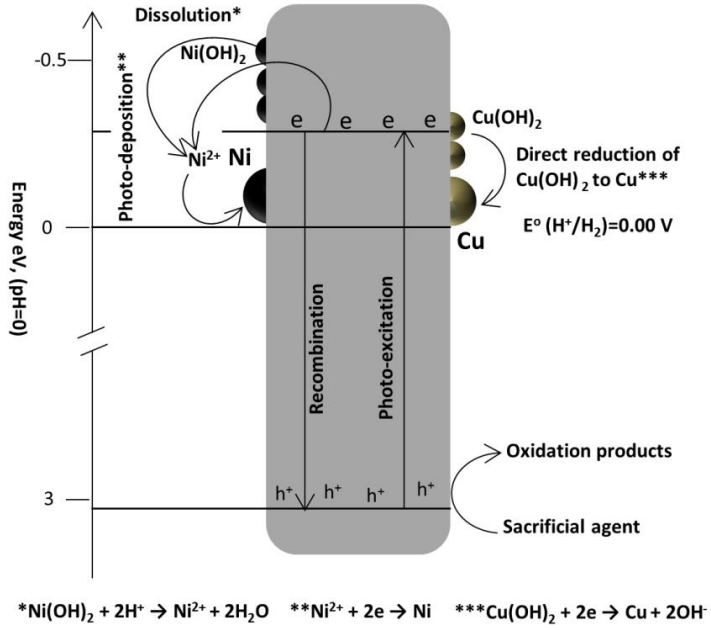

Figure 3.23: Schematic illustration for hydrogen production, charge transfer, separation and chemical conversions in $Ni(OH)_2$-$Cu(OH)_2$/TNR_{130}-400 systems under photoreaction conditions.

3.1.5 Conclusions

From above results and discussion it can be concluded that highly crystalline Titania nanorods with different phase compositions and surface areas can be fabricated by calcination

of hydrogen titanate ($H_2Ti_3O_7$) precursors obtained by treating P25 (TiO_2) hydrothermally in 10 M NaOH followed by HCl washing. It is found that nanotube like morphology prevailed up to 150 °C hydrothermal treatment. However, nanotube like morphology is dramatically transformed into nanoleaves above 150 °C. The nanotubes precursor prepared at 130 °C show maximum surface area of ca. 148 m^2/g that decreases with further increasing of the temperature. Treatment at higher temperatures than 130 °C starts to destroy the lamellar $Na_2Ti_3O_4$, an intermediate in the TiO_2 nanostructure formation process. Among the nanorods series prepared, nanorods prepared at 130 °C and calcined at 400 °C showed very high hydrogen production rates after depositing bimetallic hydroxides by co-deposition-precipitation (total metal loading ~ 1 wt.%). To compare these hydrogen production results with typical TiO_2 support P25 (80% Anatase + 20% rutile), a series of $Cu(OH)_2$-$Ni(OH)_2$/P25 photocatalysts were prepared by co-deposition-precipitation (total metal loading ~ 1 wt.%), characterized and their performance for H_2 production was evaluated. Both 0.8$Cu(OH)_2$-0.2$Ni(OH)_2$/P25 and 0.8$Ni(OH)_2$-0.2$Cu(OH)_2$/TNR_{130}-400 photocatalyst demonstrated very high hydrogen production rates (10 & 26.6 mmol $h^{-1}g^{-1}$) in 20 vol. % ethanol-water mixture and (22 & 35.1 mmol $h^{-1}g^{-1}$) from 5 vol.% glycerol-water mixtures, respectively. Detailed analyses based on reaction kinetics, photoluminescence, XPS and charge carrier scavenging suggest that both working catalysts are composed of Cu and Ni metals in their active phase. Cu^0 is produced directly by the transfer of electrons from the conduction band of TiO_2 to surface $Cu(OH)_2$ nano-clusters, whilst Ni^0 is formed indirectly through a process of gradual dissolution of $Ni(OH)_2$ to yield aqueous Ni^{2+} due to the acidic environment of the medium, followed by Ni^{2+} reduction by electron from the conduction band of the semiconductor. The high rates of H_2 production that matches those obtained with noble metals can be explained by the following rationale. An oxidized Ni atom in contact with a Cu atom may become reduced due to a considerably less negative ΔG^o of Cu oxide formation (-129 kJ mol^{-1}) when compared to that of Ni oxide formation (-430 kJ mol^{-1}) [629, 630]. This may increase hydrogen production due to the possibility of an increase in metallic character of Cu [632, 633]. The present work suggests that bimetallic Cu-Ni catalysts formed on TiO_2 nanorods are promising alternatives to noble metals for hydrogen production [607, 611].

3.1.6 Novel MOF-199 derived Cu-Cu_2O nanoparticles decorated TiO_2 photocatalysts

This section comprises of characterization results and thorough discussion of novel MOF-199 derived highly dispersed Cu-Cu_2O nanoparticles decorated TiO_2 photocatalysts for hydrogen

production and their comparison with Cu decorated TiO_2 prepared with conventional method by using aqueous metal salts. The aim of this study is to develop highly efficient and economical (noble metal free) photocatalysts for hydrogen production from water in the presence of other renewable (glycerol).

3.1.6.1 TGA analysis

MOF-199 has a large surface area of 1925 m^2g^{-1}, a total pore volume of 0.333 cm^3g^{-1} and a pore size of 9×9 A° [586]. The copper oxide building block units in MOF-199 are separated at relatively large distances by the organic linkers, thus calcination resulted in highly dispersed particles of Cu/Cu-oxide (fig. 3.24). The TGA curve of pure MOF-199 (fig. 3.24) indicates that all guest molecules like triethylamine (TEA) base (8%) and dimethylformamide (DMF) solvent (28.5%) trapped in the cages of MOF-199 are removed at about 250 °C. The third and predominant weight loss in the TGA curve (66.5%) at ~ 250-350 °C [431] is due to the thermal decomposition of the organic framework of MOF-199 itself. Beyond 350 °C there is no weight change indicating the completion of CuO nanostructures formation. Therefore, the calcination was always carried out beyond 350 °C in order to ensure the complete decomposition of MOF-199.

3.1.6.2 PXRD analysis

Fig. 3.24 bottom (a-e) shows powder x-ray diffraction PXRD patterns of synthesized materials. Fig. 3.24a and b show diffraction pattern of MOF-199 and TiO_2-MOF composite respectively where the latter clearly shows the diffraction peaks of anatase TiO_2 and MOF-199. There is slight shift in MOF-199 peaks in TiO_2-MOF composite due to interaction of TiO_2 with the MOF network. After calcining the MOF-TiO_2 composite at temperature 400 °C, Cu/Cu_2O are formed over anatase TiO_2 as confirmed by both DRS and XPS results. Diffraction patterns of the Cu species over TiO_2 were not observed in PXRD because the overall metal loading is too low (0.5-1.5%). It is clear from fig. 3.24e that pure CuO is formed by heating the MOF-199 at 400 °C in air without the formation of any residual carbon. The broad and relatively less well defined PXRD TiO_2 peaks in TiO_2 -MOF composite are due to its lower crystallinity and % presence in the composite. However, anatase TiO_2 patterns become prominent after calcining the TiO_2-MOF composite at 400 °C due to an increase in the crystallinity of TiO_2 at higher temperatures. TiO_2 peaks are even sharper in fig. 3.24d, which corresponds to the anatase TiO_2 synthesized by the same method without the MOF-199 particles. In addition, no significant variation in lattice parameters was observed for Cu-Cu_2O/TiO_2 catalysts, suggesting that the Cu species were deposited over the

surface of TiO_2 rather than being incorporated into the TiO_2 lattice. It is also interesting to note that the TiO_2 particle size and BET surface area were constant by calcining the MOF-TiO_2 composite from 350-500 °C (Table 3.7) due to the incorporation of MOF during hydrolysis of TiO_2 precursor. The TiO_2 particle size was calculated by powder XRD data using the Scherrer equation and line-widths of the anatase (101) reflection at $2\theta = 25.3°$.

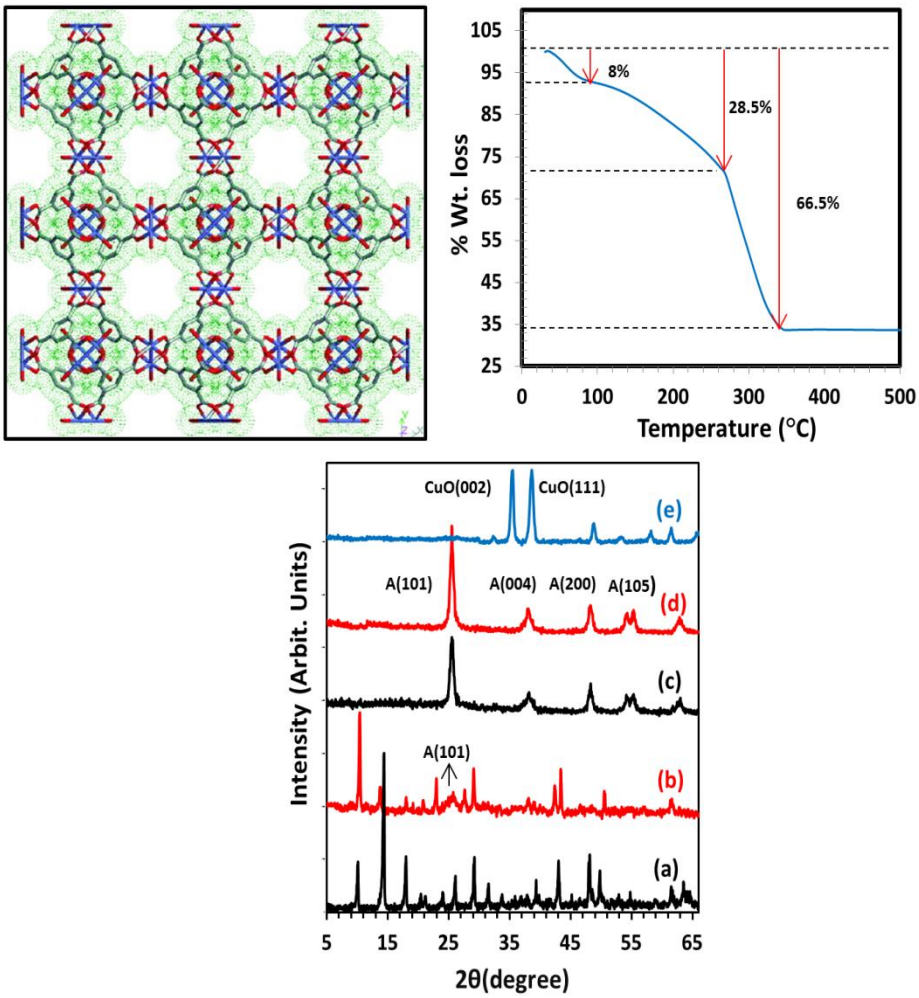

Figure 3.24: Top: (left) Framework of MOF-199 viewed down the [100] direction, showing nanochannels with a fourfold symmetry (right) TGA plot of MOF-199 at a temperature rate of 10 °C min^{-1}. Bottom: (a) PXRD patterns of MOF-199, (b) the TiO_2–MOF composite, (c) Cu–Cu_2O/TiO_2-400, (d) anatase SG-400 and (e) MOF-199-400.

3.1.6.3 UV-visible diffuse reflectance measurements

Fig. 3.25(a) shows UV-visible diffuse reflectance spectra for the different photocatalysts, whilst Fig. 3.25b compares anatase TiO_2 and TiO_2-MOF composite. All catalysts showed intense absorption below 400 nm, due to the anatase TiO_2 support (E_g = 3.15 eV). Deposition of Cu species caused the samples to absorb strongly in the visible region, though the visible absorption spectra differed considerably depending on the nominal Cu loading. The absorption edges of Cu containing photocatalysts were shifted towards the visible region due to overlap between the TiO_2 absorption and the absorption signals of the Cu_2O & Cu. The absorption spectra of fresh Cu-Cu_2O/TiO_2 photocatalysts show two broad absorption bands, one enhanced absorption band extending from 400-650 nm caused by fingerprint absorption of Cu_2O (E_g=2.1eV) species [597, 634, 635] and other relatively small band extends from 700 to 900 attributed to the surface plasmon resonance of Cu^0 [636]. Cu^{2+} ions also show the absorption at 700-900 nm however XPS results revealed the complete absence of Cu as Cu^{2+}. A small absorption shoulder at 450 nm in the case of TiO_2-MOF composite (fig. 3.25b) is partly due to the interfacial charge transfer (IFCT) from TiO_2 conduction band to Cu^{2+} in MOF-199 [637-639]. Pure anatase TiO_2 does not show any absorption above 400 nm.

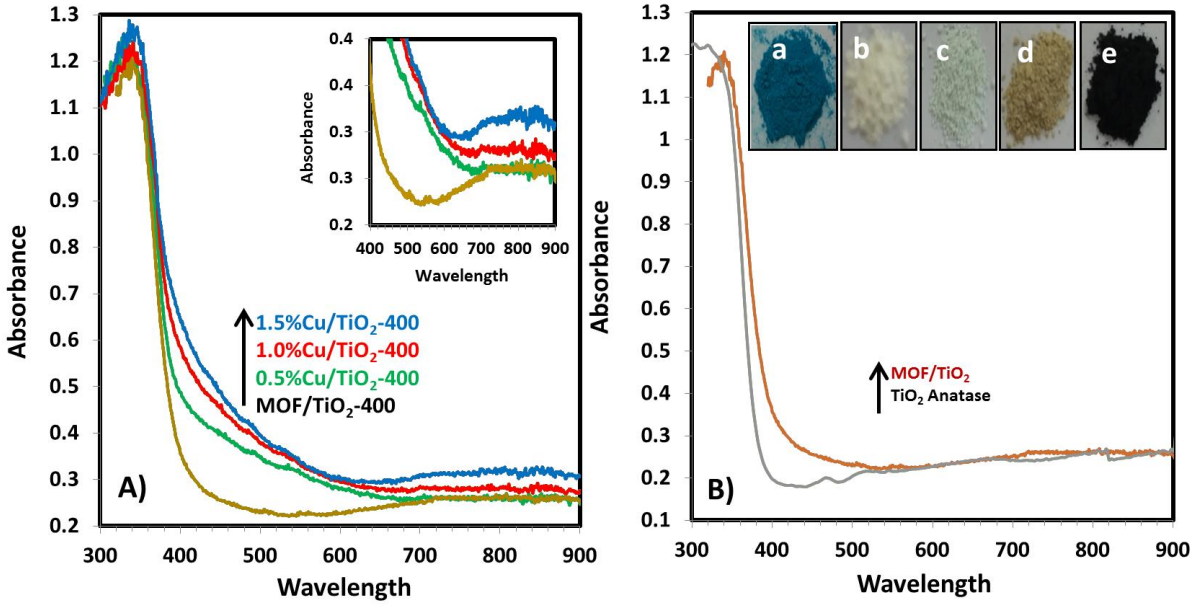

Figure 3.25: (A) UV-vis spectra of the TiO_2–MOF composite & 0.5–1.5% Cu-Cu_2O/TiO_2-400. (B) Comparison of the MOF–TiO_2 composite and anatase TiO_2; the insets are pictures of (a) MOF-199, (b) TiO_2 anatase, (c) the TiO_2–MOF-199 composite, (d) Cu–Cu_2O/TiO_2-400 °C , and (e) MOF-199-400 °C.

3.1.6.4 TEM analysis

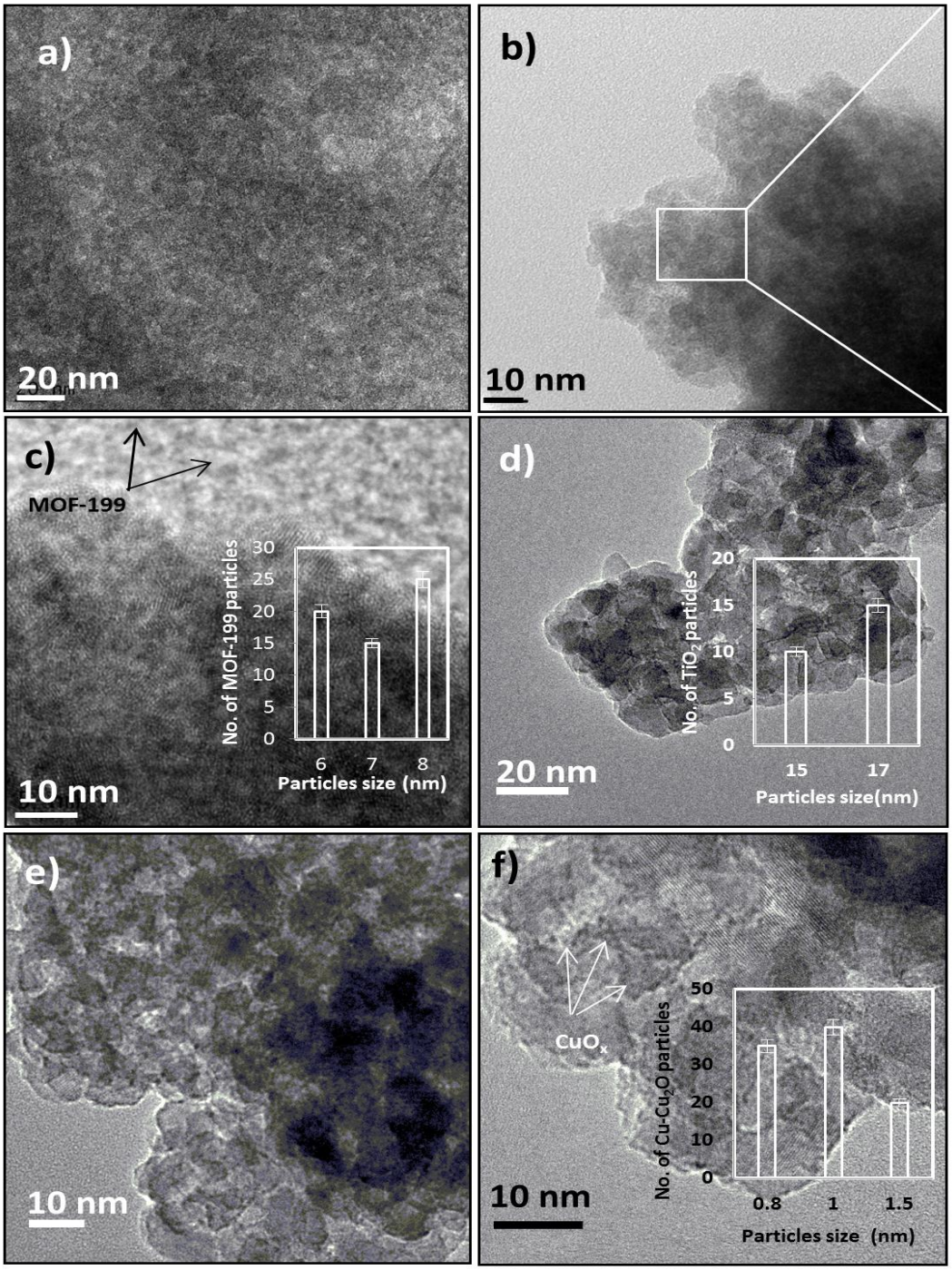

Figure 3.26: (a–c) TEM images of the TiO_2–MOF-199 composite and (d–f) Cu–Cu_2O/TiO_2-400 °C.

Fig. 3.26 shows the TEM images of the TiO_2–MOF-199 composite and that calcined at 400 °C. TEM images of the uncalcined composite reveal that semi-crystalline TiO_2 completely envelopes the MOF particles of 6–8 nm size (fig. 3.26a–c). After calcining the TiO_2–MOF-199 composite at higher temperatures, beyond 350 °C, the oxidation of the benzene tricarboxylic framework occurs which finally results in the production of highly dispersed Cu

and Cu_2O nanoparticles. Finally, well dispersed Cu and Cu_2O nanoparticles of ~0.5–1.5 nm size can be clearly seen in Fig. 3.26e and f. Banerjee and co-workers synthesized CuO nanoparticles of size 30-40 nm by calcining the MOF-199 at 550 °C [431]. Khan and co-workers produced Cu, Cu_2O and CuO particles supported over porous carbon by calcining the MOF-199 at 700-800 °C in an inert atmosphere, but metal nanoparticles were not clearly seen [585]. In the present study, very finally dispersed metal and metal oxide nanoparticles can be easily spotted over TiO_2 nanoparticles of 15-17 nm (Fig. 3.26d-f). The presence of very small particles suggests an intimate interaction of metal particles with TiO_2 support, which provides greater surface for H^+ adsorption and subsequent reduction by electron transfer from support. 4-6 nm Cu agglomerates are formed by calcining TiO_2-MOF composite at 500 °C (fig. 3.27).

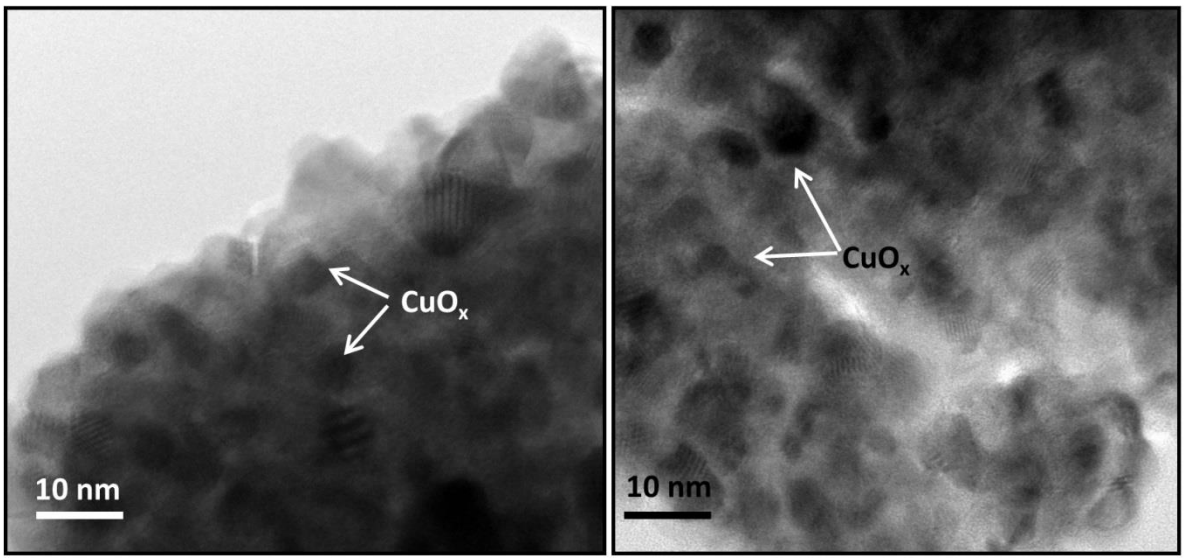

Figure 3.27: TEM images of TiO_2-MOF-500 °C.

3.1.6.5 XPS analysis

XPS analysis of MOF derived Cu species loaded TiO_2 catalyst is presented in Fig. 3.28 and Table 3.5. A survey spectrum of the MOF-derived catalyst clearly indicates the presence of C, Ti, O and Cu species. The relative concentration of each element (Ti, O, C and Cu) on the catalyst surface was calculated from Ti2p, O1s, C1s and Cu2p core–level peak areas. The surface elemental composition was found to be 0.73 at.%, 35.2 at.%, 55.8 at.%, and 8.2 at.% for Cu, Ti, O and C, respectively. This corresponds to 1.7 wt.% Cu loading on the surface. The apparent large concentration of Cu can be attributed to the fact that most of Cu atoms present on the surface were analyzed due to their small size, whereas all of the Ti and O atoms in the relatively large TiO_2 particles cannot be analyzed using XPS (a surface-sensitive technique with an X-ray penetration depth = approx. 10 nm). This also indicates that Cu is

very well distributed on the surface in the form of small particles. The $Ti2p_{3/2}$ and $Ti2p_{1/2}$ peaks were located at the binding energies of 458.9 eV and 464.6 eV respectively consistent with Ti^{+4} values in TiO_2 lattice [640]. The core level spectrum of O1s, due to its metallic oxide Ti-O bond, showed its main peak at 530.1 eV (87.5% of total surface O). A broad peak at 531.7 eV may be assigned to oxygen atoms of hydroxyl/carboxyl groups embed on the surface (12.5% of total surface O). The core level spectrum of C1s main peak at 284.8 eV was observed corresponding to the adventitious carbon (72.5% of total surface C) at the sample surface and peaks at 286.5 eV and 288.8 eV can be attributed to C-O bonds of C-O-C (18.8% of total surface C) and carboxylic species (8.7% of total surface C), respectively.

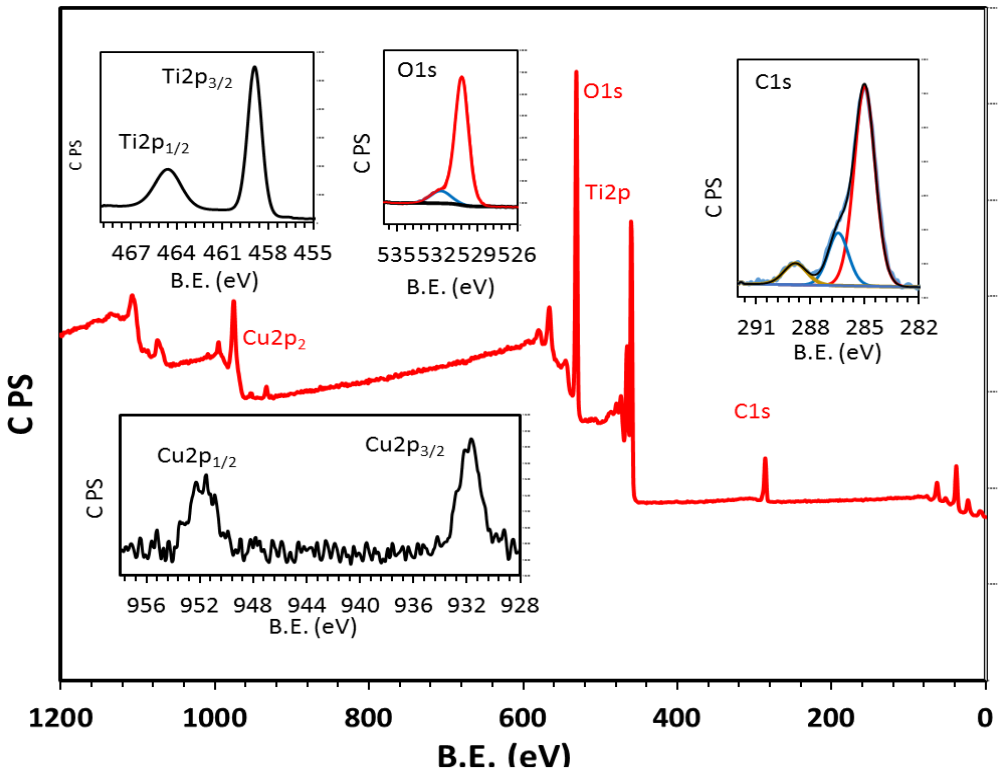

Figure 3.28: XPS survey scan and core level spectra of Ti2p, O1s, C1s and Cu2p for MOF derived 1 wt% Cu/TiO_2-400 °C.

The peak position of Cu2p XPS spectra indicated that Cu is present mainly in the form of Cu_2O ($Cu2p_{3/2}$ = 931.8 eV; $Cu2p_{1/2}$ = 951.8 eV) [641]. The absence of any satellite above Cu 2p peaks clearly indicates the absence of CuO. However, Cu may also be present in the form of Cu° as it is almost impossible to distinguish between Cu and Cu_2O using XPS [642]. We tried to map Cu LMM auger peaks to distinguish between Cu^0, Cu^{1+} and Cu^{2+}, however, we cannot resolved between three Cu species due to very low loading of Cu, lower intensity of auger peaks and interference of relatively large Ti2S peak intensity (fig. 3.29).The presence of Cu_2O was clearly indexed in optical characterization by the fingerprint absorption of Cu_2O

at 400-650 nm and absorption centered at 700-900 nm validating the presence of Cu°. Khan and coworkers observed the reduction of Cu^{2+} to Cu^{+} and Cu^{0} due to presence of carbon while calcining MOF-199 at 700-800 °C [585]. The formation of Cu^{0} and Cu_2O species over TiO_2 surface in this study might be due to the formation of intermediate carbon acting as reducing agent during calcination process [643]. Further, as for as the existence of metallic Cu at high temperature is concerned, the existence of metallic Cu at 700 °C while calcining the MOF-199 over g-C_3N_4 has been very recently reported [644].

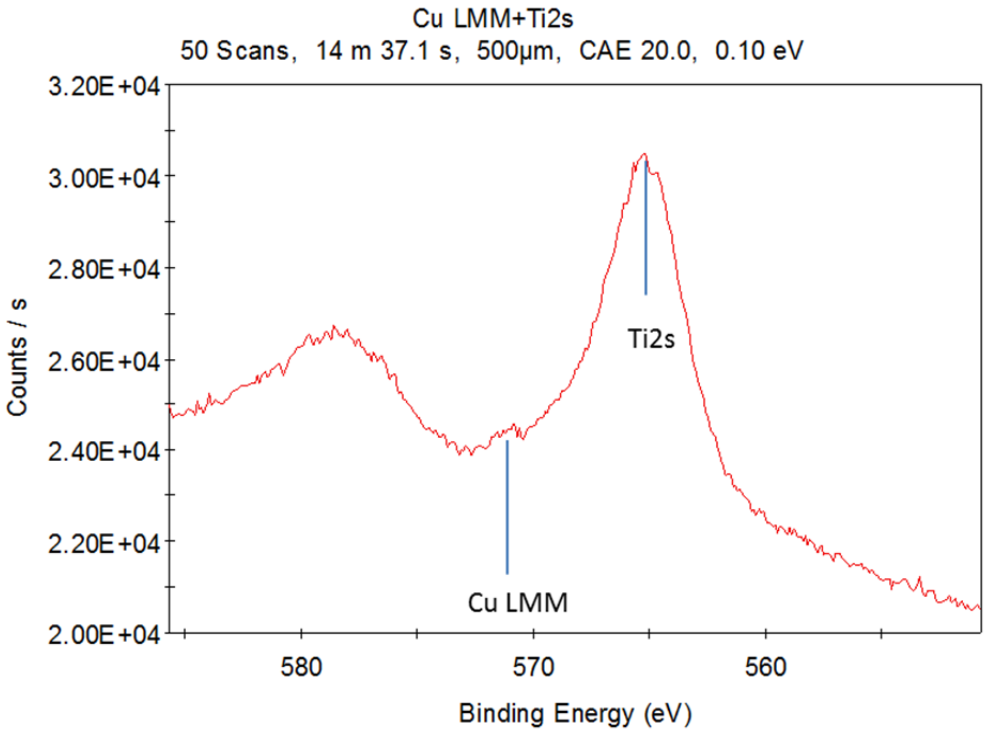

Figure 3.29: Cu LMM auger spectrum for Cu-Cu_2O/TiO_2.

From the XPS analysis it is clear that functional groups like OH and COOH are embedded during calcination at 400 °C. The XPS analysis of TiO_2-MOF-500 °C is shown in fig. 3.30. The peak position of Cu2p XPS spectra indicated that there are two kinds of Cu species. Cu $2p_{3/2}$ peaks at binding energy values of 932.9 eV and 934.2 eV corresponds to Cu_2O and CuO form, respectively [645]. The absence of any emission peak around 930 eV clearly indicates the absence of copper in metallic form. The presence of shake up structure clearly indicates that Cu^{2+} is the dominant copper species.

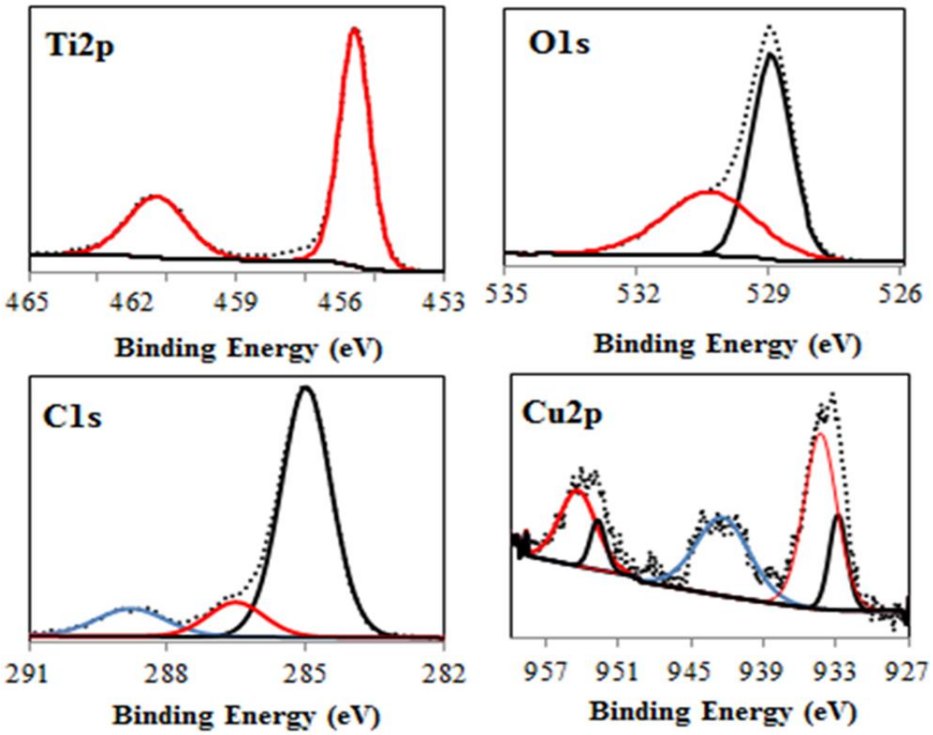

Figure 3.30: XPS core level spectra of Ti2p, O1s, C1s and Cu2p for TiO_2-MOF-500 °C.

Table 3.5: Surface elemental and % distribution of MOF derived 1wt.% Cu/TiO_2-400.

Element	Core Level	Position (eV)	FWHM (eV)	Elem. Comp. (at. %)	% Elem. Distribution
Cu	$2p_{3/2}$	931.8	2.0	0.73	Cu = 100
	$2p_{3/2}$	951.8	2.3		
Ti	$2p_{3/2}$	458.9	1.1	35.2	Ti_{TiO2} = 100
	$2p_{3/2}$	464.6	2.0		
O	1s	530.1	1.2	55.8	O_{TiO2} = 87.5
	1s	531.7	1.8		O_{OH} = 12.5
C	1s	284.8	1.4	8.2	$C_{adv.}$ = 72.5
	1s	286.5	1.4		$C_{c\text{-}o\text{-}c}$ = 18.8
	1s	288.8	1.5		C_{COOH} = 8.7

3.1.7 H_2 production photoreactions

Fig. 3.32 shows the comparison of photocatalytic activity of the 1wt.% Cu/TiO_2 materials (1wt. % Cu=Cu-Cu_2O) calcined at different temperatures for hydrogen production from water, with glycerol as a sacrificial reducing agent. Hydrogen production experiments in different glycerol to water volume ratios on 1 wt.% Cu/TiO_2-400 catalyst were also performed. An increase in rates up to 20 vol. % glycerol proportion was observed (Fig.3.31). A further increase in glycerol concentration beyond 20 vol. % resulted in a decrease in

hydrogen production rate due to increase in viscosity of the reaction mixture which decreases the dispersion of catalyst particles in the reaction mixture. Further investigations were performed in 5 vol. % glycerol-water mixture to afford reliable measurement due to the amount of hydrogen produced with our experimental set up while keeping the glycerol concentration as minimum as possible.

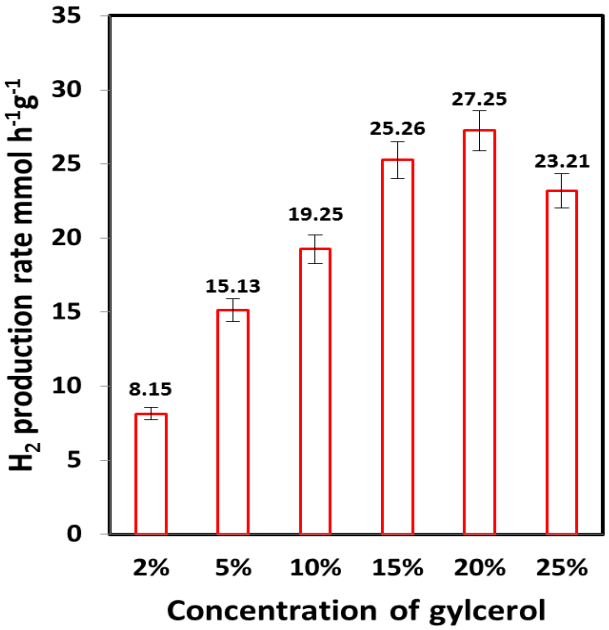

Figure 3.31: H_2 production rates over 1 wt.% Cu/TiO_2-400 from different concentrations of glycerol.

Fig. 3.32 shows that 1 wt.% Cu/TiO_2 -500 is the least active catalysts and showed hydrogen production rate five times less (2.4 mmol $h^{-1}g^{-1}$) as compared to 1 wt.% Cu/TiO_2-400 catalyst. This might be due to oxidation of Cu and Cu_2O species to CuO at relatively higher temperature and subsequent growth of CuO to larger particle size by sintering (fig. 3.27 & 3.30). It has been reported that with the increase of CuO particle size its conduction band potential becomes less negative than proton reduction potential and electrons flow to proton becomes thermodynamically unfavourable [646]. The oxidation of Cu^{1+} to Cu^{2+} at higher temperature is also reported by many others [647, 648]. A relatively lower rate of hydrogen production (9.4 mmol $h^{-1}g^{-1}$) compared to 1 wt.% Cu/TiO_2-400 was observed over 1 wt.% Cu/TiO_2-350. This might be due to remnants of carbon particles (not detected in XRD) because this catalyst was prepared by calcining the TiO_2-MOF composite at temperature near to complete oxidation of organic framework of MOF-199.

As for as the role of carbon in photocatalytic processes is concerned, there are controversies in literature about it. It is reported that despite their potential ability to aid in the quenching of

electron and hole recombination, the carbon supported titania catalysts are in fact not capable of producing measurable amounts of H_2 via photoactivation [649]. In another study, it was reported that the presence of carbon as a much more conductive material than TiO_2 able to attract electrons to its domain enabling effective e^-/h^+ separations for enhancing photocatalytic water splitting [650]. Moreover, the rate of hydrogen production over 1wt.% Cu/TiO_2-350 is increased rapidly with time due to the formation of Cu^0 from Cu_2O during photoirradiation. The lower rate at 1wt.% Cu/TiO_2-350 °C as compared to 1 wt.% Cu/TiO_2-400 may be also attributed to the lower TiO_2 crystallinity at 350 °C as compared to one obtained at 400 °C [651-653]. A very high rate of hydrogen production 15.13 mmol $h^{-1}g^{-1}$ was observed over 1 wt.% Cu/TiO_2-400 due to synergy among optimum Cu-Cu_2O species distribution, dispersion and crystallinity of TiO_2 support. For comparison, CuO/TiO_2 was prepared by conventional deposition precipitation method with overall 1% Cu loading and calcined at 400 °C but it produced a much lower rate of hydrogen production (6.52 mmol $h^{-1}g^{-1}$). From Table 3.6, it can be noted that comparatively better rates of hydrogen production are obtained over Cu supported TiO_2 photocatalyst used in this study as compared to photocatalysts prepared by conventional Cu deposition methods reported in literature. A few reports in table 3.6 show slightly better results. In these studies either a very high concentration of sacrificial reagent is used or higher amount of Cu is deposited over TiO_2.

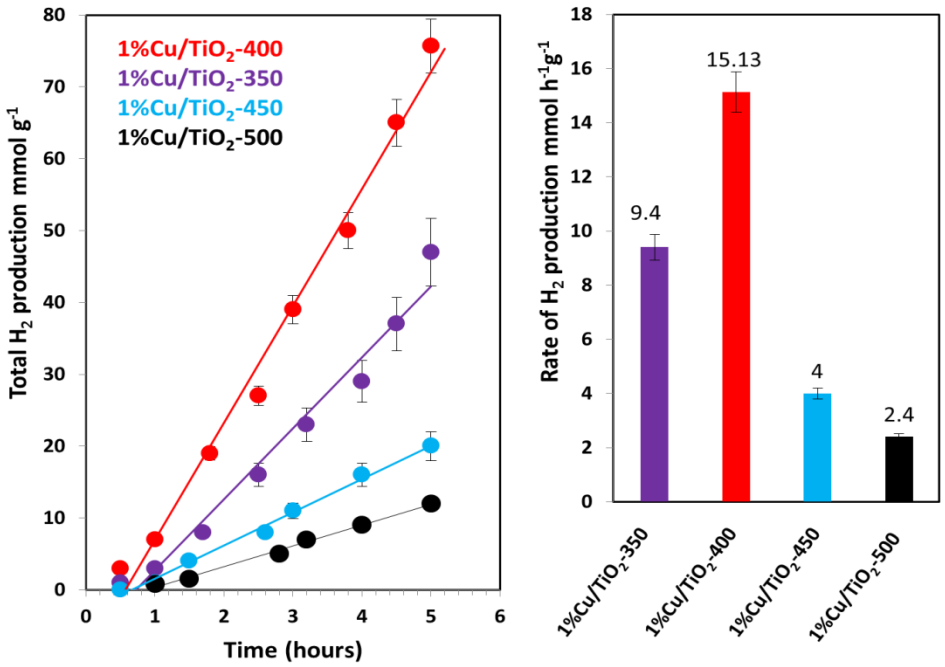

Figure 3.32: Comparison of the photocatalytic activities of 1% Cu/TiO_2-350, 1wt.% Cu/TiO_2-400, 1wt.% Cu/TiO_2-450 and 1wt.% Cu/TiO_2-500 samples for the photocatalytic H_2 production from 5 vol. % glycerol-water mixtures.

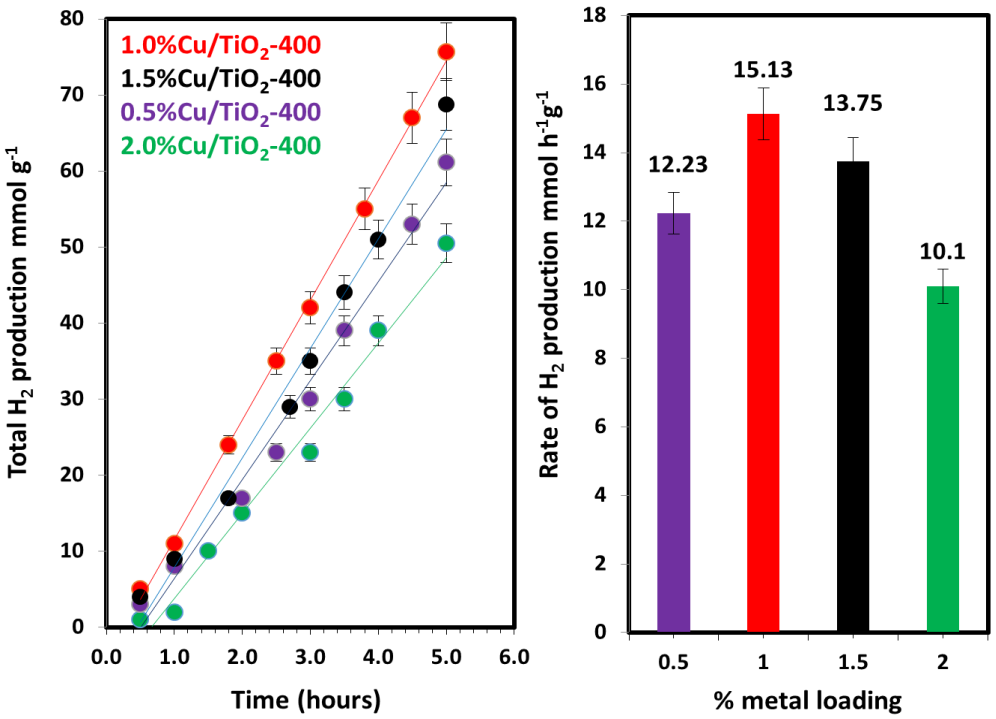

Figure 3.33: Effect of metal loading amount on hydrogen production from 5 vol. % glycerol-water mixtures over TiO_2-MOF composite calcined at 400 °C.

Fig. 3.33 shows that optimum hydrogen production rate was achieved for 1 wt. % nominal loading of Cu. A slight decrease in activity at 1.5 wt.% metal loading was observed after that a sharp decrease in activity was observed for 2 wt.% loadings. The decrease in photocatalytic activity with increasing metal loading has been observed by many other workers for which no clear explanation is yet known [607, 646, 654-656]. Upon increasing of metal particle coverage, a large fraction of the semiconductor surface may become unavailable for light absorption. It can also result in increasing surface defects at the metal-semiconductor interface, leading to an increase in e^-/h^+ recombination centres. A decrease in activity was also observed at 0.5 wt.% metal loading because metal loading below the optimum value generates fewer active sites for electron transfer as well as recombination of atomic hydrogen to generate final molecular hydrogen. There is always controversy about the overall amount of metal loading over the TiO_2. In many studied overall 1wt.% loading is considered as optimum for hydrogen production as also in the present study [603, 617]. In some other studies, 0.5 wt.% loading is reported as the optimum value [657]. In the previous section hydrogen production was studied over $Cu(OH)_2$-$Ni(OH)_2/TiO_2$ where 0.5wt.% overall metal loading was active for hydrogen production after 1wt.% metal loading [603]. The reason behind it is that on increasing metal loading maximum number of metal catalytic hot spots for

hydrogen production are formed but at the same time it blocks the light reaching the semiconductor support. In the case of 0.5% loading instead of having fewer numbers of metal particles for hydrogen production, a good rate is observed due to maximum dispersion of metal nanoparticles which allows maximum light to reach the support.

Table 3.6: Comparison of hydrogen production rates over Cu loaded photocatalysts reported in literature with that of present study.

Photocatalyst (Metal loading method)	Sacrificial reagents (vol. %)	Irradiation Source	H_2 production mmol $h^{-1}g^{-1}$	Ref.
1 wt. % Cu/TiO_2-Anatase MOF templated	5 % glycerol-water	100W lamp (UV)	15.13	Present study
1.25 wt.% CuO/TiO_2 (Complex precipitation)	80 % ethanol-water	100W lamp (UV)	20.3	2013[646]
0.5% Cu-0.5%Ni@P25 (Solvothermal)	37.5 methanol-water	300 W Xe lamp	13.5	2015[658]
29 mol % $Cu(OH)_2$/P25 (Precipitation)	0.09M ethylene glycol-water	3W LEDs (UV)	3.42	2011[659]
1.3 wt.% CuO/P25 (Impregnation)	0.1M glycerol-water	3W LEDs (UV)	2.06	2011[660]
8 atom %Cu/P25 (Chemical reduction)	10 % methanol – water	400W lamp (UV)	20	2010[661]
1 wt. % Cu_2O/P25 (Impregnation)	20 % ethanol-water	200W lamp (UV)	3.48	2009[662]
1.2 wt. % Cu/TiO_2-Anatase (Incipient wetness)	30% methanol-water	208W (UV) lights	3.2	2004[663]
1.3wt% CuO/TiO_2-Anatase (Impregnation)	0.1M glycerol-water	3W UV-LED (365 nm)	2.06	2011[660]
2.5wt% CuO/TiO_2-Anatase, (oil micro-emulsion)	50% ethanol-water	125W Hg lamp	2.7	2009[664]
10 wt. %Cu/TiO_2-Anatase (Complex precipitation)	6% menthol-water	500W Hg lamp	0.4	2009[597]
0.5wt.%Cu/P25 (Impregnation)	10% methanol water	300 W Xe lamp	1.134	2014[647]

As can be seen from Fig. 3.34, stable photocatalytic hydrogen production was observed over the duration of the experiments (16 h). The slight increase in rate with time (~8.5 %) in second run was due to the reduction of Cu_2O under photoreaction condition as observed by others [665]. Third cycle also shows increase in hydrogen production rate (~6.5%) over the

second run. This is due to the further formation of Cu in metallic form. A slight decrease in the hydrogen production rate (~4.5 %) in fourth run is due to the deposition of catalyst particles with the walls of reactor with time, thus scattering the incoming light.

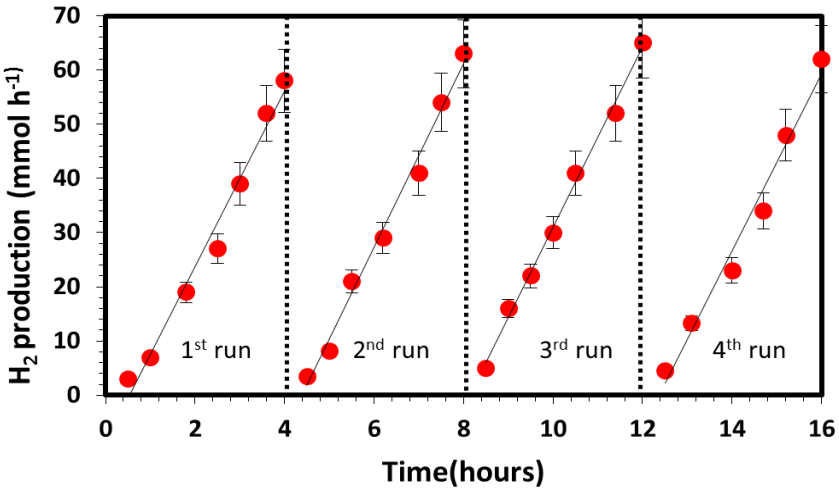

Figure 3.34: Cyclic runs for the hydrogen production experiments over 1wt.% Cu/TiO_2-400 photo catalysts by using 5 vol. % glycerol-water mixtures.

Table 3.7: Summarized structural, chemical composition and hydrogen production data for TiO_2 supports and the 1 wt.% Cu/TiO_2 photocatalysts.

Catalyst	BET surface area (m^2/g)	TiO_2 crystallite size (nm)	Cu wt.% by XPS & EDX	Cu particle size (TEM) (nm)	H_2 production (mmol $h^{-1}g^{-1}$)
TiO_2-400	85.2	(A) 15	-	-	-
1 wt.% Cu/TiO_2-350	86	(A) 15	-	-	9.4
1 wt.% Cu/TiO_2-400	85.7	(A) 15	0.73 & 0.85	0.5-1.5	15.32
1 wt.% Cu/TiO_2-450	85.5	(A) 15.12	-	-	4
1 wt.% Cu/TiO_2-500	85	(A) 15.32	-	8-10	2.5

3.1.8 Hydrogen production mechanism

Both the XPS and DRS results strongly confirm the presence of Cu species mainly as Cu_2O and relatively less amount of Cu. Anatase TiO_2 has an optical band gap of 3.15 eV which lies in UV region whereas CuO and Cu_2O have optical band gaps of 1.7 and 2.1 eV, respectively and absorb in visible region. Under UV light irradiation valence band electrons in TiO_2 are promoted to the conduction band and at the same time electrons excited in the Cu_2O conduction band also thermodynamically transferred to the conduction band of TiO_2. Finally,

electrons from the conduction band of TiO_2 are transferred to the Cu nanoparticles thus shifting the fermi level of the composite catalyst to more negative values. A negative shift in the fermi level in the composite photocatalytic system is an indication of better charge separation and more reductive power. The fermi level of semiconductor TiO_2 (9.95 eV) lies above the fermi level of Cu (7.1 eV) [666]. On loading Cu onto TiO_2, electrons flow from the former into the metal with simultaneous alignment of the fermi levels and formation of a Schottky barrier at the interface [667, 668]. The Schottky barrier allows the migration of electrons from TiO_2 into the Cu. When the sample is further exposed to UV radiation, the fermi level of TiO_2 shifts to a new quasi fermi level due to the photo-induced electrons [669]. The previous thermodynamic equilibrium state for electron transfer established at the barrier is destroyed to allow the flow of more electrons to the metal, where they can react with adsorbed H^+ to convert them to atomic H. These H atoms then combine to produce H_2 on Cu metal. The photo-induced holes are then free to diffuse to the TiO_2 surface where they react with sacrificial agent to convert them into carbonyl compounds [670].

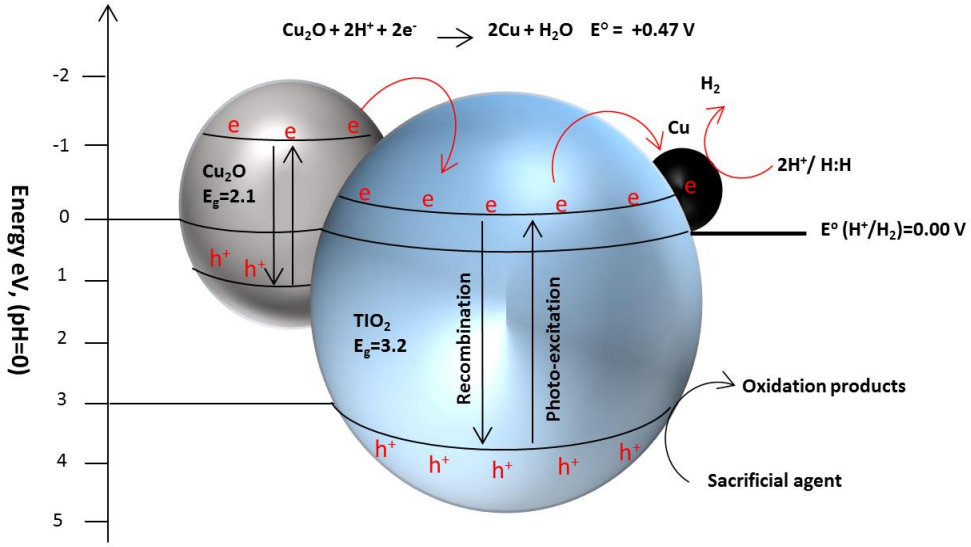

Figure 3.35: Hydrogen production mechanism over Cu-Cu_2O/TiO_2 and energy band position of Cu_2O and TiO_2.

At the same time after photoexcitation a part of the conduction band electrons in TiO_2 is directly used to reduce Cu^+ in Cu_2O to Cu^0 (Fig. 3.35). The H:H recombination rate constant on Cu is higher than that of Cu_2O and even higher than Au [665]. Once metallic Cu is formed it solely acts as electron transfer center and H:H recombination site for final molecular hydrogen production. Recently, Joo and co-workers established that electron transfer as well as electron recombination sites are required for higher rate of hydrogen production over

semiconductor photocatalytic systems [649]. Once photons have been stopped Cu^0 is gradually oxidized back to Cu^+. It appears that the main driving force for the high activity in this study is the higher dispersion of Cu species and the formation of reduced Cu at close proximity with TiO_2, further accelerating molecular hydrogen recombination. These findings suggest a new pathway to augment the performance of water-splitting photocatalysts beyond traditional approaches, such as the p-n-junction as reported in the previous studies [671-673].

3.1.9 Conclusions

From the above results and discussion it can be concluded that highly dispersed Cu-Cu_2O nanoparticles can be deposited over TiO_2 by using a metal organic framework (MOF) as a templating agent for metal nanoparticles. The TiO_2-MOF composite was prepared by hydrolysing titanium isopropoxide precursor over MOF nanoparticles by a solvothermal method, followed by the calcination of the composite at temperatures in the range of 350-500 °C. It was found that photocatalyst Cu-Cu_2O/TiO_2-400 prepared by calcining the TiO_2-MOF composite at 400 °C showed maximum activity for hydrogen production from 5% glycerol-water mixture. The activity of the photocatalyst was further augmented by the formation of Cu° from Cu_2O reduction during photoreaction by conduction band electrons of TiO_2. Hydrogen production activity was sharply decreased by further increasing the composite calcination temperature 400-500 °C due to the oxidation of Cu-Cu_2O to CuO and subsequent growth of CuO to larger particle size by sintering. Photocatalyst Cu-Cu_2O/TiO_2-350 showed slightly less activity than the Cu-Cu_2O/TiO_2-400 due to the presence of carbon as remnants of the organic framework at lower calcination temperatures. The present work presents a new strategy to develop highly dispersed metal nanoparticle over semiconductor supports by selecting MOFs containing the desired metal.

3.2 CdS based photocatalysts

Au/CdS (hexagonal phase) photocatalysts are the focus of this study. The main objective of this work is to study the effect of metal deposition methods on Au particle size and distribution for hydrogen production over Au/CdS systems in an ethanol water-electrolyte mixture and the nature of the aqueous media on the enhancement of photocatalytic activity. Au nanoparticles were deposited over hexagonal CdS particles using a novel and simple method involving reduction of Au^{3+} ions with iodide ions and finally this novel method was compared with other conventional Au loading methods. In Au/CdS system hydrogen production studies are mostly conducted in water-electrolyte mixtures. In the present work

hydrogen production was studied from a mixture of an inorganic electrolyte and organic sacrificial agent, ethanol for the first time. The role of α-hydroxyethyl radical produced from the reaction of ethanol and ^{o}OH radicle as an addition hole scavenger was discussed and the mechanism of hydrogen production from ethanol water-electrolyte mixture over Au-CdS is also proposed for the first time. This study also probed the catalyst structure after the reaction in order to probe into the restructuring of the material that has been occurred.

3.2.1 PXRD analysis

The XRD results indicate that the as-prepared CdS crystallizes mainly in the cubic phase with < 10% of the hexagonal phase (fig. 3.36A). The cubic phase remains the dominant CdS phase on heating in air up to 400 ^{o}C, while a further increase in temperature to 500 ^{o}C leads to complete oxidation to white $CdSO_4$ in less than one hour. However, heating the as-prepared cubic CdS at 600 ^{o}C in an inert environment (ca. 120 mL/min of N_2 flow rate) prevented the oxidation of CdS to $CdSO_4$ and converted cubic CdS to its hexagonal structure [48]. In the case of 3 wt. % Au/CdS prepared by the KI method, Au diffraction peak (111) can be clearly observed (fig. 3.36B). The growth of Au (111) peaks with loading amount (1-5 wt.%) in samples prepared by the KI method is presented in fig. 3.36C. The BET surface area was found equal to 33 ± 1.5 and 5 ± 0.4 m^2g^{-1} for cubic (as-prepared) and hexagonal phase (600 ^{o}C-annealed) respectively. Further effects of heat treatment details can be found in Table 3.8 and fig. 3.36A.

Table 3.8: Effect of heat treatment on CdS nanoparticles prepared by the sol-gel method.

No	Overnight Heat Treatment	CdS Phase (XRD)	Crystallite Size (XRD)	Surface Area (BET)
1	100 ^{o}C, air	Cubic	-	34 m^2g^{-1}
2	200 ^{o}C, air	Cubic	13 nm	35 m^2g^{-1}
3	300 ^{o}C, air	Cubic	14 nm	35 m^2g^{-1}
4	400 ^{o}C, air	Cubic	15 nm	32 m^2g^{-1}
5	500 ^{o}C, air	$CdSO_4$ white powder	-	-
6	600 ^{o}C, N_2 flow	Hexagonal phase	112 nm	5 m^2g^{-1}
7	800 ^{o}C, N_2 flow	Hexagonal phase	224 nm	1 m^2g^{-1}

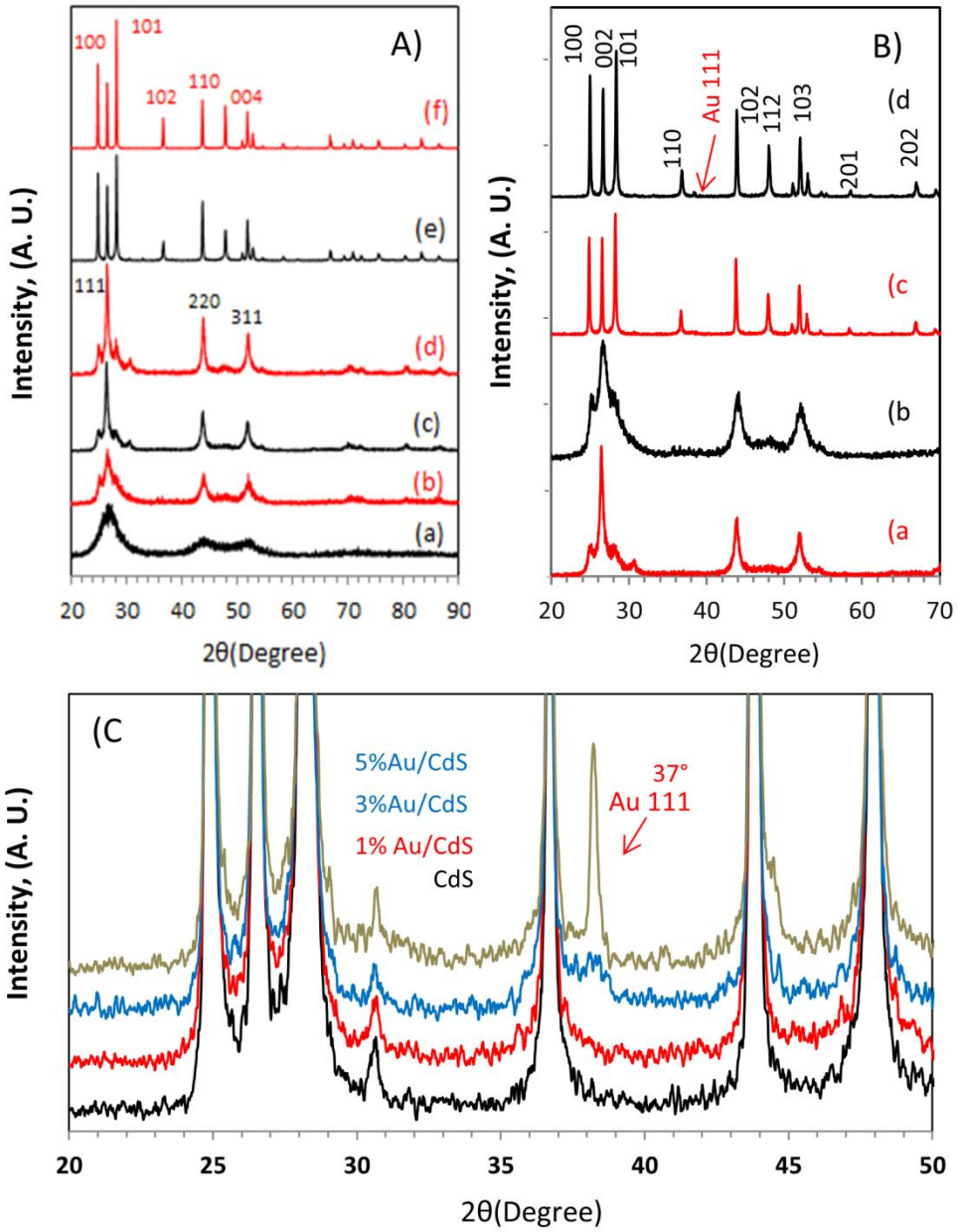

Figure 3.36: PXRD patterns for CdS (A) after annealing in air at (a) 100 ºC (b) 200 ºC (c) 300 ºC (d) 400 ºC and in continuous N_2 flow at (e) 600 ºC and (f) 800 ºC (B) comparison of 3 wt.% Au/CdS with (a) as prepared (b) 400 ºC (c) 600 ºC (C) growth of Au (111) peak with loading amount.

3.2.2 Surface properties

Surface properties such as pore diameter, pore volume and surface area of various CdS phases are shown in fig. 3.37 and table 3.9. Au was loaded on hexagonal CdS with a nominal Au wt. % loading equal to 1-5 % using a novel KI method and three other conventional methods. Actual Au loadings for 3 wt. % nominal loadings were determined using X-ray fluorescence (XRF) and ICP-OES analysis (Table 3.13). The lower Au amounts measured in

the case of KI and WI methods indicated that some of the Au is lost during filtration and centrifugation processes of these two methods, respectively. However, in the case of PD and DP method almost all of the Au is deposited on the catalyst surface. The decrease in surface area of 3wt. % Au/CdS photocatalyts prepared by different methods by the increase of Au loading amount is also observed (Table 3.13). This decrease in surface area is more prominent in the case of DP and PD methods due to maximum Au loading. It must be noted that, for the PD method, low radiation intensities similar to reported in this study are an absolute requirement. We tried to perform Au loading with same set up at radiation intensities 5 times higher than reported in this study. The deposition of Au layers on the wall of the pyrex reactor was clearly visible at the end of the experiments. In another work about Ag-photodeposition on TiO_2 we observed silver mirror formation on the wall of the reactor at relatively high radiation intensities.

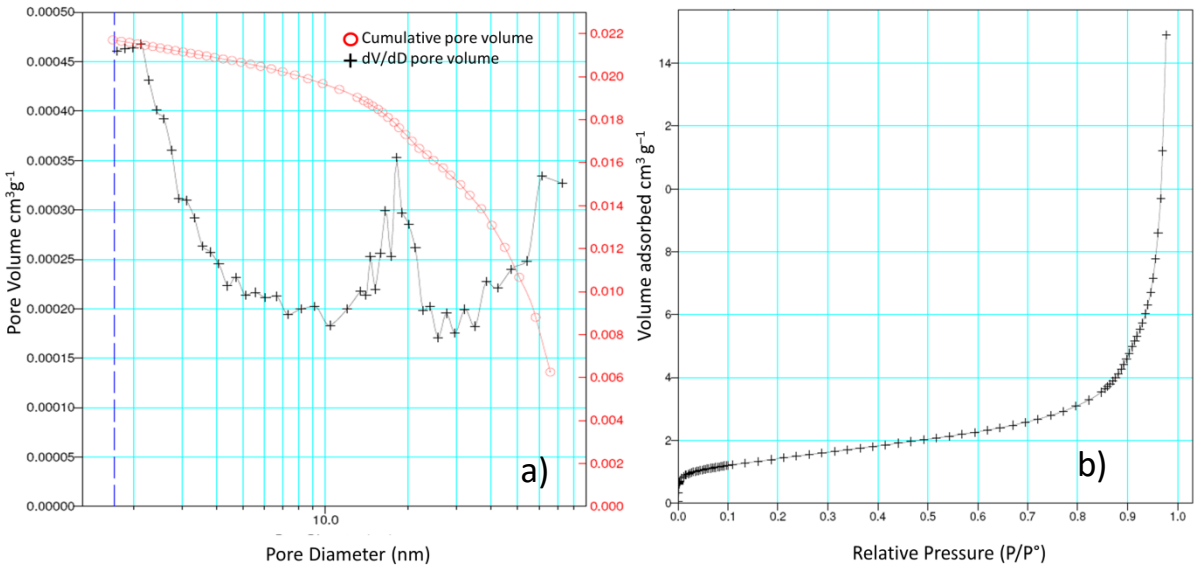

Figure 3.37: (a) Nitrogen adsorption isotherms (red) and pore size distribution (black) calculated by BJH method (b) N_2 adsorption isotherm for hexagonal CdS-600 °C.

Table 3.9: Surface properties of various CdS phases.

CdS phase(XRD)	Overnight heat treatment	Cumulative Pore volume $cm^3\ g^{-1}$	Average pore diameter Nm	BET surface area m^2g^{-1}
Cubic	as prepared	0.1560	5.302	98.7435
Cubic	400 °C	0.0725	12.321	32
Hexagonal	600 °C	0.0217	20.840	5.120
Hexagonal	800 °C	0.00895	37.253	1

3.2.3 TEM analysis

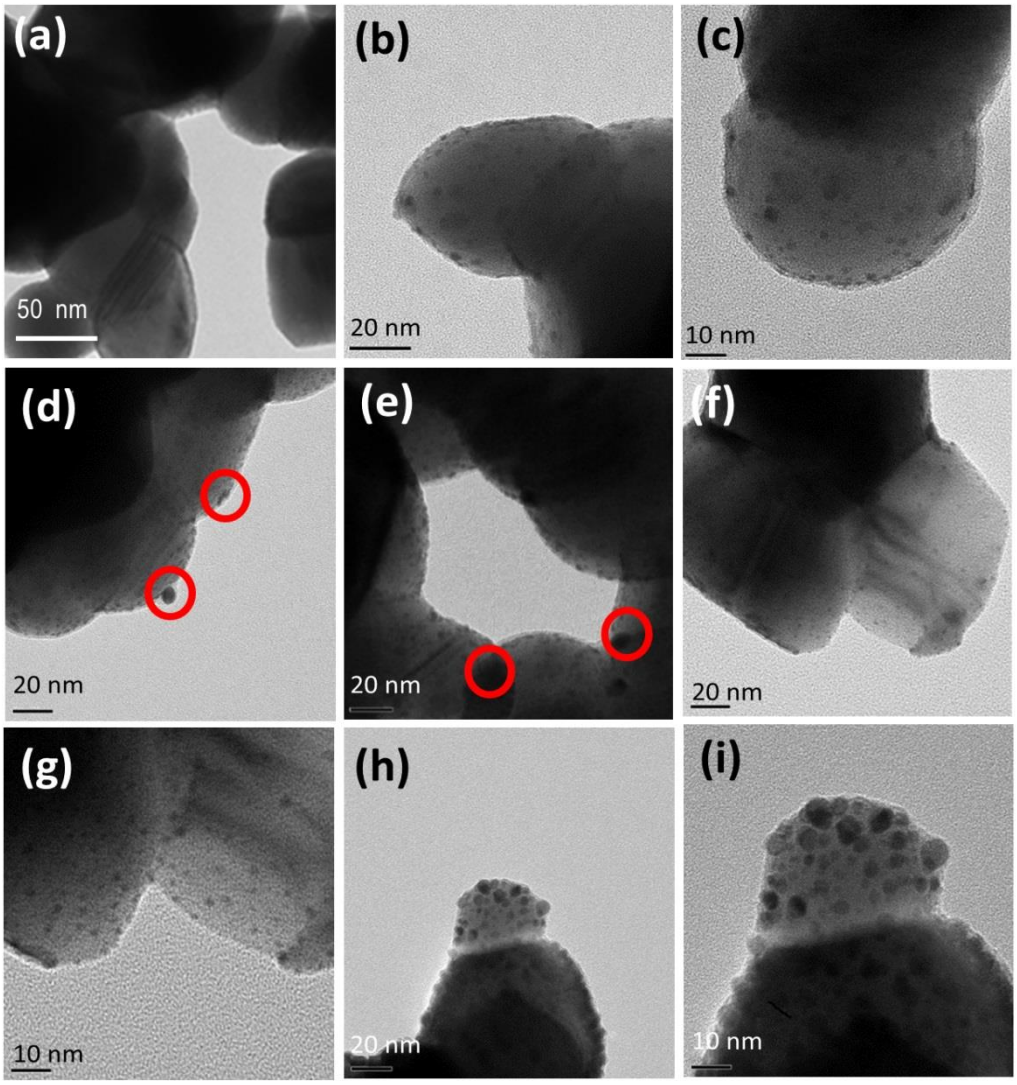

Figure 3.38: TEM images of (a) h-CdS, (b-c) 3 wt. % Au/h-CdS(KI), (d-e) 3 wt. % Au/h-CdS(DP), (f-g) 3 wt. % Au/h-CdS(WI) and (h-i) 3 wt. % Au/h-CdS(PD).

Fig. 3.38 (a–i) shows TEM images of as prepared hexagonal CdS and various Au/CdS (hexagonal) photocatalysts prepared by photo-deposition (PD), deposition precipitation (DP), incipient wetness impregnation (WI) and novel iodide reduction method (KI). TEM image (fig.3.38a) indicates a spherical particle shape of hexagonal CdS phase with an average particle size of 105 ± 5 nm. TEM images (fig. 3.38b & c) indicate that Au nanoparticles deposited by the KI method are finely dispersed over CdS with an average Au nanoparticles size of ca. 4 ± 0.6 nm (fig. 3.39a). Both DP (fig 3.38d &e) and WI (fig. 3.38f & g) loading methods produced smaller Au particles of more or less similar size with only a difference in the presence of very small fraction of widely dispersed larger Au particles in the former case. The average Au particle size in both cases was ca. 2 nm (fig. 3.39 b & c). Only one type of

very sparsely dispersed particles having size of 2-3 nm can be observed over photocatalyst fabricated by WI method. In the case of the PD method the Au particles grew into larger sizes, approximately 6 ± 2 nm due to continuous deposition of Au particles over electron rich Au nucleation cathodic sites on the CdS surface (fig. 3.38h & i). Further, the Au particles were spatially localized on some CdS particles while they were absent on others. The size of Au particle observed can be arranged in accordance with Au loading method as PD>DP>KI >WI (fig. 3.39).

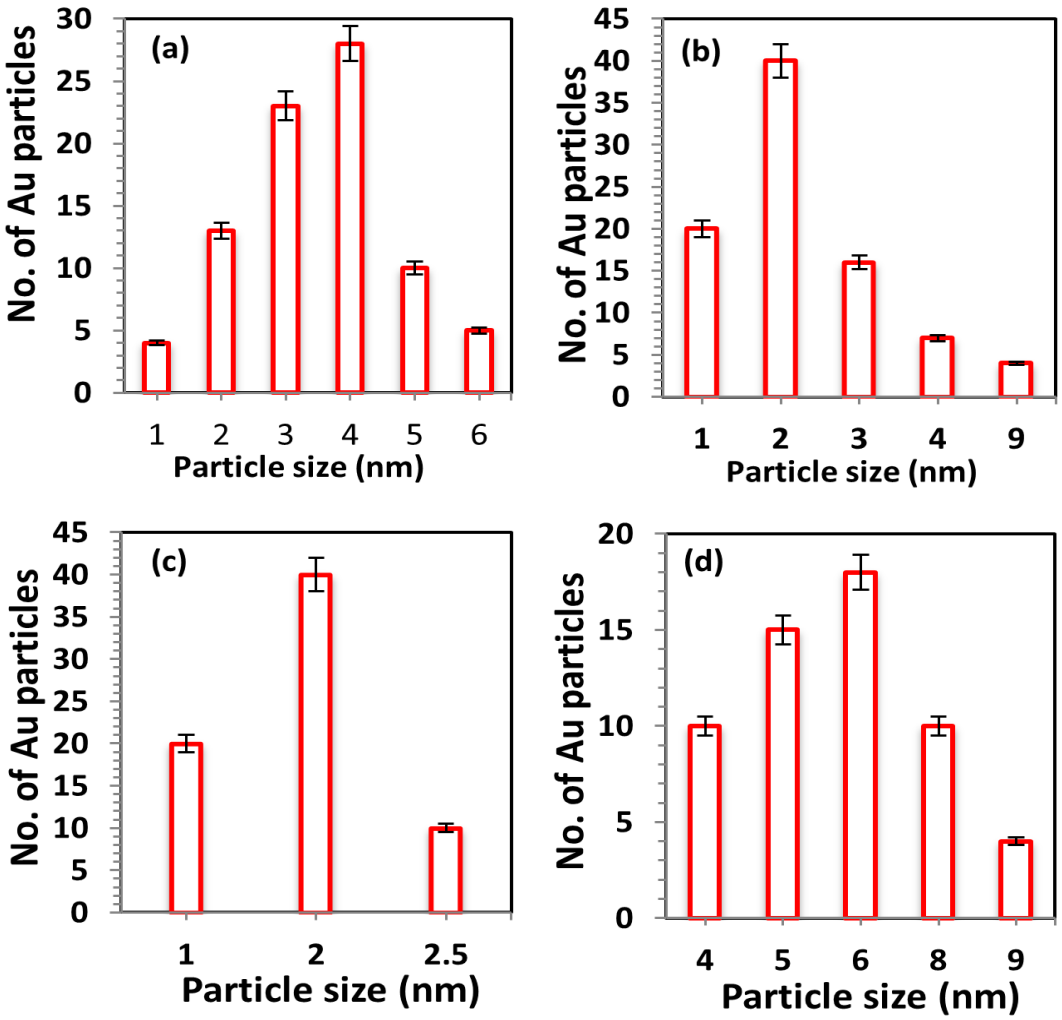

Figure 3.39: Au particle size distribution on 3 wt. % Au/CdS prepared by (a) KI method (b) DP method (c) WI method (d) PD method.

Fig. 3.40 shows TEM images for Au/h-CdS-KI photocatalysts as a function of Au loading. The average Au nanoparticle size increased with Au loading in the 1-5 wt. % range. At loadings of 1, 3 and 5 wt. % Au, the mean particle sizes of Au metal were ca. 2.1±0.5, 4±1.6 and 4.5±1.5 nm. Although the average Au particle size was about the same in the case of 3

and 5 wt. % loading, however there is a higher fraction of larger Au particles in the case of the 5 wt. % Au sample (Fig. 40 (bottom). a-c). This increase in Au particle size with loading amount is in accordance with the growth of Au(111) peak with loading amount in PXRD results (fig. 3.36 c).

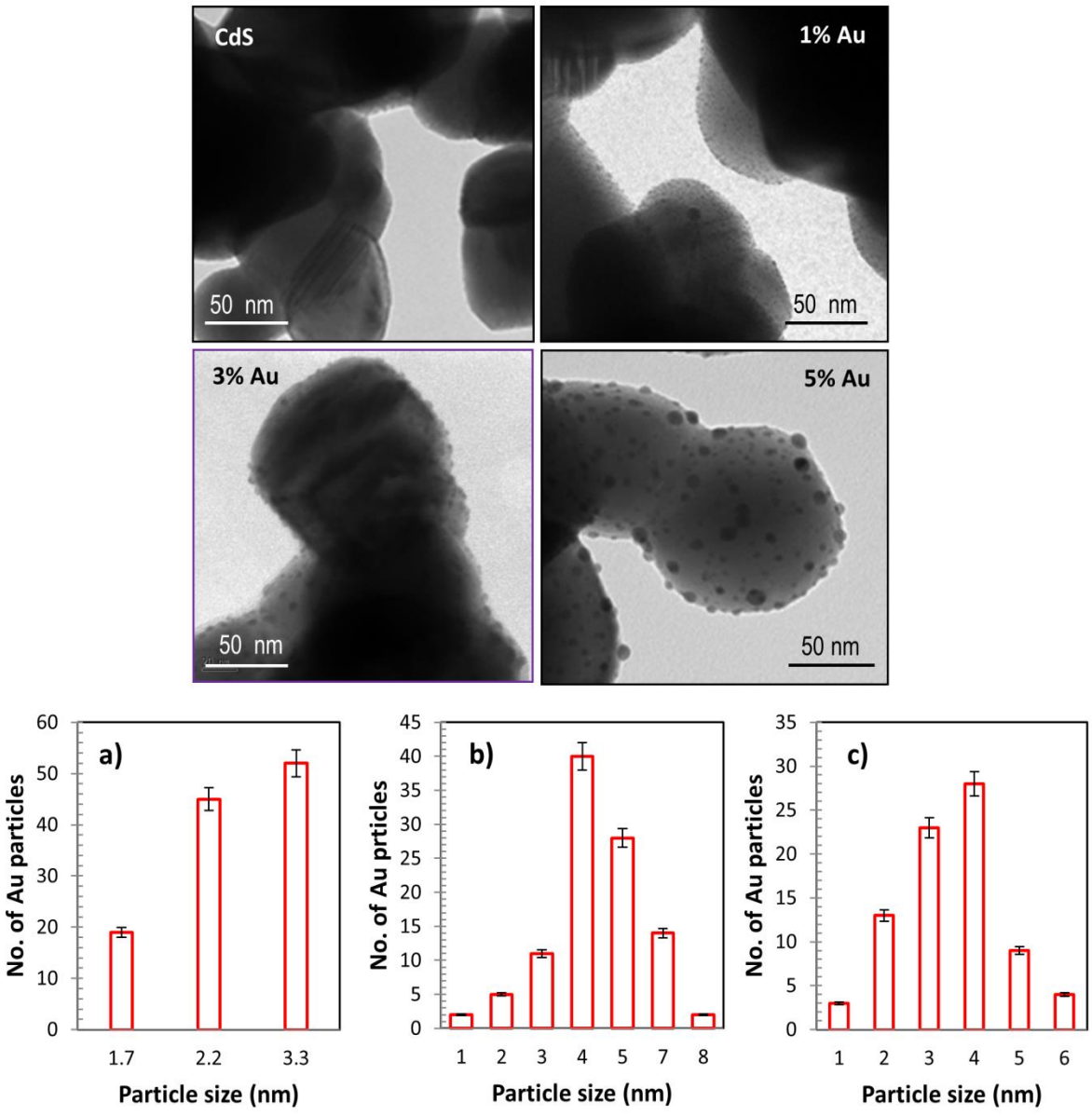

Figure 3.40: TEM images of hexagonal CdS, 1 wt. % Au/h-CdS, 3 wt. % Au/h-CdS, 5 wt.% Au/h-CdS with corresponding Au particle size distribution indicated by graphs (a), (b) and (c) respectively.

3.2.4 UV-visible diffuse reflectance measurements

UV–visible diffused reflectance spectroscopy confirmed the intrinsic band gaps of the cubic and hexagonal CdS phases to be 2.2 eV and 2.35 eV corresponding to 564 nm and 528 nm,

respectively (fig. 3.41a) [674]. The sharp absorption edge observed for the hexagonal phase is attributed to the higher crystallinity [675]. Defect states act as trap centers for charge carriers thereby increasing e^-/h^+ recombination rates and thus a lower number of charge carriers available for reactions at the surface of CdS. Au nanoparticles exhibit strong surface plasmon resonance (SPR) absorption at around 520 nm [676]. It has been shown that SPR absorption occurs in near ultraviolet, visible, and near or mid infrared regions depending on the size and shape of the gold nanoparticles as well as the refractive index of the surrounding medium [120, 677-681]. Therefore, the broad absorption band in the wavelength range of ca. 400–700 nm with a peak maximum at ca. 530–610 nm is attributable to LSPR of gold particles on CdS.

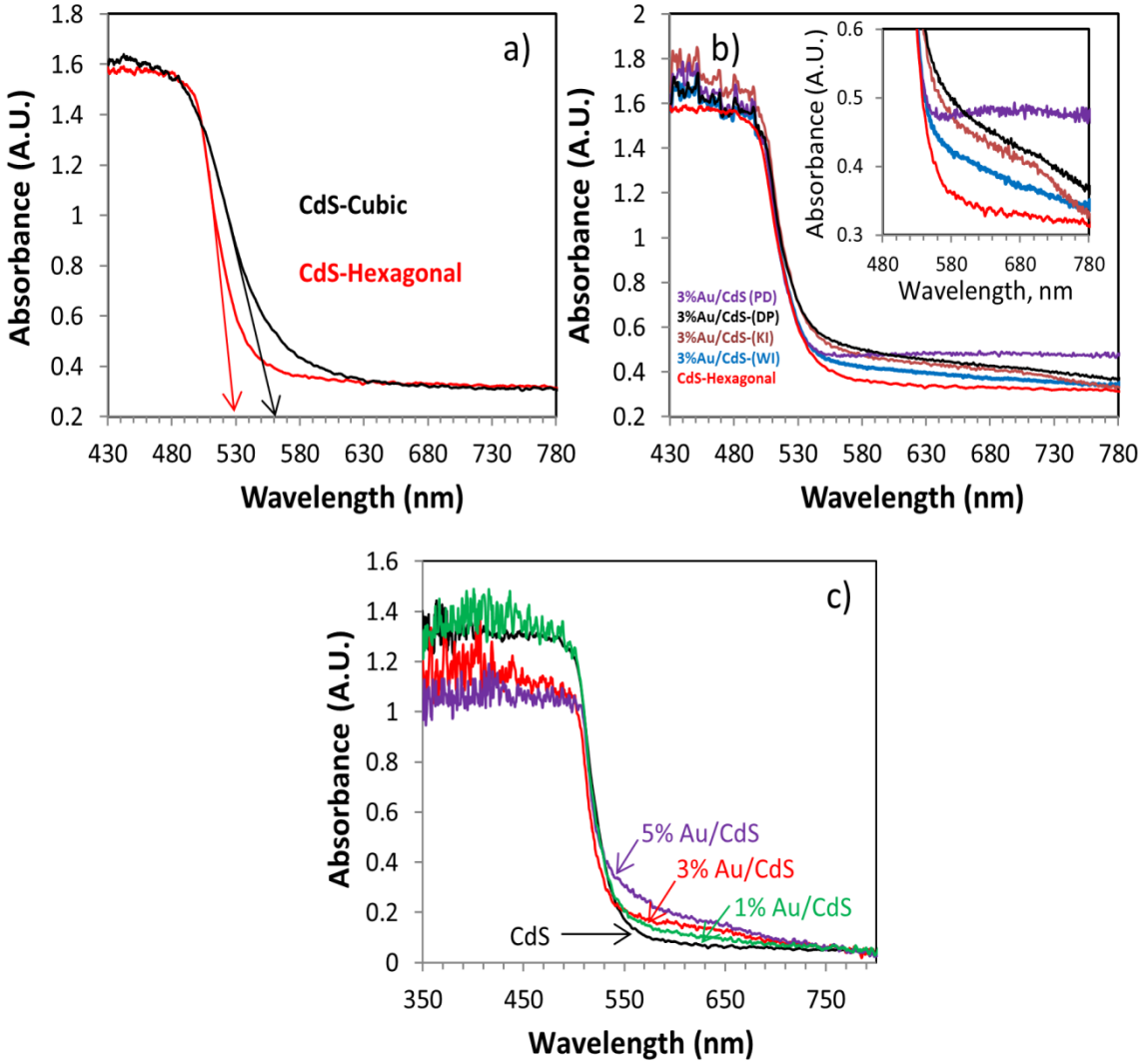

Figure 3.41: UV–visible diffused reflectance spectra of (a) cubic CdS and hexagonal CdS (b) 3%Au/h-CdS photocatalysts prepared by four different methods and (c) 1-5 wt. % Au/h-CdS prepared by KI method.

SPR absorption of Au is shifted towards longer wavelength with an increase in Au particle size. As observed in inset of fig. 3.41b, the intensity of the SPR absorption of the photocatalysts decreased in the order PD> DP = KI> WI, reflecting a corresponding decrease in the mean Au nanoparticle size. Such an extent of SPR red-shift is consistent with earlier studies [120, 591]. Cybula and co-workers observed a wide SPR band from 550 to 750 nm for Au/TiO_2 nanoparticles calcined at 350 and 400 °C where Au particles were present in a wide distribution range [682]. Kowalska and co-workers attributed absorption at 560–610 nm to surface plasmon resonance (SPR) of larger Au nanoparticles (30–60 nm) [683]. For Au colloids in solution, the dependence of the SPR intensity on the Au particle size is well established [120]. Further, the intensity of the SPR response can be related to the actual amount of Au loading as determined by the XRF and ICP-OES analysis where the response is proportional to amount of Au present. Fig. 3.41c clearly shows the increase in Au plasmon peak with increasing Au wt. %. In this case, the SPR absorption of Au is also shifted towards longer wavelength with increasing Au loading. The amount of Au loaded was measured independently by XRF analysis and was almost identical with the nominal loading (± 0.2 wt. %).

3.2.5 XPS analysis

XPS analysis of the as-prepared cubic CdS sample (fig. 3.42a) gave binding energies of 404.8 eV for $Cd3d_{5/2}$ and 161.8 eV for S2p core level peaks, confirming the synthesis of pure CdS [684]. These binding energy values were unchanged following the temperature-induced transformation of cubic CdS to hexagonal CdS (fig. 3.42b). However, the FWHM of the Cd 3d peaks decreased after high temperature treatment, suggesting Cd 3d core hole lifetimes were longer for the hexagonal CdS. Core hole lifetime has an inverse relationship with the width of the peak in XPS measurement; FWHM = h/τ where τ is the core-hole life time and h is Plank's constant [685]. In addition core hole lifetimes reflect crystallinity and electrical conductivity in the samples, both of which are clearly higher for the hexagonal CdS phase here. Other studies have related this effect to static fluctuations in valence charges due to bond length and bond angle variations in amorphous materials thus decreasing the core hole life times as compared to their crystalline counterparts [686, 687]. This was also reflected in the S2p spectra, in which the $S2p_{1/2}$ and $2p_{3/2}$ peaks are well-resolved in the case of the hexagonal CdS sample but poorly resolved in the case of the cubic CdS sample.

Table 3.10: XPS data for the as-prepared cubic CdS and hexagonal CdS.

Core Level	Position (eV) and [FWHM (eV)]	
	Cubic Phase	Hexagonal phase
Cd $3d_{5/2}$	404.8 [1.37]	404.8 [0.91]
S $2p_{3/2}$	161.8 [1.21]	161.8 [0.85]

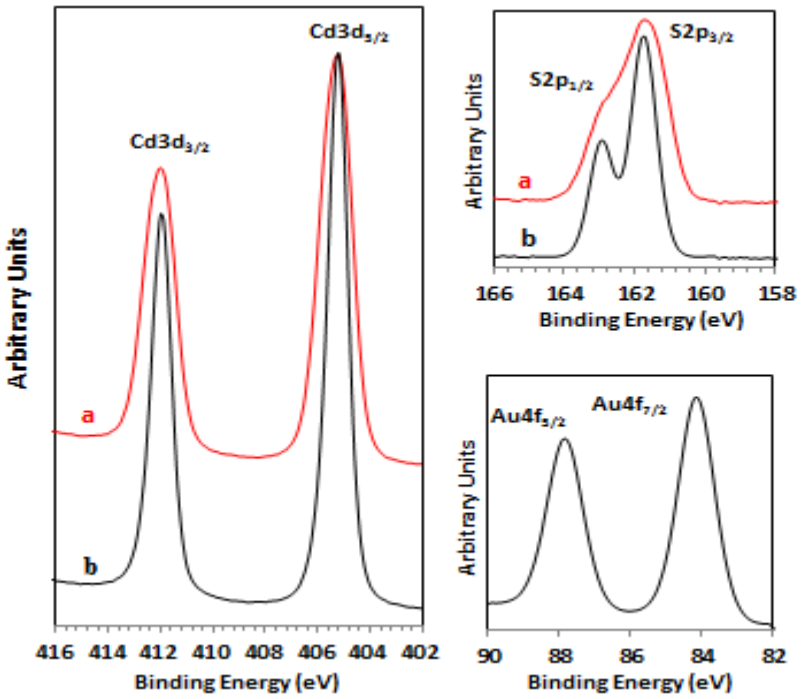

Figure 3.42: X-ray photoelectron spectra of the Cd3d, S2p and Au 4f regions for (a) as-prepared cubic CdS (b) ripened hexagonal CdS and 5 wt. % Au/h-CdS sample.

Fig. 3.43 presents the XPS analysis of as prepared (red) and used (black) Au/h-CdS-KI photocatalyst. In the case of survey scan, presence of peaks due to Au, Cd and S along with O and C can be clearly seen. As-prepared sample gave binding energies of 404.8 eV for $Cd3d_{5/2}$ and 161.8 eV for $S2p_{3/2}$ core level peaks, confirming the synthesis of pure CdS [688]. These binding energy values were unchanged following the photocatalytic tests (fig. 3.43). A binding energy of 84.1 eV for the Au $4f_{7/2}$ peak of the Au/h-CdS-KI sample before and after photocatalytic tests indicates that Au is present in the metallic state in both cases. S (in S^{2-} form): Cd ratios were found 0.91 and 0.75 for as prepared and tested catalysts respectively. The decrease in ratio is due to the formation of SO_4^{2-}/SO_3^{2-} on the CdS surface during photocatalytic reactions. The formation of SO_4^{2-}/SO_3^{2-} can be noted by the appearance of S 2p doublet with $S2p_{3/2}$ at 168 eV. The SO_4^{2-}/SO_3^{2-} are formed by the oxidation of S^{2-} into S^{6+}/S^{4+} due to the reaction of lattice S^{2-} with photo-generated holes and OH^- species formed during

photoreaction as indicated in the reaction mechanism schematic (fig. 3.53). The self-photo-corrosion of CdS has been noted by many authors [689-691]. XPS results are summarized in Table 3.11. The increase in FWHM of S $2p_{3/2}$ peak in the case of used sample is due to the formation of more than one S species i.e. $S^{6+}$and S^{4+} in this case. The presence of O1s peak is due to surface H_2O/OH species while that of C1s is due to adventitious carbon species.

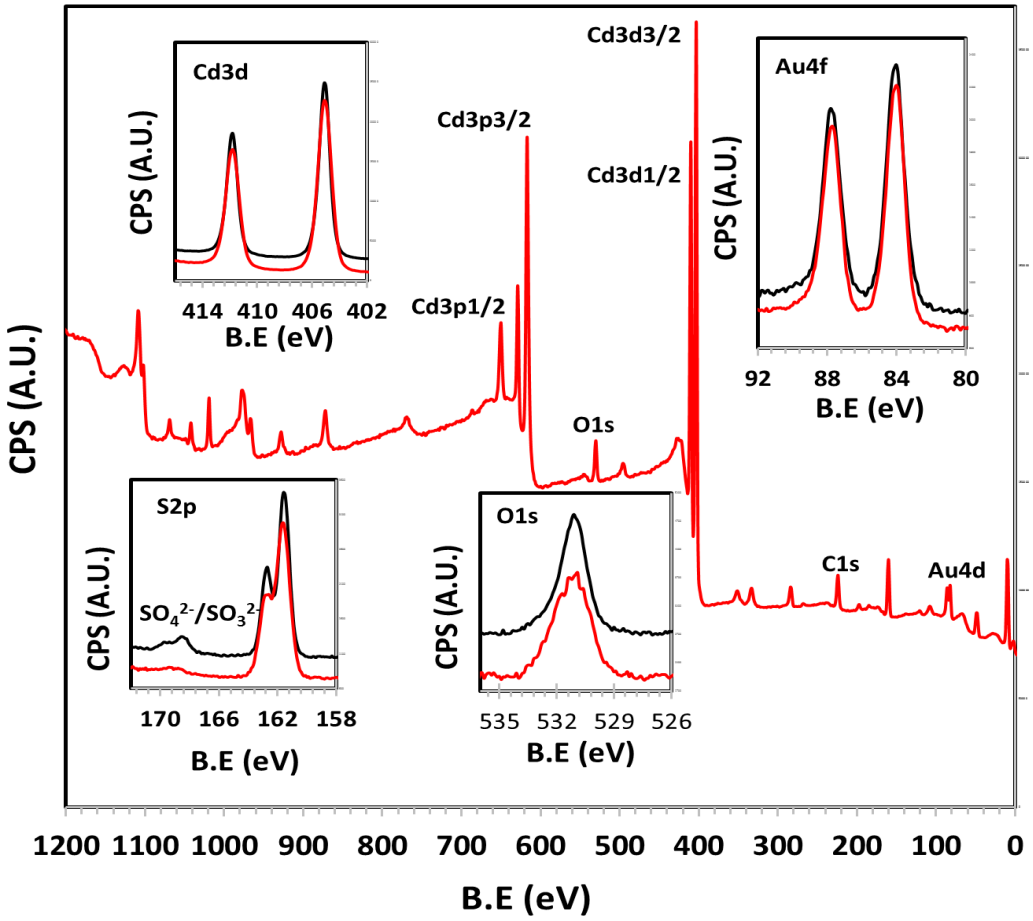

Figure 3.43: XPS analysis of 3 wt. % Au/h-CdS (KI) photocatalysts before (red) and after (black) H_2 generation experiments

Table 3.11: XPS data for the as-prepared cubic CdS, hexagonal CdS and 3wt.% Au/h-CdS-KI samples.

Core Level	Position (eV) and [FWHM (eV)]	
	As prepared	Used
$Cd3d_{5/2}$	404.8 [0.91]	404.8 [0.91]
$S2p_{3/2}$	161.8 [0.85]	161.8 [0.85]; 168.1 [0.95]
$Au4f_{7/2}$	84.1 [1.18]	84.1 [1.18]
O1s	531.2[1.73]	531.2 [1.87]

3.2.6 H_2 production photoreactions

Photocatalytic Hydrogen production was performed over various Au/CdS photocatalyts prepared by four different Au loading methods namely, incipient wet impregnation method (WI), deposition precipitation method (DP), photodeposition method (PD) and a newly developed method involving reduction of Au^{3+} ions by iodide ions using potassium iodide (KI), in ethanol water-electrolyte mixtures (0.1M Na_2S, 0.02M Na_2SO_3; pH = 13). The validity of the newly developed method in comprison to the other three conventionl methods was established. Photo-catalytic hydrogen production tests were conducted on both phases. The hexagonal phase was found active while the cubic phase was found almost inactive (results are not shown as the cubic phase showed very low activity and was considered almost inactive). It is reported that distortion in CdS_4 tetrahedron units results in the formation of an electronic dipole moment and internal electric field in hexagonal CdS crystal structure. The presence of such internal electric field is beneficial for the efficient separation and diffusion of photoinduced charge carriers. Contrarily, none of the CdS_4 distortion, internal electric field and electronic dipole moment is present in cubic CdS. This is one of the prime reasons why the hexagonal CdS is usually more active in photocatalytic performance than the cubic CdS. Moreover, the calculated charge carrier effective masses of hexagonal CdS are smaller than those of cubic CdS. The smaller effective mass of photoinduced charge carriers in hexagonal CdS facilitates the mobility, reduces the recombination rate and improves photocatalytic activity [692, 693]. This was further supported by even higher H_2 rates per unit surface area for hexagonal phase obtained at 800 °C compared to that obtained at 600 °C (not shown). Phase transformation can also be behind the considerable change in reaction rate. Such an increase in H_2 production rate has been noted in the case of TiO_2 for example where the anatase phase was found to be more active than the rutile phase [694].

Fig. 3.44 shows H_2 production performed over 1-5 wt. % Au loadings by the KI method over h-CdS from ethanol water-electrolyte mixtures. It was noted that a very high rate of H_2 production 10.5 mmol $h^{-1}g^{-1}$ was observed over photocatalyst at 3 wt.% Au loading because this loading produced maximum Au particles dispersion along with optimum Au particle size (4-6 nm) for maximum hydrogen production. Fig. 3.45 compares the H_2 production activity over a 3 wt. % Au/CdS photo-catalyst in ethanol, water-electrolyte and ethanol water-electrolyte mixtures. A weak H_2 production rate of ca. 1.38 mmol h^{-1} g^{-1} was found in pure ethanol or ethanol water system (volume ratio = 2:23), whilst no noticeable activity was observed in pure water (not shown due to extremely low hydrogen production rate as

compared to others). The rate of hydrogen production of ca. 10.80 mmol $h^{-1}g^{-1}$ with (8:92) ethanol water-electrolyte mixture was found which is about two times higher than that obtained with water electrolyte alone (the most studied reactant system for CdS photo-catalysts).

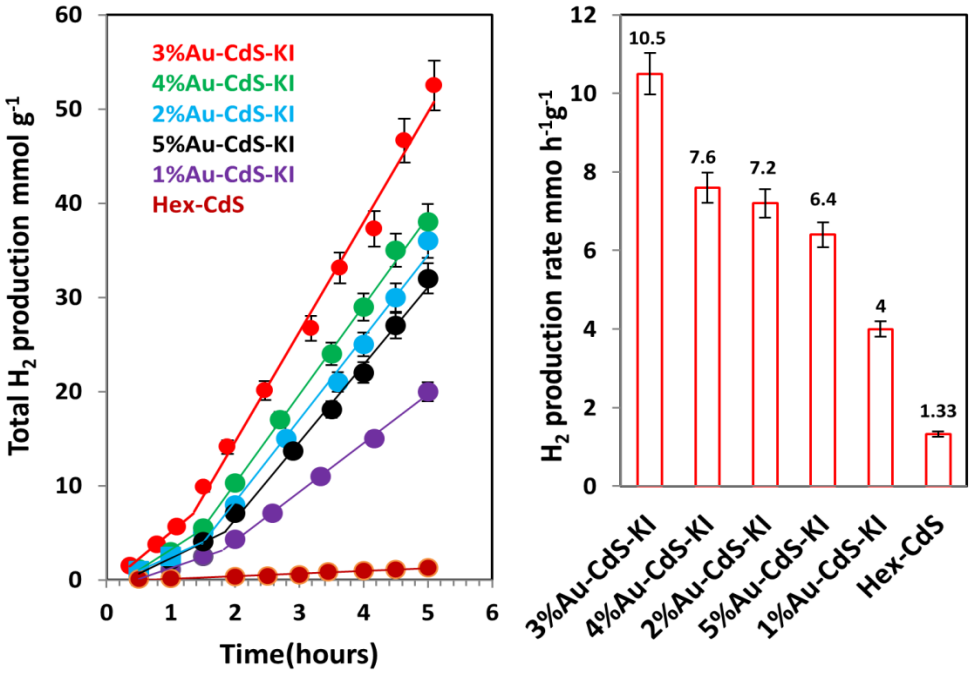

Figure 3.44: Comparison of the photocatalytic activities of h-CdS and 1-5wt. % Au/h-CdS-KI from (8:92) ethanol water-electrolyte mixtures.

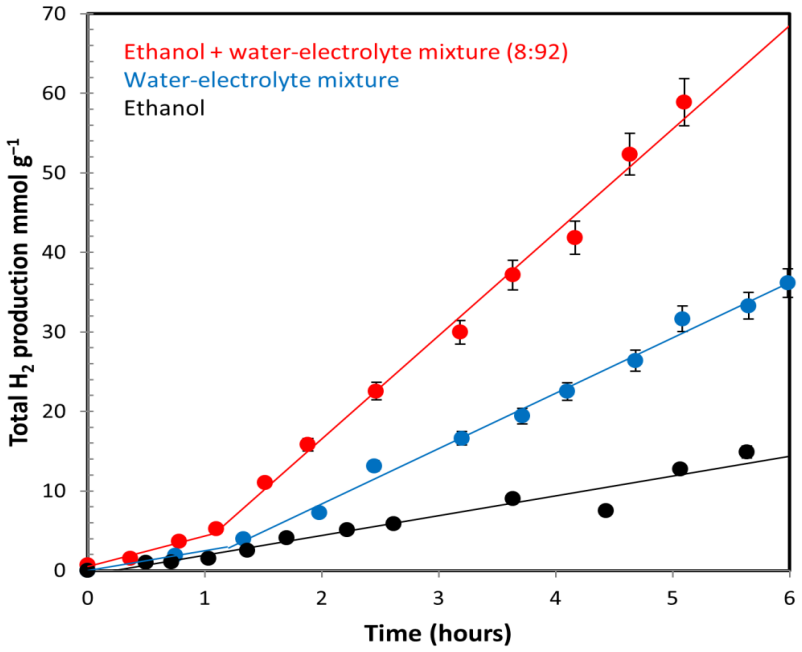

Figure 3.45: Photo-catalytic H_2 production over 3 wt. % Au/h-CdS using; ethanol, water-electrolyte and ethanol water-electrolyte system in (8:92) ratio.

It can be noted that Au enhances the rate of hydrogen production up to a 3 wt. % Au loading because photo-excited electrons in CdS under visible light are trapped by Au particles due to the lower fermi level and higher work function of Au as compared to CdS. These trapped electrons are further transferred to surface adsorbed H^+ to reduce them to H_2 [332]. Although this view has been challenged recently where the role of Au is proposed to only help in the hydrogen recombination rather than in electron trapping [111]. An increase in photo catalytic activity with increased Au loading might be related to the increase in the area of Au/CdS interface as indicated by Fig. 3.46 b. A decrease in activity with Au loading above 3 wt. % is observed. The decrease in photo catalytic hydrogen production with increasing metal deposition has been observed by many other workers for which no clear explanation is yet known [478-480, 608, 609]. This decrease in activity with Au loading beyond 3 wt. % was due to three reasons; on increasing the metal particle coverage, large fraction of the semiconductor surface may become unavailable for light absorption, increase in the surface defects at metal-semiconductor interface leading to an increase in electron-hole recombination centers and an increase in the particles size. H_2 production rate is drastically decreased by increasing the particle size as Subramanian and co-workers observed a 60 mV negative shift in flat band potential in 3 nm diameter Au particles as compared to 20 mV shift in 8 nm Au nanoparticles [695]. A negative shift in the Fermi level in composite photocatalytic system is an indication of better charge separation and more reductive power. A lower hydrogen production rate observed for Au loading below 3wt. % by the KI method was due to the production of fewer metal cathodic sites for proton reduction or atomic hydrogen recombination. The hydrogen production rates for 1-5 wt.% Au/CdS catalysts prepared by KI method are listed in Table 3.12. The third column contains the corrected XPS Au4f/Cd3d peak area ratios for Au/Cd. The last column shows the reaction rate in hydrogen molecules/(Au_{atom} s^{-1}) (considering that 1 m^2 contains ca. 5 x 10^{18} atoms of Cd or S).

Table 3.12: Rate of photo catalytic H_2 production and TOF (s^{-1}) from water-ethanol electrolyte mixtures over Au/h-CdS-KI as a function of Au loading

Au (wt. %)	Mean Au particle size (nm)	XPS Au 4f/ Cd3d (At. %)	H_2 production rate mmol $h^{-1}g^{-1}$	TOF H_2 production rate molecules Au^{-1}_{atom} s^{-1}
0	-	-	0.612	-
1	2.0±0.34	0.032	3.6	0.8
3	4.0±1.6	0.076	10.8	1
5	4.5±1.5	0.121	3.6	0.2

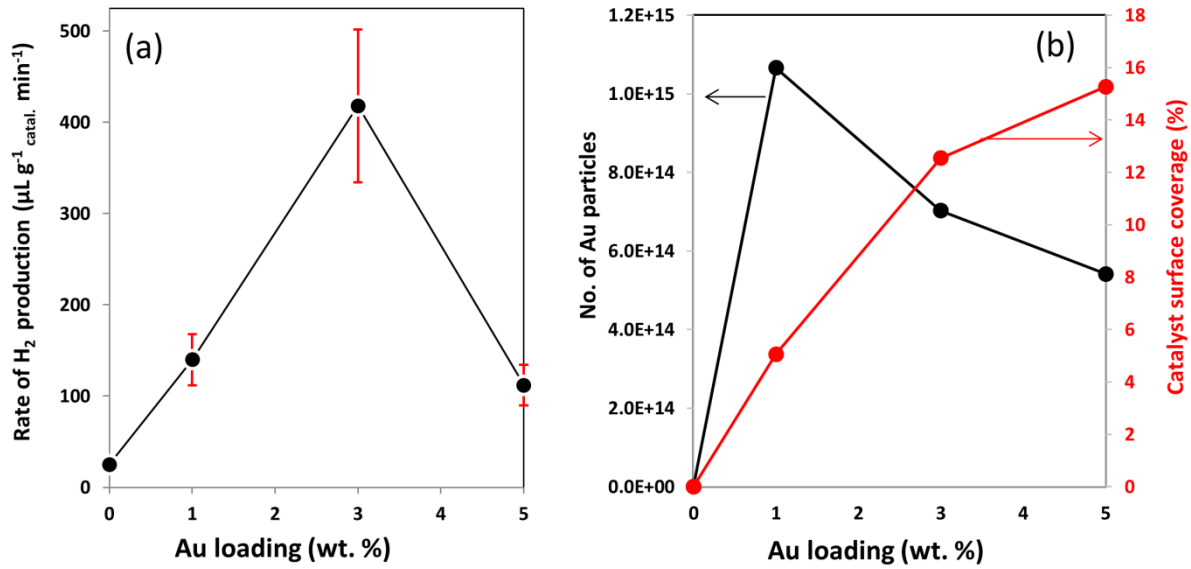

Figure 3.46: (a) Rate of photo-catalytic H_2 production from ethanol water-electrolyte mixture (8:92) over Au/h-CdS-KI as a function of Au loading (b) the total number of Au particles and % of catalyst surface area covered for 0.01 g of catalyst as a function of Au loading.

The number of Au atoms was calculated by multiplying XPS Au 4f/Cd 3d ratio (table 3.12 column 3) with total number of Cd or S atoms in a given surface area. The following formula was used to obtain TOF.

$$\text{Turn Over frequency (TOF)} = \frac{[H_2 \text{ rate (mol } g^{-1}s^{-1})] \times [\text{Avogadro's No.(Number of molecules mol}^{-1})]}{[\text{XPS } Au_{4f}/Cd_{3d} \text{ at. \% ratio}] \times [\text{BET surface area } (m^{-2}g^{-1})] \times [\text{Number of Cd or S atoms } (m^{-2})]}$$

Fig. 3.46 (a) shows the rate of H_2 production from an ethanol water-electrolyte mixture as a function of Au loading on h-CdS. In fig. 3.46 (b) the total number of Au particles were calculated from the mean size of Au particles present on Au/h-CdS using TEM images and the Au metal size (1.44 Å). Surface coverage was calculated from the area covered by each individual particle within a given distribution of metal particles normalized to total number of particles at each loading assuming that the area covered by single metal particle will be equal to the area inside its circumference [696]. Increasing the wt. % from 1 to 3% resulted in increasing the hydrogen production by about the same factor per unit mass. The nominal hydrogen production rate molecules per Au atom increased by ca. 25% (from 0.8 to 1.0 s^{-1}) while the surface coverage increased by 2.3 times [(0.076/0.032)]. Increasing the amount of Au did not substantially increase its dispersion but made larger particles instead (fig. 3.40). Still the increase of the rate with increasing Au wt. % together with increasing particle size

may indicate that on CdS, larger particles of Au (≈ 4-6 nm) are either as active as smaller particles (≈ 2-3 nm) or slightly more active (last column in table 3.12). This result may indicate that the role of Au might be (in addition to acting as electron sink) linked to the electric field generated upon illumination; due to its plasmonic resonance. In other words, the larger the particle size, the larger is the local electric field. Wang and co-workers very recently calculated that a local field enhancement factor $|E|^2/|E_o|^2$ of 5.3 can be obtained for Au/Fe_2O_3 system with Au particle size in 13-20 nm range with respect to Au particle size in 3.5-13 nm range [546]. This also indicates the absence of appreciable influence of hot electrons in the catalytic reaction as production of hot electrons is a dominant process for smaller nanostructures [548, 697, 698]. This interpretation might be in line with energy transfer (not electron transfer) scheme recently proposed [699] and is more in line with the role of metals in photo-catalytic hydrogen production where electron transfer occurs (if any) from the conduction band to the metal and not the other way around [111].

A TEM study of the 5 wt. % Au/h-CdS-KI photo-catalyst was undertaken to monitor the possible changes in the structure of the photo-catalyst during photoreaction (fig. 3.47). It was opted to monitor the activity of a 5 wt. % Au/h-CdS-KI instead of the 3 wt. % as it had larger particle size making structural analysis less prone to errors. The as-prepared 5 wt. % Au/h-CdS-KI photo-catalyst (fig. 3.47a) had Au particle size distribution in the 1-8 nm range. Au particle size increased with increasing irradiation time, reaching a maximum size of ca. 20 nm after 80 minutes (fig. 3.47b-d). After 90 minutes, steady H_2 production rate is obtained (fig. 3.44), after which the rate did not change significantly with continuous testing over a further 4.5 hours. Some of the catalysts were tested for longer periods of time to examine the effects of the sacrificial reagent concentration and surface corrosion. A decline in H_2 production rate was observed after 18 hours due to a decrease in sacrificial agent concentration by ca. 70-80% which in turn may have resulted in enhanced surface corrosion indicated by the enhanced roughness of CdS particles surface (image 3.47d). The tendency of smaller Au particles to form larger ones at the start of the reaction may be due to the strong absorption of incoming light by Au nanoparticles (plasmon resonance) due to their larger number and subsequent conversion of light energy into thermal energy. This results in an increase in the local temperature which in turn accelerates particle diffusion and leads to agglomeration [700]. The diffusion of Au on CdS single crystals has been noticed earlier and diffusion coefficient ($D = 3.33 \times 10^{-20}$ m^2s^{-1}at 300 ^oC) has been calculated [701].

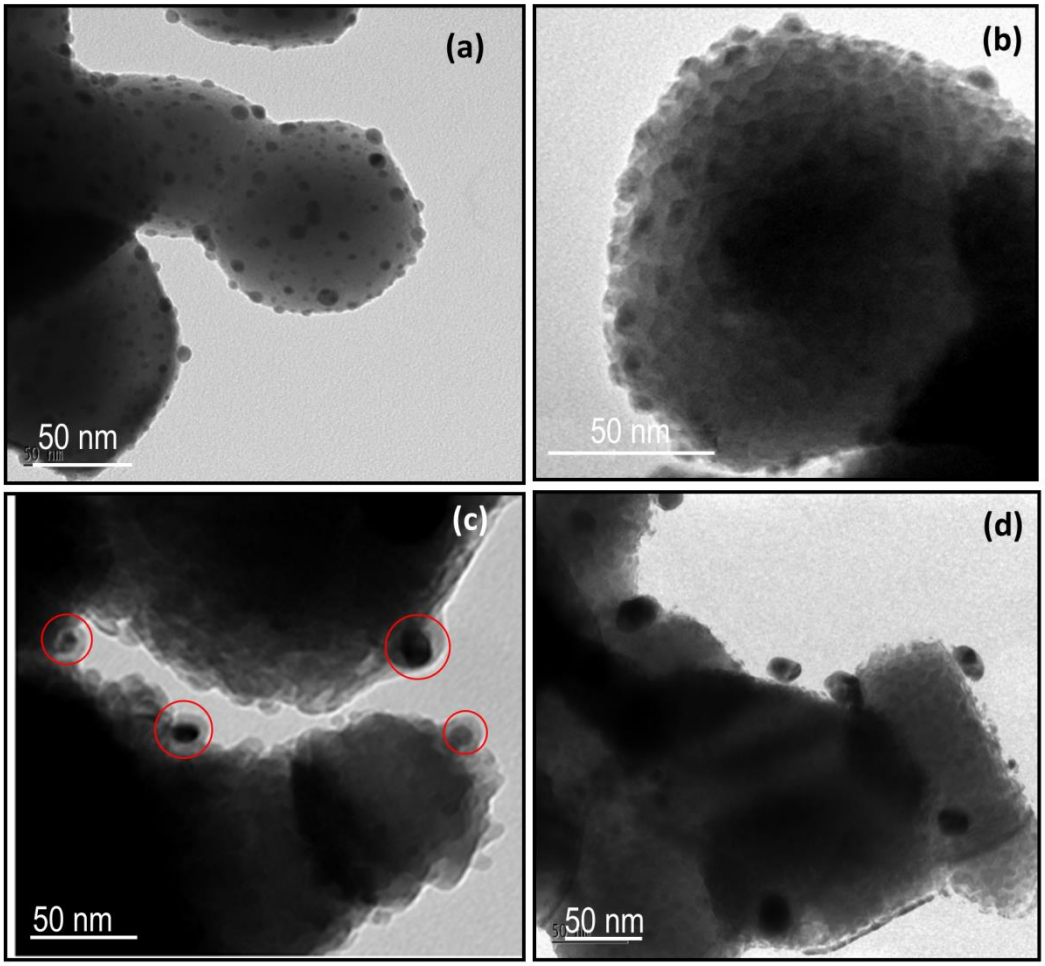

Figure 3.47: TEM images of 5 wt. % Au/h-CdS-KI photo-catalyst at various stages of the photoreaction; (a) before photoreaction, after (b) 30 minutes, (c) 90 minutes and (d) 24 hours. Au nanoparticle size increases with increasing irradiation time.

As the reaction proceeds, an increase in light absorption by CdS itself due to a decrease in the Au particles density is expected. This results in enhanced probability of electron-hole pair generation. The electrons in the conduction band of CdS migrate onto Au particles, after some specific time ca. 70-90 minutes, equilibrium is established and a constant rate of hydrogen production is observed, as indicated in Fig. 3.44. This observation is in line with the results obtained as a function of a catalyst amount (fig. 3.48). With a fixed irradiation intensity and reactor configuration, a longer induction time will be expected as the catalyst amount is increased i.e. more photo-catalyst means more photons will need to be supplied before light-induced surface aggregation of Au nanoparticles reach an equilibrium stage and a steady state reaction condition is achieved. The decreased hydrogen production in the PD and

DP methods is due to initial large Au particles size that increases further during photoreactions.

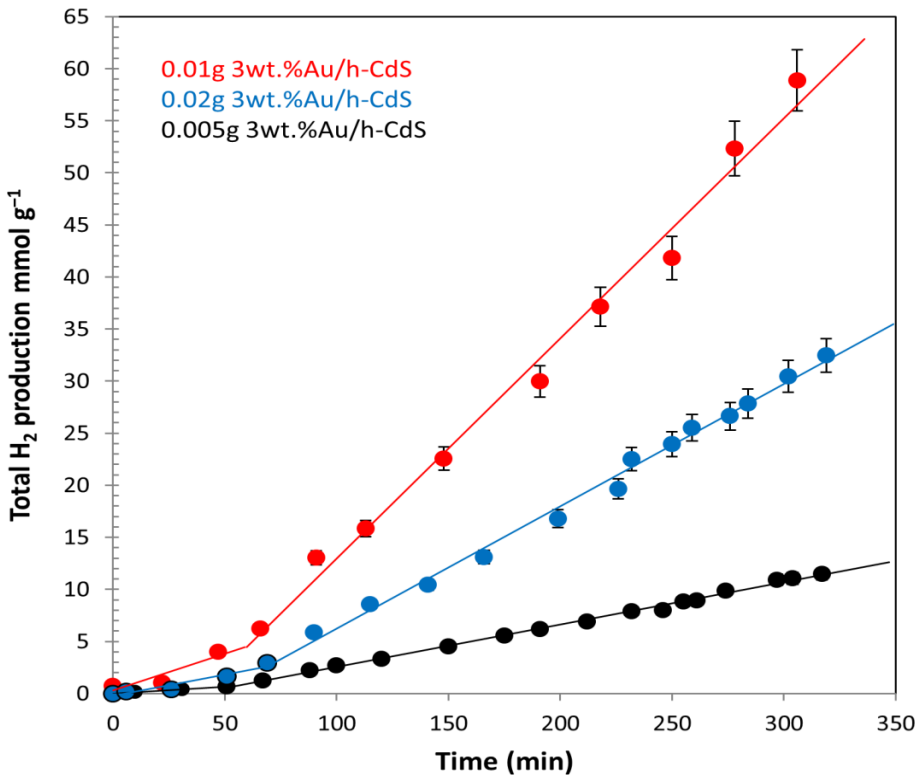

Figure 3.48: Photo-catalytic hydrogen production from ethanol water-electrolyte (0.1M Na_2S, 0.02M Na_2SO_3; pH = 13) over 3 wt. % Au/h-CdS with different catalyst amounts; 0.005g, 0.01g and 0.02g.

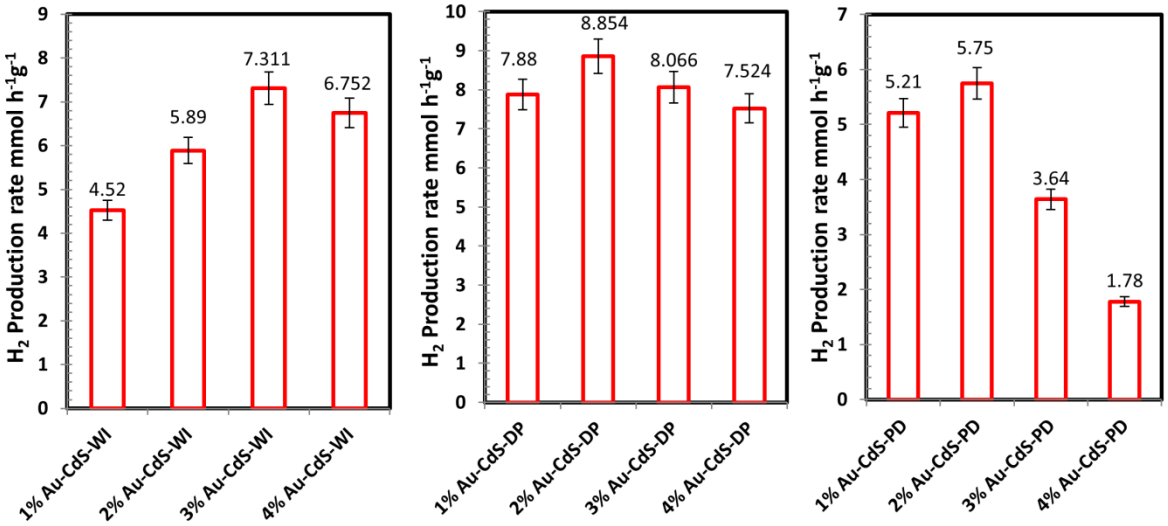

Figure 3.49: Comparison of the photocatalytic activities a) 1-4wt. % Au loading over h-CdS by WI, DP and PD methods for H_2 production from ethanol water-electrolyte mixture.

Hydrogen production rate as a function of Au loading amount for the other three Au loading methods are listed in fig. 3.49. The deposition precipitation and photodeposition methods showed maximum hydrogen production at 2 wt. % rather than 3 wt. % Au loading amount as in KI method due to maximum amount of Au deposition in these two methods as indicated by XRF and ICP results. Hydrogen production amount over 2 wt% loadings in the PD and DP methods is still less than 3 wt. % Au loading by the KI method.

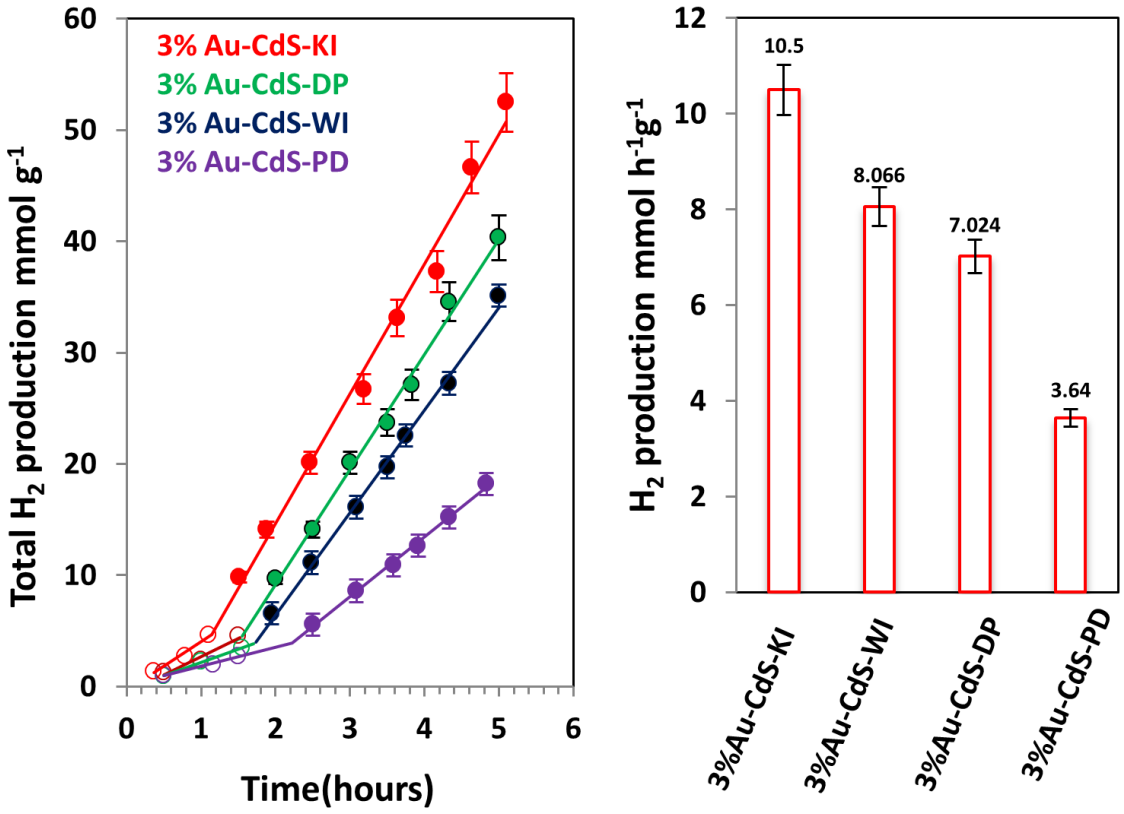

Figure 3.50: Comparison of the photocatalytic activities among 3% wt. Au/h-CdS-KI, 3 wt. % Au/h-CdS-DP, 3 wt. % Au/h-CdS-WI and 3 wt. % Au/h-CdS-PD photocatalysts for H_2 production from ethanol water-electrolyte mixture.

Fig. 3.50 shows hydrogen production over 3wt. % Au/CdS photocatalysts prepared by KI method and three other conventional Au loading methods. It was observed that conventional deposition precipitation methods (DP) generated less hydrogen 8.85 mmol $h^{-1}g^{-1}$ and 8.07 mmol $h^{-1}g^{-1}$ at 2 and 3 wt.% Au loading respectively. As discussed earlier in TEM studies (fig. 3.38) that DP methods produced nonhomogeneous Au particles, very small particles of ca. 2 nm and larger particles of 8-9 nm, this non homogeneity of Au particles dispersion might be responsible for lower hydrogen production. Despite of very small Au particles ca. 2 nm the wet impregnation method (WI) produced 7.024 mmol $h^{-1}g^{-1}$ hydrogen less than DP

method most likely due to lower overall Au loading of 2.4 ±2 wt. % as determined by XRF analysis (Table 3.13). Finally, the PD method produced hydrogen far less than all deposition methods 3.64 mmol $h^{-1}g^{-1}$. It is clearly seen in TEM images that this methods produced larger Au particles (5-6 nm) over the CdS support, allowing for lower H_2 production per unit weight of Au loading. It is interesting to note that Au particles deposited by the PD method showed maximum plasmonic effect (fig. 3.41b) but the lowest hydrogen production of all photocatalysts. Despite of offering a strong SPR effect in the visible region, the larger Au nanoparticles offer little surface for the adsorption of H^+ ion recombination. This observation indicates that optimization among particle size and plasmonic effect is necessary for enhanced hydrogen production in CdS. These results suggest that the contribution of SPR in H_2 production enhancement is very small in the case of Au/h-CdS photocatalysts.

Table 3.13: Mean particle sizes and rates of H_2 production in ethanol water-electrolyte system over Au/h-CdS prepared by four different methods. BET surface area 5 ± 0.5 m^2.

Loading method	Mean Au particle size	Total wt. % Au loading		BET surface area	Total H_2 production in 5 hours	H_2 production rate $mmolh^{-1}g^{-1}$
		(XRF)	(ICP-OES)			
Iodide reduction (KI)	3.5 ± 0.5	2.5 ± 0.3	2.4 ± 0.5	4.92	52.5	10.5
Incipient wet impregnation (WI)	1.8 ± 0.5	2.4 ± 0.2	2.2± 0.5	4.96	35.1	7.02
Deposition precipitation (DP)	2.3 ± 0.5	2.7 ± 0.3	2.7± 0.3	4.65	40.03	8.06
Photo-deposition (PD)	6 ± 1	2.8 ± 0.2	2.7± 0.3	4.56	18.2	3.64

The activity and stability of most active catalyst 3 wt. % Au/h-CdS-KI was investigated in ethanol water-electrolyte (0.1M Na_2S, 0.02M Na_2SO_3; pH = 13) mixtures. As can be seen from Fig. 3.51, a stable photocatalytic hydrogen production was observed over the duration of the experiments (16 hours). The slight decrease in rate with time (<10% for forth run) was due to the deposition of photocatalyst particles on reactor walls, thus affecting the incoming radiations and a decrease in sacrificial reagents concentration by ca. 70–80% which in turn may have resulted in enhanced surface corrosion. However, if the concentration of the sacrificial reagents is maintained, no considerable change in catalytic activity is noticed on its re-use.

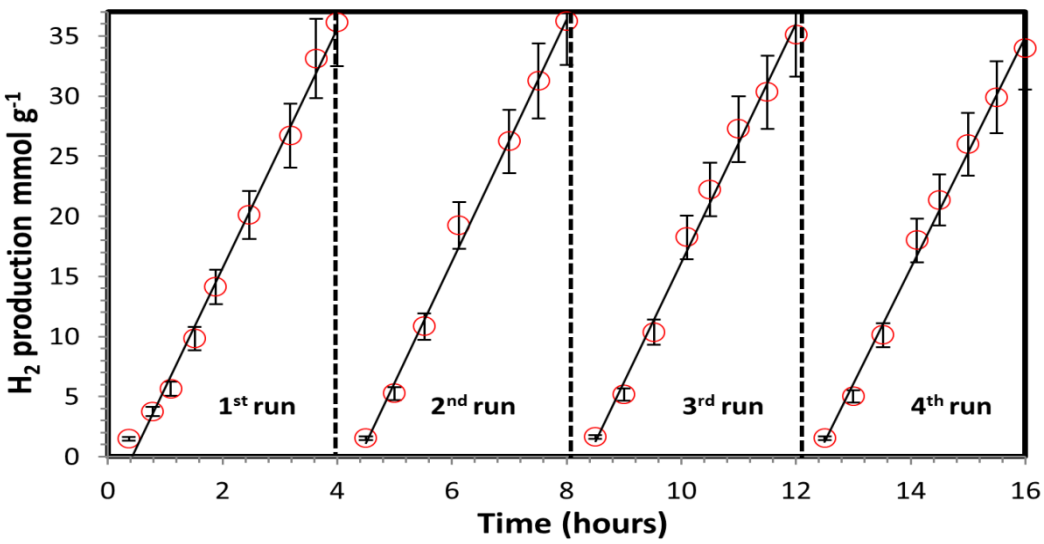

Figure 3.51: Cyclic H_2 production on 3 wt. % Au/h-CdS-KI photocatalysts using ethanol water-electrolyte mixtures.

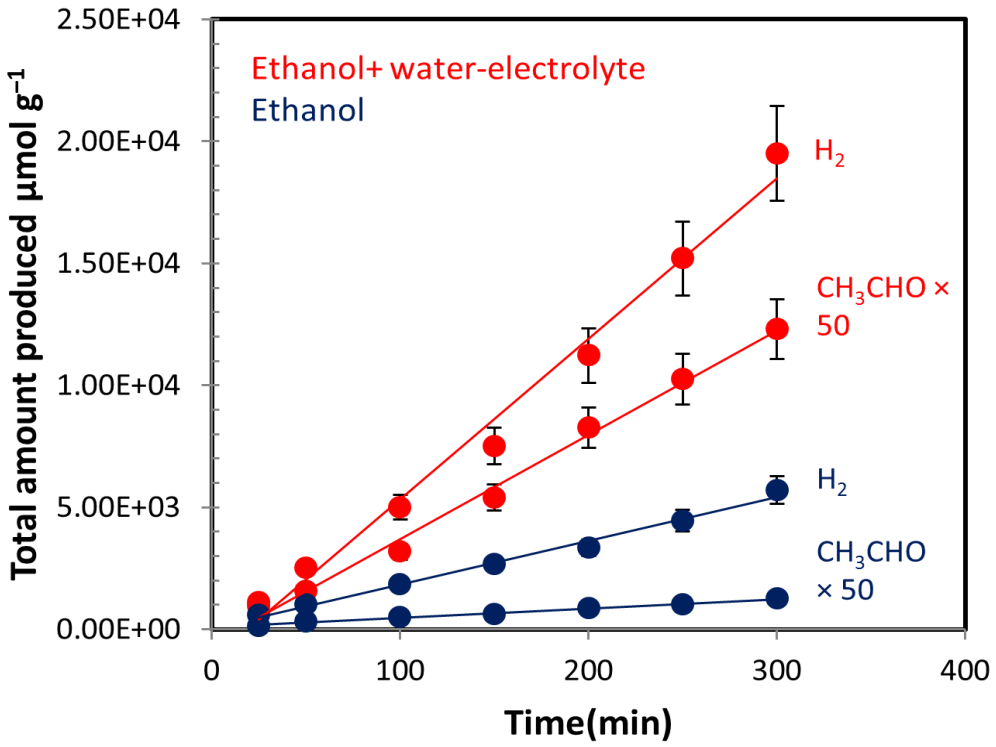

Figure 3.52: Photocatalytic H_2 and acetaldehyde production from 8% ethanol-92% water electrolyte mixture (0.1M Na_2S, 0.02M Na_2SO_3; pH = 13) and ethanol over 0.5 wt.% Au/h-CdS-KI.

3.2.7 Hydrogen production mechanism

The increased hydrogen production rates over various Au/h-CdS photocatalyst prepared by four different methods from ethanol water-electrolyte mixture (0.1M Na_2S, 0.02M Na_2SO_3;

pH = 13) compared to water electrolyte alone (the most studied reactant system for CdS photo-catalysts) can be explained by the reaction mechanism shown in Fig. 3.53. During the first step, the H_2O molecule is dissociated on the Cd–S surface to produce adsorbed Cd–OH and S–H species (step 1). Upon irradiation, electrons are promoted to the conduction band leaving holes in the valence band (step 2). A chemical reaction is initiated due to the reaction of aqueous S^{2-} ions (S^{2-}/S_2^{2-}; E = −0.14 eV versus NHE at pH = 7 [702] with the valence band holes indicated by step 5 (E = + 1.7 eV versus NHE at pH = 7 [703]. Subsequently, some of the electrons in the conduction band are trapped by Au particles on the surface (step 3) or migrated to the surface of CdS. These electrons are poised to reduce surface adsorbed H^+ to H_2 (step 4). In addition surface OH groups adsorbed on Cd atoms can react with the holes in the valence band to produce °OH radicals (step 6a) [89]. The CdS surface can be regarded mainly as comprising of nonpolar (1120) and (1010) faces, both of which have an equal number of Cd and S atoms [704-706]. Ethanol may react with these °OH radicals to produce α-hydroxyethyl radical and protonate the adsorbed OH to produce water (step 6b). Ethanol may also react directly with the holes to give the same intermediate and a proton. This α-hydroxyethyl radical (E = +1.38 at pH = 7 eV versus NHE [93]) further reacts with a hole in the valence band to produce acetaldehyde and a proton (step 7). These protons produced are converted to gaseous hydrogen by the trapped electrons on Au (step 4). There was negligible reaction for Au/CdS in water or ethanol under visible light irradiation (fig. 3.45). This implies that the first step is the reaction of valence band holes with the sulfide sacrificial agent enabling conduction band electrons to migrate onto Au particles or the surface of CdS and react with surface H^+ to give H_2. However, the α-hydroxyethyl radical produced also acts as a hole scavenger once the reaction has started, thus producing acetaldehyde and H^+ ions. This results in increased hydrogen production rates and consequently reduces the amount of sulfide sacrificial agent consumed. Acetaldehyde production in the gas phase was monitored and presented in fig. 3.52. It is worth noting that acetaldehyde is a reaction intermediate as it will (like most oxygen containing organic compounds) react to give further products that ultimately result in CO_2 (the final thermodynamic compound for organic oxidation). The reaction of gas phase acetaldehyde was studied under photo-irradiation over TiO_2 (110) single crystal [707], TiO_2 powders [708] but we are not aware of reported reaction on CdS in alkaline environment. One of the properties of acetaldehyde is its fast oxidation to acetate/acetic acid in the presence of oxygen. It has previously been shown that acetates/acetic acid react on TiO_2 via the photo-Kolbe reaction to give CH_4, C_2H_6 and CO_2 [709, 710]. These products were looked for in this

work but were not found. The low miscibility of CH_4 and C_2H_6, and their relative stability in the liquid phase at room temperature would make their detection possible if they are formed. In other words, their absence in the gas phase indicates that this pathway is not favoured on CdS at the present experimental conditions. Yet for CO_2 the situation is more complex because of its high solubility in the alkaline medium. This high solubility, associated with the expected small concentration, is probably the reason why it is not seen in the gas phase. Most likely the reaction would follow a photo-reforming, which is analogous to thermal reforming ($CH_3CHO + 3H_2O \rightarrow 5H_2 + 2CO_2$) and this would explain the increase in hydrogen production rate.

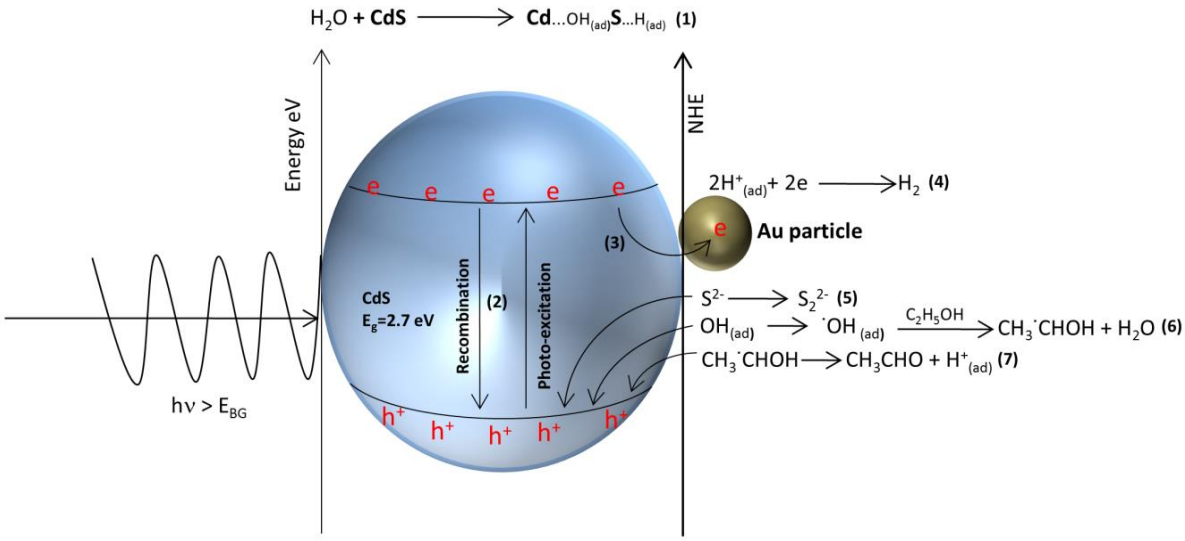

Figure 3.53: Schematic representation of the mechanism for hydrogen production from ethanol–water electrolyte mixture over Au/ h-CdS photocatalysts.

3.2.8 Conclusions

From the above results and discussion it can be concluded that nanosized CdS particles can be prepared by sol-gel method and subsequently calcined under air and inert atmosphere of nitrogen with the aim to get highly crystalline and photocatalytically active hexagonal CdS phase for hydrogen production. The crystallinity of the h-CdS photocatalyst can be monitored by PXRD. A decrease in the FWHM of 0.5 eV for Cd3d and 0.4 eV for S2p for the highly crystalline semiconductor is noticed due to an increase in the core hole life time in the crystalline phase. Au nanoparticles were deposited over hexagonal CdS by three conventional methods including; deposition precipitation (DP), incipient wet impregnation (WI), photo-deposition (PD) and a novel reductive deposition method (KI) to develop catalysts with

different overall Au loading and particle size distribution, despite of same initial nominal loading. Subsequently these photocatalysts were used as model compounds to study the effect of metal deposition method on the Au particle size and distribution. The effect of reaction medium on hydrogen production over Au/h-CdS photocatalyts prepared by KI method from ethanol water-electrolyte mixture was also thoroughly elaborated. The reductive deposition (KI) method produced Au nanoparticles with mean particle sizes between 2 nm to 5 nm by changing the initial nominal Au wt.% (from 1 to 5). The optimum rate for hydrogen production was found over 3 wt.% Au/CdS photocatalyst prepared by the KI reduction method that yielded Au particles with mean particle size of 4 nm with relatively lower experimentally determined Au loading (2.5 ± 0.3 wt. %) as compared to PD and DP methods. Prolonged photocatalytic reaction time over 0.5 wt.% Au/h-CdS-KI resulted in an increase in particle size up to 20 nm without a noticeable decrease in catalytic reactivity. Despite of very small Au particles (2-3 nm) the Au/h-CdS prepared by the WI method produced lower hydrogen production than the KI method due to lower experimentally determined Au loadings. Non-homogeneity and larger Au particle size were produced in the DP and PD methods respectively and were responsible for lower hydrogen production. This work supports the electron transfer mechanism from semiconductor to metal, which may further be facilitated by metal to semiconductor energy transfer mechanism due to Au surface plasmon resonances. It is interesting to note that Au/CdS photocatalyst showing higher plasmonic effect does not always produce more hydrogen in the visible spectral range. These results clearly suggest that optimization among particle size distribution, overall wt. % loading and plasmonic effect is required for enhanced performance. The addition of ethanol to the electrolyte (Na_2S/Na_2SO_3) further increased the production of hydrogen via additional use of holes by α-hydroxyethyl radical from the valence band of CdS, allowing for more H^+ to be reduced by the capture of electrons.

3.3 g-C_3N_4 based photocatalysts

Low visible light absorption efficiency and a high rate of photogenerated charge carrier recombination are the two major problems encountered in graphitic carbon nitride (*g*-C_3N_4) based photocatalysts for hydrogen production from water in the presence of other renewables. In the present work, Pd-Ag bimetallic as well as monometallic nanoparticles were decorated on graphitic carbon nitride photocatalysts by a simple chemical reduction method and evaluated for their ability to produce H_2 during water splitting reaction. High activity of Pd-Ag/*g*-C_3N_4 photocatalyst was attributed to the inherent property of palladium metal to quench

photogenerated electrons by the schottky barrier mechanism and strong silver absorption in the visible range by surface plasmon resonance mechanism (SPR). The physical and photophysical characteristics of the as-prepared Pd-Ag/*g*-C_3N_4 photocatalysts were studied by X-ray diffraction (XRD), UV-visible diffuse reflection spectroscopy (DRS), Transmission electron microscope (TEM), X-ray photoelectron spectroscopy (XPS) and steady state photoluminescence. The $Pd_{0.7}$-$Ag_{0.3}$/*g*-C_3N_4 photocatalyst with overall 1 *wt.* % metal loading showed very high H_2 evolution activity (1250 µmol $h^{-1}g^{-1}$), 1.5 and 5.7 times higher than Pd/*g*-C_3N_4 and Ag/*g*-C_3N_4 photocatalysts, respectively. Photocatalysts showed high stability upto continues 16 hours runs. A possible mechanism for enhanced hydrogen production over Pd-Ag/*g*-C_3N_4 due to increased visible light absorption and electron-hole recombination quenching is proposed.

3.3.1 PXRD and UV-visible diffuse reflectance analysis

PXRD patterns were used to determine the sample phase. Fig. 3.54a represents the PXRD patterns of melamine, *g*-C_3N_4 prepared at 520 °C and Pd-Ag loaded *g*-C_3N_4. The diffraction peaks of *g*-C_3N_4 at 2θ values of 13.1° and 27.4° confirm the presence of graphitic like structure. The strong diffraction peak observed at 2θ = 27.4° (002) for both *g*-C_3N_4 and Pd-Ag/*g*-C_3N_4 is characteristic of interlayer stacking of aromatic systems similar to melon like networks [711]. Peak sharpness indicates close packing of *g*-C_3N_4 and strong interlayer binding. The peak at 13.128° (210) is assigned to in-planar ordering of tri-s-triazine units. The absence of any diffraction patterns for Pd and Ag suggests that metal nanoparticles are highly dispersed over the support and low loading also makes the metal particles identification difficult. The average crystallite size determined for the *g*-C_3N_4 from PXRD data using Scherrer equation is approximately ~25 nm.

To get further insight into the bimetallic nature of cocatalysts, the PXRD patterns of Ag_5/g-C_3N_4, Pd_5/g-C_3N_4 and $Pd_{3.5}$-$Ag_{1.5}$/g-C_3N_4 composite photocatalyst with overall 5 wt. % loadings prepared under similar experimental conditions are shown in fig. 3.54b. PXRD patterns of Ag_5/g-C_3N_4 shows the main diffraction patterns at 39.8 and 47.1 due to Ag^0 (111) and Ag_2O (220) planes and Pd_5/g-C_3N_4 has main patterns at 33.8, 41.2, 54.9 and 60.5 due to PdO (101), Pd^0(111), PdO(112) and PdO(103) planes. All these patterns are replicated in the PXRD patterns of composite $Pd_{3.5}$-$Ag_{1.5}$/g-C_3N_4 without any shift. However, clear sharpening of Ag^0 (111) peak and appearance of new peak at 46.2 due to Ag^0 (200) plane and absence of any diffraction peaks due to Ag_xO_y clearly indicates the increased reducibility of Ag in

bimetallic particles. The average crystallite size determined for the *g*-C_3N_4 from PXRD data using Scherrer equation is ca. 25 nm.

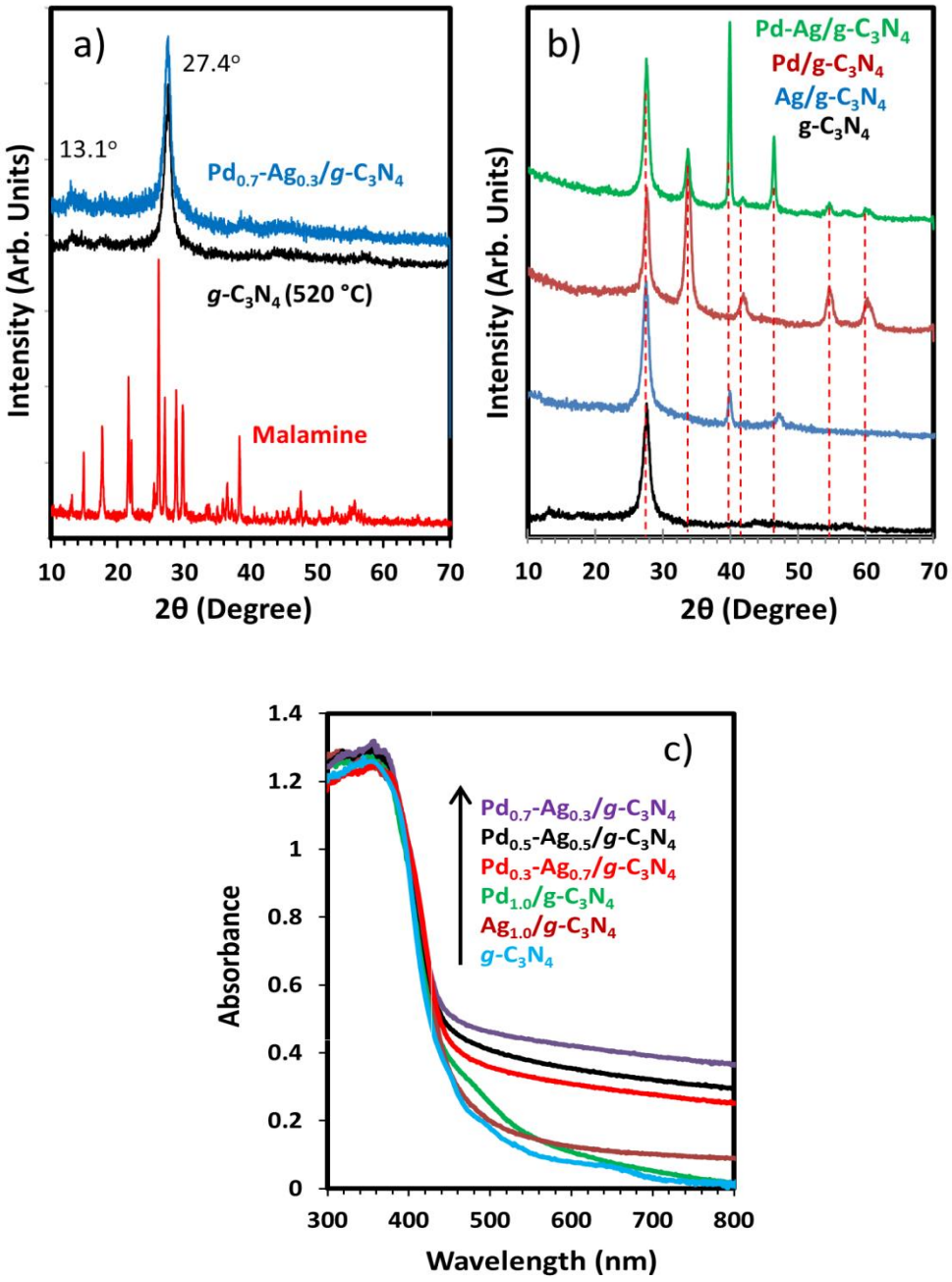

Figure 3.54: (a) PXRD patterns of melamine, *g*-C_3N_4-520 °C and $Pd_{0.7}$-$Ag_{0.3}$/*g*-C_3N_4. (b) PXRD patterns of *g*-C_3N_4-520 °C, $Pd_{3.5}$-$Ag_{1.5}$/*g*-C_3N_4 Pd_5/*g*-C_3N_4 and Ag_5/*g*-C_3N_4 with overall 5wt. % metal loading c) UV-visible diffused reflectance spectra of *g*-C_3N_4, Ag_1/ *g*-C_3N_4, Pd_1/ *g*-C_3N_4 and various Pd_x-Ag_y/ *g*-C_3N_4 photocatalyts.

The optical properties of as-prepared *g*-C_3N_4, $Pd_{1.0}$/*g*-C_3N_4, $Ag_{1.0}$/*g*-C_3N_4 and Pd_x-Ag_y/*g*-C_3N_4 photocatalysts were probed by using UV-visible diffused reflectance spectra (DRS) and

shown in fig. 3.54c. The pristine *g*-C_3N_4 sample, which has a pale yellow colour, shows absorbance at 461 nm, corresponding to a band gap of 2.7 eV, indicating comparatively limited visible light utilization ability. The steepness of the absorbance curve indicates that this absorption is attributed to the band gap electronic transitions. Metal nanoparticles show strong absorption all the way upto 800 nm extending into the strong intrinsic *g*-C_3N_4 absorption due to surface plasmon resonance (SPR) as well as d-d transitions of both metals. This effect was much more pronounced as compared to individual metal deposition. It must be noted that Ag nanoparticles of similar size as observed in this study exhibit SPR at 410-480 nm, however, it can shift over a wide range of wavelength depending upon their size, shape and refractive index of the surrounding medium [117, 712]. In the present study instead of strong plasmon peak of silver nanoparticle an extended absorption in the visible region was observed. The absence of this peak strongly confirmed that Ag particles are small and uniformly dispersed as a result of which their SPR peak might be buried in the strong g-C_3N_4 absorption [712]. Pd metal always shows extended absorbance in the visible range up to 650 nm [713]. On loading both Pd and Ag nanoparticles, a striking visible light absorbance was observed due to positive electronic synergism among Pd, Ag and *g*-C_3N_4 support. On depositing Pd and Ag nanoparticles the colour of *g*-C_3N_4 changed to grey which enormously increased the visible light absorption by conspicuous band gap reduction of 0.2 eV. The Pd-Ag nanoparticles loaded g-C_3N_4 clearly exhibits much stronger light absorption in visible region as compared to individual Pd and Ag supported g-C_3N_4 indicating the formation of bimetallic nanoparticles in addition to monometallic particles. In summary, the DRS results show that the simultaneous deposition of Pd and Ag metals could highly improve photocatalytic ability of g-C_3N_4 by expanding its visible light absorption range.

3.3.2 HRTEM and XPS analysis

HR-TEM analyses of the photocatalysts were performed to investigate the morphology, size and structures of composite photocatalysts. The pristine g-C_3N_4 sample displays an aggregated morphology showing large size and the layer structure of g-C_3N_4 (fig. 3.55a). The HR-TEM images at low and high magnifications indicate the presence of highly dispersed metal nanoparticles on the *g*-C_3N_4 Fig. 3.55(c-e). Fig. 3.55d is showing a conspicuous interface between support and metal nanoparticles clusters. The uniformly dispersed metal nanoparticles on g-C_3N_4 surface develop an intimate contact with *g*-C_3N_4 and facilitate charge transfer between metal nanoparticles and semiconductor support. Careful inspection of metal nanoparticles sizes revealed three kind of metal particles including ~8-10 nm

bimetallic, ~3-5 nm Ag monometallic and sub nanometeric Ag monometallic particles. The existence of bimetallic Pd-Ag nanoparticles (~8-10 nm) can be validated by carefully measuring the lattice parameters. Two different kinds of lattice fringes with crystal spacing equal to 0.236 nm and 0.225 nm can be ascribed to face centred cubic Ag (111) and Pd (111) crystallographic planes, respectively. The existence of bimetallic as well as monometallic nature was further confirmed by energy dispersive spectroscopy (EDS) analysis when electron beam was focused on each of these particles individually (fig. 3.55e). Similar metal particle composition and size distribution has been observed and reported in detail on TiO_2. The deposition of mono and bimetallic nanoparticles highly improves the visible light absorbance (DRS) as well as photocatalytic activity (photoreactions).

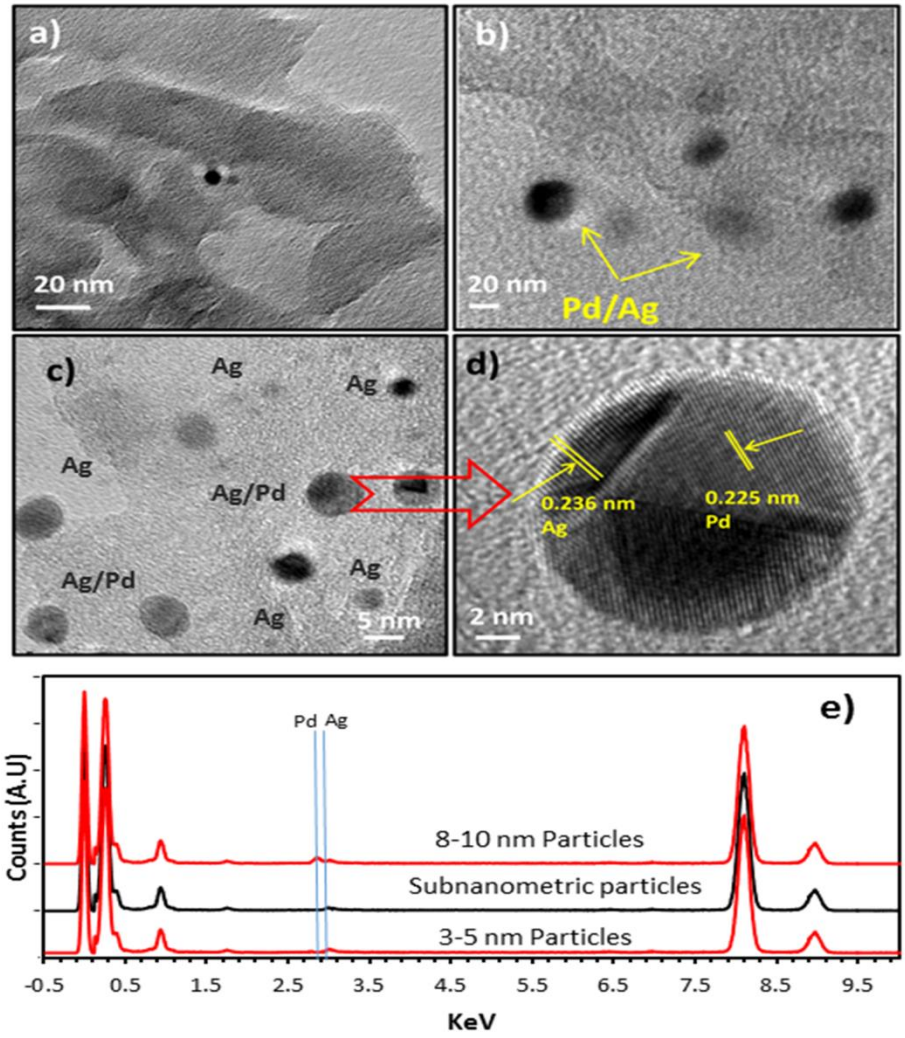

Figure 3.55: High resolution transmission electron microscopy (HR-TEM) images of $Pd_{0.7}$-$Ag_{0.3}$/g-C_3N_4 photocatalysts at low and high magnification (a-d) and Energy Dispersive spectroscopy analysis of metal nanoparticle from figure d (bottom).

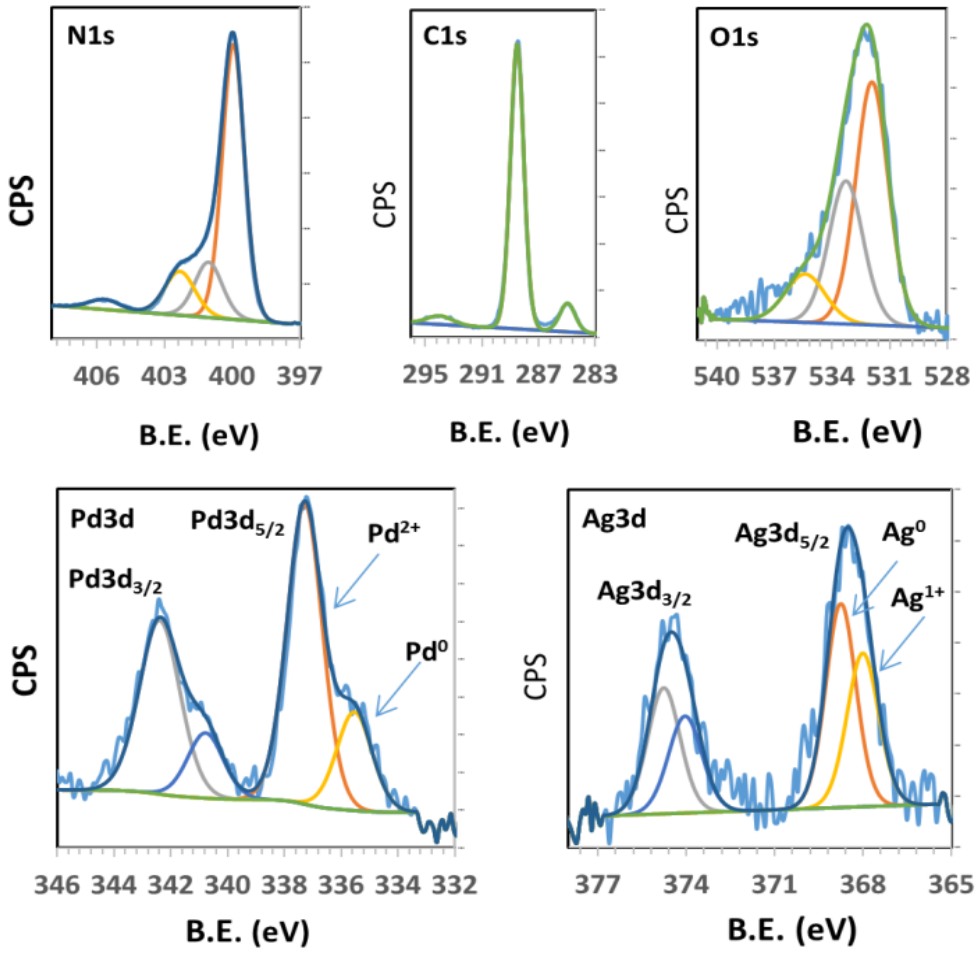

Figure 3.56: XPS results of fresh bimetallic $Pd_{0.7}$-$Ag_{0.3}$/g-C_3N_4 photocatalyst.

XPS analysis was conducted to elucidate the surface structure of *g*-C_3N_4 and chemical states of Pd and Ag. The C1s can be fitted for three distinct peaks at 285, 288.5 and 294 eV. The first peak can be attributed to adsorbed carbon and defect containing sp^2-hybridized carbon atoms present in graphitic domains. The second dominant peak at 288.5 eV belongs to sp^2-hybradized carbon in *g*-C_3N_4 lattice [714]. Third peak at 294 eV binding energy is assigned to π-excitation [715]. The N1s XPS peaks can be deconvoluted into four peaks centered at 399.9, 401.1, 402.3 and 405.7 eV. The predominant peak at a binding energy of 399.9 eV is attributed to the sp^2-hybridized nitrogen atoms in triazine rings, which dominate g-C_3N_4 structure [569, 716]. The peak at about 401.1 eV is assigned to the tertiary nitrogen N–$(C)_3$ [715]. The peak at 402.3 eV indicates the presence of amino functional group (C–N–H), which might be related to the structural defects and incomplete condensation in the polymerization process [716]. The additional weak peak at 405.7 eV could be ascribed to π-excitation [714]. All these peaks are shifted to higher binding energy values as compared to bare g-C_3N_4 indicating a strong interaction of Pd-Ag with the support. The two peaks at

approximately 368.6 and 374.7 eV can be attributed to $Ag3d_{5/2}$ and $Ag3d_{3/2}$, respectively. These two peaks can be further deconvoluted into two peaks, at about 368/368.7 eV and 374/ 374.8 eV, respectively. The peaks at 368 and 374 eV are attributed to Ag^{1+} of Ag_2O (44.2%), and those at 368.7 and 374.8 eV are ascribed to the metal Ag^0. This is in line with the earlier studies where Ag in higher oxidation states has been observed to possess lower binding energies as compared to metallic Ag [717]. These results indicate that Ag is present mainly as Ag^0 [712]. Furthermore, the Pd 3d spectra of $Pd_{0.7}$-$Ag_{0.3}$/g-C_3N_4 could be fitted into asymmetric peaks, suggesting the existence of two states of Pd species. The Pd $3d_{5/2}$ peak at 335.5 eV and Pd $3d_{3/2}$ peak at 340.8 eV are attributed to the metallic Pd^0, where the binding energy peaks shown at 337.3 and 342.4 eV are originated form of Pd^{2+}, respectively. XPS results clearly indicate that the reducibility of Ag is increased due to close proximity of Pd over g-C_3N_4 under present conditions suggesting the bimetallic nanoparticles formation in addition to monometallic particles in line with UV-Vis and XRD results [718, 719].

Table 3.14: XPS analysis of bimetallic $Pd_{0.7}$-$Ag_{0.3}$/g-C_3N_4 photocatalyst.

Element	Core level	Position (eV)	FWHM	% Elem. Comp	Speciation
C	C1s	285.0	1.3	43.3	9.8
	C1s	288.5	1.1		85.3
	C1s	294.0	2.1		4.9
N	N1s	399.9	1.1	52.6	65.7
	N1s	401.1	1.4		16.6
	N1s	402.3	1.6		14.3
	N1s	405.7	1.6		3.4
Pd	$Pd3d_{3/2}$	337.3	1.5	0.35	75.2
	$Pd3d_{1/2}$	342.4	1.7		
	$Pd3d_{3/2}$	335.5	1.5		24.8
	$Pd3d_{1/2}$	340.8	1.6		
Ag	$Ag3d_{3/2}$	368.7	1.2	0.09	60.0
	$Ag3d_{1/2}$	374.8	1.3		
	$Ag3d_{3/2}$	368.0	1.3		44.2
	$Ag3d_{1/2}$	374.0	1.3		
O	O1s	531.9	2.0	3.3	53.4
	O1s	533.3	2.1		33.4
	O1s	535.4	2.4		13.1

3.3.3 H_2 production photoreactions

The photocatalytic hydrogen production activities of various photocatalysts were evaluated in 10 vol.% triethanolamine (TEOA)-water mixture under visible light irradiations. Fig. 3.57 displays the H_2 production over different photocatalysts. The pure *g*-C_3N_4 sample without

metal particle loading showed negligible hydrogen production ability due to higher recombination rates of photogenerated charge carriers. After introducing each 1 wt% of Pd and Ag over g-C_3N_4 the hydrogen production was suddenly increased to 840 and 220 µmmol $h^{-1}g^{-1}$ respectively. Recently Pd is emerging as a very active co-catalyst for hydrogen production even more than Au and Pt. The enhanced activity of Pd as compared to its rivals might be related to its following properties. 1) Its maximum dispersion on semiconductor surface and optimized Schottky barrier formation [720]. 2) It has higher density of states in the vicinity of the semiconductor fermi level as compared to Pt and Au. The fermi level of Pd is around 0.2 eV higher than the Fermi level of Pt (-10.8 eV) [721]. 3) Pd also has much lower electron affinity and hence electron trapping capability which may enable facile electron transfer from Pd to proton [168]. Silver can increase the H_2 production rate due to enhanced visible light absorption related to its strong surface plasmon effect. It was observed in the present study that on increasing the silver loading in Pd-Ag nanoclusters a decrease in the hydrogen production rate was seen while an increase in the Pd loading increases the rate. This trend can be attributed to higher catalytic activity of Pd than Ag for H_2 production reaction, mainly due to the appropriate Schottky barrier among other factors. However, this trend is disrupted for $Pd_{0.3}$-$Ag_{0.7}$/g-C_3N_4 photocatalyst which gave a maximum H_2 production rate (1250 µmol $h^{-1}g^{-1}$) even greater than $Pd_{1.0}$/g-C_3N_4 (840 µmol $h^{-1}g^{-1}$). This indicates that apart from electron trapping via Schottky barrier formation, some other mechanism is operative. The highest rate obtained at $Pd_{0.7}$-$Ag_{0.3}$/g-C_3N_4 is due to positive synergism achieved by enhanced visible light absorption by Ag plasmonic mechanism and photoexcited electrons trapping by Pd Schottky enhanced mechanism.

Fig. 3.58a represents the effect of overall metal loading amount over *g*-C_3N_4. A maximum hydrogen production rate was achieved at an overall nominal metal loading amount of 1 wt.%. A slight decrease in hydrogen production activity at 1.5 wt. % loading was observed and after that a sharp decrease in activity was observed for 2 to 3 wt. % loadings. This decrease in activity by increasing metal loading has been observed by many others; however, no clear explanation for this is given yet. This decrease in activity might be due to the increase in the opacity of photocatalyst samples which decreases the light transmission to the support. Higher metal loadings can also result in increased surface defects at the metal–semiconductor interface, leading to an increase in e^-/h^+ recombination centers. Lower amounts of hydrogen production were also observed at 0.5 wt. % loading. This is because the generation of less number of active metal sites over *g*-C_3N_4 for proton reduction or hydrogen recombination. As a consequence, a suitable content of Pd-Ag nanoparticles is crucial for

optimized photocatalytic performance of Pd-Ag/*g*-C_3N_4 photocatalysts. To gain insight into the electron scavenging ability of different cocatalysts, steady-state photoluminescence (PL) of *g*-C_3N_4, $Pd_{1.0}$/g-C_3N_4, $Ag_{1.0}$/g-C_3N_4 and $Pd_{0.7}$-$Ag_{0.3}$/g-C_3N_4 samples were conducted and the results are presented in Fig. 3.58b. It can be observed that $Pd_{1.0}$/*g*-C_3N_4 exhibits lowest PL intensity. This clearly indicates that Pd metal is highly active in trapping photo-excited electron present in the conduction band of the *g*-C_3N_4. Conversely, there is less difference in PL intensities of g-C_3N_4 and $Ag_{1.0}$/*g*-C_3N_4. This shows that Ag is not as active for electron trapping as Pd. The photocatalyst $Pd_{0.7}$-$Ag_{0.3}$/g-C_3N_4 is also showing good electron trapping behaviour but less than $Pd_{1.0}$/g-C_3N_4. These results indicate that electron trapping is not the only factor to enhance hydrogen production rate at least over metal supported *g*-C_3N_4 under present conditions.

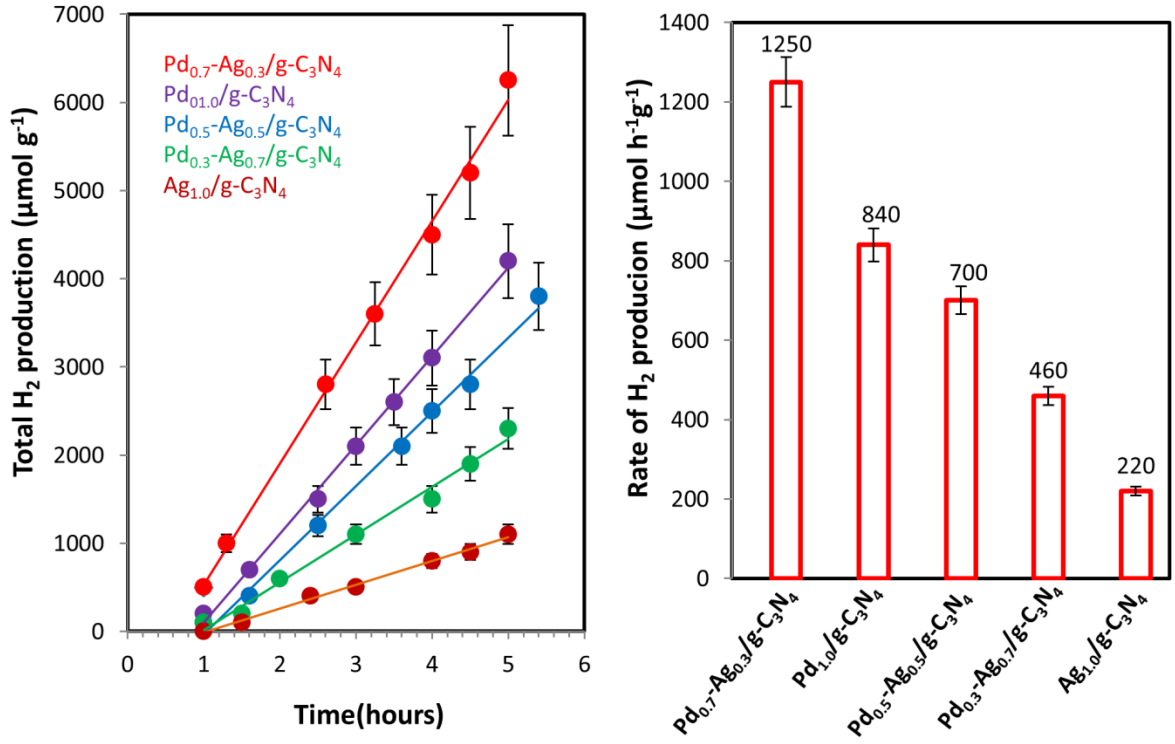

Figure 3.57: Comparison of H_2 production over $Pd_{1.0}$/g-C_3N_4, $Ag_{1.0}$/g-C_3N_4, $Pd_{0.7}$-$Ag_{0.3}$/g-C_3N_4, $Pd_{0.5}$-$Ag_{0.5}$/g-C_3N_4, $Pd_{0.3}$-$Ag_{0.7}$/g-C_3N_4 photocatalyst from 10 vol% triethanolamine-water mixtures.

The activity and stability of $Pd_{0.7}$-$Ag_{0.3}$/*g*-C_3N_4 photocatalyst was investigated in 10 vol. % triethanolamine-water mixture. As can be seen from Fig. 3.59, stable photocatalytic hydrogen production was observed over the duration of the experiments (16 h). The slight decrease in rate with time was due to the deposition of catalyst particles on the reactor walls with time,

thus scattering away the incoming light radiation and also due to decrease of triethanolamine concentration as sacrificial reagent.

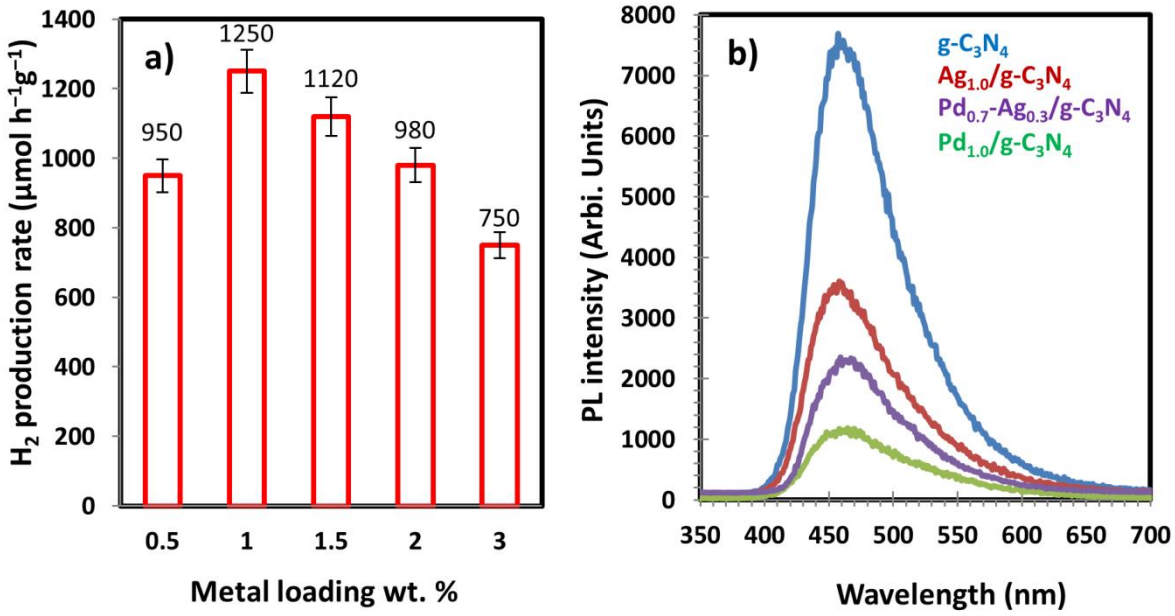

Figure 3.58: (a) Effect of metal loading amount on H_2 production in 10 vol.% triethanolamine-water mixtures (b) steady state photoluminescence (PL) measurements.

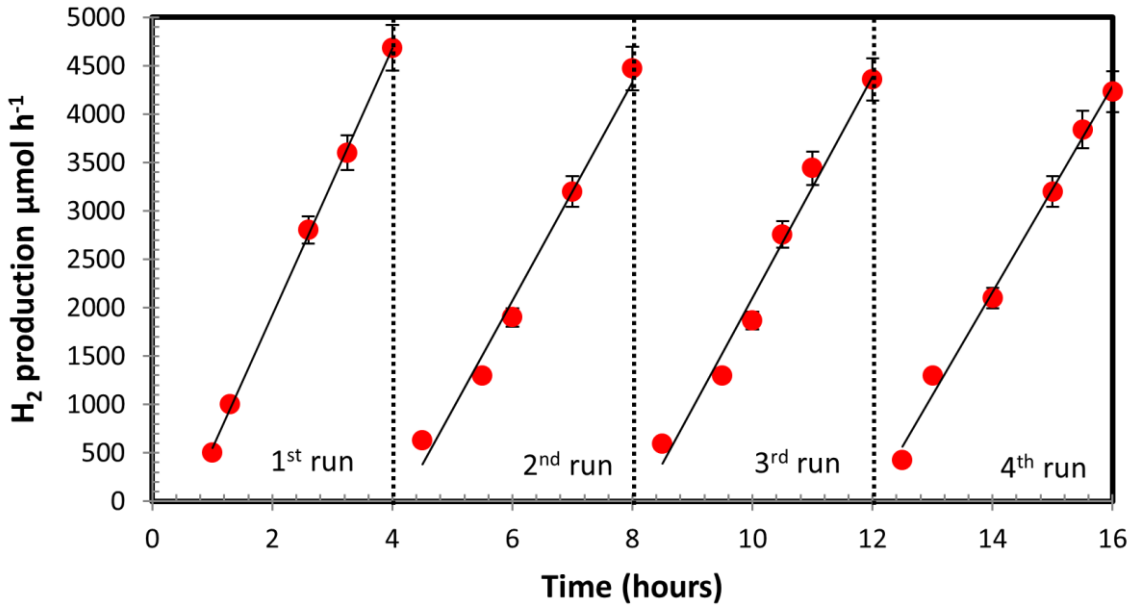

Figure 3.59: Cyclic runs for the hydrogen production experiments with $Pd_{0.7}$-$Ag_{0.3}$/g-C_3N_4 catalysts using 10 vol% triethanolamine-water mixtures.

In order to further probe into the effect of visible light harvesting and electron scavenging abilities of $Pd_{0.7}$-$Ag_{0.3}$/*g*-C_3N_4 photocatalysts, rhodamine B dye degradation experiments were

carried under direct solar irradiations for fixed time intervals of 70 min. The absorption spectra were collected in 400-600 nm range during the monitoring process. For comparison, the performances of pure g-C_3N_4, $Ag_{1.0}$/g-C_3N_4 and $Pd_{1.0}$/g-C_3N_4 photocatalyst were also investigated under similar conditions (Fig. 3.60a). It was observed that the photocatalytic activity of pristine g-C_3N_4 for rhodamine B degradation is very little due to the absence of electron transfer site to generate$O_2^{-\cdot}$, a photocatalytically active species for rhodamine B dye degradation. There is a great debate in literature about the nature of active species for dye degradation over semiconductor photocatalyst. However, most of the studies depicted superoxide radicles as an active species for rhodamine B degradation. Again $Pd_{0.7}$-$Ag_{0.3}$/*g*-C_3N_4 photocatalyst showed the superior activities for dye degradation as compared to monometallic counterparts.

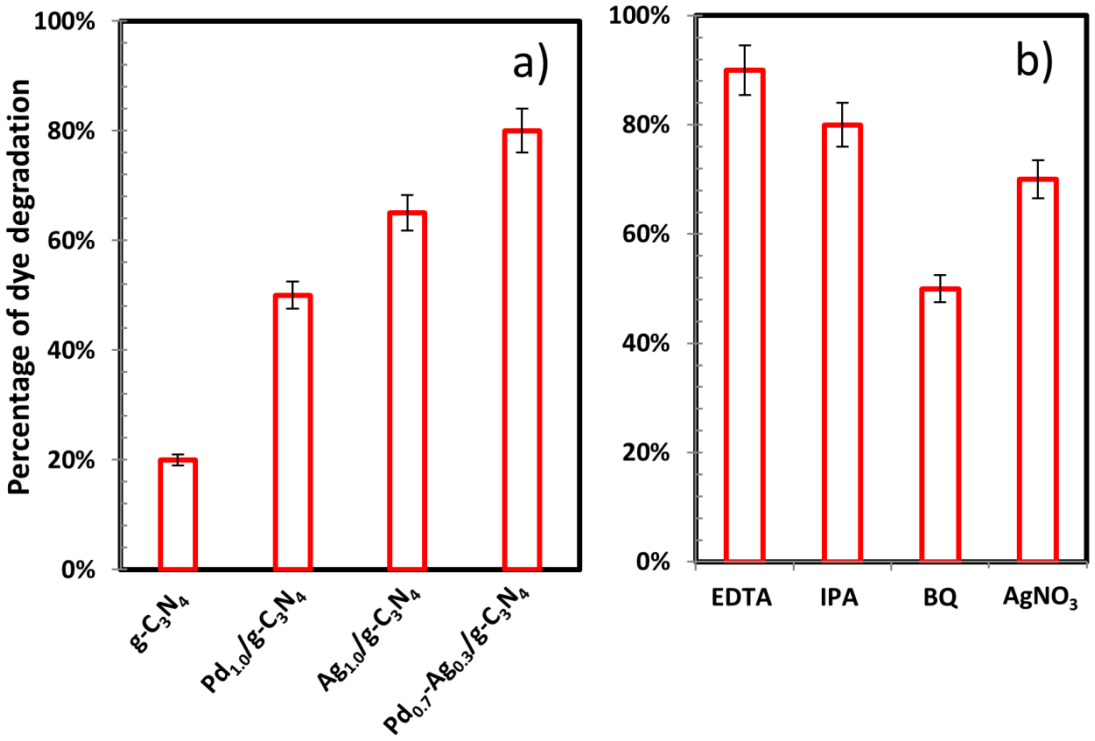

Figure 3.60: Rhodamine B dye degradation over different mono and bimetallic photocatalyst for 70 min irradiation time b) effect of active species scavengers for dye degradation over $Pd_{0.7}$-$Ag_{0.3}$/g-C_3N_4 photocatalyst during 70 min of degradation time.

In present study, different scavengers were also employed to detect active species; 50 mM isopropanol (IPA) (as a OH^- quencher), 50 mM $AgNO_3$ as an electron quencher, 50 mM benzoquinone (BQ) as a $O_2^{-\cdot}$ quencher and 50 mM ethylenediamine tetraacetic acid (EDTA) as a holes quencher (Fig. 3.60b). The photocatalytic degradation of rhodamine B is not

affected by the addition of isopropanol (IPA) while the degradation is quenched drastically in the presence of benzoquinone (BQ) and partially due to $AgNO_3$. Therefore, it can be concluded that the superoxide anions ($O_2^{-\cdot}$) and electrons are the main reactive species generated by the photocatalysts for dye degradation under sunlight irradiation. In the presence of Na_2EDTA, a hole scavenger, the rate of dye degradation was even higher than those of obtained without any scavenger. A plausible explanation for this is that in the presence of hole scavenger more electrons will be available for formation of superoxide radicals. These results suggest that role of OH^- radicals or h^+ is negligible in this degradation process while electrons/superoxide radical are the main active species. So, the highest activity of $Pd_{0.7}$-$Ag_{0.3}$/g-C_3N_4 as compared to $Pd_{1.0}$/g-C_3N_4 and $Ag_{1.0}$/g-C_3N_4 is explained on the same rationale that supports hydrogen production. Pd is more active for electron transfer from the conduction band of g-C_3N_4 to generate superoxide radicals whereas Ag is mainly associated to increase the electron population in the g-C_3N_4 by visible light absorption as well as by hot electron transfer and energy transfer surface plasmon effect.

3.3.4 Hydrogen production Mechanism

Based on characterization results, unique optical properties, very efficient visible light hydrogen production and rhodamine B degradation on bimetallic photocatalysts, a possible mechanism for photocatalytic H_2 production is proposed and illustrated in Fig. 3.61. Upon visible light irradiation, e^-/h^+ pairs are generated in the polymeric semiconductor g-C_3N_4. However, these photoinduced e^-/h^+ are likely to recombine without any metal co-catalyst. The enhanced rate of H_2 evolution over $Pd_{0.7}$-$Ag_{0.3}$/g-C_3N_4 can be attributed to synergistic effect between Pd-Ag nanoparticles. By introducing Pd-Ag nanoparticles in optimized amounts, two concurrent factors operate synergistically. One of the major drawbacks of g-C_3N_4 is that it absorbs very limited amount of visible light (< 515 nm). The Ag nanoparticles present in nanoclusters, in addition to acting as hydrogen production cathodic sites, mainly scavenging the visible light by surface plasmon effect that can result from direct energy transfer (DET), resonant energy transfer (RET) as well as field effect. On the other hand Pd-Ag present in the nanoclusters mainly quenches the recombination rate by accepting the conduction band electrons. At the same time, holes in the valence band of g-C_3N_4 are consumed by triethanolamine (TEOA) sacrificial regent. Therefore, the e^-/h^+ recombination process is effectively prohibited by the presence of Pd-Ag and visible light absorption efficiency is

enhanced by Ag SPR effect, resulting in improvement of H_2 production for the Pd-Ag/g-C_3N_4 photocatalyst.

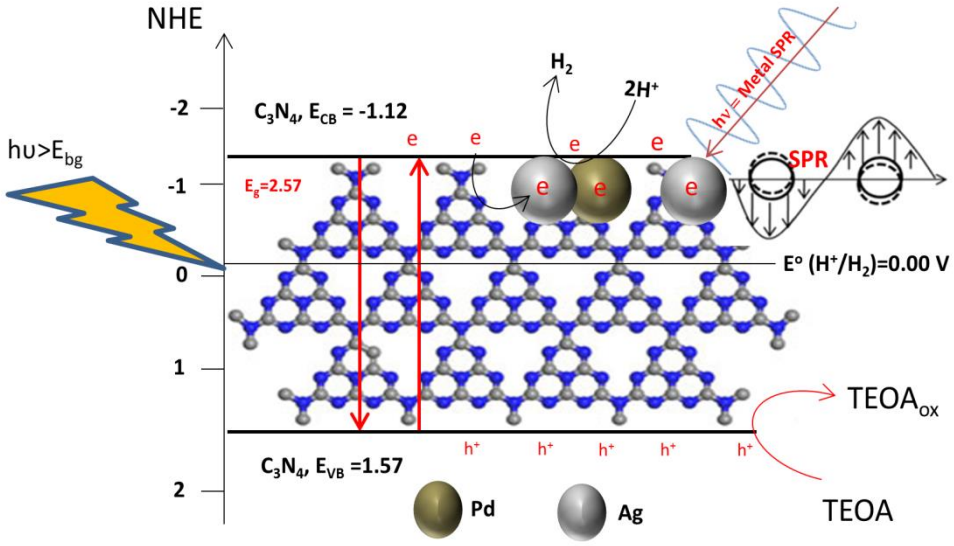

Figure 3.61: Schematic illustration of the hydrogen production and charge transfer in $Pd_{0.7}$-$Ag_{0.3}$/g-C_3N_4 photocatalysts under visible light irradiations.

3.3.5 Conclusions

The present work addressed the two main issues of g-C_3N_4, i) limited visible light absorption and ii) high recombination rate of photoinduced charge carriers in photocatalytic water splitting reaction. The Ag and Pd co-catalysts were successfully deposited over g-C_3N_4 by simple chemical reduction method. The UV-VIS, HRTEM and XPS studies revealed that both metals are mainly present in the form of mono- as well as bimetallic nanoparticles. The Ag as monometallic nanoparticles extends the visible light absorption by surface plasmon effect while Ag-Pd bimetallic nanoparticles decrease the e-/h+ recombination rate by forming highly rectifying schottky barrier with appropriate height. The $Pd_{0.7}$-$Ag_{0.3}$/g-C_3N_4 photocatalyst with overall 1 wt. % metal loading showed very high H_2 evolution activity (1250 µmol $h^{-1}g^{-1}$), 1.5 and 5.7 times higher than Pd/g-C_3N_4 and Ag/g-C_3N_4 photocatalysts, respectively. Photocatalysts showed high stability up to continuous 16 h run. A possible mechanism for enhanced hydrogen production over Pd-Ag/g-C_3N_4 due to increase in visible light absorption and electron-hole recombination quenching is proposed.

3.4 Summary of work

The main focus of present study was to fabricate economical, highly stable and efficient photocatalysts for hydrogen production from water in the presence of other renewable (water in the presence of methanol, ethanol, glycerol, triethanol amine and inorganic electrolytes). The work has been started with the synthesis of highly crystalline TiO_2 nanorods with different phase compositions and surface area by the calcination of hydrogen titanate ($H_2Ti_3O_7$) precursors obtained by treating P25 (TiO_2) hydrothermally in 10 M NaOH followed by washing with HCl solution. The nanorod aggregates prepared at 130 °C showed maximum surface area of ca. 148 m^2/g that decreases with the further increase in the reaction temperature. Hydrothermal reaction at a temperature greater than 130 °C resulted in destruction of lamellar $Na_2Ti_3O_4$, an intermediate in the nanorod formation process. Among the nanorod series prepared, nanorods prepared at 130 °C and calcined at 400 °C showed very high hydrogen production rates after depositing bimetallic hydroxides by co-deposition-precipitation (total metal loading ~ 1 wt.%). The hydrogen production activity of nanorods was then compared with typical TiO_2 support P25 (80% Anatase + 20% rutile). Both $0.8Cu(OH)_2$-$0.2Ni(OH)_2$/P25 and $0.8Ni(OH)_2$-$0.2Cu(OH)_2$/TNR_{130}-400 photocatalysts demonstrated very high hydrogen production rates (10 & 26.6 mmol $h^{-1}g^{-1}$) in 20 vol. % ethanol-water mixture and (22 & 35.1 mmol $h^{-1}g^{-1}$) from 5 vol.% glycerol-water mixtures, respectively. Detailed analyses based on reaction kinetics, photoluminescence, XPS and charge carrier scavenging suggest that both working catalysts are composed of Cu and Ni atoms in the metallic phase. Cu^0 is produced directly by the transfer of electrons from the conduction band of TiO_2 to the surface of $Cu(OH)_2$ nano-clusters, whilst Ni^0 is formed indirectly through a process of gradual dissolution of $Ni(OH)_2$ to yield aqueous Ni^{2+} due to the acidic environment of the medium, followed by Ni^{2+} reduction by the electron from the conduction band of the semiconductor. The high rates of H_2 production matches with those obtained from noble metals based photocatalysts can be explained by the following rationale. An oxidized Ni atom in contact with a Cu atom may become reduced due to a considerably less negative ΔG^o of Cu oxide formation (-129 kJ mol^{-1}) when compared to that of Ni oxide formation (-430 kJ mol^{-1}). This may increase hydrogen production due to the possibility of an increase in metallic character of Cu. This work suggests that bimetallic Cu-Ni catalysts formed on 1D TiO_2 nanorods are promising alternatives to noble metals for hydrogen production. Following this work, a new strategy was introduced to produce highly dispersed Cu-Cu_2O nanoparticles over TiO_2 by using a metal organic framework (MOF) as a templating agent. The TiO_2-MOF composite was prepared by hydrolysing titanium

isopropoxide precursor over MOF nanoparticles by a solvothermal method, followed by the calcination of the composite at temperatures in the range of 350-500 °C. It was found that the photocatalyst Cu-Cu_2O/TiO_2-400 prepared by calcining the TiO_2-MOF composite at 400 °C showed maximum activity for hydrogen production from 5% glycerol-water mixture. The activity of the photocatalyst was further augmented by the formation of Cu^0 from Cu_2O reduction by photoexcited conduction band electrons in TiO_2. Hydrogen production activity was sharply decreased by further increasing the composite calcination temperature 400-500 °C due to the oxidation of Cu-Cu_2O to CuO and subsequent growth of CuO to larger particle size by sintering. Photocatalyst Cu-Cu_2O/TiO_2 -350 produced at 350 °C showed slightly less activity than the Cu-Cu_2O/TiO_2-400 due to the presence of carbon as remnants of the organic framework at lower temperatures. In order to improve photocatalytic hydrogen production in visible light, smaller band gap semiconductors CdS and g-C_3N_4 were focused on for further study. The nanosized CdS particles were prepared by sol-gel method and subsequently calcined under air and inert atmosphere of nitrogen with the aim to get highly crystalline and photocatalytically active hexagonal CdS phase for hydrogen production. Au nanoparticles were deposited over hexagonal CdS by three conventional methods including; deposition precipitation (DP), incipient wet impregnation (WI), photo-deposition (PD) and a novel reductive deposition method (KI) to fabricate catalysts with different overall Au loadings and particle size distribution despite of same initial nominal loading. Subsequently these photocatalysts were used as model compounds to study the effect of metal deposition method on the Au particle size and distribution. The effect of reaction medium on hydrogen production over Au/h-CdS photocatalyts prepared by KI method from ethanol water-electrolyte mixture was also thoroughly elaborated. Reductive deposition (KI) method produced Au nanoparticles with mean particles sizes between 2 nm to 5 nm by changing the initial nominal Au wt.% (from 1 to 5). The optimum rate for hydrogen production was found over 3 wt.% Au/CdS photocatalyst prepared by KI reduction method that yielded Au particles with mean particle size of 4 nm with relatively lower experimentally determined Au loading (2.5 ± 0.3 wt. %) as compared to PD and DP methods. Prolonged photocatalytic reaction time over 0.5 wt.% Au/h-CdS-KI resulted in increase in particle size up to 20 nm without noticeable decrease in catalytic reactivity. Despite of very small Au particles (2-3 nm) the Au/h-CdS prepared by WI method produced lower hydrogen production than KI method due to less experimentally determined Au loadings. Non-homogeneity and larger Au particle size produced in DP and PD methods respectively, were responsible for lower hydrogen production. This work supports the electron transfer mechanism from semiconductor to metal

which may further be facilitated by metal to semiconductor energy transfer mechanism due to Au surface plasmon resonance. It is interesting to note that Au/CdS photocatalyst showing higher plasmonic effect is not always produce more hydrogen in visible range. These results clearly suggest that optimization among particle size distribution, overall wt. % loading and plasmonic effect is required for enhanced performance. The addition of ethanol to the electrolyte (Na_2S/Na_2SO_3) further increased the production of hydrogen via additional use of holes by α-hydroxyethyl radical from the valence band of CdS allowing for more H^+ to be reduced by the capture of electrons. In the final part of this study, a fruitful effort was attempted to address two main issues of *g*-C_3N_4, i) limited visible light absorption and ii) high recombination rate of photoinduced charge carriers. In this context Pd-Ag bimetallic as well as monometallic nanoparticles were successfully deposited over *g*-C_3N_4 by simple chemical reduction method. A highly positive synergistic response both in optical and photocatalytical properties was observed in resulting photocatalysts in which sliver nanoparticles extends the visible light absorption by surface plasmon effect and Pd-Ag bimetallic nanoparticles decreases the e^-/h^+ recombination rate by forming highly rectifying schottky barrier. The $Pd_{0.7}$-$Ag_{0.3}$/*g*-C_3N_4 photocatalyst with overall 1 wt. % metal loading showed very high H_2 evolution activity (1250 μmol $h^{-1}g^{-1}$), 1.5 and 5.7 times higher than Pd/*g*-C_3N_4 and Ag/*g*-C_3N_4 photocatalysts, respectively. Photocatalysts showed high stability upto continues 16 hours run. A possible mechanism for enhanced hydrogen production over Pd-Ag/*g*-C_3N_4 due to increase in visible light absorption and electron-hole recombination quenching is proposed.

References

4.1 References

1. Navarro R., M. Pena, J. Fierro, Hydrogen production reactions from carbon feedstocks: fossil fuels and biomass. Chem. Rev., 2007. 107(10): 3952-3991.
2. Lewis N.S., D.G. Nocera, Powering the planet: Chemical challenges in solar energy utilization. Proc. Natl Acad Sci., 2006. 103(43): 15729-15735.
3. Lior N., Energy resources and use: The present situation and possible paths to the future. Energy, 2008. 33(6):842-857.
4. Dosado A.G., W. T. Chen, A. Chan, D. Sun-Waterhouse, G.I. Waterhouse, Novel Au/TiO_2 photocatalysts for hydrogen production in alcohol–water mixtures based on hydrogen titanate nanotube precursors. J. Catal., 2015. 330: 238-254.
5. Armor J.N., The multiple roles for catalysis in the production of H_2. Appl. Catal. A-Gen., 1999. 176(2):159-176.
6. Oros-Ruiz S., R. Zanella, R. López, A. Hernández-Gordillo, R. Gómez, Photocatalytic hydrogen production by water/methanol decomposition using Au/TiO_2 prepared by deposition–precipitation with urea. J. Hazard. Mater., 2013. 263: 2-10.
7. Oros-Ruiz S., R. Zanella, R. López, A. Hernández-Gordillo, R. Gómez, Photocatalytic hydrogen production by water/methanol decomposition using Au/TiO_2 prepared by deposition–precipitation with urea. J. Hazard. Mater., 2013. 263(0): 2-10.
8. Veziroglu T. N. S., 21st Century's energy: Hydrogen energy system, Energy Convers. Manage, 2008. 49: 1820–1831.
9. Liu S. H., H. R. Syu, One-step fabrication of N-doped mesoporous TiO_2 nanoparticles by self-assembly for photocatalytic water splitting under visible light. Appl. Energ., 2012. 100: 148-154.
10. Jae S., Photo-catalytic water splitting under visible light with particulate semiconductors catalyst. Catal. Surv. Asia, 2005. 9: 217–228.
11. Momirlan M., T. Veziroğlu, Recent directions of world hydrogen production. Renew. Sust. Energ. Rev., 1999. 3(2–3): 219-231.
12. Rioche C., S. Kulkarni, F.C. Meunier, J.P. Breen, R. Burch, Steam reforming of model compounds and fast pyrolysis bio-oil on supported noble metal catalysts. Appl. Catal. B-Environ., 2005. 61(1–2): 130-139.
13. Athanasios N. Fatsikostas, D.I.K.a.X.E.V., Steam reforming of biomass-derived ethanol for the production of hydrogen for fuel cell applications. (Communication) Chem. Commun., 2001: 851-852.

14. Hohn K.L., Y. C. Lin, Catalytic Partial Oxidation of Methanol and Ethanol for Hydrogen Generation. Chem. Sus. Chem., 2009. 2(10): 927-940.
15. Konrad Geissler, E.N., Frederic Vogel, Thanh-Binh Truong, Peter Hottinger and Alexander Wokaun, Autothermal methanol reforming for hydrogen production in fuel cell applications. Phys. Chem. Chem. Phys., 2001. 3: 289-293.
16. Turn S., C. Kinoshita, Z. Zhang, D. Ishimura, J. Zhou, An experimental investigation of hydrogen production from biomass gasification. Int. J. Hydrogen Energy, 1998. 23(8): 641-648.
17. Lu Y.J., L. J. Guo, C.M. Ji, X. M. Zhang, X. H. Hao, Q.H. Yan, Hydrogen production by biomass gasification in supercritical water: A parametric study. Int. J. Hydrogen Energy, 2006. 31(7): 822-831.
18. Guo Y., S.Z. Wang, D. H. Xu, Y.M. Gong, H.H. Ma, X.Y. Tang, Review of catalytic supercritical water gasification for hydrogen production from biomass. Renew. Sust. Energ. Rev., 2010. 14(1): 334-343.
19. Woodward J., M. Orr, K. Cordray, E. Greenbaum, Biotechnology: Enzymatic production of biohydrogen. Nature, 2000. 405(6790): 1014-1015.
20. Cortright R.D.D., R. R.; Dumesic, J. A., Hydrogen from catalytic reforming of biomass-derived hydrocarbons in liquid water, Nature (London, United Kingdom), 2002. 418(6901): 964-967.
21. Fujishima A., K. Honda, Electrochemical Photolysis of Water at a Semiconductor Electrode. Nature, 1972. 238(5358): 37-38.
22. Grigoriev S.A., V.I. Porembsky, V.N. Fateev, Pure hydrogen production by PEM electrolysis for hydrogen energy. Int. J. Hydrogen Energy, 2006. 31(2): 171-175.
23. Steinfeld A., Solar hydrogen production via a two-step water-splitting thermochemical cycle based on Zn/ZnO redox reactions. Int. J. Hydrogen Energy, 2002. 27(6): 611-619.
24. Mohapatra S.K., M. Misra, V.K. Mahajan, K.S. Raja, Design of a Highly Efficient Photoelectrolytic Cell for Hydrogen Generation by Water Splitting: Application of TiO_2-xC_x Nanotubes as a Photoanode and Pt/TiO_2 Nanotubes as a Cathode. J. Phys. Chem. C, 2007. 111(24): 8677-8685.
25. Osterloh F.E., Inorganic Materials as Catalysts for Photochemical Splitting of Water. Chem. Mater, 2007. 20(1): 35-54.

26. Chen X., S.S. Mao, Titanium Dioxide Nanomaterials: Synthesis, Properties, Modifications, and Applications. Chem. Rev., 2007. 107(7): 2891-2959.
27. Kudo A., H. Kato, I. Tsuji, Strategies for the Development of Visible-light-driven Photocatalysts for Water Splitting. Chem. Lett., 2004. 33(12): 1534-1539.
28. Maeda K.T., Kentaro; Lu, Daling; Takata, Tsuyoshi; Saito, Nobuo; Inoue, Yasunobu; Domen Kazunari, Photocatalyst releasing hydrogen from water. Nature (London, UK), 2006. 440 (7082): 295.
29. Kasahara A., K. Nukumizu, T. Takata, J.N. Kondo, M. Hara, H. Kobayashi, K. Domen $LaTiO_2N$ as a visible-light (≤600 nm)-driven photocatalyst. J. Phys. Chem. B, 2002. 107(3): 791-797.
30. Cortright R.D, R. R.; Dumesic, J. A., Hydrogen from catalytic reforming of biomass-derived hydrocarbons in liquid water. Nature (London, UK), (2002). 418(6901): 964-967.
31. Deluga G.A., J.R. Salge, Renewable Hydrogen from Ethanol by Autothermal Reforming. Science, 2004. 303(5660): 993-997.
32. Holladay J.D., J. Hu, D.L. King, Y. Wang, An overview of hydrogen production technologies. Catal. Today, 2009. 139(4): 244-260.
33. Liu Z., W. Hou, P. Pavaskar, M. Aykol, S.B. Cronin, Plasmon resonant enhancement of photocatalytic water splitting under visible illumination. Nano Lett., 2011. 11(3): 1111-1116.
34. Liu S., J. Yu, M. Jaroniec, Tunable Photocatalytic Selectivity of Hollow TiO_2 Microspheres Composed of Anatase Polyhedra with Exposed (001) Facets. J. Am. Chem. Soc., 2010. 132(34): 11914-11916.
35. Park J.H., S. Kim, A.J. Bard, Novel Carbon-Doped TiO_2 Nanotube Arrays with High Aspect Ratios for Efficient Solar Water Splitting. Nano Lett., 2005. 6(1): 24-28.
36. Yang H.G., G. Liu, S.Z. Qiao, C.H. Sun, Y.G. Jin, S.C. Smith, J. Zou, H.M. Cheng, G.Q. Lu, Solvothermal Synthesis and Photoreactivity of Anatase TiO_2 Nanosheets with Dominant (001) Facets. J. Am. Chem. Soc., 2009. 131(11): 4078-4083.
37. Majeed I., M.A. Nadeem, M. Al-Oufi, M.A. Nadeem, G. Waterhouse, A. Badshah, J. Metson, H. Idriss, On the role of metal particle size and surface coverage for photo-catalytic hydrogen production: A case study of the Au/CdS system. Appl. Catal. B-Environ., 2016. 182: 266-276.
38. Shimura K.,H. Yoshida, Heterogeneous photocatalytic hydrogen production from water and biomass derivatives. Energ. Environ. Sci., 2011. 4(7): 2467-2481.

39. Kudo A.,Y. Miseki, Heterogeneous photocatalyst materials for water splitting. Chem. Soc. Rev., 2009. 38(1): 253-278.
40. Ran J., J. Zhang, J. Yu, M. Jaroniec, S.Z. Qiao, Earth-abundant cocatalysts for semiconductor-based photocatalytic water splitting. Chem. Soc. Rev., 2014. 43(22): 7787-7812.
41. Abe R., Recent progress on photocatalytic and photoelectrochemical water splitting under visible light irradiation. J. Photochem. Photobiol C: Photochem. Rev., 2010. 11(4): 179-209.
42. Moriya Y., T. Takata, K. Domen, Recent progress in the development of (oxy)nitride photocatalysts for water splitting under visible-light irradiation. Coord. Chem. Rev., 2013. 257(13–14): 1957-1969.
43. Nowotny J., C.C. Sorrell, T. Bak, L.R. Sheppard, Solar-hydrogen: Unresolved problems in solid-state science. Sol. Energy, 2005. 78(5): 593-602.
44. Kudo A., K. Omori, H. Kato, A Novel Aqueous Process for Preparation of Crystal Form-Controlled and Highly Crystalline $BiVO_4$ Powder from Layered Vanadates at Room Temperature and Its Photocatalytic and Photophysical Properties. J. Am. Chem. Soc., 1999. 121(49): 11459-11467.
45. Bak T., J. Nowotny, M. Rekas, C.C. Sorrell, Photo-electrochemical hydrogen generation from water using solar energy. Materials-related aspects. Int. J. Hydrogen Energy, 2002. 27(10): 991-1022.
46. Wad A., Photocatalytic properties of TiO_2. Chem. Mater., 1993. 5:280–283.
47. Fujishima, A., X. Zhang, D.A. Tryk, TiO_2 photocatalysis and related surface phenomena. Surf. Sci. Rep., 2008. 63(12): 515-582.
48. Silva L.A., S.Y. Ryu, J. Choi, W. Choi, M.R. Hoffmann, Photocatalytic Hydrogen Production with Visible Light over Pt-Interlinked Hybrid Composites of Cubic-Phase and Hexagonal-Phase CdS. J. Phys. Chem. C, 2008. 112(32): 12069-12073.
49. Levinson R., P. Berdahl, H. Akbari, Solar spectral optical properties of pigments-Part I: model for deriving scattering and absorption coefficients from transmittance and reflectance measurements. Sol. Energ. Mat. Sol. C., 2005. 89(4): 319-349.
50. Wu N. L.,M. S. Lee, Enhanced TiO_2 photocatalysis by Cu in hydrogen production from aqueous methanol solution. Int. J. Hydrogen Energy, 2004. 29(15): p. 1601-1605.
51. Tseng I.H., J.C.S. Wu, Chemical states of metal-loaded titania in the photoreduction of CO_2. Catal. Today, 2004. 97(2–3):113-119.

52. Penner S.S., Steps toward the hydrogen economy. Energy, 2006. 31(1): p. 33-43.
53. Choi, H.-J.,M. Kang, Hydrogen production from methanol/water decomposition in a liquid photosystem using the anatase structure of Cu loaded. Int. J. Hydrogen Energy, 2007. 32(16): 3841-3848.
54. Hoffmann M.R., S.T. Martin, W. Choi, D.W. Bahnemann, Environmental applications of semiconductor photocatalysis. Chem. Rev., 1995. 95(1): 69-96.
55. Li Y., Y. Xie, S. Peng, G. Lu, S. Li, Photocatalytic hydrogen generation in the presence of chloroacetic acids over Pt/TiO_2. Chemosphere, 2006. 63(8): 1312-1318.
56. Yu J., H. Yu, B. Cheng, M. Zhou, X. Zhao, Enhanced photocatalytic activity of TiO_2 powder (P25) by hydrothermal treatment. J. Mol. Catal-A Chem., 2006. 253(1–2): 112-118.
57. Tsuji I., H. Kato, H. Kobayashi, A. Kudo, Photocatalytic H_2 Evolution Reaction from Aqueous Solutions over Band Structure-Controlled $(AgIn)_xZn_2(1-x)S_2$ Solid Solution Photocatalysts with Visible-Light Response and Their Surface Nanostructures. J. Am. Chem. Soc., 2004. 126(41): 13406-13413.
58. Zou Z.Y., Jinhua; Sayama, Kazuhlro; Arakawa, Hironorl, Direct splitting of water under visible light irradiation with an oxide semiconductor photocatalys. Nature (London, UK) (2001). 414(6864): 625-627.
59. Anpo M.,M. Takeuchi, The design and development of highly reactive titanium oxide photocatalysts operating under visible light irradiation. J. Catal., 2003. 216(1–2): 505-516.
60. Lewis N.S., Light work with water. Nature, 2001. 414(6864): 589-590.
61. Linic S., P. Christopher, D.B. Ingram, Plasmonic-metal nanostructures for efficient conversion of solar to chemical energy. Nat. Mater., 2011. 10(12): 911-921.
62. Vernes J., The Mysterious Island. New American Library, NY, 1986 (New American Library).
63. Jiang H., H. Endo, H. Natori, M. Nagai, K. Kobayashi, Fabrication and efficient photocatalytic degradation of methylene blue over $CuO/BiVO_4$ composite under visible-light irradiation. Mater. Res. Bull., 2009. 44(3): 700-706.
64. Ge L., Novel $Pd/BiVO_4$ composite photocatalysts for efficient degradation of methyl orange under visible light irradiation. Mater. Chem. Phys., 2008. 107(2–3): 465-470.
65. Yu J., J. Ran, Facile preparation and enhanced photocatalytic H_2-production activity of $Cu(OH)_2$ cluster modified TiO_2. Energ. Environ. Sci., 2011. 4(4): 1364-1371.
66. Gratzel M., Photoelectrochemical cells. Nature, 2001. 414(6861): 338-344.

67. Chen S., L. W. Wang, Thermodynamic Oxidation and Reduction Potentials of Photocatalytic Semiconductors in Aqueous Solution. Chem. Mater., 2012. 24(18): 3659-3666.

68. Xu Y., M.A.A. Schoonen, The absolute energy positions of conduction and valence bands of selected semiconducting minerals. Am. Mineral., 2000. 85(3-4): 543-556.

69. Wu N. L., M. S. Lee, Z.J. Pon, J.Z. Hsu, Effect of calcination atmosphere on TiO_2 photocatalysis in hydrogen production from methanol/water solution. J. Photochem. Photobiol. A-Chem., 2004. 163(1–2): 277-280.

70. Nuhu A., J. Soares, M. Gonzalez-Herrera, A. Watts, G. Hussein, M. Bowker, Methanol oxidation on Au/TiO_2 catalysts. Top Catal., 2007. 44(1-2): 293-297.

71. Kudo A., Photocatalysis and solar hydrogen production. Pure Appl. Chem., 2007. 79(11): 1917-1927.

72. Linsebigler A.L., G. Lu, J.T. Yates Jr, Photocatalysis on TiO_2 surfaces: principles, mechanisms, and selected results. Chem. Rev., 1995. 95(3): 735-758.

73. Skinner D.E., D.P. Colombo Jr, J.J. Cavaleri, R.M. Bowman, Femtosecond investigation of electron trapping in semiconductor nanoclusters. J. Phys. Chem., 1995. 99(20): 7853-7856.

74. Yamaguti K.,S. Sato, Photolysis of water over metallized powdered titanium dioxide. Journal of the Chemical Society, Faraday Transactions 1: Phys. Chem. Cond. Phases, 1985. 81(5): 1237-1246.

75. Chatterjee D.,S. Dasgupta, Visible light induced photocatalytic degradation of organic pollutants. J. Photochem. Photobiol. C: Photochem. Rev., 2005. 6(2): 186-205.

76. Kowalska E., R. Abe, B. Ohtani, Visible light-induced photocatalytic reaction of gold-modified titanium (IV) oxide particles: action spectrum analysis. Chem. Commun., 2009(2): 241-243.

77. Bard A.J., M.A. Fox, Artificial Photosynthesis: Solar Splitting of Water to Hydrogen and Oxygen. Acc. Chem. Res., 1995. 28(3): 141-145.

78. Baba R., S. Nakabayashi, A. Fujishima, K. Honda, Investigation of the mechanism of hydrogen evolution during photocatalytic water decomposition on metal-loaded semiconductor powders. J. Phys. Chem., 1985. 89(10): 1902-1905.

79. Henglein, A., Small-particle research: physicochemical properties of extremely small colloidal metal and semiconductor particles. Chem. Rev., 1989. 89(8): 1861-1873.

80. Zhang J.Z., Ultrafast Studies of Electron Dynamics in Semiconductor and Metal Colloidal Nanoparticles: Effects of Size and Surface. Accounts Chem. Res., 1997. 30(10): 423-429.

81. Thomas K.G.,P.V. Kamat, Chromophore-Functionalized Gold Nanoparticles. Accounts Chem. Res., 2003. 36(12): 888-898.

82. Kamat P.V.,D. Meisel, Nanoparticles in advanced oxidation processes. Curr. Opin. Colloid Interface Sci., 2002. 7(5–6): 282-287.

83. Choi W., A. Termin, M.R. Hoffmann, The Role of Metal Ion Dopants in Quantum-Sized TiO_2: Correlation between Photoreactivity and Charge Carrier Recombination Dynamics. J. Phys. Chem., 1994. 98(51): 13669-13679.

84. Young C., T.M. Lim, K. Chiang, J. Scott, R. Amal, Photocatalytic oxidation of toluene and trichloroethylene in the gas-phase by metallised (Pt, Ag) titanium dioxide. Appl. Catal. B-Environ., 2008. 78(1): 1-10.

85. Sreethawong T. ,S. Yoshikawa, Comparative investigation on photocatalytic hydrogen evolution over Cu, Pd, and Au-loaded mesoporous TiO_2 photocatalysts. Catal. Commun., 2005. 6(10): 661-668.

86. Chen X., S.S. Mao, Titanium dioxide nanomaterials: synthesis, properties, modifications, and applications. Chem. Rev., 2007. 107(7): 2891-2959.

87. Yoon J.W., T. Sasaki, N. Koshizaki, Dispersion of nanosized noble metals in TiO_2 matrix and their photoelectrode properties. Thin Solid Films, 2005. 483(1): 276-282.

88. Ohtani B., K. Iwai, S. Nishimoto, S. Sato, Role of Platinum Deposits on Titanium(IV) Oxide Particles: Structural and Kinetic Analyses of Photocatalytic Reaction in Aqueous Alcohol and Amino Acid Solutions. J. Phys. Chem. B, 1997. 101(17): 3349-3359.

89. Kamat P.V., Photophysical, Photochemical and Photocatalytic Aspects of Metal Nanoparticles. J. Phys. Chem. B, 2002. 106(32): 7729-7744.

90. Subramanian V., E.E. Wolf, P.V. Kamat, Influence of Metal/Metal Ion Concentration on the Photocatalytic Activity of TiO_2−Au Composite Nanoparticles. Langmuir, 2002. 19(2): 469-474.

91. Wu M.C., A. Sápi, A. Avila, M. Szabó, J. Hiltunen, M. Huuhtanen, G. Tóth, Á. Kukovecz, Z. Kónya, R. Keiski, W.F. Su, H. Jantunen, K. Kordás, Enhanced photocatalytic activity of TiO_2 nanofibers and their flexible composite films: Decomposition of organic dyes and efficient H_2 generation from ethanol-water mixtures. Nano Res., 2011. 4(4): 360-369.

92. Chiarello G.L., E. Selli, L. Forni, Photocatalytic hydrogen production over flame spray pyrolysis-synthesised TiO_2 and Au/TiO_2. Appl. Catal. B-Environ., 2008. 84(1–2): 332-339.

93. Chiarello G.L., M.H. Aguirre, E. Selli, Hydrogen production by photocatalytic steam reforming of methanol on noble metal-modified TiO_2. J. Catal., 2010. 273(2): 182-190.

94. Sadeghi M., W. Liu, T.G. Zhang, P. Stavropoulos, B. Levy, Role of Photoinduced Charge Carrier Separation Distance in Heterogeneous Photocatalysis: Oxidative Degradation of CH_3OH Vapor in Contact with Pt/TiO_2 and Cofumed TiO_2−Fe_2O_3. J. Phys. Chem., 1996. 100(50): 19466-19474.

95. Wu M.C., J. Hiltunen, A. Sápi, A. Avila, W. Larsson, H. C. Liao, M. Huuhtanen, G. Tóth, A. Shchukarev, N. Laufer, Á. Kukovecz, Z. Kónya, J.P. Mikkola, R. Keiski, W.F. Su, Y.F. Chen, H. Jantunen, P.M. Ajayan, R. Vajtai, K. Kordás, Nitrogen-Doped Anatase Nanofibers Decorated with Noble Metal Nanoparticles for Photocatalytic Production of Hydrogen. ACS Nano, 2011. 5(6): 5025-5030.

96. Subramanian V., E. Wolf, P.V. Kamat, Semiconductor−Metal Composite Nanostructures. To What Extent Do Metal Nanoparticles Improve the Photocatalytic Activity of TiO_2 Films? J. Phys. Chem. B, 2001. 105(46): 11439-11446.

97. Hirakawa T.,P.V. Kamat, Photoinduced Electron Storage and Surface Plasmon Modulation in Ag@TiO_2 Clusters. Langmuir, 2004. 20(14): 5645-5647.

98. Bisquert J., A. Zaban, P. Salvador, Analysis of the Mechanisms of Electron Recombination in Nanoporous TiO_2 Dye-Sensitized Solar Cells. Nonequilibrium Steady-State Statistics and Interfacial Electron Transfer via Surface States. J. Phys. Chem. B, 2002. 106(34): 8774-8782.

99. Wood A., M. Giersig, P. Mulvaney, Fermi Level Equilibration in Quantum Dot−Metal Nanojunctions. J. Phys. Chem. B, 2001. 105(37): 8810-8815.

100. Subramanian V., E.E. Wolf, P.V. Kamat, Green Emission to Probe Photoinduced Charging Events in ZnO−Au Nanoparticles. Charge Distribution and Fermi-Level Equilibration. J. Phys. Chem. B, 2003. 107(30): 7479-7485.

101. Burgeth G.,H. Kisch, Photocatalytic and photoelectrochemical properties of titania–chloroplatinate (IV). Coord. Chem. Rev., 2002. 230(1–2): 41-47.

102. Subramanian V., E.E. Wolf, P.V. Kamat, Catalysis with TiO_2/Gold Nanocomposites. Effect of Metal Particle Size on the Fermi Level Equilibration. J. Am. Chem. Soc., 2004. 126(15): 4943-4950.

103. Chen, Gold nanoelectrodes of varied size: Transition to molecule-like charging. Science, 1998. 280(5372): 2098-2101.

104. Jakob M., H. Levanon, P.V. Kamat, Charge Distribution between UV-Irradiated TiO_2 and Gold Nanoparticles: Determination of Shift in the Fermi Level. Nano Lett., 2003. 3(3): 353-358.

105. Gerischer H., A mechanism of electron hole pair separation in illuminated semiconductor particles. J. Phys. Chem., 1984. 88(25): 6096-6097.

106. Leung D.Y.C., X. Fu, C. Wang, M. Ni, M.K.H. Leung, X. Wang, X. Fu, Hydrogen Production over Titania-Based Photocatalysts. Chem. Sus. Chem., 2010. 3(6): 681-694.

107. Park J.Y., J. Renzas, A. Contreras, G.A. Somorjai, The genesis and importance of oxide–metal interface controlled heterogeneous catalysis; the catalytic nanodiode. Top. Catal., 2007. 46(1-2): 217-222.

108. Kamat P.V., I. Bedja, S. Hotchandani, Photoinduced Charge Transfer between Carbon and Semiconductor Clusters. One-Electron Reduction of C_{60} in Colloidal TiO_2 Semiconductor Suspensions. J. Phys. Chem., 1994. 98(37): 9137-9142.

109. Gomathisankar P., D. Yamamoto, H. Katsumata, T. Suzuki, S. Kaneco, Photocatalytic hydrogen production with aid of simultaneous metal deposition using titanium dioxide from aqueous glucose solution. Int. J. Hydrogen Energy., 2013. 38(14): 5517-5524.

110. Kraeutler B., A.J. Bard, Heterogeneous photocatalytic preparation of supported catalysts. Photodeposition of platinum on titanium dioxide powder and other substrates. J. Am. Chem. Soc., 1978. 100(13): 4317-4318.

111. Joo J.B., R. Dillon, I. Lee, Y. Yin, C.J. Bardeen, F. Zaera, Promotion of atomic hydrogen recombination as an alternative to electron trapping for the role of metals in the photocatalytic production of H_2. Proc. Natl. Acad. Sci., 2014. 111(22):7942-7947.

112. Kuo H. L., C.Y. Kuo, C.H. Liu, J.H. Chao, C.H. Lin, A highly active bi-crystalline photocatalyst consisting of TiO_2(B) nanotube and anatase particle for producing H_2 gas from neat ethanol. Catal. Lett., 2007. 113(1-2): 7-12.

113. Yang, Y., C.H. Chang, H. Idriss, Photo-catalytic production of hydrogen form ethanol over M/TiO_2 catalysts (M= Pd, Pt or Rh). Appl. Catal. B-Environ., 2006. 67(3): 217-222.

114. El-Sayed M.A., Some Interesting Properties of Metals Confined in Time and Nanometer Space of Different Shapes. Acc. Chem. Res., 2001. 34(4): 257-264.

115. Rayalu S.S., D. Jose, M.V. Joshi, P.A. Mangrulkar, K. Shrestha, K. Klabunde, Photocatalytic water splitting on Au/TiO_2 nanocomposites synthesized through various routes: Enhancement in photocatalytic activity due to SPR effect. Appl. Catal. B-Environ., 2013. 142: 684-693.

116. Thimsen E., F. Le Formal, M. Grätzel, S.C. Warren, Influence of Plasmonic Au Nanoparticles on the Photoactivity of Fe_2O_3 Electrodes for Water Splitting. Nano Lett., 2010. 11(1): 35-43.

117. Ingram D.B.,S. Linic, Water splitting on composite plasmonic-metal/semiconductor photoelectrodes: evidence for selective plasmon-induced formation of charge carriers near the semiconductor surface. J. Am. Chem. Soc., 2011. 133(14): 5202-5205.

118. Rycenga M., C.M. Cobley, J. Zeng, W. Li, C.H. Moran, Q. Zhang, D. Qin, Y. Xia, Controlling the synthesis and assembly of silver nanostructures for plasmonic applications. Chem. Rev., 2011. 111(6): 3669-3712.

119. Naya S, A. Inoue, H. Tada, Visible Light Activity Enhancement of Gold Nanoparticle-Loaded Titanium (IV) Dioxide by Preferential Excitation of Localized Surface Plasmon Resonance. Chem. Phys. Chem., 2011. 12(15): 2719-2723.

120. Chen H., X. Kou, Z. Yang, W. Ni, J. Wang, Shape-and size-dependent refractive index sensitivity of gold nanoparticles. Langmuir, 2008. 24(10): 5233-5237.

121. Chen H., L. Shao, K.C. Woo, T. Ming, H. Q. Lin, J. Wang, Shape-dependent refractive index sensitivities of gold nanocrystals with the same plasmon resonance wavelength. J. Phys. Chem. C, 2009. 113(41): 17691-17697.

122. Mock J.J., D.R. Smith, S. Schultz, Local refractive index dependence of plasmon resonance spectra from individual nanoparticles. Nano Lett., 2003. 3(4): 485-491.

123. Macwan D., C. Balasubramanian, P. Dave, S. Chaturvedi, Thermal plasma synthesis of nanotitania and its characterization. J. Saudi Chem. Soc., 2014. 18(3): 234-244.

124. Kimura K., S. Naya, Y. Jin-nouchi, H. Tada, TiO_2 crystal form-dependence of the Au/TiO_2 plasmon photocatalyst's activity. J. Phys. Chem. C, 2012. 116(12): 7111-7117.

125. Jovic V., Z.H. Al-Azri, W.T. Chen, D. Sun-Waterhouse, H. Idriss, G.I. Waterhouse, Photocatalytic H_2 Production from Ethanol–Water Mixtures Over Pt/TiO_2 and Au/TiO_2 Photocatalysts: A Comparative Study. Top. Catal., 2013. 56(12): 1139-1151.

126. Chen W. T., A. Chan, Z.H. Al-Azri, A.G. Dosado, M.A. Nadeem, D. Sun-Waterhouse, H. Idriss, G.I. Waterhouse, Effect of TiO_2 polymorph and alcohol

sacrificial agent on the activity of Au/TiO_2 photocatalysts for H_2 production in alcohol–water mixtures. J. Catal., 2015. 329: 499-513.

127. Tian Y., T. Tatsuma, Mechanisms and applications of plasmon-induced charge separation at TiO_2 films loaded with gold nanoparticles. J. Am. Chem. Soc., 2005. 127(20): 7632-7637.
128. Gomes Silva, C.u., R. Juárez, T. Marino, R. Molinari, H. García, Influence of excitation wavelength (UV or visible light) on the photocatalytic activity of titania containing gold nanoparticles for the generation of hydrogen or oxygen from water. J. Am. Chem. Soc., 2010. 133(3): 595-602.
129. Zhou X., C. Hu, X. Hu, T. Peng, J. Qu, Plasmon-Assisted Degradation of Toxic Pollutants with Ag−AgBr/Al_2O_3 under Visible-Light Irradiation. J. Phys. Chem. C, 2010. 114(6): 2746-2750.
130. Kowalska E., O.O.P. Mahaney, R. Abe, B. Ohtani, Visible-light-induced photocatalysis through surface plasmon excitation of gold on titania surfaces. Phys. Chem. Chem. Phys., 2010. 12(10): 2344-2355.
131. Kumar M.K., S. Krishnamoorthy, L.K. Tan, S.Y. Chiam, S. Tripathy, H. Gao, Field effects in plasmonic photocatalyst by precise SiO_2 thickness control using atomic layer deposition. ACS Catal., 2011. 1(4): 300-308.
132. Tian Y.,T. Tatsuma, Plasmon-induced photoelectrochemistry at metal nanoparticles supported on nanoporous TiO_2. Chem. Commun., 2004(16): 1810-1811.
133. Primo A., T. Marino, A. Corma, R. Molinari, H. Garcia, Efficient visible-light photocatalytic water splitting by minute amounts of gold supported on nanoparticulate CeO_2 obtained by a biopolymer templating method. J. Am. Chem. Soc., 2011. 133(18): 6930-6933.
134. Christopher P., D.B. Ingram, S. Linic, Enhancing photochemical activity of semiconductor nanoparticles with optically active Ag nanostructures: photochemistry mediated by Ag surface plasmons. J. Phys. Chem. C, 2010. 114(19): 9173-9177.
135. Awazu K., M. Fujimaki, C. Rockstuhl, J. Tominaga, H. Murakami, Y. Ohki, N. Yoshida, T. Watanabe, A Plasmonic Photocatalyst Consisting of Silver Nanoparticles Embedded in Titanium Dioxide. J. Am. Chem. Soc., 2008. 130(5): 1676-1680.
136. Seh Z.W., S. Liu, M. Low, S.Y. Zhang, Z. Liu, A. Mlayah, M.Y. Han, Janus Au-TiO_2 Photocatalysts with Strong Localization of Plasmonic Near-Fields for Efficient Visible-Light Hydrogen Generation. Adv. Mater., 2012. 24(17): 2310-2314.

137. Moon S. C., H. Mametsuka, S. Tabata, E. Suzuki, Photocatalytic production of hydrogen from water using TiO_2 and B/TiO_2. Catal. Today, 2000. 58(2): 125-132.

138. Abe R., K. Sayama, H. Arakawa, Significant effect of iodide addition on water splitting into H_2 and O_2 over Pt-loaded TiO_2 photocatalyst: suppression of backward reaction. Chem. Phys. Lett., 2003. 371(3-4): 360-364.

139. Bamwenda G.R., T. Uesigi, Y. Abe, K. Sayama, H. Arakawa, The photocatalytic oxidation of water to O_2 over pure CeO_2, WO_3, and TiO_2 using Fe^{3+} and Ce^{4+} as electron acceptors. Appl. catal. A-Gen., 2001. 205(1-2):117-128.

140. Li Y., G. Lu, S. Li, Photocatalytic production of hydrogen in single component and mixture systems of electron donors and monitoring adsorption of donors by in situ infrared spectroscopy. Chemosphere, 2003. 52(5): 843-850.

141. Park M.S., M. Kang, The preparation of the anatase and rutile forms of Ag–TiO2 and hydrogen production from methanol/water decomposition. Mater. Lett., 2008. 62(2): 183-187.

142. Chiarello G.L., L. Forni, E. Selli, Photocatalytic hydrogen production by liquid-and gas-phase reforming of CH_3OH over flame-made TiO_2 and Au/TiO_2. Catal. Today, 2009. 144(1): 69-74.

143. Lin W.C., W.D. Yang, I.L. Huang, T.S. Wu, Z.J. Chung, Hydrogen Production from Methanol/Water Photocatalytic Decomposition Using $Pt/TiO_2{-}xN_x$ Catalyst. Energ. Fuels, 2009. 23(4): 2192-2196.

144. Sreethawong T., C. Junbua, S. Chavadej, Photocatalytic H_2 production from water splitting under visible light irradiation using Eosin Y-sensitized mesoporous-assembled Pt/TiO_2 nanocrystal photocatalyst. J. Power Sources, 2009. 190(2): 513-524.

145. Jang J.S., W. Li, S.H. Oh, J.S. Lee, Fabrication of CdS/TiO_2 nano-bulk composite photocatalysts for hydrogen production from aqueous H_2S solution under visible light. Chem. Phys. Lett., 2006. 425(4): 278-282.

146. Koca A., M. Şahin, Photocatalytic hydrogen production by direct sun light from sulfide/sulfite solution. Int. J. Hydrogen Energy, 2002. 27(4): 363-367.

147. Bamwenda G.R., H. Arakawa, The photoinduced evolution of O_2 and H_2 from a WO_3 aqueous suspension in the presence of Ce^{4+}/Ce^{3+}. Sol. Energ. Mater. Sol. C, 2001. 70(1): 1-14.

148. Abe R., K. Sayama, K. Domen, H. Arakawa, A new type of water splitting system composed of two different TiO_2 photocatalysts (anatase, rutile) and a IO^{3-}/I^- shuttle redox mediator. Chem. Phys. Lett., 2001. 344(3): 339-344.

149. Sayama K., K. Mukasa, R. Abe, Y. Abe, H. Arakawa, A new photocatalytic water splitting system under visible light irradiation mimicking a Z-scheme mechanism in photosynthesis. J. Photochem. Photobiol. A-Chem., 2002. 148(1): 71-77.

150. Lee K., W.S. Nam, G. Young Han, Photocatalytic water-splitting in alkaline solution using redox mediator. 1: Parameter study. Int. J. Hydrogen Energy, 2004. 29(13): 1343-1347.

151. Fu X., J. Long, X. Wang, D.Y. Leung, Z. Ding, L. Wu, Z. Zhang, Z. Li, X. Fu, Photocatalytic reforming of biomass: a systematic study of hydrogen evolution from glucose solution. Int. J. Hydrogen Energy, 2008. 33(22): 6484-6491.

152. Kawai T.,T. Sakata, Conversion of carbohydrate into hydrogen fuel by a photocatalytic process. Nature, 1980. 286(5772): 474-476.

153. Ishikawa A., T. Takata, J.N. Kondo, M. Hara, H. Kobayashi, K. Domen, Oxysulfide $Sm_2Ti_2S_2O_5$ as a stable photocatalyst for water oxidation and reduction under visible light irradiation ($\lambda \leq 650$ nm). J. Am. Chem. Soc., 2002. 124(45): 13547-13553.

154. Jang J.S., H.G. Kim, V.R. Reddy, S.W. Bae, S.M. Ji, J.S. Lee, Photocatalytic water splitting over iron oxide nanoparticles intercalated in $HTiNb(Ta)O_5$ layered compounds. J. Catal., 2005. 231(1): 213-222.

155. Nakamura R., T. Tanaka, Y. Nakato, Mechanism for visible light responses in anodic photocurrents at N-doped TiO_2 film electrodes. J. Phys. Chem. B, 2004. 108(30): 10617-10620.

156. Kato H., M. Hori, R. Konta, Y. Shimodaira, A. Kudo, Construction of Z-scheme type heterogeneous photocatalysis systems for water splitting into H_2 and O_2 under visible light irradiation. Chem. Lett., 2004. 33(10): 1348-1349.

157. Abe R., T. Takata, H. Sugihara, K. Domen, Photocatalytic overall water splitting under visible light by TaON and WO_3 with an IO_3^-/I^- shuttle redox mediator. Chem. Commun., 2005(30): 3829-3831.

158. Hara K., K. Sayama, H. Arakawa, Photocatalytic hydrogen and oxygen formation over SiO_2-supported RuS_2 in the presence of sacrificial donor and acceptor. Appl. Catal. A-Gen., 1999. 189(1): 127-137.

159. Linkous C.A., C. Huang, J.R. Fowler, UV photochemical oxidation of aqueous sodium sulfide to produce hydrogen and sulfur. J. Photochem. Photobiol. A-Chem., 2004. 168(3): 153-160.

160. Yang S., L. Gao, New Method to Prepare Nitrogen Doped Titanium Dioxide and Its Photocatalytic Activities Irradiated by Visible Light. J. Am. Ceram. Soc., 2004. 87(9): 1803-1805.

161. Liu H., J. Yuan, W. Shangguan, Photochemical reduction and oxidation of water including sacrificial reagents and Pt/TiO_2 catalyst. Energ. Fuels, 2006. 20(6): 2289-2292.

162. Sun W., S. Zhang, Z. Liu, C. Wang, Z. Mao, Studies on the enhanced photocatalytic hydrogen evolution over Pt/PEG-modified TiO_2 photocatalysts. Int. J. Hydrogen Energy, 2008. 33(4): 1112-1117.

163. Li Y., G. Lu, S. Li, Photocatalytic hydrogen generation and decomposition of oxalic acid over platinized TiO_2. Appl. Catal. A-Gen., 2001. 214(2): 179-185.

164. Al-Mazroai L.S., M. Bowker, P. Davies, A. Dickinson, J. Greaves, D. James, L. Millard, The photocatalytic reforming of methanol. Catal Today, 2007. 122(1): 46-50.

165. Sreethawong, T., T. Puangpetch, S. Chavadej, S. Yoshikawa, Quantifying influence of operational parameters on photocatalytic H_2 evolution over Pt-loaded nanocrystalline mesoporous TiO_2 prepared by single-step sol–gel process with surfactant template. J. Power Sources., 2007. 165(2): 861-869.

166. Daskalaki V.M., P. Panagiotopoulou, D.I. Kondarides, Production of peroxide species in Pt/TiO_2 suspensions under conditions of photocatalytic water splitting and glycerol photoreforming. Chem. Eng. J., 2011. 170(2): 433-439.

167. Jaeger C.D., A. J. Bard, Spin trapping and electron spin resonance detection of radical intermediates in the photodecomposition of water at titanium dioxide particulate systems. J. Phys. Chem., 1979. 83(24): 3146-3152.

168. Bowker M., C. Morton, J. Kennedy, H. Bahruji, J. Greves, W. Jones, P.R. Davies, C. Brookes, P. Wells, N. Dimitratos, Hydrogen production by photoreforming of biofuels using Au, Pd and Au–Pd/TiO_2 photocatalysts. J. Catal., 2014. 310: 10-15.

169. Bahruji H., M. Bowker, P.R. Davies, F. Pedrono, New insights into the mechanism of photocatalytic reforming on Pd/TiO_2. Appl. Catal. B-Environ., 2011. 107(1–2): 205-209.

170. Priebe J.B., Jr. Radnik, A.J. Lennox, M.-M. Pohl, M. Karnahl, D. Hollmann, K. Grabow, U. Bentrup, H. Junge, M. Beller, Solar Hydrogen Production by Plasmonic

Au–TiO_2 Catalysts: Impact of Synthesis Protocol and TiO_2 Phase on Charge Transfer Efficiency and H_2 Evolution Rates. ACS Catal., 2015. 5(4): 2137-2148.

171. Cowan A.J., C.J. Barnett, S.R. Pendlebury, M. Barroso, K. Sivula, M. Grätzel, J.R. Durrant D.R. Klug, Activation energies for the rate-limiting step in water photooxidation by nanostructured α-Fe_2O_3 and TiO_2. J. Am. Chem. Soc., 2011. 133(26): 10134-10140.
172. Mills A., R.H. Davies, D. Worsley, Water purification by semiconductor photocatalysis. Chem. Soc. Rev., 1993. 22(6): 417-425.
173. A. Ajmal, I.Majeed., R.N. Malik, M. Iqbal, M. Arif Nadeem, I. Hussain, S. Yousuf, Zeshan, G. Mustafa, M.I. Zafar, M. Amtiaz Nadeem, Photocatalytic degradation of textile dyes on Cu_2O-CuO/TiO_2 anatase powders. J. Environ. Chem. Eng., 2016. 4: 2138–2146.
174. Shangguan W., Hydrogen evolution from water splitting on nanocomposite photocatalysts. Sci. Technol. Adv. Mater., 2007. 8(1): 76-81.
175. Youngblood W.J., S. H.A. Lee, K. Maeda, T.E. Mallouk, Visible light water splitting using dye-sensitized oxide semiconductors. Acc. Chem. Res., 2009. 42(12): 1966-1973.
176. Maeda K., K. Domen, Photocatalytic water splitting: recent progress and future challenges. J. Phys. Chem. Lett., 2010. 1(18): 2655-2661.
177. Kandiel T.A., A. Feldhoff, L. Robben, R. Dillert, D.W. Bahnemann, Tailored Titanium Dioxide Nanomaterials: Anatase Nanoparticles and Brookite Nanorods as Highly Active Photocatalysts. Chem. Mater., 2010. 22(6): 2050-2060.
178. Li J.G., T. Ishigaki, X. Sun, Anatase, Brookite, and Rutile Nanocrystals via Redox Reactions under Mild Hydrothermal Conditions: Phase-Selective Synthesis and Physicochemical Properties. J. Phys. Chem. C, 2007. 111(13): 4969-4976.
179. Nadeem A., G. Waterhouse, J. Metson, H. Idriss. Hydrogen production by photoreaction of ethanol over Au/TiO_2 anatase: the effect of TiO_2 particle size. in SPIE Solar Energy + Technology. 2010: Int. Soc. Optics Photonics.
180. Tay Q., X. Liu, Y. Tang, Z. Jiang, T.C. Sum, Z. Chen, Enhanced Photocatalytic Hydrogen Production with Synergistic Two-Phase Anatase/Brookite TiO_2 Nanostructures. J. Phys. Chem. C, 2013. 117(29): 14973-14982.
181. Scanlon D.O., C.W. Dunnill, J. Buckeridge, S.A. Shevlin, A.J. Logsdail, S.M. Woodley, C.R.A. Catlow, M.J. Powell, R.G. Palgrave, I.P. Parkin, Band alignment of rutile and anatase TiO_2. Nat. Mater., 2013. 12(9): 798-801.

182. Dosado A.G., W. T. Chen, A. Chan, D. Sun-Waterhouse, G.I. Waterhouse, Novel Au/TiO_2 photocatalysts for hydrogen production in alcohol–water mixtures based on hydrogen titanate nanotube precursors. J. Catal., 2015. 330: 238-254.

183. Rothenberger G., J. Moser, M. Graetzel, N. Serpone, D.K. Sharma, Charge carrier trapping and recombination dynamics in small semiconductor particles. J. Am. Chem. Soc., 1985. 107(26): 8054-8059.

184. Bahruji H., M. Bowker, C. Brookes, P.R. Davies, I. Wawata, The adsorption and reaction of alcohols on TiO_2 and Pd/TiO_2 catalysts. Appl. Catal. A-Gen., 2013. 454: 66-73.

185. Bahruji H., M. Bowker, P.R. Davies, J. Kennedy, D.J. Morgan, The importance of metal reducibility for the photo-reforming of methanol on transition metal-TiO_2 photocatalysts and the use of non-precious metals. Int. J. Hydrogen Energy, 2015. 40(3): 1465-1471.

186. Bowker M., C. Morton, J. Kennedy, H. Bahruji, J. Greves, W. Jones, P.R. Davies, C. Brookes, P.P. Wells, N. Dimitratos, Hydrogen production by photoreforming of biofuels using Au, Pd and Au–Pd/TiO_2 photocatalysts. J. Catal., 2014. 310: 10-15.

187. Bowker M., H. Bahruji, J. Kennedy, W. Jones, G. Hartley, C. Morton, The Photocatalytic Window: Photo-Reforming of Organics and Water Splitting for Sustainable Hydrogen Production. Catal. Lett., 2015. 145(1): 214-219.

188. Nadeem M.A., M. Murdoch, G.I.N. Waterhouse, J.B. Metson, M.A. Keane, J. Llorca, H. Idriss, Photoreaction of ethanol on Au/TiO_2 anatase: Comparing the micro to nanoparticle size activities of the support for hydrogen production. J. Photochem. Photobiol. A-Chem., 2010. 216(2–3): 250-255.

189. Yu J., L. Qi, M. Jaroniec, Hydrogen production by photocatalytic water splitting over Pt/TiO_2 nanosheets with exposed (001) facets. J. Phys. Chem. C, 2010. 114(30): 13118-13125.

190. Xu S., A.J. Du, J. Liu, J. Ng, D.D. Sun, Highly efficient CuO incorporated TiO_2 nanotube photocatalyst for hydrogen production from water. Int. J. Hydrogen Energy, 2011. 36(11): 6560-6568.

191. Paxton A T, T.-N.L., Electronic structure of reduced titanium dioxide. Phys. Rev. B, 1998. 57: 1579–1584.

192. Banerjee S, G.J., Muraleedharan P, Physics and chemistry of photocatalytic titanium dioxide:Visualization of bactericidal activity using atomic force microscopy. Current Sci., 2006. 90: 1378–1383.

193. Wisitsoraat A., A. Tuantranont, E. Comini, G. Sberveglieri, W. Wlodarski, Characterization of n-type and p-type semiconductor gas sensors based on NiO_x doped TiO_2 thin films. Thin Solid Films, 2009. 517(8): 2775-2780.

194. Nicholls D., Complexes and First-Row Transition Elements. MacMillan Edu., HK, (1974).

195. Bokhimi X., A. Morales, M. Aguilar, J.A. Toledo-Antonio, F. Pedraza, Local order in titania polymorphs. Int. J. Hydrogen Energy, 2001. 26(12): 1279-1287.

196. Mo S. D.,W. Ching, Electronic and optical properties of three phases of titanium dioxide: Rutile, anatase, and brookite. Phys. Rev. B, 1995. 51(19): 13023.

197. McLintock I.S.,M. Ritchie, Reactions on titanium dioxide; photo-adsorption and oxidation of ethylene and propylene. Trans. Faraday Soc., 1965. 61: 1007-1016.

198. Thompson T.L., J.T. Yates, Surface science studies of the photoactivation of TiO_2 new photochemical processes. Chem. Rev., 2006. 106(10): 4428-4453.

199. Dubrovinsky L.S., N.A. Dubrovinskaia, V. Swamy, J. Muscat, N.M. Harrison, R. Ahuja, B. Holm, B. Johansson, Materials science: The hardest known oxide. Nature, 2001. 410(6829): 653-654.

200. Pelaez M., N.T. Nolan, S.C. Pillai, M.K. Seery, P. Falaras, A.G. Kontos, P.S.M. Dunlop, J.W.J. Hamilton, J.A. Byrne, K. O'Shea, M.H. Entezari, D.D. Dionysiou, A review on the visible light active titanium dioxide photocatalysts for environmental applications. Appl. Catal. B-Environ., 2012. 125(0): 331-349.

201. Moellmann J., S. Ehrlich, R. Tonner, S. Grimme, A DFT-D study of structural and energetic properties of TiO_2 modifications. Journal of Physics: Cond. Matter, 2012. 24(42): 424206.

202. Gupta S., M. Tripathi, A review of TiO_2 nanoparticles. Chin. Sci. Bull., 2011. 56(16): 1639-1657.

203. Diebold U., The surface science of titanium dioxide. Surf. Sci. Rep., 2003. 48(5–8): 53-229.

204. Zhang Z., C. C. Wang, R. Zakaria, J.Y. Ying, Role of Particle Size in Nanocrystalline TiO_2-Based Photocatalysts. J. Phys. Chem. B, 1998. 102(52): 10871-10878.

205. Baiju K.V., S. Shukla, K.S. Sandhya, J. James, K.G.K. Warrier, Photocatalytic Activity of Sol−Gel-Derived Nanocrystalline Titania. J. Phys. Chem. C, 2007. 111(21): 7612-7622.

206. Cotton F.A., G. Wilkinson, C. Murillo, M. Bochmann, Advanced Inorganic Chemistry John Wiley & Sons. Inc., NY. 1999.
207. Hadjiivanov K.I.,D.G. Klissurski, Surface chemistry of titania (anatase) and titania-supported catalysts. Chem. Soc. Rev., 1996. 25(1): 61-69.
208. Grätzel M., The artificial leaf, molecular photovoltaics achieve efficient generation of electricity from sunlight. Comments Inorg. Chem., 1991. 12(2-3): 93-111.
209. Tang H., K. Prasad, R. Sanjines, P. Schmid, F. Levy, Electrical and optical properties of TiO_2 anatase thin films. J. Appl. Phys., 1994. 75: 2042.
210. Sanjinés R., H. Tang, H. Berger, F. Gozzo, G. Margaritondo, F. Lévy, Electronic structure of anatase TiO_2 oxide. J. Appl. Phys., 1994. 75(6): 2945-2951.
211. Kowalczyk S.P., F.R. McFeely, L. Ley, V.T. Gritsyna, D.A. Shirley, The electronic structure of $SrTiO_3$ and some simple related oxides (MgO, Al_2O_3, SrO, TiO_2). Solid State Commun., 1977. 23(3): 161-169.
212. Forro L., O. Chauvet, D. Emin, L. Zuppiroli, H. Berger, F. Lévy, High mobility n-type charge carriers in large single crystals of anatase (TiO_2). J. Appl. Phys., 1994. 75(1): 633-635.
213. Tang H., F. Lévy, H. Berger, P.E. Schmid, Urbach tail of anatase TiO_2. Phys. Rev. B, 1995. 52(11): 7771-7774.
214. Sclafani A., L. Palmisano, M. Schiavello, Influence of the preparation methods of titanium dioxide on the photocatalytic degradation of phenol in aqueous dispersion. J. Phys. Chem., 1990. 94(2): 829-832.
215. Colbeau-Justin C., M. Kunst, D. Huguenin, Structural influence on charge-carrier lifetimes in TiO_2 powders studied by microwave absorption. J. Mater. Sci., 2003. 38(11): 2429-2437.
216. Sumita T., T. Yamaki, S. Yamamoto, A. Miyashita, Photo-induced surface charge separation of highly oriented TiO_2 anatase and rutile thin films. Appl. Surf. Sci., 2002. 200(1–4): 21-26.
217. Bezrodna, T., G. Puchkovska, V. Shimanovska, I. Chashechnikova, T. Khalyavka, J. Baran, Pyridine-TiO_2 surface interaction as a probe for surface active centers analysis. Appl. Surf. Sci., 2003. 214(1–4): 222-231.
218. Torimoto T., N. Nakamura, S. Ikeda, B. Ohtani, Discrimination of the active crystalline phases in anatase-rutile mixed titanium(iv) oxide photocatalysts through action spectrum analyses. Phys. Chem. Chem. Phys., 2002. 4(23): 5910-5914.

219. Karakitsou K.E., X.E. Verykios, Effects of altervalent cation doping of titania on its performance as a photocatalyst for water cleavage. J. Phys. Chem., 1993. 97(6): 1184-1189.

220. Jitputti J., Y. Suzuki, S. Yoshikawa, Synthesis of TiO_2 nanowires and their photocatalytic activity for hydrogen evolution. Catal. Commun., 2008. 9(6): 1265-1271.

221. Goto H., Y. Hanada, T. Ohno, M. Matsumura, Quantitative analysis of superoxide ion and hydrogen peroxide produced from molecular oxygen on photoirradiated TiO_2 particles. J. Catal., 2004. 225(1): p. 223-229.

222. Andersson M., L. Österlund, S. Ljungström, A. Palmqvist, Preparation of Nanosize Anatase and Rutile TiO_2 by Hydrothermal Treatment of Microemulsions and Their Activity for Photocatalytic Wet Oxidation of Phenol. J. Phys. Chem. B, 2002. 106(41): 10674-10679.

223. Yang D., H. Liu, Z. Zheng, Y. Yuan, J. C. Zhao, E.R. Waclawik, X. Ke, H. Zhu, An efficient photocatalyst structure: TiO_2(B) nanofibers with a shell of anatase nanocrystals. J. Am. Chem. Soc., 2009. 131(49): 17885-17893.

224. Park N.G., J. van de Lagemaat, A.J. Frank, Comparison of Dye-Sensitized Rutile- and Anatase-Based TiO_2 Solar Cells. J. Phys. Chem. B, 2000. 104(38): 8989-8994.

225. Riegel G.,J.R. Bolton, Photocatalytic Efficiency Variability in TiO_2 Particles. J. Phys. Chem., 1995. 99(12): 4215-4224.

226. Torimoto T., N. Nakamura, S. Ikeda, B. Ohtani, Discrimination of the active crystalline phases in anatase–rutile mixed titanium (IV) oxide photocatalysts through action spectrum analyses. Phys. Chem. Chem. Phys., 2002. 4(23): 5910-5914.

227. Sclafani, A., J.M. Herrmann, Comparison of the Photoelectronic and Photocatalytic Activities of Various Anatase and Rutile Forms of Titania in Pure Liquid Organic Phases and in Aqueous Solutions. J. Phys. Chem., 1996. 100(32): 13655-13661.

228. Lucarelli L., V. Nadtochenko, J. Kiwi, Environmental Photochemistry: Quantitative Adsorption and FTIR Studies during the TiO_2-Photocatalyzed Degradation of Orange II. Langmuir, 1999. 16(3): 1102-1108.

229. Stafford U.G., K. A. Kamat, P. V. Varma, Chemical Mechanism of Inorganic Oxidants in the TiO_2/UV Process: Increased Rates of Degradation of Chlorinated Hydrocarbons. Chem. Phys. Lett., 1993,: 205, 55.

230. Bahnemann D.W.B., D. Goslich, R.; Hilgendorff, M.; Weichgrebe, D., Photocatalytic Purification and Treatment of Water and Air Elsevier Science Publishers: Amsterdam, 1993.

231. Nishimoto S., B. Ohtani, H. Kajiwara, T. Kagiya, Correlation of the crystal structure of titanium dioxide prepared from titanium tetra-2-propoxide with the photocatalytic activity for redox reactions in aqueous propan-2-ol and silver salt solutions. J. Chem. Soc., Faraday Trans. 1: Phys. Chem. Cond. Phases, 1985. 81(1): 61-68.

232. Ohno T., D. Haga, K. Fujihara, K. Kaizaki, M. Matsumura, Unique Effects of Iron(III) Ions on Photocatalytic and Photoelectrochemical Properties of Titanium Dioxide. J. Phys. Chem. B, 1997. 101(33): 6415-6419.

233. Liu L., H. Zhao, J.M. Andino, Y. Li, Photocatalytic CO_2 reduction with H_2O on TiO_2 nanocrystals: Comparison of anatase, rutile, and brookite polymorphs and exploration of surface chemistry. ACS Catal., 2012. 2(8): 1817-1828.

234. Zhang H., J.F. Banfield, Understanding Polymorphic Phase Transformation Behavior during Growth of Nanocrystalline Aggregates: Insights from TiO_2. J. Phys. Chem. B, 2000. 104(15): 3481-3487.

235. Hu Y., H.L. Tsai, C.L. Huang, Effect of brookite phase on the anatase–rutile transition in titania nanoparticles. J. Eur. Ceramic Soc., 2003. 23(5): 691-696.

236. Zhang Q., L. Gao, J. Guo, Effects of calcination on the photocatalytic properties of nanosized TiO_2 powders prepared by $TiCl_4$ hydrolysis. Appl. Catal. B-Environ., 2000. 26(3): 207-215.

237. Muscat J., V. Swamy, N.M. Harrison, First-principles calculations of the phase stability of TiO_2. Phys. Rev. B, 2002. 65(22): 224112.

238. Levchenko A.A., G. Li, J. Boerio-Goates, B.F. Woodfield, A. Navrotsky, TiO_2 Stability Landscape: Polymorphism, Surface Energy, and Bound Water Energetics. Chem. Mater., 2006. 18(26): 6324-6332.

239. Gribb A.A., J.F. Banfield, Particle size effects on transformation kinetics and phase stability in nanocrystalline TiO_2. Am. Mineral., 1997. 82(7): 717-728.

240. Diebold U., N. Ruzycki, G.S. Herman, A. Selloni, One step towards bridging the materials gap: surface studies of TiO_2 anatase. Catal. Today, 2003. 85(2): 93-100.

241. Zhang H., M. Finnegan, J.F. Banfield, preparing single-phase nanocrystalline anatase from amorphous titania with particle sizes tailored by temperature. Nano Lett., 2000. 1(2): 81-85.

242. Banfield J., Thermodynamic analysis of phase stability of nanocrystalline titania. J. Mater. Chem., 1998. 8(9): 2073-2076.

243. Saponjic Z.V., N.M. Dimitrijevic, D.M. Tiede, A.J. Goshe, X. Zuo, L.X. Chen, A.S. Barnard, P. Zapol, L. Curtiss, T. Rajh, Shaping Nanometer-Scale Architecture Through Surface Chemistry. Adv. Mater., 2005. 17(8): 965-971.

244. Li W., C. Ni, H. Lin, C. Huang, S.I. Shah, Size dependence of thermal stability of TiO_2 nanoparticles. J. Appl. Phys., 2004. 96(11): 6663-6668.

245. Testino A., I.R. Bellobono, V. Buscaglia, C. Canevali, M. D'Arienzo, S. Polizzi, R. Scotti, F. Morazzoni, Optimizing the Photocatalytic Properties of Hydrothermal TiO_2 by the Control of Phase Composition and Particle Morphology. A Systematic Approach. J. Am. Chem. Soc., 2007. 129(12): 3564-3575.

246. Hu Y., H. L. Tsai, C.L. Huang, Phase transformation of precipitated TiO_2 nanoparticles. Mater. Sci. Eng. A, 2003. 344(1): 209-214.

247. Yu J. G., H. G. Yu, B. Cheng, X. J. Zhao, J.C. Yu, W. K. Ho, The effect of calcination temperature on the surface microstructure and photocatalytic activity of TiO_2 thin films prepared by liquid phase deposition. J. Phys. Chem. B, 2003. 107(50): 13871-13879.

248. You X., F. Chen, J. Zhang, Effects of calcination on the physical and photocatalytic properties of TiO_2 powders prepared by sol–gel template method. J. Sol-Gel Sci. Technol., 2005. 34(2): 181-187.

249. Zhang H., J.F. Banfield, Polymorphic Transformations and Particle Coarsening in Nanocrystalline Titania Ceramic Powders and Membranes. J. Phys. Chem. C, 2007. 111(18): 6621-6629.

250. Zhang H., J.F. Banfield, Size Dependence of the Kinetic Rate Constant for Phase Transformation in TiO_2 Nanoparticles. Chem. Mater., 2005. 17(13): 3421-3425.

251. Banfield J.F., B.L. Bischoff, M.A. Anderson, TiO_2 accessory minerals: coarsening, and transformation kinetics in pure and doped synthetic nanocrystalline materials. Chem. Geology, 1993. 110(1–3): 211-231.

252. Zhang, J., M. Li, Z. Feng, J. Chen, C. Li, UV Raman Spectroscopic Study on TiO_2. Phase Transformation at the Surface and in the Bulk. J. Phys. Chem. B, 2005. 110(2): 927-935.

253. Zhang J., Y. Hu, M. Matsuoka, H. Yamashita, M. Minagawa, H. Hidaka, M. Anpo, Relationship between the Local Structures of Titanium Oxide Photocatalysts and

Their Reactivities in the Decomposition of NO. J. Phys. Chem. B, 2001. 105(35): 8395-8398.

254. Anpo M.,J.M. Thomas, Single-site photocatalytic solids for the decomposition of undesirable molecules. Chem. Commun., 2006(31): 3273-3278.
255. Lin W., H. Frei, Photochemical CO_2 Splitting by Metal-to-Metal Charge-Transfer Excitation in Mesoporous ZrCu(I)-MCM-41 Silicate Sieve. J. Am. Chem. Soc., 2005. 127(6): 1610-1611.
256. Lin W., H. Han, H. Frei, CO_2 Splitting by H_2O to CO and O_2 under UV Light in TiMCM-41 Silicate Sieve. J. Phys. Chem. B, 2004. 108(47): 18269-18273.
257. Liu Z., R.J. Davis, Investigation of the Structure of Microporous Ti-Si Mixed Oxides by X-ray, UV Reflectance, FT-Raman, and FT-IR Spectroscopies. J. Phys. Chem., 1994. 98(4): 1253-1261.
258. Notari B., R.J. Willey, M. Panizza, G. Busca, Which sites are the active sites in TiO_2–SiO_2 mixed oxides? Catal. Today, 2006. 116(2): 99-110.
259. Hurum D.C., A.G. Agrios, S.E. Crist, K.A. Gray, T. Rajh, M.C. Thurnauer, Probing reaction mechanisms in mixed phase TiO_2 by EPR. J. Electron Spectrosc., 2006. 150(2–3): 155-163.
260. Wu C., Y. Yue, X. Deng, W. Hua, Z. Gao, Investigation on the synergetic effect between anatase and rutile nanoparticles in gas-phase photocatalytic oxidations. Catal. Today, 2004. 93–95(0): 863-869.
261. Hurum D.C., A.G. Agrios, K.A. Gray, T. Rajh, M.C. Thurnauer, Explaining the Enhanced Photocatalytic Activity of Degussa P25 Mixed-Phase TiO_2 Using EPR. The J. Phys. Chem. B, 2003. 107(19): 4545-4549.
262. Li G., L. Chen, M.E. Graham, K.A. Gray, A comparison of mixed phase titania photocatalysts prepared by physical and chemical methods: The importance of the solid–solid interface. J. Mol. Catal A-Chem., 2007. 275(1–2): 30-35.
263. Liu Z., X. Zhang, S. Nishimoto, M. Jin, D.A. Tryk, T. Murakami, A. Fujishima, Anatase TiO_2 nanoparticles on rutile TiO_2 nanorods: A heterogeneous nanostructure via layer-by-layer assembly. Langmuir, 2007. 23(22): 10916-10919.
264. Hurum D.C., K.A. Gray, T. Rajh, M.C. Thurnauer, Recombination Pathways in the Degussa P25 Formulation of TiO_2: Surface versus Lattice Mechanisms. J. Phys. Chem. B, 2004. 109(2): 977-980.

265. Li G., N.M. Dimitrijevic, L. Chen, J.M. Nichols, T. Rajh, K.A. Gray, The Important Role of Tetrahedral Ti^{4+} Sites in the Phase Transformation and Photocatalytic Activity of TiO_2 Nanocomposites. J. Am. Chem. Soc., 2008. 130(16): 5402-5403.

266. Kominami H., J. Kato, S. Murakami, Y. Ishii, M. Kohno, K. Yabutani, T. Yamamoto, Y. Kera, M. Inoue, T. Inui, B. Ohtani, Solvothermal syntheses of semiconductor photocatalysts of ultra-high activities. Catal. Today, 2003. 84(3–4): 181-189.

267. Wang, C.C., J.Y. Ying, Sol−Gel Synthesis and Hydrothermal Processing of Anatase and Rutile Titania Nanocrystals. Chem. Mater., 1999. 11(11): 3113-3120.

268. Sreethawong T., Y. Suzuki, S. Yoshikawa, Synthesis, characterization, and photocatalytic activity for hydrogen evolution of nanocrystalline mesoporous titania prepared by surfactant-assisted templating sol–gel process. J. Solid State Chem., 2005. 178(1): 329-338.

269. Sreethawong T., Y. Suzuki, S. Yoshikawa, Photocatalytic evolution of hydrogen over nanocrystalline mesoporous titania prepared by surfactant-assisted templating sol–gel process. Catal. Commun., 2005. 6(2): 119-124.

270. Korzhak A.V., N.I. Ermokhina, A.L. Stroyuk, V.K. Bukhtiyarov, A.E. Raevskaya, V.I. Litvin, S.Y. Kuchmiy, V.G. Ilyin, P.A. Manorik, Photocatalytic hydrogen evolution over mesoporous TiO_2/metal nanocomposites. J. Photochem. Photobiol. A-Chem., 2008. 198(2-3): 126-134.

271. Ohtani B., Y. Ogawa, S. Nishimoto, Photocatalytic activity of amorphous-anatase mixture of titanium (IV) oxide particles suspended in aqueous solutions. J. Phys. Chem. B, 1997. 101(19): 3746-3752.

272. Li Z., B. Hou, Y. Xu, D. Wu, Y. Sun, W. Hu, F. Deng, Comparative study of sol–gel-hydrothermal and sol–gel synthesis of titania–silica composite nanoparticles. J. Solid State Chem., 2005. 178(5): 1395-1405.

273. Djaoued Y., S. Badilescu, P. Ashrit, D. Bersani, P. Lottici, J. Robichaud, Study of anatase to rutile phase transition in nanocrystalline titania films. J. Sol-Gel Sci. Technol., 2002. 24(3): 255-264.

274. Long M., W. Cai, H. Chen, J. Xu, Preparation, characterization and photocatalytic activity of visible light driven chlorine-doped TiO_2. Front. Chem. China, 2007. 2(3): 278-282.

275. Yu J.C., J. Yu, W. Ho, Z. Jiang, L. Zhang, Effects of F-doping on the photocatalytic activity and microstructures of nanocrystalline TiO_2 powders. Chem. Mater., 2002. 14(9): 3808-3816.

276. Todorova N., T. Giannakopoulou, G. Romanos, T. Vaimakis, J. Yu, C. Trapalis, Preparation of Fluorine-Doped TiO_2 Photocatalysts with Controlled Crystalline Structure. Int. J. Photoenergy, 2008. 2008.

277. Teoh W.Y., L. Mädler, D. Beydoun, S.E. Pratsinis, R. Amal, Direct (one-step) synthesis of TiO_2 and Pt/TiO_2 nanoparticles for photocatalytic mineralisation of sucrose. Chem. Eng. Sci., 2005. 60(21): 5852-5861.

278. Huang B.S., F.Y. Chang, M.Y. Wey, Photocatalytic properties of redox-treated Pt/TiO_2 photocatalysts for H_2 production from an aqueous methanol solution. Int. J. Hydrogen Energy, 2010. 35(15): 7699-7705.

279. Huang B.S., F.Y. Chang, M.Y. Wey, Photocatalytic properties of redox-treated Pt/TiO_2 photocatalysts for H_2 production from an aqueous methanol solution. Int. J Hydrogen Energy, 2010. 35(15): 7699-7705.

280. Melián E.P., O.G. Díaz, A.O. Méndez, C.R. López, M.N. Suárez, J.D. Rodríguez, J. Navío, D.F. Hevia, J.P. Peña, Efficient and affordable hydrogen production by water photo-splitting using TiO_2-based photocatalysts. Int. J. Hydrogen Energy, 2013. 38(5): 2144-2155.

281. Liu R., H. Yoshida, S. Fujita, M. Arai, Photocatalytic hydrogen production from glycerol and water with NiO_x/TiO_2 catalysts. Appl. Catal. B-Environ., 2014. 144: 41-45.

282. Saif M., M. Abdel-Mottaleb, Titanium dioxide nanomaterial doped with trivalent lanthanide ions of Tb, Eu and Sm: preparation, characterization and potential applications. Inorganica. Chimica. Acta, 2007. 360(9): 2863-2874.

283. Wang Z., D. Xia, G. Chen, T. Yang, Y. Chen, The effects of different acids on the preparation of TiO_2 nanostructure in liquid media at low temperature. Mater. Chem. Phys., 2008. 111(2): 313-316.

284. Sun H., H. Liu, J. Ma, X. Wang, B. Wang, L. Han, Preparation and characterization of sulfur-doped TiO_2/Ti photoelectrodes and their photoelectrocatalytic performance. J. Hazard. Mater., 2008. 156(1): 552-559.

285. Sun T., J. Fan, E. Liu, L. Liu, Y. Wang, H. Dai, Y. Yang, W. Hou, X. Hu, Z. Jiang, Fe and Ni co-doped TiO_2 nanoparticles prepared by alcohol-thermal method: Application in hydrogen evolution by water splitting under visible light irradiation. Powder Technol., 2012. 228: 210-218.

286. Kang M., Synthesis of Fe/TiO_2 photocatalyst with nanometer size by solvothermal method and the effect of H_2O addition on structural stability and photodecomposition of methanol. J. Mol. Catal. A-Chem., 2003. 197(1): 173-183.

287. Pan L., J. J. Zou, X. Zhang, L. Wang, Photoisomerization of norbornadiene to quadricyclane using transition metal doped TiO_2. Indus. Eng. Chem. Res., 2010. 49(18): 8526-8531.

288. Luo H., T. Takata, Y. Lee, J. Zhao, K. Domen, Yan, Photocatalytic Activity Enhancing for Titanium Dioxide by Co-doping with Bromine and Chlorine. Chem. Mater., 2004. 16(5): 846-849.

289. Pulido Melián, E., O. González Díaz, A. Ortega Méndez, C.R. López, M. Nereida Suárez, J. Doña Rodríguez, J. Navío, D. Fernández Hevia, J. Pérez Peña, Efficient and affordable hydrogen production by water photo-splitting using TiO_2-based photocatalysts. Int. J. Hydrogen Energy, 2013. 38(5): 2144-2155.

290. Ding J., T.J. McAvoy, R.E. Cavicchi, S. Semancik, Surface state trapping models for SnO_2-based microhotplate sensors. Sensors Actuat. B-Chem., 2001. 77(3): 597-613.

291. Anpo M., K. Chiba, M. Tomonari, S. Coluccia, M. Che, M.A. Fox, Photocatalysis on Native and Platinum-Loaded TiO_2 and ZnO Catalysts; Origin of Different Reactivities on Wet and Dry Metal Oxide. Bull. Chem. Soc. Japan, 1991. 64(2): 543-551.

292. Gas'kov A.M.,M.N. Rumyantseva, Nature of Gas Sensitiv.ity in Nanocrystalline Metal Oxides. Russ. J. Appl. Chem., 2001. 74(3): 440-444.

293. Kavan L., M. Grätzel, S.E. Gilbert, C. Klemenz, H.J. Scheel, Electrochemical and Photoelectrochemical Investigation of Single-Crystal Anatase. J. Am. Chem. Soc., 1996. 118(28): 6716-6723.

294. Shen Q., K. Katayama, T. Sawada, M. Yamaguchi, Y. Kumagai, T. Toyoda, Photoexcited hole dynamics in TiO_2 nanocrystalline films characterized using a lens-free heterodyne detection transient grating technique. Chem. Phys. Lett., 2006. 419(4–6): 464-468.

295. Sumita T., T. Yamaki, S. Yamamoto, A. Miyashita, Photo-induced surface charge separation of highly oriented TiO_2 anatase and rutile thin films. Appl. Surf. Sci., 2002. 200(1): 21-26.

296. Taishi Sumita, T.Y., Shunya Yamamoto and Atsumi Miyashita,, A new characterization method of photocatalytic activity in semiconductor photocatalysts. department of materials development, Japan Atomic Energy Research Institute, Watanuki 1233, Takasaki, Gunma 370-1292, Japan, 2001.

297. Kavan L., M. Grätzel, S. Gilbert, C. Klemenz, H. Scheel, Electrochemical and photoelectrochemical investigation of single-crystal anatase. J. Am. Chem. Soc., 1996. 118(28): 6716-6723.

298. Ohno T., D. Haga, K. Fujihara, K. Kaizaki, M. Matsumura, Unique effects of iron (III) ions on photocatalytic and photoelectrochemical properties of titanium dioxide. J. Phys. Chem. B, 1997. 101(33): 6415-6419.

299. Schindler, K.M.,M. Kunst, Charge-carrier dynamics in titania powders. J. Phys. Chem., 1990. 94(21): 8222-8226.

300. Xu M., Y. Gao, E.M. Moreno, M. Kunst, M. Muhler, Y. Wang, H. Idriss, C. Wöll, Photocatalytic Activity of Bulk TiO_2 Anatase and Rutile Single Crystals Using Infrared Absorption Spectroscopy. Phys. Rev. Lett., 2011. 106(13): 138-302.

301. Bezrodna T., G. Puchkovska, V. Shimanovska, I. Chashechnikova, T. Khalyavka, J. Baran, Pyridine-TiO_2 surface interaction as a probe for surface active centers analysis. Appl. Surf. Sci., 2003. 214(1): 222-231.

302. Nadeem M.A., K.A. Connelly, H. Idriss, The photoreaction of TiO_2 single crystal and powder with organic adsorbates. Int. J. Nanotechnol., 2012. 9(1): 121-162.

303. Shockley W., W.T. Read, Jr., Statistics of the Recombinations of Holes and Electrons. Phys. Rev., 1952. 87(5): 835-842.

304. Hall R.N., Electron-Hole Recombination in Germanium. Phys. Rev., 1952. 87(2): 387-387.

305. Zhang Z., J.T. Yates, Direct Observation of Surface-Mediated Electron–Hole Pair Recombination in TiO_2(110). J. Phys. Chem. C, 2010. 114(7): 3098-3101.

306. Liqiang J., Q. Yichun, W. Baiqi, L. Shudan, J. Baojiang, Y. Libin, F. Wei, F. Honggang, S. Jiazhong, Review of photoluminescence performance of nano-sized semiconductor materials and its relationships with photocatalytic activity. Sol. Energy Mater. Sol. C, 2006. 90(12): 1773-1787.

307. Agrios A.G., P. Pichat, Recombination rate of photogenerated charges versus surface area: Opposing effects of TiO_2 sintering temperature on photocatalytic removal of phenol, anisole, and pyridine in water. J. Photochem. Photobiol. A-Chem., 2006. 180(1): 130-135.

308. Enríquez R., A.G. Agrios, P. Pichat, Probing multiple effects of TiO_2 sintering temperature on photocatalytic activity in water by use of a series of organic pollutant molecules. Catal. Today, 2007. 120(2): 196-202.

309. Xu Z.L., T.S. Chung, Y. Huang, Effect of polyvinylpyrrolidone molecular weights on morphology, oil/water separation, mechanical and thermal properties of polyetherimide/polyvinylpyrrolidone hollow fiber membranes. J. Appl. Polymer Sci., 1999. 74(9): 2220-2233.

310. Stroyuk A.L., A.I. Kryukov, S.Y. Kuchmii, V.D. Pokhodenko, Quantum Size Effects in Semiconductor Photocatalysis. Theor. Exp. Chem., 2005. 41(4): 207-228.

311. Serpone N., Relative photonic efficiencies and quantum yields in heterogeneous photocatalysis. J. Photochem. Photobiol. A-Chem., 1997. 104(1): 1-12.

312. Nadeem M., K. Connelly, H. Idriss, The photoreaction of TiO_2 and Au/TiO_2 single crystal and powder with organic adsorbates. Int. J. Nanotechnol., 2012. 9(1):121-162.

313. Connelly K.A.,H. Idriss, The photoreaction of TiO_2 and Au/TiO_2 single crystal and powder surfaces with organic adsorbates. Emphasis on hydrogen production from renewables. Green Chem., 2012. 14(2):260-280.

314. Peng K.Q., X. Wang, X.L. Wu, S.T. Lee, Platinum nanoparticle decorated silicon nanowires for efficient solar energy conversion. Nano Lett., 2009. 9(11): 3704-3709.

315. Nakato Y., H. Tsubomura, Structures and functions of thin metal layers on semiconductor electrodes. J. Photochem., 1985. 29(1–2): 257-266.

316. Sreethawong T., S. Yoshikawa, Enhanced photocatalytic hydrogen evolution over Pt supported on mesoporous TiO_2 prepared by single-step sol–gel process with surfactant template. Int. J. Hydrogen Energy, 2006. 31(6): 786-796.

317. Jakob M., H. Levanon, P.V. Kamat, Charge distribution between UV-irradiated TiO_2 and gold nanoparticles: determination of shift in the Fermi level. Nano Lett., 2003. 3(3): 353-358.

318. Galinska A., J. Walendziewski, Photocatalytic water splitting over $Pt\text{-}TiO_2$ in the presence of sacrificial reagents. Energ. Fuels, 2005. 19(3): 1143-1147.

319. Engweiler J., J. Harf, A. Baiker, WO_x/TiO_2 Catalysts Prepared by Grafting of Tungsten Alkoxides: Morphological Properties and Catalytic Behavior in the Selective Reduction of NO by NH_3. J. Catal., 1996. 159(2): 259-269.

320. Vinodgopal K., P.V. Kamat, Enhanced rates of photocatalytic degradation of an azo dye using SnO_2/TiO_2 coupled semiconductor thin films. Environ. Sci. Technol., 1995. 29(3): 841-845.

321. Maira A., K. Yeung, C. Lee, P. Yue, C. Chan, Size Effects in Gas-Phase Photo-oxidation of Trichloroethylene Using Nanometer-Sized TiO_2 Catalysts. J. Catal., 2000. 192(1): 185-196.

322. Khan S.U., M. Al-Shahry, W.B. Ingler, Efficient photochemical water splitting by a chemically modified n-TiO_2. Science, 2002. 297(5590): 2243-2245.

323. Abe R., K. Sayama, H. Arakawa, Efficient hydrogen evolution from aqueous mixture of I^- and acetonitrile using a merocyanine dye-sensitized Pt/TiO_2 photocatalyst under visible light irradiation. Chem. Phys. Lett., 2002. 362(5): 441-444.

324. Alonso-Vante, N., H. Colell, H. Tributsch, Influence of low temp. and electrical field strength on oxygen evolution (photo) catalysis with n-ruthenium disulfide electrodes. J. Phys. Chem., 1993. 97(31): 8261-8268.

325. Zieliñska B., E. Borowiak-Palen, R.J. Kalenczuk, Photocatalytic hydrogen generation over alkaline-earth titanates in the presence of electron donors. Int. J. Hydrogen Energy, 2008. 33(7): 1797-1802.

326. Yu, J., J. Ran, Facile preparation and enhanced photocatalytic H_2-production activity of $Cu(OH)_2$ cluster modified TiO_2. Energy Environ. Sci., 2011. 4(4): 1364-1371.

327. Bandara J., H. Weerasinghe, Solid-state dye-sensitized solar cell with p-type NiO as a hole collector. Sol. Energy Mater. Sol. C., 2005. 85(3): 385-390.

328. Bandara J., C.P.K. Udawatta, C.S.K. Rajapakse, Highly stable CuO incorporated TiO_2 catalyst for photocatalytic hydrogen production from H_2O. Photochem. Photobiol. Sci., 2005. 4(11): 857-861.

329. Yin H., Y. Wada, T. Kitamura, S. Kambe, S. Murasawa, H. Mori, T. Sakata, S. Yanagida, Hydrothermal synthesis of nanosized anatase and rutile TiO_2 using amorphous phase TiO_2. J. Mater. Chem., 2001. 11(6): 1694-1703.

330. Luis A., M. Neves, M. Mendonça, O. Monteiro, Influence of calcination parameters on the TiO_2 photocatalytic properties. Mater. Chem. Phys., 2011. 125(1): 20-25.

331. Zhang S., H. Wang, M. Yeung, Y. Fang, H. Yu, F. Peng, $Cu(OH)_2$-modified TiO_2 nanotube arrays for efficient photocatalytic hydrogen production. Int. J. Hydrogen Energy, 2013. 38(18): 7241-7245.

332. Murdoch M., G. Waterhouse, M. Nadeem, J. Metson, M. Keane, R. Howe, J. Llorca, H. Idriss, The effect of gold loading and particle size on photocatalytic hydrogen production from ethanol over Au/TiO_2 nanoparticles. Nat. Chem., 2011. 3(6): 489-492.

333. Henderson M.A., W.S. Epling, C.H. Peden, C.L. Perkins, Insights into photoexcited electron scavenging processes on TiO_2 obtained from studies of the reaction of O_2 with OH groups adsorbed at electronic defects on TiO_2(110). J. Phys. Chem. B, 2003. 107(2): 534-545.

334. Peral J., X. Domènech, D.F. Ollis, Heterogeneous photocatalysis for purification, decontamination and deodorization of air. J. Chem. Technol. Biotechnol., 1997. 70(2): 117-140.

335. Bedja I., P.V. Kamat, Capped semiconductor colloids. Synthesis and photoelectrochemical behavior of TiO_2 capped SnO_2 nanocrystallites. J. Phys. Chem., 1995. 99(22): 9182-9188.

336. Zhang Z., J.T. Yates Jr, Direct observation of surface-mediated electron− hole pair recombination in TiO_2 (110). J. Phys. Chem. C, 2010. 114(7): 3098-3101.

337. Palmer F.L., B.R. Eggins, H.M. Coleman, The effect of operational parameters on the photocatalytic degradation of humic acid. J. Photochem. Photobiol. A-Chem., 2002. 148(1): 137-143.

338. Lathasree S., A.N. Rao, B. SivaSankar, V. Sadasivam, K. Rengaraj, Heterogeneous photocatalytic mineralisation of phenols in aqueous solutions. J. Mol. Catal. A-Chem., 2004. 223(1): 101-105.

339. Das D.P., K. Parida, B.R. De, Photocatalytic reduction of hexavalent chromium in aqueous solution over titania pillared zirconium phosphate and titanium phosphate under solar radiation. J. Mol. Catal. A-Chem., 2006. 245(1): 217-224.

340. Parks G.A., The isoelectric points of solid oxides, solid hydroxides, and aqueous hydroxo complex systems. Chem. Rev., 1965. 65(2): 177-198.

341. Van Riemsdijk, W., G. Bolt, L. Koopal, J. Blaakmeer, Electrolyte adsorption on heterogeneous surfaces: adsorption models. J. Colloid Interface Sci., 1986. 109(1): 219-228.

342. Fujita S., H. Kawamori, D. Honda, H. Yoshida, M. Arai, Photocatalytic hydrogen production from aqueous glycerol solution using NiO/TiO_2 catalysts: Effects of preparation and reaction conditions. Appl. Catal. B-Environ., 2016. 181: 818-824.

343. Wu Y., G. Lu, S. Li, The Role of Cu(I) Species for Photocatalytic Hydrogen Generation Over CuO_x/TiO_2. Catal. Lett., 2009. 133(1-2): 97-105.

344. Bacsa R., J. Kiwi, Effect of rutile phase on the photocatalytic properties of nanocrystalline titania during the degradation of p-coumaric acid. Appl. Catal. B-Environ., 1998. 16(1): 19-29.

345. Yu J., B. Wang, Effect of calcination temperature on morphology and photoelectrochemical properties of anodized titanium dioxide nanotube arrays. Appl. Catal. B-Environ., 2010. 94(3): 295-302.

346. Araña Mesa, F.J., J.M. Doña-Rodríguez, D. Portillo-Carrizo, C. Fernández Rodríguez, J. Pérez Peña, O.M. Gonzalez-Diaz, J. Navío, M. Macías, Photocatalytic degradation of phenolic compounds with new TiO_2 catalysts. 2010.

347. Pulido Melián, E., O. González Díaz, J. Doña Rodríguez, G. Colón, J. Navío, J. Pérez Peña, Effect of hydrothermal treatment on structural and photocatalytic properties of TiO_2 synthesized by sol–gel method. Appl. Catal. A-Gen., 2012. 411:153-159.

348. Yu J., H. Yu, B. Cheng, M. Zhou, X. Zhao, Enhanced photocatalytic activity of TiO_2 powder (P25) by hydrothermal treatment. J. Mol. Catal. A-Chem., 2006. 253(1): 112-118.

349. Komaguchi K., H. Nakano, A. Araki, Y. Harima, Photoinduced electron transfer from anatase to rutile in partially reduced TiO_2(P-25) nanoparticles: An ESR study. Chem. Phys. Lett., 2006. 428(4–6): 338-342.

350. Bacsa R.R., J. Kiwi, Effect of rutile phase on the photocatalytic properties of nanocrystalline titania during the degradation of p-coumaric acid. Appl. Catal. B-Environ., 1998. 16(1): 19-29.

351. Sun B.,P.G. Smirniotis, Interaction of anatase and rutile TiO_2 particles in aqueous photooxidation. Catal. Today, 2003. 88(1–2): 49-59.

352. Sayama K.,H. Arakawa, Significant effect of carbonate addition on stoichiometric photodecomposition of liquid water into hydrogen and oxygen from platinum–titanium (IV) oxide suspension. J. Chem. Soc., Chem. Commun., 1992(2): 150-152.

353. Bickley R.I., T. Gonzalez-Carreno, J.S. Lees, L. Palmisano, R.J. Tilley, A structural investigation of titanium dioxide photocatalysts. J. Solid State Chem., 1991. 92(1): 178-190.

354. Sun B., A.V. Vorontsov, P.G. Smirniotis, role of platinum deposited on TiO_2 in phenol photocatalytic oxidation. Langmuir, 2003. 19(8): 3151-3156.

355. Leytner S., J.T. Hupp, Evaluation of the energetics of electron trap states at the nanocrystalline titanium dioxide/aqueous solution interface via time-resolved photoacoustic spectroscopy. Chem. Phys. Lett., 2000. 330(3): 231-236.

356. Ohno T., K. Sarukawa, K. Tokieda, M. Matsumura, Morphology of a TiO_2 photocatalyst (Degussa, P-25) consisting of anatase and rutile crystalline phases. J. Catal., 2001. 203(1): p. 82-86.

357. Emeline A.V., L.G. Smirnova, G.N. Kuzmin, L.L. Basov, N. Serpone, Spectral dependence of quantum yields in gas–solid heterogeneous photosystems: Influence of

anatase/rutile content on the photostimulated adsorption of dioxygen and dihydrogen on titania. J. Photochem. Photobiol. A-Chem., 2002. 148(1–3): . 97-102.

358. Tang H., K. Prasad, R. Sanjinès, P.E. Schmid, F. Lévy, Electrical and optical properties of TiO_2 anatase thin films. J. Appl. Phys., 1994. 75(4): 2042.
359. Kawahara T., Y. Konishi, H. Tada, N. Tohge, J. Nishii, S. Ito, A Patterned TiO_2(Anatase)/TiO_2(Rutile) Bilayer-Type Photocatalyst: Effect of the Anatase/Rutile Junction on the Photocatalytic Activity. Angew. Chemie, 2002. 114(15): 2935-2937.
360. Jiang D., S. Zhang, H. Zhao, photocatalytic degradation characteristics of different organic compounds at TiO_2 nanoporous film electrodes with mixed anatase/rutile phases. Environ. Sci. Technol., 2006. 41(1): 303-308.
361. Kawahara T., T. Ozawa, M. Iwasaki, H. Tada, Photocatalytic activity of rutile–anatase coupled TiO_2 particles prepared by a dissolution–reprecipitation method. J. Colloid Interface Sci., 2003. 267(2): 377-381.
362. Komaguchi K., H. Nakano, A. Araki, Y. Harima, Photoinduced electron transfer from anatase to rutile in partially reduced TiO_2(P-25) nanoparticles: An ESR study. Chem. Phys. Lett., 2006. 428(4): 338-342.
363. Hurum D.C., K.A. Gray, T. Rajh, M.C. Thurnauer, Photoinitiated Reactions of 2,4,6 TCP on Degussa P25 Formulation TiO_2: Wavelength-Sensitive Decomposition. The J. Phys. Chem. B, 2004. 108(42): 16483-16487.
364. Leytner S., J. T. Hupp, Evaluation of the energetics of electron trap states at the nanocrystalline titanium dioxide/aqueous solution interface via time-resolved photoacoustic spectroscopy. Chem. Phys. Lett., 2000. 330(3–4): 231-236.
365. Ohno T., K. Sarukawa, M. Matsumura, Photocatalytic activities of pure rutile particles isolated from TiO_2 powder by dissolving the anatase component in HF solution. J. Phys. Chem. B, 2001. 105(12): 2417-2420.
366. Kho Y.K., A. Iwase, W.Y. Teoh, L. Mädler, A. Kudo, R. Amal, Photocatalytic H_2 evolution over TiO_2 nanoparticles. The synergistic effect of anatase and rutile. J. Phys. Chem. C, 2010. 114(6): 2821-2829.
367. Zhang J., Q. Xu, Z. Feng, M. Li, C. Li, Importance of the Relationship between Surface Phases and Photocatalytic Activity of TiO_2. Angew. Chem. Int. Ed., 2008. 47(9): 1766-1769.
368. Jovic V., Z.H.N. Al-Azri, W.T. Chen, D. Sun-Waterhouse, H. Idriss, G.I.N. Waterhouse, Photocatalytic H_2 Production from Ethanol–Water Mixtures Over

Pt/TiO_2 and Au/TiO_2 Photocatalysts: A Comparative Study. Top. Catal., 2013. 56(12): 1139-1151.

369. Bowker M., Photocatalytic Hydrogen Production and Oxygenate Photoreforming. Catal. Lett., 2012. 142(8): 923-929.
370. Chen W. T., A. Chan, Z.H. Al-Azri, A.G. Dosado, M.A. Nadeem, D. Sun-Waterhouse, H. Idriss, G.I. Waterhouse, Effect of TiO_2 polymorph and alcohol sacrificial agent on the activity of Au/TiO_2 photocatalysts for H_2 production in alcohol–water mixtures. J. Catal., 2015. 329: 499-513.
371. Chen W., D. Wang, X. Du, Y. He, S. Chen, Q. Shao, C. Ma, B. Huang, A. Chen, P. Zhao, X. Qu, X. Li, Glioma cells escaped from cytotoxicity of temozolomide and vincristine by communicating with human astrocytes. Med. Oncol., 2015. 32(3): 1-13.
372. Xu S., D.D. Sun, Significant improvement of photocatalytic hydrogen generation rate over TiO_2 with deposited CuO. Int. J. Hydrogen Energy., 2009. 34(15): 6096-6104.
373. Choi H.J., M. Kang, Hydrogen production from methanol/water decomposition in a liquid photosystem using the anatase structure of Cu loaded TiO_2. Int. J. Hydrogen Energy, 2007. 32(16): 3841-3848.
374. Liu R., H. Yoshida, S.. Fujita, M. Arai, Photocatalytic hydrogen production from glycerol and water with NiO_x/TiO_2 catalysts. Appl. Catal. B-Environ., 2014. 144(0): 41-45.
375. Sreethawong T., Y. Suzuki, S. Yoshikawa, Photocatalytic evolution of hydrogen over mesoporous TiO_2 supported NiO photocatalyst prepared by single-step sol–gel process with surfactant template. Int. J. Hydrogen Energy, 2005. 30(10): 1053-1062.
376. Lalitha, K., G. Sadanandam, V.D. Kumari, M. Subrahmanyam, B. Sreedhar, N.Y. Hebalkar, Highly stabilized and finely dispersed Cu_2O/TiO_2: a promising visible sensitive photocatalyst for continuous production of hydrogen from glycerol: water mixtures. J. Phys. Chem. C, 2010. 114(50): 22181-22189.
377. Jing D., Y. Zhang, L. Guo, Study on the synthesis of Ni doped mesoporous TiO_2 and its photocatalytic activity for hydrogen evolution in aqueous methanol solution. Chem. Phys. Lett., 2005. 415(1): 74-78.
378. Chen W. T., V. Jovic, D. Sun-Waterhouse, H. Idriss, G.I.N. Waterhouse, The role of CuO in promoting photocatalytic hydrogen production over TiO_2. Int. J. Hydrogen Energy, 2013. 38(35): 15036-15048.

379. Xu B., L. Dong, Y. Chen, Influence of CuO loading on dispersion and reduction behavior of CuO/TiO_2 (anatase) system. J. Chem. Soc., Faraday Transactions, 1998. 94(13): 1905-1909.

380. Singh D.P., N.R. Neti, A.S.K. Sinha, O.N. Srivastava, Growth of Different Nanostructures of Cu_2O (Nanothreads, Nanowires, and Nanocubes) by Simple Electrolysis Based Oxidation of Copper. J. Phys. Chem. C, 2007. 111(4): 1638-1645.

381. Xu S., J. Ng, X. Zhang, H. Bai, D.D. Sun, Fabrication and comparison of highly efficient Cu incorporated TiO_2 photocatalyst for hydrogen generation from water. Int. J. Hydrogen Energy., 2010. 35(11): 5254-5261.

382. Kondo J., Cu_2O as a photocatalyst for overall water splitting under visible light irradiation. Chem. Commun., 1998(3): 357-358.

383. Morales J., J. Espinos, A. Caballero, A. Gonzalez-Elipe, J.A. Mejias, XPS study of interface and ligand effects in supported Cu_2O and CuO nanometric particles. J. Phys. Chem. B, 2005. 109(16): 7758-7765.

384. Sui Y., W. Fu, H. Yang, Y. Zeng, Y. Zhang, Q. Zhao, Y. Li, X. Zhou, Y. Leng, M. Li, Low temperature synthesis of Cu_2O crystals: shape evolution and growth mechanism. Crys. Growth Des., 2009. 10(1): 99-108.

385. Nian J.N., C.C. Hu, H. Teng, Electrodeposited p-type Cu_2O for H_2 evolution from photoelectrolysis of water under visible light illumination. Int. J. Hydrogen Energy., 2008. 33(12): 2897-2903.

386. Chen S., M. Paulose, C. Ruan, G.K. Mor, O.K. Varghese, D. Kouzoudis, C.A. Grimes, Electrochemically synthesized CdS nanoparticle-modified TiO_2 nanotube-array photoelectrodes: Preparation, characterization, and application to photoelectrochemical cells. J. Photochem. Photobiol. A-Chem., 2006. 177(2): 177-184.

387. Huang L., S. Zhang, F. Peng, H. Wang, H. Yu, J. Yang, S. Zhang, H. Zhao, Electrodeposition preparation of octahedral Cu_2O loaded TiO_2 nanotube arrays for visible light-driven photocatalysis. Scripta Materialia, 2010. 63(2): 159-161.

388. Mor G.K., O.K. Varghese, R.H. Wilke, S. Sharma, K. Shankar, T.J. Latempa, K.-S. Choi, C.A. Grimes, p-Type Cu− Ti− O nanotube arrays and their use in self-biased heterojunction photoelectrochemical diodes for hydrogen generation. Nano Lett., 2008. 8(7): 1906-1911.

389. Sakata, Y., T. Yamamoto, T. Okazaki, H. Imamura, S. Tsuchiya, Generation of visible light response on the photocatalyst of a copper ion containing TiO_2. Chem. Lett., 1998. 27(12): 1253-1254.

390. Gerischer, H., On the stability of semiconductor electrodes against photodecomposition. J. Electroanal. Chem. Interfacial Electrochem., 1977. 82(1): 133-143.

391. Praliaud, H., S. Mikhailenko, Z. Chajar, M. Primet, Surface and bulk properties of Cu–ZSM-5 and Cu/Al_2O_3 solids during redox treatments. Correlation with the selective reduction of nitric oxide by hydrocarbons. Appl. Catal. B-Environ., 1998. 16(4): 359-374.

392. Colon, G., M. Maicu, M.s. Hidalgo, J. Navio, Cu-doped TiO_2 systems with improved photocatalytic activity. Appl. Catal. B-Environ., 2006. 67(1): 41-51.

393. Irie, H., S. Miura, K. Kamiya, K. Hashimoto, Efficient visible light-sensitive photocatalysts: grafting Cu (II) ions onto TiO_2 and WO_3 photocatalysts. Chem. Phys. Lett., 2008. 457(1): 202-205.

394. Fujishima A., T.N. Rao, D.A. Tryk, Titanium dioxide photocatalysis. J. Photochem. Photobiol. C-Photochem. Rev., 2000. 1(1): 1-21.

395. Ko Y.G., W.Y. Lee, Effects of Nickel-Loading Method on the Water-Splitting Activity of a Layered $NiO_x/Sr_4Ti_3O_{10}$ Photocatalyst. Catal. Lett., 2002. 83(3-4): 157-160.

396. Xi Z., C. Li, L. Zhang, M. Xing, J. Zhang, Synergistic effect of Cu_2O/TiO_2 heterostructure nanoparticle and its high H_2 evolution activity. Int. J. Hydrogen Energy, 2014. 39(12):6345-6353.

397. Bandara J., C. Udawatta, C. Rajapakse, Highly stable CuO incorporated TiO_2 catalyst for photocatalytic hydrogen production from H_2O. Photochem. Photobiol. Sci., 2005. 4(11): 857-861.

398. Meyer B., A. Polity, D. Reppin, M. Becker, P. Hering, P. Klar, T. Sander, C. Reindl, J. Benz, M. Eickhoff, Binary copper oxide semiconductors: From materials towards devices. Physica. Status. Solid, 2012. 249(8): 1487-1509.

399. Paracchino A., J.C. Brauer, J. E. Moser, E. Thimsen, M. Graetzel, Synthesis and characterization of high-photoactivity electrodeposited Cu_2O solar absorber by photoelectrochemistry and ultrafast spectroscopy. J. Phys. Chem. C, 2012. 116(13): 7341-7350.

400. Paracchino, A., V. Laporte, K. Sivula, M. Grätzel, E. Thimsen, Highly active oxide photocathode for photoelectrochemical water reduction. Nat. Mater., 2011. 10(6): 456-461.

401. So W. W., K. J. Kim, S. J. Moon, Photo-production of hydrogen over the CdS–TiO_2 nano-composite particulate films treated with $TiCl_4$. Int. J. Hydrogen Energy, 2004. 29(3): 229-234.

402. Jang J.S., S.M. Ji, S.W. Bae, H.C. Son, J.S. Lee, Optimization of CdS/TiO_2 nano-bulk composite photocatalysts for hydrogen production from Na_2S/Na_2SO_3 aqueous electrolyte solution under visible light ($\lambda \geq$ 420 nm). J. photochem. photobiol.. A-Chem., 2007. 188(1): 112-119.

403. Jang J.S., S.H. Choi, H.G. Kim, J.S. Lee, Location and state of Pt in platinized CdS/TiO_2 photocatalysts for hydrogen production from water under visible light. J. Phys. Chem. C, 2008. 112(44): 17200-17205.

404. Jang J.S., H.G. Kim, U.A. Joshi, J.W. Jang, J.S. Lee, Fabrication of CdS nanowires decorated with TiO_2 nanoparticles for photocatalytic hydrogen production under visible light irradiation. Int. J. Hydrogen Energy, 2008. 33(21): 5975-5980.

405. Cao J., B. Xu, H. Lin, B. Luo, S. Chen, Novel heterostructured Bi_2S_3/BiOI photocatalyst: facile preparation, characterization and visible light photocatalytic performance. Dalton Trans., 2012. 41(37): 11482-11490.

406. Jiang J., X. Zhang, P. Sun, L. Zhang, ZnO/BiOI heterostructures: photoinduced charge-transfer property and enhanced visible-light photocatalytic activity. J. Phys. Chem. C, 2011. 115(42): 20555-20564.

407. Sarkar D., C.K. Ghosh, S. Mukherjee, K.K. Chattopadhyay, Three dimensional Ag_2O/TiO_2 type-II (p–n) nanoheterojunctions for superior photocatalytic activity. ACS Appl. Mater. Interfaces, 2012. 5(2): 331-337.

408. Wang X., G. Liu, G.Q. Lu, H.M. Cheng, Stable photocatalytic hydrogen evolution from water over ZnO–CdS core–shell nanorods. Int. J. Hydrogen Energy, 2010. 35(15): 8199-8205.

409. Shifu C., Z. Sujuan, L. Wei, Z. Wei, Study on the photocatalytic activity of p–n junction photocatalyst Cu_2O/TiO_2. J. Nanosci. Nanotechnol., 2009. 9(7): 4397-4403.

410. Chen Y., J.C. Crittenden, S. Hackney, L. Sutter, D.W. Hand, Preparation of a novel TiO_2-based pn junction nanotube photocatalyst. Environ. Sci. Technol., 2005. 39(5): 1201-1208.

411. Zheng L., Y. Zheng, C. Chen, Y. Zhan, X. Lin, Q. Zheng, K. Wei, J. Zhu, Network structured SnO_2/ZnO heterojunction nanocatalyst with high photocatalytic activity. Inorg. Chem., 2009. 48(5): 1819-1825.

412. Sinatra L., A. LaGrow, W. Peng, A. Kirmani, A. Amassian, H. Idriss, O. Bakr, A Au/Cu_2O–TiO_2 system for photo-catalytic hydrogen production. A pn-junction effect or a simple case of in situ reduction? J. Catal., 2015. 322: 109-117.

413. Cheng W. Y., T. H. Yu, K.J. Chao, S. Y. Lu, Cu_2O-decorated CdS nanostructures for high efficiency visible light driven hydrogen production. Int. J. Hydrogen Energy, 2013. 38(23): 9665-9672.

414. Sinatra L., A.P. LaGrow, W. Peng, A.R. Kirmani, A. Amassian, H. Idriss, O.M. Bakr, A Au/Cu_2O–TiO_2 system for photo-catalytic hydrogen production. A pn-junction effect or a simple case of in situ reduction? J. Catal., 2015. 322: 109-117.

415. Zhang S., B. Peng, S. Yang, Y. Fang, F. Peng, The influence of the electrodeposition potential on the morphology of Cu_2O/TiO_2 nanotube arrays and their visible-light-driven photocatalytic activity for hydrogen evolution. Int. J. Hydrogen Energy, 2013. 38(32): 13866-13871.

416. Sinatra L., A. LaGrow, W. Peng, A. Kirmani, A. Amassian, H. Idriss, O. Bakr, A Au/Cu_2O–TiO_2 system for photo-catalytic hydrogen production. A pn-junction effect or a simple case of in situ reduction? J. Catal., 2015. 322: 109-117.

417. Bowker M., D. James, P. Stone, R. Bennett, N. Perkins, L. Millard, J. Greaves, A. Dickinson, Catalysis at the metal-support interface: exemplified by the photocatalytic reforming of methanol on Pd/TiO_2. J. Catal., 2003. 217(2): 427-433.

418. Khan M.A.S., M.K. Kesharwani, T. Bandyopadhyay, B. Ganguly, Solvolysis of chemical warfare agent VX is more efficient with hydroxylamine anion: A computational study. J. Mol. Graph. Model., 2009. 28(2): 177-182.

419. Yu J., Y. Hai, M. Jaroniec, Photocatalytic hydrogen production over CuO-modified titania. J. Colloid Interface Sci., 2011. 357(1): 223-228.

420. Jung M., J. Scott, Y.H. Ng, Y. Jiang, R. Amal, CuO_x dispersion and reducibility on TiO_2 and its impact on photocatalytic hydrogen evolution. Int. J. Hydrogen Energy, 2014. 39(24): 12499-12506.

421. Xu S., D.D. Sun, Significant improvement of photocatalytic hydrogen generation rate over TiO_2 with deposited CuO. Int. J. Hydrogen Energy, 2009. 34(15): 6096-6104.

422. Yasomanee J., J. Bandara, Multi-electron storage of photoenergy using Cu_2O–TiO_2 thin film photocatalyst. Sol. Energy Mater. Sol. C., 2008. 92(3): 348-352.

423. Yoong L., F.K. Chong, B.K. Dutta, Development of copper-doped TiO_2 photocatalyst for hydrogen production under visible light. Energy, 2009. 34(10): 1652-1661.

424. He J., J. Wang, Y. Chen, J. Zhang, D. Duan, Y. Wang, Z. Yan, A dye-sensitized Pt@UiO-66(Zr) metal-organic framework for visible-light photocatalytic hydrogen production. Chem. Commun., 2014. 50(53): 7063-7066.

425. He J., Z. Yan, J. Wang, J. Xie, L. Jiang, Y. Shi, F. Yuan, F. Yu, Y. Sun, Significantly enhanced photocatalytic hydrogen evolution under visible light over CdS embedded on metal-organic frameworks. Chem. Commun., 2013. 49(60): 6761-6763.

426. Ke F., L. Wang, J. Zhu, Multifunctional Au-Fe_3O_4@MOF core-shell nanocomposite catalysts with controllable reactivity and magnetic recyclability. Nanoscale, 2015. 7(3): 1201-1208.

427. Zhu H., B. Yang, J. Xu, Z. Fu, M. Wen, T. Guo, S. Fu, J. Zuo, S. Zhang, Construction of Z-scheme type CdS–Au–TiO_2 hollow nanorod arrays with enhanced photocatalytic activity. Appl. Catal. B-Environ., 2009. 90(3–4): 463-469.

428. Khan I.A., S. Ullah, F. Nasim, M. Choucair, M.A. Nadeem, A. Iqbal, A. Badshah, M.A. Nadeem, Cr_2O_3–carbon composite as a new support material for efficient methanol electrooxidation. Mater. Res. Bull., 2016. 77: 221-227.

429. Lin R., L. Shen, Z. Ren, W. Wu, Y. Tan, H. Fu, J. Zhang, L. Wu, Enhanced photocatalytic hydrogen production activity via dual modification of MOF and reduced graphene oxide on CdS. Chem. Commun., 2014. 50(62): 8533-8535.

430. Wang Y., Y. Zhang, Z. Jiang, G. Jiang, Z. Zhao, Q. Wu, Y. Liu, Q. Xu, A. Duan, C. Xu, Controlled fabrication and enhanced visible-light photocatalytic hydrogen production of Au@CdS/MIL-101 heterostructure. Appl. Catal. B-Environ., 2016. 185: 307-314.

431. Banerjee A., U. Singh, V. Aravindan, M. Srinivasan, S. Ogale, Synthesis of CuO nanostructures from Cu-based metal organic framework (MOF-199) for application as anode for Li-ion batteries. Nano Energy, 2013. 2(6): 1158-1163.

432. Khan I.A., A. Badshah, M.A. Nadeem, N. Haider, M.A. Nadeem, A copper based metal-organic framework as single source for the synthesis of electrode materials for high-performance supercapacitors and glucose sensing applications. Int. J. Hydrogen Energy, 2014. 39(34): 19609-19620.

433. Müller M., X. Zhang, Y. Wang, R.A. Fischer, Nanometer-sized titania hosted inside MOF-5. Chem. Commun., 2009(1): 119-121.

434. Yu, J., Y. Hai, B. Cheng, Enhanced photocatalytic H_2-production activity of TiO_2 by $Ni(OH)_2$ cluster modification. J. Phys. Chem. C, 2011. 115(11): 4953-4958.

435. Domingo, A., A. Rodríguez-Fortea, M. Swart, C. de Graaf, R. Broer, Ab initio absorption spectrum of NiO combining molecular dynamics with the embedded cluster approach in a discrete reaction field. Phys. Rev. B, 2012. 85(15): 155143.

436. Rodriguez J.A., J.C. Hanson, A.I. Frenkel, J.Y. Kim, M. Pérez, Experimental and theoretical studies on the reaction of H_2 with NiO: role of O_2 vacancies and mechanism for oxide reduction. J. Am. Chem. Soc., 2002. 124(2): 346-354.

437. Ren L., Y. P. Zeng, D. Jiang, The improved photocatalytic properties of P-type NiO loaded porous TiO_2 sheets prepared via freeze tape-casting. Solid State Sci., 2010. 12(1): 138-143.

438. Chen W. T., A. Chan, D. Sun-Waterhouse, T. Moriga, H. Idriss, G.I.N. Waterhouse, Ni/TiO_2: A promising low-cost photocatalytic system for solar H_2 production from ethanol–water mixtures. J. Catal., 2015. 326: 43-53.

439. Fritzsche W., T.A. Taton, Metal nanoparticles as labels for heterogeneous, chip-based DNA detection. Nanotechnol., 2003. 14(12):

440. Hu M., J. Chen, Z. Y. Li, L. Au, G.V. Hartland, X. Li, M. Marquez, Y. Xia, Gold nanostructures: engineering their plasmonic properties for biomedical applications. Chem. Soc. Rev., 2006. 35(11): 1084-1094.

441. Pillai S., K. Catchpole, T. Trupke, M. Green, Surface plasmon enhanced silicon solar cells. J. appl. phys., 2007. 101(9): 093105.

442. Narayanan R., M.A. El-Sayed, Catalysis with transition metal nanoparticles in colloidal solution: nanoparticle shape dependence and stability. J. Phys. Chem. B, 2005. 109(26): 12663-12676.

443. Barnes W.L., A. Dereux, T.W. Ebbesen, Surface plasmon subwavelength optics. Nature, 2003. 424(6950): 824-830.

444. Garcia M., Surface plasmons in metallic nanoparticles: fundamentals and applications. J. Phys. D-Appl. Phys., 2012. 45(38): 389-501.

445. Li L., Z. Xu, F. Liu, Y. Shao, J. Wang, H. Wan, S. Zheng, Photocatalytic nitrate reduction over $Pt–Cu/TiO_2$ catalysts with benzene as hole scavenger. J. Photochem. Photobiol. A-Chem., 2010. 212(2): 113-121.

446. Yamauchi M., R. Abe, T. Tsukuda, K. Kato, M. Takata, Highly selective ammonia synthesis from nitrate with photocatalytically generated hydrogen on $CuPd/TiO_2$. J. Am. Chem. Soc., 2011. 133(5): 1150-1152.

447. Chiarello G.L., A. Di Paola, L. Palmisano, E. Selli, Effect of titanium dioxide crystalline structure on the photocatalytic production of hydrogen. Photochem. Photobiol. Sci., 2011. 10(3): 355-360.

448. Kumar D.P., N.L. Reddy, B. Srinivas, V. Durgakumari, V. Roddatis, O. Bondarchuk, M. Karthik, Y. Ikuma, M. Shankar, Stable and active CuxO/TiO_2 nanostructured catalyst for proficient hydrogen production under solar light irradiation. Sol. Energy Mater. Sol. C., 2016. 146: 63-71.

449. Hoyer P., Formation of a titanium dioxide nanotube array. Langmuir, 1996. 12(6): 1411-1413.

450. Mao J., L. Ye, K. Li, X. Zhang, J. Liu, T. Peng, L. Zan, Pt-loading reverses the photocatalytic activity order of anatase TiO_2 (001) and (010) facets for photoreduction of CO_2 to CH_4. Appl. Catal. B-Environ., 2014. 144: 855-862.

451. Liu N., Y. Zhao, X. Wang, H. Peng, G. Li, Facile synthesis and enhanced photocatalytic properties of truncated bipyramid-shaped anatase TiO_2 nanocrystals. Mater. Lett., 2013. 102–103: 53-55.

452. Zhang, S., L. M. Peng, Q. Chen, G. Du, G. Dawson, W. Zhou, Formation Mechanism of $H_2Ti_3O_7$ Nanotubes. Phys. Rev. Lett., 2003. 91(25): 256103.

453. Kasuga, T., M. Hiramatsu, A. Hoson, T. Sekino, K. Niihara, Formation of titanium oxide nanotube. Langmuir, 1998. 14(12): 3160-3163.

454. Yuan, Z.Y., W. Zhou, B. L. Su, Hierarchical interlinked structure of titanium oxide nanofibers. Chem. Commun., 2002(11): 1202-1203.

455. Ou, H.H., S.L. Lo, Review of titania nanotubes synthesized via the hydrothermal treatment: Fabrication, modification, and application. Separation and Purification Technol., 2007. 58(1): 179-191.

456. Ma, R., K. Fukuda, T. Sasaki, M. Osada, Y. Bando, Structural features of titanate nanotubes/nanobelts revealed by Raman, X-ray absorption fine structure and electron diffraction characterizations. J. Phys. Chem.-B, 2005. 109(13): 6210-6214.

457. Thorne A., A. Kruth, D. Tunstall, J.T. Irvine, W. Zhou, Formation, structure, and stability of titanate nanotubes and their proton conductivity. J. Phys. Chem. B, 2005. 109(12): 5439-5444.

458. Morgado E., M.A. de Abreu, G.T. Moure, B.A. Marinkovic, P.M. Jardim, A.S. Araujo, Characterization of nanostructured titanates obtained by alkali treatment of TiO_2-anatases with distinct crystal sizes. Chem. Mater., 2007. 19(4): 665-676.

459. Chen Y.,L. Guo, Highly efficient visible-light-driven photocatalytic hydrogen production from water using $Cd_{0.5}Zn_{0.5}S$/TNTs (titanate nanotubes) nanocomposites without noble metals. J. Mater. Chem., 2012. 22(15): 7507-7514.

460. Dang H., X. Dong, Y. Dong, Y. Zhang, S. Hampshire, TiO_2 nanotubes coupled with nano-$Cu(OH)_2$ for highly efficient photocatalytic hydrogen production. Int. J. Hydrogen Energy, 2013. 38(5): 2126-2135.

461. Long L., J. Li, L. Wu, X. Li, Enhanced photocatalytic performance of platinized CdS/TiO_2 by optimizing calcination temperature of TiO_2 nanotubes. Mater. Sci. Semicond. Proc., 2014. 26: 107-111.

462. Wu M. C., A. Sápi, A. Avila, M. Szabó, J. Hiltunen, M. Huuhtanen, G. Tóth, Á. Kukovecz, Z. Kónya, R. Keiski, Enhanced photocatalytic activity of TiO_2 nanofibers and their flexible composite films: Decomposition of organic dyes and efficient H_2 generation from ethanol-water mixtures. Nano Res., 2011. 4(4): 360-369.

463. Liu Y., Z. Wang, W. Wang, X. An, S. Mi, J. Tang, W. Huang, Sandwich $SrTiO_3$/TiO_2/H-Titanate nanofiber composite photocatalysts for efficient photocatalytic hydrogen evolution. Appl. Surf. Sci., 2014. 315: 314-322.

464. Wu M. C., J. Hiltunen, A. Sápi, A. Avila, W. Larsson, H.-C. Liao, M. Huuhtanen, G. Tóth, A. Shchukarev, N. Laufer, Nitrogen-doped anatase nanofibers decorated with noble metal nanoparticles for photocatalytic production of hydrogen. ACS Nano, 2011. 5(6): 5025-5030.

465. D'Elia D., C. Beauger, J.F. Hochepied, A. Rigacci, M. H. Berger, N. Keller, V. Keller-Spitzer, Y. Suzuki, J.C. Valmalette, M. Benabdesselam, Impact of three different TiO_2 morphologies on hydrogen evolution by methanol assisted water splitting: nanoparticles, nanotubes and aerogels. Int. J. Hydrogen Energy, 2011. 36(22): 14360-14373.

466. Ni M., M.K.H. Leung, K. Sumathy, D.Y.C. Leung, Potential of renewable hydrogen production for energy supply in Hong Kong. Int. J. Hydrogen Energy, 2006. 31(10): 1401-1412.

467. Haryanto, A., S. Fernando, N. Murali, S. Adhikari, Current status of hydrogen production techniques by steam reforming of ethanol: A Rev.. Energy Fuels, 2005. 19(5): 2098-2106.

468. Padikkaparambil, S., Y. Zahira, S. Viswanathan, B. Njarakkattuvalappil, A. Zubair, An Enthusiastic Glance in to the Visible Responsive Photocatalysts for Energy

Production and Pollutant Removal, with Special Emphasis on Titania. Int. J. Photoenergy, 2012. 2012:19.

469. Shangguan W., A. Yoshida, Photocatalytic hydrogen evolution from water on nanocomposites incorporating cadmium sulfide into the interlayer. J. Phys. Chem. B, 2002. 106(47): 12227-12230.

470. Lei Z., G. Ma, M. Liu, W. You, H. Yan, G. Wu, T. Takata, M. Hara, K. Domen, C. Li, Sulfur-substituted and zinc-doped In $(OH)_3$: a new class of catalyst for photocatalytic H_2 production from water under visible light illumination. J. Catal., 2006. 237(2): 322-329.

471. Fujishiro Y., S. Uchida, T. Sato, Synthesis and photochemical properties of semiconductor pillared layered compounds. International J. Inorg. Mater. 1999. 1(1): 67-72.

472. Tsuji I., H. Kato, H. Kobayashi, A. Kudo, Photocatalytic H_2 evolution reaction from aqueous solutions over band structure-controlled $(AgIn)_xZn_2(1-x)S_2$ solid solution photocatalysts with visible-light response and their surface nanostructures. J. Am. Chem. Soc., 2004. 126(41): 13406-13413.

473. Kato H., A. Kudo, H. Kobayashi, I. Tsuji, Photocatalytic H_2 evolution reaction from aqueous solutions over band structure-controlled $(Agln)_xZn_2$ $(1-x)S_2$. J. Am. Chem. Soc. JACS, 2004. 126(41):13406-13413.

474. Tsuji I., H. Kato, A. Kudo, Visible Light Induced H_2 Evolution from an Aqueous Solution Containing Sulfide and Sulfite over a $ZnS–CuInS_2–AgInS_2$ Solid Solution Photocatalyst. Angew. Chem., 2005. 117(23): 3631-3634.

475. Bashir S., A.K. Wahab, H. Idriss, Synergism and photocatalytic water splitting to hydrogen over Pt/TiO_2 catalysts: Effect of particle size. Catal. Today, 2015. 240: 242-247.

476. Wahab A.K., M. Al-Oufi, S. Bashir, Y. Al-Salik, H. Katsiev, I. H., Photocatalyst, method of preparation, photolysis system W.P. 13T & I0037-WO-PCT, Editor. 2013.

477. Waterhouse, G.I.N., A.K. Wahab, M. Al-Oufi, V. Jovic, D.H. Anjum, D. Sun-Waterhouse, J. Llorca, H. Idriss, Hydrogen production by Tuning the Photonic Band Gap with the Electronic Band Gap of TiO_2. Sci. Rep., 2013. 3: 2849.

478. Chen W. T., H. Idriss, G.I.N. Waterhouse, Efficient photocatalytic H_2 Production from Ethanol-Water Mixtures over CuO/TiO_2 Photocatalysts. . Int. J. Hydrogen Energy, 2013. 38: 15036-15048.

479. Jovic V., W.T. Chen, D. Sun-Waterhouse, M.G. Blackford, H. Idriss, G.I.N. Waterhouse, Effect of gold loading and TiO_2 support composition on the activity of Au/TiO_2 photocatalysts for H_2 production from ethanol–water mixtures. J. Catal., 2013. 305(0): 307-317.

480. Jovic V., Z.H.N. Al-Azria, D. Sun-Waterhouse, H. Idriss, G.I.N. Waterhouse, Photocatalytic H_2 Production from Bioethanol over Au/TiO_2 and Pt/TiO_2 Photocatalysts under UV Irradiation – A Comparative Study. . Top. Catal., 2013. 56: 1139-1151.

481. Al-Oufi M., A.K. Wahab, S. Bashir, Y. Al-Salik, H. Idriss, Photocatalytic hydrogen production from water over Ag-Pd-Au deposited on titanium dioxide materials. US Patent, Editor. 2014.

482. Chen X.,W. Shangguan, Hydrogen production from water splitting on CdS-based photocatalysts using solar light. Front. Energy, 2013. 7(1):111-118.

483. Ryu S.Y., W. Balcerski, T.K. Lee, M.R. Hoffmann, Photocatalytic production of hydrogen from water with visible light using hybrid catalysts of CdS attached to microporous and mesoporous Silicas. J. Phys. Chem. C, 2007. 111(49): 18195-18203.

484. Datta S., M. Kabir, T. Saha-Dasgupta, Effects of shape and composition on the properties of CdS nanocrystals. Phys. Rev. B, 2012. 86(11): 115307.

485. Reber J.F.,M. Rusek, Photochemical hydrogen production with platinized suspensions of cadmium sulfide and cadmium zinc sulfide modified by silver sulfide. J. Phys. Chem., 1986. 90(5): 824-834.

486. Jang J. S., W. Li, S.H. OH, J.S. Lee, Fabrication of CdS/TiO_2 nano-bulk composite photocatalysts for hydrogen production from aqueous H_2S solution under visible light. Chem. Phys. Lett., 2006. 425(4–6): 278-282.

487. Carp O., C.L. Huisman, A. Reller, Photoinduced reactivity of titanium dioxide. Prog. Solid State Chem., 2004. 32(1–2): 33-177.

488. Matsumura M., S. Furukawa, Y. Saho, H. Tsubomura, Cadmium sulfide photocatalyzed hydrogen production from aqueous solutions of sulfite: effect of crystal structure and preparation method of the catalyst. J. Phys. Chem., 1985. 89(8): 1327-1329.

489. Soltani N., E. Gharibshahi, E. Saion, Band gap of cubic and hexagonal CdS quantum dots-Experimental and theoretical studies. Chalcogenide Lett., 2012. 9: 321 - 328.

490. Chen C.C., A. Herhold, C. Johnson, A. Alivisatos, Size dependence of structural metastability in semiconductor nanocrystals. Science, 1997. 276(5311): 398-401.

491. Banerjee R., R. Jayakrishnan, P. Ayyub, Effect of the size-induced structural transformation on the band gap in CdS nanoparticles. J. Phys-Condensed Matter, 2000. 12(50): 10647.

492. Zhang J., S. Wageh, A. Al-Ghamdi, J. Yu, New understanding on the different photocatalytic activity of wurtzite and zinc-blende CdS. Appl. Catal. B-Environ., 2016. 192: 101-107.

493. Bandaranayake R., G. Wen, J. Lin, H. Jiang, C. Sorensen, Structural phase behavior in II–VI semiconductor nanoparticles. Appl. Phys. Lett., 1995. 67(6): 831-833.

494. Swayambunathan V., D. Hayes, K.H. Schmidt, Y. Liao, D. Meisel, Thiol surface complexation on growing cadmium sulfide clusters. J. Am. Chem. Soc., 1990. 112(10): 3831-3837.

495. Herron N., Y. Wang, H. Eckert, Synthesis and characterization of surface-capped, size-quantized cadmium sulfide clusters. Chemical control of cluster size. J. Am. Chem. Soc., 1990. 112(4): 1322-1326.

496. Bao N., L. Shen, T. Takata, K. Domen, A. Gupta, K. Yanagisawa, C.A. Grimes, Facile Cd−Thiourea Complex Thermolysis Synthesis of Phase-Controlled CdS Nanocrystals for Photocatalytic Hydrogen Production under Visible Light. J. Phys. Chem. C, 2007. 111(47): 17527-17534.

497. Bao N., L. Shen, T. Takata, K. Domen, A. Gupta, K. Yanagisawa, C.A. Grimes, Facile Cd-thiourea complex thermolysis synthesis of phase-controlled CdS nanocrystals for photocatalytic hydrogen production under visible light. J. Phys. Chem. C, 2007. 111(47): 17527-17534.

498. Li Y., L. Tang, S. Peng, Z. Li, G. Lu, Phosphate-assisted hydrothermal synthesis of hexagonal CdS for efficient photocatalytic hydrogen evolution. Cryst. Eng. Comm., 2012. 14(20): 6974-6982.

499. Manna L., D.J. Milliron, A. Meisel, E.C. Scher, A.P. Alivisatos, Controlled growth of tetrapod-branched inorganic nanocrystals. Nat. Mater., 2003. 2(6): 382-385.

500. Dong M., J. Zhang, J. Yu, Effect of effective mass and spontaneous polarization on photocatalytic activity of wurtzite and zinc-blende ZnS. APL Mater., 2015. 3(10): 104404.

501. Zhao Z.Y., W.W. Dai, Structural, electronic, and optical properties of Eu-doped BiOX (X= F, Cl, Br, I): a DFT+ U study. Inorg. Chem., 2014. 53(24): 13001-13011.

502. Luo M., W. Yao, C. Huang, Q. Wu, Q. Xu, Shape effects of Pt nanoparticles on hydrogen production via Pt/CdS photocatalysts under visible light. J. Mater. Chem. A, 2015. 3(26): 13884-13891.

503. Yao W., X. Song, C. Huang, Q. Xu, Q. Wu, Enhancing solar hydrogen production via modified photochemical treatment of Pt/CdS photocatalyst. Catal. Today, 2013. 199: 42-47.

504. Li C., J. Yuan, B. Han, L. Jiang, W. Shangguan, TiO_2 nanotubes incorporated with CdS for photocatalytic hydrogen production from splitting water under visible light irradiation. Int. J. Hydrogen Energ., 2010. 35(13): 7073-7079.

505. Jang J.S., S.M. Ji, S.W. Bae, H.C. Son, J.S. Lee, Optimization of CdS/TiO_2 nano-bulk composite photocatalysts for hydrogen production from Na_2S/Na_2SO_3 aqueous electrolyte solution under visible light ($\lambda \geq 420$nm). J. Photochem. Photobiol. A-Chem., 2007. 188(1): 112-119.

506. Huang L., X. Wang, J. Yang, G. Liu, J. Han, C. Li, Dual cocatalysts loaded type I CdS/ZnS core/shell nanocrystals as effective and stable photocatalysts for H_2 evolution. J. Phys. Chem. C, 2013. 117(22): 11584-11591.

507. Zong X., J. Han, G. Ma, H. Yan, G. Wu, C. Li, Photocatalytic H_2 evolution on CdS loaded with WS_2 as cocatalyst under visible light irradiation. J. Phys. Chem. C, 2011. 115(24): 12202-12208.

508. Zong X., G. Wu, H. Yan, G. Ma, J. Shi, F. Wen, L. Wang, C. Li, Photocatalytic H_2 evolution on MoS_2/CdS catalysts under visible light irradiation. J. Phys. Chem. C, 2010. 114(4): 1963-1968.

509. Shangguan W., A. Yoshida, Synthesis and photocatalytic properties of CdS-intercalated metal oxides. Sol. Energy Mater. Sol. C., 2001. 69(2): 189-194.

510. Gao X.F., W.T. Sun, Z.D. Hu, G. Ai, Y.L. Zhang, S. Feng, F. Li, L.M. Peng, An efficient method to form heterojunction CdS/TiO_2 photoelectrodes using highly ordered TiO_2 nanotube array films. J. Phys. Chem. C, 2009. 113(47): 20481-20485.

511. Barpuzary D., Z. Khan, N. Vinothkumar, M. De, M. Qureshi, Hierarchically grown urchinlike CdS@ZnO and CdS@Al_2O_3 heteroarrays for efficient visible-light-driven photocatalytic hydrogen generation. J. Phys. Chem. C, 2011. 116(1): 150-156.

512. Cao J., J.Z. Sun, H.Y. Li, J. Hong, M. Wang, A facile room-temperature chemical reduction method to TiO_2@CdS core/sheath heterostructure nanowires. J. Mater. Chem., 2004. 14(7): 1203-1206.

513. Das K.,S. De, Optical Properties of the Type-II Core− Shell TiO_2@CdS Nanorods for photovoltaic applications. J. Phys. Chem. C, 2009. 113(9): p. 3494-3501.

514. Jia H., H. Xu, Y. Hu, Y. Tang, L. Zhang, TiO_2 CdS core–shell nanorods films: Fabrication and dramatically enhanced photoelectrochemical properties. Electrochem. Commun., 2007. 9(3): 354-360.

515. Zhang J., J. Yu, M. Jaroniec, J.R. Gong, Noble Metal-Free Reduced Graphene Oxide-$Zn_xCd_{1-x}S$ Nanocomposite with Enhanced Solar Photocatalytic H_2-Production Performance. Nano Lett., 2012. 12(9): 4584-4589.

516. Gao P., J. Liu, S. Lee, T. Zhang, D.D. Sun, High quality graphene oxide-CdS-Pt nanocomposites for efficient photocatalytic hydrogen evolution. J. Mater. Chem., 2012. 22(5): 2292-2298.

517. Lee H., K. Heo, A. Maaroof, Y. Park, S. Noh, J. Park, J. Jian, C. Lee, M. J. Seong, S. Hong, High-performance photoconductive channels based on (Carbon Nanotube)–(CdS Nanowire) hybrid nanostructures. Small, 2012. 8(11): 1650-1656.

518. Yang T.T., W. T. Chen, Y. J. Hsu, K.H. Wei, T.Y. Lin, T. W. Lin, Interfacial charge carrier dynamics in core−shell Au-CdS nanocrystals. J. Phys. Chem. C, 2010. 114(26): 11414-11420.

519. Yang J., H. Yan, X. Wang, F. Wen, Z. Wang, D. Fan, J. Shi, C. Li, Roles of cocatalysts in Pt–PdS/CdS with exceptionally high quantum efficiency for photocatalytic hydrogen production. J. Catal., 2012. 290: 151-157.

520. Luo M., Y. Liu, J. Hu, H. Liu, J. Li, One-pot synthesis of CdS and Ni-doped CdS hollow spheres with enhanced photocatalytic activity and durability. ACS Appl. Mater. Interfaces, 2012. 4(3): 1813-1821.

521. Wang X., M. Liu, Q. Chen, K. Zhang, J. Chen, M. Wang, P. Guo, L. Guo, Synthesis of CdS/CNTs photocatalysts and study of hydrogen production by photocatalytic water splitting. Int. J. Hydrogen. Energy, 2013. 38(29): 13091-13096.

522. Wang H., W. Chen, J. Zhang, C. Huang, L. Mao, Nickel nanoparticles modified CdS–A potential photocatalyst for hydrogen production through water splitting under visible light irradiation. Int. J. Hydrogen. Energy, 2015. 40(1): 340-345.

523. Chen X., W. Chen, H. Gao, Y. Yang, W. Shangguan, In situ photodeposition of NiO_x on CdS for hydrogen production under visible light: enhanced activity by controlling solution environment. Appl. Catal. B-Environ., 2014. 152: 68-72.

524. Serpone N., E. Borgarello, M. Grätzel, Visible light induced generation of hydrogen from H_2S in mixed semiconductor dispersions; improved efficiency through inter-particle electron transfer. J. Chem. Soc. Chem. Commun., 1984(6): 342-344.

525. Harada,H., T. Sakata, T. Ueda, Effect of semiconductor on photocatalytic decomposition of lactic acid. J. Am. Chem. Soc., 1985. 107(6): 1773-1774.

526. Li Q., Z. Chen, X. Zheng, Z. Jin, Study of photoreduction of hexachloroplatinate (2-) on cadmium sulfide. J. Phys. Chem., 1992. 96(14): 5959-5962.

527. Park H., W. Choi, M.R. Hoffmann, Effects of the preparation method of the ternary CdS/TiO_2/Pt hybrid photocatalysts on visible light-induced hydrogen production. J. Mater. Chem., 2008. 18(20): 2379-2385.

528. Di T., B. Zhu, J. Zhang, B. Cheng, J. Yu, Enhanced photocatalytic H_2 production on CdS nanorod using cobalt-phosphate as oxidation cocatalyst. Appl. Surf. Sci., 2016. 389: 775-782.

529. Haruta M., Size- and support-dependency in the catalysis of gold. Catal. Today, 1997. 36(1): 153-166.

530. Yang T. T., W. T. Chen, Y. J. Hsu, K. H. Wei, T.Y. Lin, T. W. Lin, Interfacial charge carrier dynamics in core−shell Au-CdS nanocrystals. J. Phys. Chem. C, 2010. 114(26): 11414-11420.

531. Amrollahi R., M.S. Hamdy, G. Mul, Understanding promotion of photocatalytic activity of TiO_2 by Au nanoparticles. J. Catal., 2014. 319: 194-199.

532. Majeed I., M.A. Nadeem, M. Al-Oufi, M.A. Nadeem, G. Waterhouse, A. Badshah, J. Metson, H. Idriss, On the role of metal particle size and surface coverage for photo-catalytic hydrogen production: A case study of the Au/CdS system. Appl. Catal. B-Environ., 2016. 182: 266-276.

533. Zhou H., L. Ding, T. Fan, J. Ding, D. Zhang, Q. Guo, Leaf-inspired hierarchical porous CdS/Au/N-TiO_2 heterostructures for visible light photocatalytic hydrogen evolution. Appl. Catal. B-Environ., 2014. 147: 221-228.

534. Yin X. L., J. Liu, W. J. Jiang, X. Zhang, J.-S. Hu, L.J. Wan, Urchin-like Au@ CdS/WO_3 micro/nano heterostructure as a visible-light driven photocatalyst for efficient hydrogen generation. Chem. Commun., 2015. 51(72):13842-13845.

535. Zhou H., J. Pan, L. Ding, Y. Tang, J. Ding, Q. Guo, T. Fan, D. Zhang, Biomass-derived hierarchical porous $CdS/M/TiO_2$ (M= Au, Ag, Pt, Pd) ternary heterojunctions for photocatalytic hydrogen evolution. Int. J. Hydrogen Energy, 2014. 39(29): 16293-16301.

536. Tada H., T. Mitsui, T. Kiyonaga, T. Akita, K. Tanaka, All-solid-state Z-scheme in CdS–Au–TiO_2 three-component nanojunction system. Nat. Mater., 2006. 5(10): 782-786.

537. Ma X., K. Zhao, H. Tang, Y. Chen, C. Lu, W. Liu, Y. Gao, H. Zhao, Z. Tang, New insight into the role of gold nanoparticles in Au@ CdS core–shell nanostructures for hydrogen evolution. Small, 2014. 10(22): 4664-4670.

538. Khon E., A. Mereshchenko, A.N. Tarnovsky, K. Acharya, A. Klinkova, N.N. Hewa-Kasakarage, I. Nemitz, M. Zamkov, Suppression of the plasmon resonance in Au/CdS colloidal nanocomposites. Nano Lett., 2011. 11(4): 1792-1799.

539. Zhang J., Y. Tang, K. Lee, M. Ouyang, Nonepitaxial growth of hybrid core-shell nanostructures with large lattice mismatches. Science, 2010. 327(5973):1634-1638.

540. Singh R.,B. Pal, Influence of Au photodeposition and doping in CdS nanorods: optical and photocatalytic study. Particul. Sci. Technol., 2015. 33(1): 53-58.

541. Delannoy L., N. El Hassan, A. Musi, N.N. Le To, J. M. Krafft, C. Louis, Preparation of supported gold nanoparticles by a modified incipient wetness impregnation method. J. Phys. Chem. B, 2006. 110(45): 22471-22478.

542. Kumar N., V.K. Komarala, V. Dutta, In-situ synthesis of Au–CdS plasmonic photocatalyst by continuous spray pyrolysis and its visible light photocatalysis. Chem. Eng. J., 2014. 236: 66-74.

543. Rayalu S.S., D. Jose, M.V. Joshi, P.A. Mangrulkar, K. Shrestha, K. Klabunde, Photocatalytic water splitting on Au/TiO_2 nanocomposites synthesized through various routes: Enhancement in photocatalytic activity due to SPR effect. Appl. Catal. B-Environ., 2013. 142–143(0): 684-693.

544. Mead C.,W. Spitzer, Fermi level position at metal-semiconductor interfaces. Phys. Rev., 1964. 134(3A): A713.

545. Wu K., W.E. Rodríguez-Córdoba, Y. Yang, T. Lian, Plasmon-induced hot electron transfer from the Au tip to CdS rod in CdS-Au nanoheterostructures. Nano Lett., 2013. 13(11): 5255-5263.

546. Wang B.,S. Qu, Absorption spectra and near-electric field enhancement effects of Au and Ag-Fe_3O_4 dimers. Appl. Surf. Sci., 2014. 292: 1002-1008.

547. Yu, K., Y. Tian, T. Tatsuma, Size effects of gold nanaoparticles on plasmon-induced photocurrents of gold-TiO_2 nanocomposites. Phys. Chem. Chem. Phys., 2006. 8(46): 5417-5420.

548. Clavero, C., Plasmon-induced hot-electron generation at nanoparticle/metal-oxide interfaces for photovoltaic and photocatalytic devices. Nature Photonics, 2014. 8(2): 95-103.

549. Pleskov Y. V., Y. Y. Gurevich, Semiconductor photoelectrochemistry. 1986: Consultants Bureau, New York, NY. Medium: X; Size: Pages: 422.

550. Meissner D., C. Benndorf, R. Memming, Photocorrosion of cadmium sulfide: Analysis by photoelectron spectroscopy. Appl. Surf. Sci., 1987. 27(4): 423-436.

551. Shen P., S. Zhao, D. Su, Y. Li, A. Orlov, Outstanding activity of sub-nm Au clusters for photocatalytic hydrogen production. Appl. Catal. B-Environ., 2012. 126: 153-160.

552. Yun H. J., H. Lee, N.D. Kim, D.M. Lee, S. Yu, J. Yi, A combination of two visible-light responsive photocatalysts for achieving the Z-scheme in the solid state. ACS Nano, 2011. 5(5): 4084-4090.

553. Sathish M., B. Viswanathan, R.P. Viswanath, Alternate synthetic strategy for the preparation of CdS nanoparticles and its exploitation for water splitting. Int. J. Hydrogen Energy., 2006. 31(7): 891-898.

554. Li Y., J. Du, S. Peng, D. Xie, G. Lu, S. Li, Enhancement of photocatalytic activity of cadmium sulfide for hydrogen evolution by photoetching. Int. J. Hydrogen Energy, 2008. 33(8): 2007-2013.

555. Girginer B., G. Galli, E. Chiellini, N. Bicak, Preparation of stable CdS nanoparticles in aqueous medium and their hydrogen generation efficiencies in photolysis of water. Int. J. Hydrogen Energy, 2009. 34(3): 1176-1184.

556. Bao N., L. Shen, T. Takata, K. Domen, Self-templated synthesis of nanoporous CdS nanostructures for highly efficient photocatalytic hydrogen production under visible light. Chem. Mater., 2007. 20(1): 110-117.

557. Wang X., K. Maeda, A. Thomas, K. Takanabe, G. Xin, J.M. Carlsson, K. Domen, M. Antonietti, A metal-free polymeric photocatalyst for hydrogen production from water under visible light. Nat. Mater., 2009. 8(1): 76-80.

558. Zheng Y., L. Lin, X. Ye, F. Guo, X. Wang, Helical graphitic carbon nitrides with photocatalytic and optical activities. Angew. Chem. Int. Ed., 2014. 53(44): 11926-11930.

559. Liu A.Y., M. L. Cohen, Prediction of new low compressibility solids. Science, 1989. 245(4920): 841-842.

560. Wang Y., X. Wang, M. Antonietti, Polymeric graphitic carbon nitride as a heterogeneous organocatalyst: From Photochemistry to Multipurpose Catalysis to Sustainable Chemistry. Angew. Chem. Int. Ed., 2012. 51(1): 68-89.

561. Zhang Y., Q. Pan, G. Chai, M. Liang, G. Dong, Q. Zhang, J. Qiu, Synthesis and luminescence mechanism of multicolor-emitting g-C_3N_4 nanopowders by low temperature thermal condensation of melamine. Sci. Rep., 2013. 3: 1943.

562. Li Y., J. Zhang, Q. Wang, Y. Jin, D. Huang, Q. Cui, G. Zou, Nitrogen-rich carbon nitride hollow vessels: Synthesis, characterization, and their properties. J. Phys. Chem. B, 2010. 114(29): 9429-9434.

563. Yan H., Y. Chen, S. Xu, Synthesis of graphitic carbon nitride by directly heating sulfuric acid treated melamine for enhanced photocatalytic H_2 production from water under visible light. Int. J. Hydrogen Energy, 2012. 37(1): 125-133.

564. Fu J., B. Chang, Y. Tian, F. Xi, X. Dong, Novel C_3N_4-CdS composite photocatalysts with organic-inorganic heterojunctions: In situ synthesis, exceptional activity, high stability and photocatalytic mechanism. J. Mater. Chem. A, 2013. 1(9): 3083-3090.

565. Yan S. C., Z. S. Li, Z.G. Zou, Photodegradation of rhodamine B and methyl orange over boron-doped g-C_3N_4 under visible light irradiation. Langmuir, 2010. 26(6): 3894-3901.

566. Yan S. C., Z. S. Li, Z. G. Zou, Photodegradation Performance of g-C_3N_4 Fabricated by Directly Heating Melamine. Langmuir, 2009. 25(17): 10397-10401.

567. Gillan E.G., Synthesis of Nitrogen-Rich Carbon Nitride Networks from an Energetic Molecular Azide Precursor. Chem. Mater., 2000. 12(12): 3906-3912.

568. Yang J., X. Wu, X. Li, Y. Liu, M. Gao, X. Liu, L. Kong, S. Yang, Synthesis and characterization of nitrogen-rich carbon nitride nanobelts by pyrolysis of melamine. Appl. Phys. A, 2011. 105(1): 161-166.

569. Li Y., J. Zhang, Q. Wang, Y. Jin, D. Huang, Q. Cui, G. Zou, Nitrogen-rich carbon nitride hollow vessels: synthesis, characterization, and their properties. J. Phys. Chem. B, 2010. 114(29): 9429-9434.

570. Yan S., Z. Li, Z. Zou, Photodegradation performance of g-C_3N_4 fabricated by directly heating melamine. Langmuir, 2009. 25(17): 10397-10401.

571. Wang Y., X. Wang, M. Antonietti, Polymeric graphitic carbon nitride as a heterogeneous organocatalyst: From photochemistry to multipurpose catalysis to sustainable chemistry. Angew. Chem. Int. Ed., 2012. 51(1): 68-89.

572. Chen X., J. Zhang, X. Fu, M. Antonietti, X. Wang, Fe-g-C_3N_4-Catalyzed Oxidation of Benzene to Phenol Using Hydrogen Peroxide and Visible Light. J. Am. Chem. Soc., 2009. 131(33): 11658-11659.

573. Dong F., L. Wu, Y. Sun, M. Fu, Z. Wu, S.C. Lee, Efficient synthesis of polymeric g-C_3N_4 layered materials as novel efficient visible light driven photocatalysts. J. Mater. Chem., 2011. 21(39): 15171-15174.

574. Ye C., J. X. Li, Z. J. Li, X. B. Li, X. B. Fan, L.-P. Zhang, B. Chen, C. H. Tung, L. Z. Wu, Enhanced Driving Force and Charge Separation Efficiency of Protonated g-C_3N_4 for Photocatalytic O_2 Evolution. ACS Catal., 2015. 5(11): 6973-6979.

575. Cao S., J. Yu, g-C_3N_4-based photocatalysts for hydrogen generation. J. Phys. Chem. Lett., 2014. 5(12): 2101-2107.

576. Chen L., X. Zeng, P. Si, Y. Chen, Y. Chi, D.-H. Kim, G. Chen, Gold nanoparticle-graphite-like C_3N_4 nanosheet nanohybrids used for electrochemiluminescent immunosensor. Ana. Chem., 2014. 86(9): 4188-4195.

577. Bai X., R. Zong, C. Li, D. Liu, Y. Liu, Y. Zhu, Enhancement of visible photocatalytic activity via Ag@C_3N_4 core–shell plasmonic composite. Appl. Catal. B-Environ., 2014. 147: 82-91.

578. Chang C., Y. Fu, M. Hu, C. Wang, G. Shan, L. Zhu, Photodegradation of bisphenol A by highly stable palladium-doped mesoporous graphite carbon nitride (Pd/mpg-C_3N_4) under simulated solar light irradiation. Appl. Catal. B-Environ., 2013. 142–143: 553-560.

579. Liu G., P. Niu, C. Sun, S.C. Smith, Z. Chen, G.Q. Lu, H. M. Cheng, Unique electronic structure induced high photoreactivity of sulfur-doped graphitic C_3N_4. J. Am. Chem. Soc., 2010. 132(33): 11642-11648.

580. Tian Y., B. Chang, J. Lu, J. Fu, F. Xi, X. Dong, Hydrothermal synthesis of graphitic carbon nitride–Bi_2WO_6 heterojunctions with enhanced visible light photocatalytic activities. ACS Appl. Mater. Interfaces, 2013. 5(15): 7079-7085.

581. Chen D., K. Wang, D. Xiang, R. Zong, W. Yao, Y. Zhu, Significantly enhancement of photocatalytic performances via core–shell structure of ZnO@mpg-C_3N_4. Appl. Catal. B-Environ., 2014. 147: 554-561.

582. Bu Y., Z. Chen, W. Li, Using electrochemical methods to study the promotion mechanism of the photoelectric conversion performance of Ag-modified mesoporous g-C_3N_4 heterojunction material. Appl. Catal. B-Environ., 2014. 144: 622-630.

583. Bai X., L. Wang, R. Zong, Y. Zhu, Photocatalytic activity enhanced via g-C_3N_4 nanoplates to nanorods. J. Phys. Chem. C, 2013. 117(19): 9952-9961.

584. Dosado A.G., W. T. Chen, A. Chan, D. Sun-Waterhouse, G.I.N. Waterhouse, Novel Au/TiO_2 photocatalysts for hydrogen production in alcohol–water mixtures based on hydrogen titanate nanotube precursors. J. Catal., 2015. 330: 238-254.

585. Khan I. A., A. Badshah, M. A. Nadeem, N. Haider, M. A. Nadeem, A copper based metal-organic framework as single source for the synthesis of electrode materials for high-performance supercapacitors and glucose sensing applications. Int. J. Hydrogen Energy, 2014. 39(34): 19609-19620.

586. Chui S. S.Y., S.M. F. Lo, J.P. Charmant, A.G. Orpen, I.D. Williams, A chemically functionalizable nanoporous material $[Cu_3(TMA)_2(H_2O)_3]_n$. Science, 1999. 283(5405): 1148-1150.

587. Nadeem A., J. Muir, K. Connelly, B. Adamson, B. Metson, H. Idriss, Ethanol photo-oxidation on a rutile TiO_2 (110) single crystal surface. Phys. Chem. Chem. Phys., 2011. 13(17): 7637-7643.

588. Yan H., J. Yang, G. Ma, G. Wu, X. Zong, Z. Lei, J. Shi, C. Li, Visible-light-driven hydrogen production with extremely high quantum efficiency on Pt–PdS/CdS photocatalyst. J. Catal., 2009. 266(2): 165-168.

589. Brunauer S., P.H. Emmett, E. Teller, Adsorption of gases in multimolecular layers. J Am. Chem. Soc., 1938. 60(2): 309-319.

590. Barrett E.P., L.G. Joyner, P.P. Halenda, The determination of pore volume and area distributions in porous substances. I. Computations from nitrogen isotherms. J. Am. Chem. Soc., 1951. 73(1): 373-380.

591. Dosado A.G., W. T. Chen, A. Chan, D. Sun-Waterhouse, G.I. Waterhouse, Novel Au/TiO_2 photocatalysts for hydrogen production in alcohol–water mixtures based on hydrogen titanate nanotube precursors. J. Catal., 2015. 330: 238-254.

592. Hanaor D.A.H.,C.C. Sorrell, Review of the anatase to rutile phase transformation. J. Mater. Sci., 2011. 46(4): 855-874.

593. Chen W. T., A. Chan, V. Jovic, D. Sun-Waterhouse, K.. Murai, H. Idriss, G.I.N. Waterhouse, Effect of the TiO_2 Crystallite Size, TiO_2 Polymorph and Test Conditions on the Photo-Oxidation Rate of Aqueous Methylene Blue. Top. Catal., 2015. 58(2): 85-102.

594. Bokhimi X., A. Morales, O. Novaro, T. López, O. Chimal, M. Asomoza, R. Gómez, Effect of Copper Precursor on the Stabilization of Titania Phases, and the Optical

Properties of Cu/TiO_2 Prepared with the Sol−Gel Technique. Chem. Mater., 1997. 9(11): 2616-2620.

595. Qiu X., M. Miyauchi, H. Yu, H. Irie, K. Hashimoto, Visible-Light-Driven Cu (II)−(Sr_{1-y} Na_y)(Ti_{1-x} Mo_x) O_3 Photocatalysts Based on Conduction Band Control and Surface Ion Modification. J. Am. Chem. Soc., 2010. 132(43): 15259-15267.

596. Irie H., K. Kamiya, T. Shibanuma, S. Miura, D.A. Tryk, T. Yokoyama, K. Hashimoto, Visible light-sensitive Cu (II)-grafted TiO_2 photocatalysts: activities and X-ray absorption fine structure analyses. J. Phys. Chem. C, 2009. 113(24): 10761-10766.

597. Yoong L., F.K. Chong, B.K. Dutta, Development of copper-doped TiO_2 photocatalyst for hydrogen production under visible light. Energy, 2009. 34(10): 1652-1661.

598. Chen X., L. Liu, P.Y. Yu, S.S. Mao, Increasing Solar Absorption for Photocatalysis with Black Hydrogenated Titanium Dioxide Nanocrystals. Science, 2011. 331(6018): 746-750.

599. Chusuei C.C., M.A. Brookshier, D.W. Goodman, Correlation of relative X-ray photoelectron spectroscopy shake-up intensity with CuO particle size. Langmuir, 1999. 15(8): 2806-2808.

600. Martin L., H. Martinez, D. Poinot, B. Pecquenard, F.d.r. Le Cras, Comprehensive X-ray photoelectron spectroscopy study of the conversion reaction mechanism of CuO in lithiated thin film electrodes. J. Phys. Chem. C, 2013. 117(9): 4421-4430.

601. Huang L., F. Peng, F.S. Ohuchi, “In situ” XPS study of band structures at Cu_2O/TiO_2 heterojunctions interface. Surf. Sci., 2009. 603(17): 2825-2834.

602. Shamraiz U., A. Badshah, R.A. Hussain, M.A. Nadeem, S. Saba, Surfactant free fabrication of copper sulphide (CuS–Cu_2S) nanoparticles from single source precursor for photocatalytic applications. J. Saudi Chem. Soc., 2015.

603. Majeed I., M. A. Nadeem, E. Hussain, G. I. N. Waterhouse, A. Badshah, A. Iqbal, M.A. Nadeem, H. Idriss, On the Synergism between Cu and Ni for Photocatalytic Hydrogen Production and their Potential as Substitutes of Noble Metals. Chem. Cat. Chem., 2016. 8(19): 3146-3155.

604. Murdoch M, G. I. N. Waterhouse, M. A. Nadeem, J. B. Metson, M.A. Keane, R.F. Howe, Llorca J, Idriss H, The effect of gold loading and particle size on photocatalytic hydrogen production from ethanol over Au/TiO_2 nanoparticles. Nat. Chem., 2011. 3(6): 489-492.

605. Jovic V., W. T. Chen, D. Sun-Waterhouse, M.G. Blackford, H. Idriss, G.I. Waterhouse, Effect of gold loading and TiO_2 support composition on the activity of Au/TiO_2 photocatalysts for H_2 production from ethanol–water mixtures. J. Catal., 2013. 305: 307-317.

606. Xuming Z., C. Yu Lim, L. Ru-Shi, T. Din Ping, Plasmonic photocatalysis. Rep. Prog. Phys., 2013. 76(4).

607. Jovic V., Z. N. Al-Azri, W. T. Chen, D. Sun-Waterhouse, H. Idriss, G. N. Waterhouse, Photocatalytic H_2 Production from Ethanol–Water Mixtures Over Pt/TiO_2 and Au/TiO_2 Photocatalysts: A Comparative Study. Top. Catal., 2013. 56(12): 1139-1151.

608. Bowker M., L. Millard, J. Greaves, D. James, J. Soares, Photocatalysis by au nanoparticles: Reforming of methanol. Gold Bull, 2004. 37(3-4): 170-173.

609. Bowker M., Sustainable hydrogen production by the application of ambient temperature photocatalysis. Green Chem., 2011. 13(9): 2235-2246.

610. Meng Q J. Wang, Q. Xie, H.. Dong, X.. Li, Water splitting on TiO_2 nanotube arrays. Catal. Today, 2011. 165(1): 145-149.

611. Al-Azri Z.H.N., W.T. Chen, A. Chan, V. Jovic, T. Ina, H. Idriss, G.I.N. Waterhouse, The roles of metal co-catalysts and reaction media in photocatalytic hydrogen production: Performance evaluation of M/TiO_2 photocatalysts (M = Pd, Pt, Au) in different alcohol–water mixtures. J. Catal., 2015. 329: 355-367.

612. Chen W.T., A. Chan, Z.H.N. Al-Azri, A.G. Dosado, M.A. Nadeem, D. Sun-Waterhouse, H. Idriss, G.I.N. Waterhouse, Effect of TiO_2 polymorph and alcohol sacrificial agent on the activity of Au/TiO_2 photocatalysts for H_2 production in alcohol–water mixtures. J. Catal., 2015. 329: 499-513.

613. Bahruji H., M. Bowker, P.R. Davies, F. Pedrono, New insights into the mechanism of photocatalytic reforming on Pd/TiO_2. Appl. Catal. B-Environ., 2011. 107(1): 205-209.

614. Majeed I., M.A. Nadeem, M. Al-Oufi, M.A. Nadeem, G.I.N. Waterhouse, A. Badshah, J.B. Metson, H. Idriss, On the role of metal particle size and surface coverage for photo-catalytic hydrogen production: A case study of the Au/CdS system. Appl. Catal. B-Environ., 2016. 182: 266-276.

615. Nadeem A.M., J.M.R. Muir, K.A. Connelly, B.T. Adamson, B.J. Metson, H. Idriss, Ethanol photo-oxidation on a rutile $TiO_2(110)$ single crystal surface. Phys. Chem. Chem. Phys., 2011. 13(17): 7637-7643.

616. Balzani V.,F. Scandola, Energy Resources through Photochemistry and Catalysis ed. M. Gratzel. 1983, NY-Acad.

617. Tian H. S. Z. Kang, X. Li, L. Qin, M. Ji, J. Mu, Fabrication of an efficient noble metal-free TiO_2-based photocatalytic system using Cu–Ni bimetallic deposit as an active center of H_2 evolution from water. Sol. Energy Mater. Sol. C., 2015. 134: 309-317.

618. Yu J., Y. Hai, B. Cheng, Enhanced photocatalytic H_2-production activity of TiO_2 by Ni $(OH)_2$ cluster modification. J. Phys. Chem. C, 2011. 115(11): 4953-4958.

619. Hong Y., P. Shi, P. Wang, W. Yao, Improved photocatalytic activity of CdS/reduced graphene oxide (RGO) for H_2 evolution by strengthening the connection between CdS and RGO sheets. Int. J. Hydrogen Energy, 2015. 40(22): 7045-7051.

620. Ortega Méndez J.A., C.R. López, E. Pulido Melián, O. González Díaz, J.M. Doña Rodríguez, D. Fernández Hevia, M. Macías, Production of hydrogen by water photo-splitting over commercial and synthesised Au/TiO_2 catalysts. Appl. Catal. B-Environ., 2014. 147(0): 439-452.

621. Gärtner F., S. Losse, A. Boddien, M.M. Pohl, S. Denurra, H. Junge, M. Beller, Hydrogen evolution from water/alcohol mixtures: effective in situ generation of an active Au/TiO_2 catalyst. Chem. Sus. Chem., 2012. 5(3): 530-533.

622. Gallo A., M. Marelli, R. Psaro, V. Gombac, T. Montini, P. Fornasiero, R. Pievo, V. Dal Santo, Bimetallic Au–Pt/TiO_2 photocatalysts active under UV-A and simulated sunlight for H_2 production from ethanol. Green Chem., 2012. 14(2): 330-333.

623. Wu M. C., P. H. Lee, D. L. Lee, Enhanced photocatalytic activity of palladium decorated TiO_2 nanofibers containing anatase-rutile mixed phase. Int. J. Hydrogen Energy, 2015. 40(13): 4558-4566.

624. Su R., R. Tiruvalam, A.J. Logsdail, Q. He, C.A. Downing, M.T. Jensen, N. Dimitratos, L. Kesavan, P.P. Wells, R. Bechstein, Designer Titania-Supported Au–Pd Nanoparticles for Efficient Photocatalytic Hydrogen Production. ACS Nano, 2014. 8(4): 3490-3497.

625. Al-Azri Z.H.N., W.-T. Chen, A. Chan, V. Jovic, T. Ina, H. Idriss, G.I.N. Waterhouse, The roles of metal co-catalysts and reaction media in photocatalytic hydrogen production: Performance evaluation of M/TiO_2 photocatalysts (M= Pd, Pt, Au) in different alcohol–water mixtures. J. Catal., 2015. 329: 355-367.

626. Elzinga E. J., R. J. Reeder, X-ray absorption spectroscopy study of Cu^{2+} and Zn^{2+} adsorption complexes at the calcite surface: Implications for site-specific metal

incorporation preferences during calcite crystal growth. Geochimica et Cosmochimica Acta, 2002. 66(22): 3943-3954.

627. Yang M. Q., Y. Zhang, N. Zhang, Z.-R. Tang, Y.-J. Xu, Visible-Light-Driven Oxidation of Primary C–H Bonds over CdS with Dual Co-catalysts Graphene and TiO_2. Sci. Rep., 2013. 3: 3314.
628. Mattigod S.V., D. Rai, A.R. Felmy, L. Rao, Solubility and solubility product of crystalline $Ni(OH)_2$. J. Sol. Chem.. 26(4): 391-403.
629. Jacobson D.M.,G. Humpston, Principles of Brazing,. 2005, Materials Park, Ohio 44073-0002: ASM Int.
630. Lid D.R., CRC Handbook of Chemistry and Physics, 76th ed. 1995-1996, Boca Raton, Florida, USA CRC Press Inc.
631. Majeed I., M.A. Nadeem, E. Hussain, G.I. Waterhouse, A. Badshah, A. Iqbal, M.A. Nadeem, H. Idriss, On the Synergism between Cu and Ni for Photocatalytic Hydrogen Production and their Potential as Substitutes of Noble Metals. Chem. Cat. Chem., 2016.
632. Chen W.T., A. Chan, D. Sun-Waterhouse, T. Moriga, H. Idriss, G.I. Waterhouse, Ni/TiO_2: A promising low-cost photocatalytic system for solar H_2 production from ethanol–water mixtures. J. Catal., 2015. 326: 43-53.
633. Skriver H. L., N. M. Rosengaard, Surface energy and work function of elemental metals. Phys. Rev. B, 1992. 46(11): 7157-7168.
634. Sui Y. W. Fu, H. Yang, Y. Zeng, Y. Zhang, Q. Zhao, Y. Li, X. Zhou, Y. Leng, M. Li, Low temperature synthesis of Cu_2O crystals: shape evolution and growth mechanism. Cryst. Growth Des., 2009. 10(1): 99-108.
635. Li Z., J. Liu, D. Wang, Y. Gao, J. Shen, $Cu_2O/Cu/TiO_2$ nanotube Ohmic heterojunction arrays with enhanced photocatalytic hydrogen production activity. Int. J. Hydrogen Energy, 2012. 37(8): 6431-6437.
636. Chan G.H., J. Zhao, E.M. Hicks, G.C. Schatz, R.P. Van Duyne, Plasmonic properties of copper nanoparticles fabricated by nanosphere lithography. Nano Lett., 2007. 7(7): 1947-1952.
637. Qiu X., M. Miyauchi, H. Yu, H. Irie, K. Hashimoto, Visible-Light-Driven Cu (II)−$(Sr_{1-y}Na_y)(Ti_{1-x}Mo_x)O_3$ Photocatalysts Based on Conduction Band Control and Surface Ion Modification. JACS, 2010. 132(43): 15259-15267.

638. Yu H., H. Irie, K. Hashimoto, Conduction band energy level control of titanium dioxide: toward an efficient visible-light-sensitive photocatalyst. JACS, 2010. 132(20): p. 6898-6899.

639. Irie H., K. Kamiya, T. Shibanuma, S. Miura, D.A. Tryk, T. Yokoyama, K. Hashimoto, Visible light-sensitive Cu (II)-grafted TiO_2 photocatalysts: activities and X-ray absorption fine structure analyses. J. Phys. Chem. C, 2009. 113(24): 10761-10766.

640. Nadeem M. A., G. I. N. Waterhouse, H. Idriss, A study of ethanol reactions on O_2-treated Au/TiO_2. Effect of support and metal loading on reaction selectivity. Surf. Sci., 2016. 650: 40-50.

641. Shamraiz U., A. Badshah, R.A. Hussain, M.A. Nadeem, S. Saba, Surfactant free fabrication of copper sulphide (CuS–Cu_2S) nanoparticles from single source precursor for photocatalytic applications. J. Saudi Chem. Soc., 2015.

642. Ajmal A., I. Majeed, R.N. Malik, M. Iqbal, M.A. Nadeem, I. Hussain, S. Yousaf, Zeshan, G. Mustafa, M.I. Zafar, M.A. Nadeem, Photocatalytic degradation of textile dyes on Cu_2O-CuO/TiO_2 anatase powders. J. Env. Chem. Eng., 2016. 4(2): 2138-2146.

643. Jiang H. L., B. Liu, Y.-Q. Lan, K. Kuratani, T. Akita, H. Shioyama, F. Zong, Q. Xu, From Metal–Organic Framework to Nanoporous Carbon: Toward a Very High Surface Area and Hydrogen Uptake. JACS, 2011. 133(31): 11854-11857.

644. Jayaramulu K., T. Toyao, V. Ranc, C. Rosler, M. Petr, R. Zboril, Y. Horiuchi, M. Matsuoka, R.A. Fischer, An in situ porous cuprous oxide/nitrogen-rich graphitic carbon nanocomposite derived from a metal-organic framework for visible light driven hydrogen evolution. J. Mater. Chem. A, 2016. 4(46): 18037-18042.

645. Al-Kuhaili M.F., Characterization of copper oxide thin films deposited by the thermal evaporation of cuprous oxide (Cu_2O). Vacuum, 2008. 82(6): 623-629.

646. Chen W. T., V. Jovic, D. Sun-Waterhouse, H. Idriss, G.I.N. Waterhouse, The role of CuO in promoting photocatalytic hydrogen production over TiO_2. Int. J. Hydrogen Energy, 2013. 38(35): 15036-15048.

647. Jung M., J. Scott, Y.H. Ng, Y. Jiang, R. Amal, CuO_x dispersion and reducibility on TiO_2 and its impact on photocatalytic hydrogen evolution. Int. J. Hydrogen Energy, 2014. 39(24): 12499-12506.

648. Wu Y., G. Lu, S. Li, The Role of Cu(I) Species for Photocatalytic Hydrogen Generation Over CuO_x /TiO_2. Catal. Lett., 2009. 133(1): 97-105.

649. Joo J.B., R. Dillon, I. Lee, Y. Yin, C.J. Bardeen, F. Zaera, Promotion of atomic hydrogen recombination as an alternative to electron trapping for the role of metals in the photocatalytic production of H_2. PNAS, 2014. 111(22): 7942-7947.

650. Chao K.J., W.Y. Cheng, T.H. Yu, S.Y. Lu, Large enhancements in hydrogen production of TiO_2 through a simple carbon decoration. Carbon, 2013. 62: 69-75.

651. Majeed I., M.A. Nadeem, M. Al-Oufi, M.A. Nadeem, G. Waterhouse, A. Badshah, J. Metson, H. Idriss, On the role of metal particle size and surface coverage for photo-catalytic hydrogen production: A case study of the Au/CdS system. Appl. Catal. B-Environ., 2016. 182: 266-276.

652. Nadeem M., K. Connelly, H. Idriss, The photoreaction of TiO_2 and Au/TiO_2 single crystal and powder with organic adsorbates. Int. J. Nanotechnol., 2012. 9(1-2): 121-162.

653. Nadeem M.A., I. Majeed, G.I.N. Waterhouse, H. Idriss, Study of ethanol reactions on H_2 reduced Au/TiO_2 anatase and rutile: effect of metal loading on reaction selectivity. Catal. Struct. React., 2015. 1(1): 61-70.

654. Jovic V., W.T. Chen, D. Sun-Waterhouse, M.G. Blackford, H. Idriss, G.I. Waterhouse, Effect of gold loading and TiO_2 support composition on the activity of Au/TiO_2 photocatalysts for H_2 production from ethanol–water mixtures. J. Catal., 2013. 305: 307-317.

655. Bowker M., L. Millard, J. Greaves, D. James, J. Soares, Photocatalysis by au nanoparticles: Reforming of methanol. Gold Bull., 2004. 37(3-4): 170-173.

656. Bowker M., Sustainable hydrogen production by the application of ambient temperature photocatalysis. Green Chem., 2011. 13(9): 2235-2246.

657. Chen, W. T., A. Chan, Z. H. N. Al-Azri, A.G. Dosado, M.A. Nadeem, D. Sun-Waterhouse, H. Idriss, G. I. N. Waterhouse, Effect of TiO_2 polymorph and alcohol sacrificial agent on the activity of Au/TiO_2 photocatalysts for H_2 production in alcohol–water mixtures. J. Catal., 2015. 329: 499-513.

658. Tian H., S. Z. Kang, X. Li, L. Qin, M. Ji, J. Mu, Fabrication of an efficient noble metal-free TiO_2-based photocatalytic system using Cu–Ni bimetallic deposit as an active center of H_2 evolution from water. Sol. Energy Mater. Sol. C., 2015. 134: 309-317.

659. Yu J., J. Ran, Facile preparation and enhanced photocatalytic H_2-production activity of $Cu(OH)_2$ cluster modified TiO_2. Energy Environ. Sci., 2011. 4(4): 1364-1371.

660. Yu J., Y. Hai, M. Jaroniec, Photocatalytic hydrogen production over CuO-modified titania. J. Colloid Interface Sci., 2011. 357(1): 223-228.

661. Xu, S., J. Ng, X. Zhang, H. Bai, D.D. Sun, Fabrication and comparison of highly efficient Cu incorporated TiO_2 photocatalyst for hydrogen generation from water. Int. J. Hydrogen Energy., 2010. 35(11): 5254-5261.

662. Wu Y., G. Lu, S. Li, The Role of Cu (I) Species for Photocatalytic Hydrogen Generation Over CuO_x/TiO_2. Catal. Lett., 2009. 133(1-2): 97-105.

663. Wu N. L.,M. S. Lee, Enhanced TiO_2 photocatalysis by Cu in hydrogen production from aqueous methanol solution. Int. J. Hydrogen Energy., 2004. 29(15):1601-1605.

664. Gombac, V., L. Sordelli, T. Montini, J.J. Delgado, A. Adamski, G. Adami, M. Cargnello, S. Bernal, P. Fornasiero, CuO_x– TiO_2 Photocatalysts for H_2 Production from Ethanol and Glycerol Solutions. J. Phys. Chem. A, 2009. 114(11): 3916-3925.

665. Sinatra L., A. LaGrow, W. Peng, A. Kirmani, A. Amassian, H. Idriss, O. Bakr, A Au/Cu_2O–TiO_2 system for photo-catalytic hydrogen production. A pn-junction effect or a simple case of in situ reduction? J. Catal., 2015. 322: 109-117.

666. Michaelson H.B., The work function of the elements and its periodicity. J. Appl. Phys., 1977. 48(11): 4729-4733.

667. Wang X., J. C. Yu, H.Y. Yip, L. Wu, P.K. Wong, S.Y. Lai, A mesoporous Pt/TiO_2 nanoarchitecture with catalytic and photocatalytic functions. Chem. Eur. J., 2005. 11(10): 2997-3004.

668. Linsebigler A.L., G. Lu, J.T. Yates Jr, Photocatalysis on TiO_2 surfaces: principles, mechanisms, and selected results. Chem. Rev., 1995. 95(3): 735-758.

669. Bisquert J., A. Zaban, P. Salvador, Analysis of the mechanisms of electron recombination in nanoporous TiO_2 dye-sensitized solar cells. Nonequilibrium steady-state statistics and interfacial electron transfer via surface states. J. Phys. Chem. B, 2002. 106(34): 8774-8782.

670. Reztsova T., C. H. Chang, J. Koresh, H. Idriss, Dark-and Photoreactions of Ethanol and Acetaldehyde over TiO_2/Carbon Molecular Sieve Fibers. J. Catal., 1999. 185(1): 223-235.

671. Siripala W., A. Ivanovskaya, T.F. Jaramillo, S.H. Baeck, E.W. McFarland, A Cu_2O/TiO_2 heterojunction thin film cathode for photoelectrocatalysis. Sol. Energy Mater. Sol. C., 2003. 77(3): 229-237.

672. Wang M., L. Sun, Z. Lin, J. Cai, K. Xie, C. Lin, p-n Heterojunction photoelectrodes composed of Cu_2O-loaded TiO_2 nanotube arrays with enhanced photoelectrochemical and photoelectrocatalytic activities. Energy Environ. Sci., 2013. 6(4): 1211-1220.

673. Cheng W.Y., T.H. Yu, K.J. Chao, S.Y. Lu, Cu_2O Decorated Mesoporous TiO_2 Beads as a Highly Efficient Photocatalyst for Hydrogen Production. Chem. Cat. Chem., 2014. 6(1): 293-300.

674. Zelaya Angel, O., J. Alvarado Gil, R. Lozada Morales, H. Vargas, A.F. Da Silva, Band-gap shift in CdS semiconductor by photoacoustic spectroscopy: Evidence of a cubic to hexagonal lattice transition. Appl. Phys. Lett., 1994. 64(3): 291-293.

675. Kim J. I., J. Kim, J. Lee, D.R. Jung, H. Kim, H. Choi, S. Lee, S. Byun, S. Kang, B. Park, Photoluminescence enhancement in CdS quantum dots by thermal annealing. Nanoscale Res. Lett., 2012. 7(1): 1-7.

676. Lahiri D., V. Subramanian, T. Shibata, E.E. Wolf, B. Bunker, P.V. Kamat, Photoinduced transformations at semiconductor/metal interfaces: X-ray absorption studies of titania/gold films. J. Appl. Phys., 2003. 93(5): 2575-2582.

677. Park J. E., T. Momma, T. Osaka, Spectroelectrochemical phenomena on surface plasmon resonance of Au nanoparticles immobilized on transparent electrode. Electrochim. Acta, 2007. 52(19): 5914-5923.

678. Dhara S., R. Kesavamoorthy, P. Magudapathy, M. Premila, B. Panigrahi, K. Nair, C. Wu, K. Chen, L. Chen, Quasiquenching size effects in gold nanoclusters embedded in silica matrix. Chem. Phys. Lett., 2003. 370(1): 254-260.

679. Zhu J., L. Huang, J. Zhao, Y. Wang, Y. Zhao, L. Hao, Y. Lu, Shape dependent resonance light scattering properties of gold nanorods. Mater. Sci Eng: B, 2005. 121(3): 199-203.

680. Templeton A.C., J.J. Pietron, R.W. Murray, P. Mulvaney, Solvent refractive index and core charge influences on the surface plasmon absorbance of alkanethiolate monolayer-protected gold clusters. J. Phys. Chem. B, 2000. 104(3): 564-570.

681. Chen W. T., A. Chan, Z. H. Al-Azri, A. G. Dosado, M. A. Nadeem, D. Sun-Waterhouse, H. Idriss, G.I. Waterhouse, Effect of TiO_2 polymorph and alcohol sacrificial agent on the activity of Au/TiO_2 photocatalysts for H_2 production in alcohol–water mixtures. J. Catal., 2015. 329: 499-513.

682. Cybula A., G. Nowaczyk, M. Jarek, A. Zaleska, Preparation and characterization of Au/Pd modified-TiO_2 photocatalysts for phenol and toluene degradation under visible light: the effect of calcination temperature. J. Nanomater., 2014. 2014: 2.

683. Kowalska E., O.O.P. Mahaney, R. Abe, B. Ohtani, Visible-light-induced photocatalysis through surface plasmon excitation of gold on titania surfaces. Phys Chem. Chem. Phys., 2010. 12(10): 2344-2355.

684. Stoev M., A. Katerski, XPS and XRD study of photoconductive CdS films obtained by a chemical bath deposition process. J. Mater. Chem., 1996. 6(3): 377-380.

685. Kolasinski K.W., Surface science: foundations of catalysis and nanoscience. 2nd ed. 2008, West Sussex PO19 8SQ, Eng. John Wiley Sons.

686. Nelin C. J., P. S. Bagus, M.A. Brown, M. Sterrer, H.J. Freund, Analysis of the Broadening of X-ray Photoelectron Spectroscopy Peaks for Ionic Crystals. Angew. Chem. Int. Ed., 2011. 50(43):10174-10177.

687. Ley L., J. Reichardt, R. Johnson, Static charge fluctuations in amorphous silicon. Phys. Rev. Lett., 1982. 49(22): 1664.

688. Stoev, M.,A. Katerski, XPS and XRD study of photoconductive CdS films obtained by a chemical bath deposition process. J. Mater. Chem., 1996. 6(3): 377-380.

689. Meissner D., C. Benndorf, R. Memming, Photocorrosion of cadmium sulfide: analysis by photoelectron spectroscopy. Appl. Surf. Sci., 1987. 27(4): 423-436.

690. Huang L., X. Wang, J. Yang, G. Liu, J. Han, C. Li, Dual cocatalysts loaded type I CdS/ZnS core/shell nanocrystals as effective and stable photocatalysts for H_2 evolution. J. Phys. Chem. C, 2013. 117(22): 11584-11591.

691. Liangbo F., W. Hanqing, J. Zhensheng, L. Qinglin, S. Mengyang, Investigation of the relation between the photogenerated intermediate radicals and the photocorrosion of CdS in aqueous and aqueous ethanol dispersions of Pt/CdS. J. Photochem. Photobiol. A-Chem., 1991. 56(1): 89-100.

692. Zhang J., S. Wageh, A. Al-Ghamdi, J. Yu, New understanding on the different photocatalytic activity of wurtzite and zinc-blende CdS. Appl. Catal B-Environ, 2016. 192: 101-107.

693. Zhao Z.Y., W.W. Dai, Structural, electronic, and optical properties of Eu-doped BiOX (X= F, Cl, Br, I): a DFT+ U study. Inorg Chem, 2014. 53(24): 13001-13011.

694. Nadeem M.A., I. Majeed, G.I. Waterhouse, H. Idriss, Study of ethanol reactions on H_2 reduced Au/TiO_2 anatase and rutile: effect of metal loading on reaction selectivity. Catal., Struct. React., 2015. 1(2): 61-70.

695. Subramanian V., E. E. Wolf, P.V. Kamat, Catalysis with TiO_2/Gold Nanocomposites. Effect of Metal Particle Size on the Fermi Level Equilibration. J. Am. Chem. Soc., 2004. 126(15): 4943-4950.

696. Nadeem M., I. Majeed, G.I.N. Waterhouse, H. Idriss, Study of ethanol reactions on H_2 reduced Au/TiO_2 anatase and rutile: effect of metal loading on reaction selectivity. Catal., Struct. React., 2014. 1(2): 61-70.

697. Linic S., P. Christopher, D.B. Ingram, Plasmonic-metal nanostructures for efficient conversion of solar to chemical energy. Nat. Mater., 2011. 10(12): 911-921.

698. Yu K., Y. Tian, T. Tatsuma, Size effects of gold nanaoparticles on plasmon-induced photocurrents of gold–TiO_2 nanocomposites. Phys. Chem. Chem. Phys., 2006. 8(46): 5417-5420.

699. Amrollahi R., M.S. Hamdy, G. Mul, Understanding promotion of photocatalytic activity of TiO_2 by Au nanoparticles. J. Catal., 2014. 319(0): 194-199.

700. Zhang Y., C. Gu, A.M. Schwartzberg, S. Chen, J.Z. Zhang, Optical trapping and light-induced agglomeration of gold nanoparticle aggregates. Phys. Rev. B, 2006. 73(16).

701. Sullivan J.L., An ultrasonic identification of diffusion mechanisms in CdS. IEEE Trans. Sonics Ultrasonics, 1985. 32(1): 71-75.

702. Janssen A., S. Meijer, J. Bontsema, G. Lettinga, Application of the redox potential for controling a sulfide oxidizing bioreactor. Biotechnol. bioeng., 1998. 60(2): 147-155.

703. Vogel R., P. Hoyer, H. Weller, Quantum-sized PbS, CdS, Ag_2S, Sb_2S_3, and Bi_2S_3 particles as sensitizers for various nanoporous wide-bandgap semiconductors. J. Phys. Chem., 1994. 98(12): 3183-3188.

704. Barnard A.S., H. Xu, First principles and thermodynamic modeling of CdS surfaces and nanorods. J. Phys. Chem. C, 2007. 111(49): 18112-18117.

705. Singaevsky A., Y. Piryatinski, D. Grynko, O. Dimitriev, Asymmetric effect of (000) and (0001) facets on surface and interface properties of CdS single crystal. Appl. Phys. A-Mater. Sci. Proc., 2011. 104(1): 493-502.

706. Koppenol W., J. Butler, Energetics of interconversion reactions of oxyradicals. Adv. Free Radical Bio. Med., 1985. 1(1): 91-131.

707. Zehr, R. T.,M. A. Henderson, Acetaldehyde photochemistry on TiO_2(110). Surf. Sci., 2008. 602(13): 2238-2249.

708. Reztsova T., C.H. Chang, J. Koresh, H. Idriss, Dark- and Photoreactions of Ethanol and Acetaldehyde over TiO_2/Carbon Molecular Sieve Fibers. J. Catal., 1999. 185(1): 223-235.

709. Wilson J. N., H. Idriss, Effect of surface reconstruction of TiO_2(001) single crystal on the photoreaction of acetic acid. J. Catal., 2003. 214(1): 46-52.

710. Wilson J. N., H. Idriss, Structure sensitivity and photocatalytic reactions of semiconductors. Effect of the last layer atomic arrangement. J. Am. Chem. Soc., 2002. 124(38): 11284-11285.

711. Schwinghammer K., B. Tuffy, M.B. Mesch, E. Wirnhier, C. Martineau, F. Taulelle, W. Schnick, J. Senker, B.V. Lotsch, Triazine based Carbon Nitrides for Visible Light Driven Hydrogen Evolution. Angew. Chem. Int. Ed., 2013. 52(9): 2435-2439.

712. Bao Y., K. Chen, AgCl/Ag/g-C_3N_4 Hybrid Composites: Preparation, Visible Light-Driven Photocatalytic Activity and Mechanism. Nano-Micro Lett., 2016. 8(2): 182-192.

713. Hussain E., I. Majeed, M.A. Nadeem, A. Badshah, Y. Chen, M.A. Nadeem, R. Jin, Titania-Supported Palladium/Strontium Nanoparticles (Pd/Sr-NPs@ P25) for Photocatalytic H_2 Production from Water Splitting. J. Phys. Chem. C, 2016. 120(31): 17205-17213.

714. Guo Q., Y. Xie, X. Wang, S. Zhang, T. Hou, S. Lv, Synthesis of carbon nitride nanotubes with the C_3N_4 stoichiometry via a benzene-thermal process at low temperatures. Chem. Commun., 2004(1): 26-27.

715. Dementjev A. P., A. de Graaf, M.C.M. van de Sanden, K.I. Maslakov, A.V. Naumkin, A.A. Serov, X-Ray photoelectron spectroscopy reference data for identification of the C_3N_4 phase in carbon–nitrogen films. Diamond Related Mater., 2000. 9(11): 1904-1907.

716. Ding Z., X. Chen, M. Antonietti, X. Wang, Synthesis of Transition Metal-Modified Carbon Nitride Polymers for Selective Hydrocarbon Oxidation. Chem. Sus. Chem., 2011. 4(2): 274-281.

717. Ferraria A. M., A. P. Carapeto, A.M. Botelho do Rego, X-ray photoelectron spectroscopy: Silver salts revisited. Vacuum, 2012. 86(12): 1988-1991.

718. Chang C., Y. Fu, M. Hu, C. Wang, G. Shan, L. Zhu, Photodegradation of bisphenol A by highly stable palladium-doped mesoporous graphite carbon nitride (Pd/mpg-C_3N_4) under simulated solar light irradiation. Appl. Catal. B-Environ., 2013. 142: 553-560.

719. Han C., L. Wu, L. Ge, Y. Li, Z. Zhao, AuPd bimetallic nanoparticles decorated graphitic carbon nitride for highly efficient reduction of water to H_2 under visible light irradiation. Carbon, 2015. 92: 31-40.

720. Al-Azri Z. H., W. T. Chen, A. Chan, V. Jovic, T. Ina, H. Idriss, G.I. Waterhouse, The roles of metal co-catalysts and reaction media in photocatalytic hydrogen production: Performance evaluation of M/TiO_2 photocatalysts (M= Pd, Pt, Au) in different alcohol–water mixtures. J. Catal., 2015. 329: 355-367.

721. Ismail A. A., S. A. Al-Sayari, D. Bahnemann, Photodeposition of precious metals onto mesoporous TiO_2 nanocrystals with enhanced their photocatalytic activity for methanol oxidation. Catal. Today, 2013. 209: 2-7.